

On the Structure, Dynamics, and Chemistry  
of Ultra-long-range Rydberg Molecules

Dissertation

zur Erlangung des Doktorgrades

an der Fakultät für Mathematik, Informatik und Naturwissenschaften

Fachbereich Physik der Universität Hamburg

vorgelegt von

Frederic Hummel

Hamburg

2021

Gutachter der Dissertation:

Prof. Dr. Peter Schmelcher  
Prof. Dr. Henning Moritz

Zusammensetzung der Prüfungskommission:

Prof. Dr. Daniela Pfannkuche  
Prof. Dr. Peter Schmelcher  
Prof. Dr. Henning Moritz  
Prof. Dr. Andreas Hemmerich  
Priv. Doz. Dr. Tim Laarmann

Vorsitzende der Prüfungskommission:

Prof. Dr. Daniela Pfannkuche

Datum der Disputation:

2. Juli 2021

Vorsitzender des Fach-Promotionsausschusses PHYSIK:

Prof. Dr. Wolfgang Hansen

Leiter des Fachbereichs PHYSIK:

Prof. Dr. Günter H. W. Sigl

Dekan der Fakultät MIN:

Prof. Dr. Heinrich Graener

## Abstract

In this cumulative thesis, we investigate ultra-long-range Rydberg molecules (ULRM), consisting of one highly excited Rydberg atom and one or several ground-state atoms, and occurring in ultracold atomic quantum gases. The molecular binding mechanism is based on the attractive Coulomb interaction between the Rydberg electron and the positively charged core of the Rydberg atom, as well as on the attractive low-energy electron–atom scattering off the neutral atoms. This electron–atom interaction can be modeled by a generalized Fermi pseudo potential including  $s$ - and  $p$ -wave contact interactions. In the Born-Oppenheimer approximation, this spawns oscillatory adiabatic potential energy surfaces that support vibrational bound states whose huge bond lengths are on the order of thousands of Bohr radii. We obtain these potentials via diagonalization of the electronic Hamiltonian within a finite basis set of electronic orbitals or via Green’s function methods. The corresponding vibrational eigenstates are retrieved from solutions of the time-independent few-body Schrödinger equation using finite difference methods and discrete variable representations.

Our research spans different aspects of ULRM. One focus is the impact of spin interactions onto the diatomic molecular structure in the presence of an external magnetic field. The description of the molecular system includes the electronic spins of the atomic valence electrons as well as the nuclear spins and their interactions. In the case of dominant  $s$ -wave scattering, the spin structure allows for control over the molecular binding energy via the mixing of the singlet and triplet scattering channels. In the case of dominant  $p$ -wave scattering, the underlying fine structure of the ionic electron–atom system engenders a unique alignment mechanism of the molecular axis with respect to the field axis. The experimental observation of this alignment is utilized to perform a high-precision measurement of the ionic fine-structure splitting. In the absence of external fields, the presence of spin-spin and spin-orbit interactions is experimentally confirmed by unique doublet and triplet substructures of the vibrational levels.

A second focus is the formulation of specific applications of ULRM in broader physical frameworks. We propose a certain class of ULRM bound by singlet  $p$ -wave interaction as the ideal initial state for the photoassociation of a heavy Rydberg system. Heavy Rydberg systems are bound pairs of oppositely charged ions that resemble a Rydberg atom, but in which the electron is replaced by a heavy anion. Beyond that, we identify conical intersections in the potential energy surfaces of diatomic ULRM spanned in the adiabatic parameter of the internuclear distance and the synthetic dimension of the electron energy. The conical intersections have observable consequences for the rates of angular-momentum-changing transitions of colliding ground-state atoms with Rydberg atoms that can be obtained from a beyond Born-Oppenheimer treatment of the coupled potentials. Furthermore, we undertake a first investigation of the nuclear quantum dynamics of ULRM exposed to external electric fields, paving the way for the study of molecular decay processes and ultracold chemistry. The wave-packet propagation is obtained from the multiconfigurational time-dependent Hartree method that solves the time-dependent Schrödinger equation *ab initio*.

The third and final focus is on the formation of triatomic ULRM consisting of one Rydberg atom in an electronically mixed state of high angular momenta and two ground-state atoms. Here, the Rydberg electron takes the role of a mediator, inducing nontrivial inter-atomic three-body interactions. Stable trimer equilibrium configurations can be deduced from dimer states via a simple building principle. Different classes of trimers show largely varying geometric arrangement as well as confinement and, correspondingly, in some cases, the vibrational bending and stretching modes adiabatically decouple.



## Zusammenfassung

Diese kumulative Dissertation widmet sich der Erforschung von ultralangreichweitigen Rydberg-Molekülen (ULRM). Diese bestehen aus einem hochangeregten Rydberg-Atom und einem oder mehreren Atomen im Grundzustand und treten in ultrakalten, atomaren Quantengasen auf. Die Molekülbindung entsteht durch die anziehende Wechselwirkung des Rydberg-Elektrons sowohl mit dem positiv geladenen, ionischen Kern des Rydberg-Atoms im Coulomb-Potential, als auch mit den neutralen Atomen durch Streuung bei sehr niedriger kinetischer Energie. Diese Wechselwirkung zwischen einem Elektron und einem neutralen Atom kann durch ein verallgemeinertes Fermi-Pseudopotential modelliert werden, das  $s$ - und  $p$ -Wellen-Streuung berücksichtigt. Im Rahmen der Born-Oppenheimer-Näherung ergeben sich dadurch oszillierende Potentialkurven, die gebundene Vibrationszustände mit gigantischen Bindungslängen von tausenden Bohr'schen Atomradien aufweisen. Wir erhalten diese Potentiale durch Diagonalisierung des elektronischen Hamiltonians in einem finiten Basissatz bestehend aus Elektronorbitalen oder unter Verwendung der Green'schen Funktion des Coulomb-Problems. Die dazugehörigen Vibrationszustände ergeben sich aus der Lösung der zeitunabhängigen Schrödingergleichung mit Hilfe von Finite-Differenzen-Methoden und Diskrete-Variablen-Repräsentierung.

In dieser Arbeit befassen wir uns mit drei unterschiedlichen Aspekten von ULRM: Den ersten Schwerpunkt stellt der Einfluss von Spin-Wechselwirkungen und externen Magnetfeldern auf die Struktur zweiatomiger Moleküle dar. Eine vollständige Beschreibung des Systems muss sowohl die Elektron-Spins von beiden Valenzelektronen als auch die Kernspins und deren Wechselwirkung untereinander berücksichtigen. Wenn der dominierende Beitrag der Wechselwirkungen durch  $s$ -Wellen-Streuung gegeben ist, bietet der Einfluss des Magnetfelds auf die Spin-Struktur, aufgrund der Mischung von Singlet- und Triplet-Streukanälen, die Möglichkeit zur Kontrolle der molekularen Bindungsenergien. Im Falle dominierender  $p$ -Wellen-Streuung ermöglicht die zugrundeliegende Feinstruktur des ionischen Systems aus neutralem Atom und Elektron einen spezifischen Mechanismus, durch den sich das Molekül mit einer bestimmten Orientierung relativ zur Magnetfeldachse ausrichtet. Wir machen uns die experimentelle Beobachtung dieser Ausrichtung des Moleküls zu Nutze um ein Präzisionsexperiment zur Messung der ionischen Feinstruktur durchzuführen. Auch ohne externe Magnetfelder können wir die Spin-Spin- und Spin-Bahn-Wechselwirkungen durch spezifische Zwillings- und Drillings-Substrukturen in den Zustandsenergien der Moleküle experimentell nachweisen.

Der zweite Schwerpunkt ist die Formulierung konkreter Anwendungen von ULRM innerhalb eines größeren physikalischen Rahmens. Wir schlagen eine bestimmte Klasse von ULRM, die durch Singlet,  $p$ -Wellen-Streuung entstehen, als den idealen Anfangszustand für die Photoassoziiierung von sogenannten schweren Rydberg Systemen vor. Schwere Rydberg Systeme bestehen aus einem gebundenen Paar entgegengesätzlich geladener Ionen. Diese ähneln einem Rydberg-Atom, in dem das Elektron durch ein Ion gleicher Kernmasse ersetzt wurde. Darüber hinaus identifizieren wir konische Durchschneidungen in den Potentialflächen von zweiatomigen ULRM, die durch den adiabatischen Parameter, der den nuklearen Abstand angibt, und durch die synthetische Dimension der Elektronenenergie aufgespannt werden. Diese konischen Durchschneidungen haben experimentell zugängliche Auswirkungen auf die Übergangsraten von Drehimpulsveränderungen des Rydberg-Elektrons, die durch Zusammenstöße von Rydberg-Atomen mit Atomen im Grundzustand verursacht werden. Dafür bedarf es einer theoretischen Betrachtung, die über die Born-Oppenheimer-Näherung hinaus geht. Außerdem führen wir eine erste Untersuchung der Quantendynamik von ULRM, die sich in einem externen elektrischen Feld befinden, durch. Dies ebnet den Weg für die weitere Erforschung von Zerfalls- und chemischen Prozessen bei ultrakalten Temperaturen. Die Zeitentwicklung des quantenmechanischen Wellenpakets wird durch die multiconfigurational time-dependent Hartree-Methode berechnet, welche

die zeitabhängige Schrödinger-Gleichung *ab initio* löst.

Der letzte Schwerpunkt ist die Formation von dreiatomigen ULRM, die aus einem Rydberg-Atom und zwei Atomen im Grundzustand bestehen, wobei sich das Rydberg-Elektron in einem gemischten Zustand hoher Drehimpulse befindet. In diesem Fall vermittelt das Elektron eine nicht triviale Dreikörper-Wechselwirkung zwischen den Atomen. Stabile Gleichgewichtskonfigurationen des dreiatomigen Moleküls können mit Hilfe eines einfachen Aufbauprinzips von den Zuständen eines zweiatomigen Moleküls abgeleitet werden. Die verschiedenen Klassen dreiatomiger Moleküle weisen extrem unterschiedliche geometrische Anordnungen auf. Auch die Stärke der Bindung in Bezug auf unterschiedliche Freiheitsgrade des Moleküls kann stark variieren, was dazu führt, dass in einigen Fällen die verschiedenen Schwingungsmoden adiabatisch entkoppeln.

# Contents

<b>Preface</b>	<b>1</b>
<b>1 Introduction</b>	<b>3</b>
1.1 Ultra-long-range Rydberg molecules . . . . .	4
1.2 Diatomic Rydberg molecules . . . . .	6
1.3 Polyatomic Rydberg molecules . . . . .	11
1.4 External fields . . . . .	13
1.5 Spin interactions . . . . .	14
1.6 Quantum vibrational dynamics . . . . .	16
<b>2 Outline of the scientific contributions</b>	<b>19</b>
2.1 Spin interactions in low- $l$ molecules . . . . .	19
2.2 Chemical and dynamical processes in high- $l$ molecules . . . . .	24
2.3 Structure of triatomic high- $l$ molecules . . . . .	28
2.4 Review . . . . .	30
<b>3 Publications</b>	<b>33</b>
3.1 Spin-interaction effects for ultralong-range Rydberg molecules in a magnetic field	35
3.2 Alignment of s-state Rydberg molecules in magnetic fields . . . . .	45
3.3 Precision spectroscopy of negative-ion resonances in ultralong-range Rydberg molecules . . . . .	53
3.4 Observation of spin-orbit-dependent electron scattering using long-range Rydberg molecules . . . . .	65
3.5 An ultracold heavy Rydberg system formed from ultra-long-range molecules bound in a stairwell potential . . . . .	79
3.6 Synthetic dimension-induced conical intersections in Rydberg molecules . . . . .	89
3.7 Electric field-induced wave-packet dynamics and geometrical rearrangement of Trilobite Rydberg molecules . . . . .	97
3.8 Building principle of triatomic Trilobite Rydberg molecules . . . . .	107
3.9 Triatomic Butterfly molecules . . . . .	115
3.10 Ultralong-range Rydberg molecules . . . . .	125
<b>4 Conclusion</b>	<b>141</b>
4.1 Discussion . . . . .	141
4.2 Perspectives . . . . .	144
<b>Bibliography</b>	<b>145</b>
<b>Dank</b>	<b>163</b>



# Preface

This cumulative dissertation bases on the following sequence of publications, which throughout the thesis will be referenced with double brackets [[.]].

- [[1]] F. Hummel, C. Fey and P. Schmelcher *Spin-interaction effects for ultralong-range Rydberg molecules in a magnetic field*. Phys. Rev. A **97**, 043422 (2018).
- [[2]] F. Hummel, C. Fey and P. Schmelcher *Alignment of s-state Rydberg molecules in magnetic fields*. Phys. Rev. A **99**, 023401 (2019).
- [[3]] F. Engel, T. Dieterle, F. Hummel, C. Fey, P. Schmelcher, R. Löw, T. Pfau and F. Meinert *Precision spectroscopy of negative-ion resonances in ultralong-range Rydberg molecules*. Phys. Rev. Lett. **123**, 073003 (2019).
- [[4]] M. Deiß, S. Haze, J. Wolf, L. Wang, F. Meinert, C. Fey, F. Hummel, P. Schmelcher and J. Hecker-Denschlag *Observation of spin-orbit-dependent electron scattering using long-range Rydberg molecules*. Phys. Rev. Res. **2**, 013047 (2020).
- [[5]] F. Hummel, P. Schmelcher, H. Ott, and H. R. Sadeghpour *An ultracold heavy Rydberg system formed from ultra-long-range molecules bound in a stairwell potential*. New J. Phys. **22**, 063060 (2020).
- [[6]] F. Hummel, M. Eiles, and P. Schmelcher *Synthetic dimension-induced conical intersections in Rydberg molecules*. Phys. Rev. Lett. **127**, 023003 (2021).
- [[7]] F. Hummel, K. Keiler, and P. Schmelcher *Electric field-induced wave-packet dynamics and geometrical rearrangement of Trilobite Rydberg molecules*. Phys. Rev. A **103**, 022827 (2021).
- [[8]] C. Fey, F. Hummel and P. Schmelcher *Building principle of triatomic Trilobite Rydberg molecules*. Phys. Rev. A **99**, 022506 (2019).
- [[9]] M. Eiles, C. Fey, F. Hummel and P. Schmelcher *Triatomic Butterfly molecules*. J. Phys. B: At. Mol. Opt. Phys. **53**, 084001 (2020).
- [[10]] C. Fey, F. Hummel and P. Schmelcher *Ultralong-range Rydberg molecules*. Mol. Phys. **118:2**, e1679401 (2020).

## Outline

This thesis is organized as follows: Chapter 1 provides an introduction to the field of Rydberg physics and its history. The subject of this thesis, ultra-long-range Rydberg molecules, are introduced in section 1.1. Section 1.2 provides a detailed overview of diatomic molecules including their experimental observation and theoretical description. The following sections introduce polyatomic molecules (1.3) as well as the treatment and consequences of external fields (1.4) and the electronic and nuclear spins (1.5). Section 1.6 serves as a brief overview of a method to study the molecular dynamics. In chapter 2, we present the outlines of our research contributions [[1-10]] published in peer-reviewed scientific journals. The contributions themselves are provided in chapter 3. Finally, chapter 4 is comprised of a concluding discussion and an outlook on future perspectives.

## Declaration of the personal contributions to the publications [[1-10]]

All analytical and computational work, as well as the writing of the manuscripts for the articles [[1,2,5,7]], was carried out by myself on the basis of regular exchange with the coauthors, in particular Peter Schmelcher. The papers [[6,9]] result from close collaboration with Matthew Eiles. We jointly performed the analytical and numerical evaluation, the analysis, and the writing of the manuscripts. For the collaborations with the experimental groups in Stuttgart and Ulm, presented in the articles [[3,4]], I was involved in the planning of the experiments regarding the identification of spectral regions for measurements, performed the numerical calculations and wrote the sections of the manuscripts focusing on the theory and analysis of the experiment. For the article [[8]], the computational work was performed by Christian Fey. We planned and coordinated the project together and discussed its results. The review article [[10]] is based on Christian Fey's dissertation. I was closely involved with the majority of the projects that form his thesis and contributed to the text and figures of the manuscript.

## List of abbreviations <sup>1</sup>

BEC	Bose-Einstein condensate(s)
CI	conical intersection(s)
DOF	degree(s) of freedom
HRS	heavy Rydberg system(s)
MCTDH	Multi-Configuration Time-Dependent Hartree method
OBD	one-body density (densities)
PES	potential energy surface(s)
SPF	single particle functions(s)
ULRM	ultra-long-range Rydberg molecule(s)

---

<sup>1</sup>abbreviations may be singular or plural as indicated by the brackets.

# Chapter 1

## Introduction

Throughout the 19th century, physicists have observed and cataloged atomic spectra, eventually culminating in the work of Johannes Rydberg in 1889, who successfully described the universal structure of simple atoms in his famous empirical Rydberg formula [1]. It took another three decades and the development of modern quantum theory to explain the physical origin of this formula. Thereby, Erwin Schrödinger [2], Werner Heisenberg [3], and Paul Dirac [4] have revolutionized our understanding of the microscopic world.

Rydberg atoms are atoms with exaggerated properties. They are characterized by a highly excited single-electron state of high principal quantum number  $n$ . The extent of the electronic cloud scales as  $n^2$ : An atom in the state  $n = 10$  is one hundred times larger than a ground-state atom. In the laboratory, realizable quantum numbers reach  $n \sim 300$  [5] and allow one to tune the atom's radius from angstroms to micrometers. Astrophysical measurements confirmed Rydberg states of carbon with  $n \sim 1000$  in extrasolar supernova remnants [6]. The huge size of Rydberg atoms endows them with extreme susceptibility to external fields and with long-range interactions with other particles. Simultaneously, they are equipped with long radiative life times that scale as  $n^3$ .

In the 20th century, Rydberg physics was devoted to the development of a precise understanding of the fundamental properties of Rydberg atoms and their interactions. In pioneering experiments, Edoardo Amaldi and Emilio Segrè studied spectra of Rydberg states in a buffer gas [7, 8]. Rydberg research was particularly facilitated by advances in atomic beam experiments [9, 10] and the invention of tunable laser systems [11]. This allowed researchers to understand their collision properties in great detail [12–16] as well as to investigate the interaction of Rydberg atoms with the electro-magnetic field [17, 18]. A highlight displaying the sensitivity of Rydberg states to microwave fields is certainly the nobel-prize awarded series of experiments by Haroche and coworkers, who used Rydberg atoms to monitor the time-dependent creation and annihilation of single photons in a cavity [19].

The end of the 20th century marked a new era of quantum mechanics and atomic physics. With the advent of sophisticated new techniques to cool and trap atoms [20–22], the control of the quantum state of a system reached a new level. This is impressively demonstrated by the realization of Bose-Einstein condensation [23–25]. An atomic gas cooled to quantum degeneracy allows for an unprecedented degree of control of the ensemble, or even of single atoms, by eliminating the thermal motion almost completely. However, typical ultracold systems, although highly versatile, are usually dominated by short-range interactions.

This enabled the ultimate boost of Rydberg research as Rydberg atoms uniquely allow for the introduction of long-range interactions. In the year 2000, three ground-breaking papers mark the significance of Rydberg atoms for modern physics: the prediction of the blockade mechanism [26], tuning of atomic interactions via Rydberg dressing [27], and the prediction of a novel molecular binding mechanism between Rydberg atoms and ground-state atoms [28]. Firstly, the strong interaction among Rydberg atoms leads to an energy shift of the atomic spectra [29, 30]. The presence of a Rydberg atom, therefore, strongly suppresses excitation

of additional Rydberg atoms in its vicinity by the same energy [31–36]. Secondly, the same principle can be exploited to induce long-range interactions between ground-state atoms by admixing with Rydberg character via an off-resonantly detuned dressing laser [37–41]. Finally, it was realized that a Rydberg atom can trap ground-state atoms in regions of maximal electronic density due to an attractive scattering interaction between the Rydberg electron and the neutral ground-state atom [42–44].

Today, Rydberg physics is broadly characterized by applications for example in the context of quantum sensing [45, 46] and quantum simulation [47, 48]. Rydberg atoms have been employed in the framework of quantum information processing [49–51] with the implementation of single-photon switches [52–54], single-photon transistors [55], and photon-photon gates [56–58] with relevance in quantum communication and networking applications. Rydberg states have also been used to create superatoms [59–61], anti-blockade [62–64], and Rydberg optical Feshbach resonances [65, 66]. An outstanding recent application of Rydberg atoms is the realization of quantum simulators with up to 51 atoms in a chain of optical tweezers [67] and even up to 256 atoms in a two-dimensional array of optical tweezers [68–71] with the prospect of creating a universal quantum computer based on this platform [72–77].

In this thesis, we focus on a novel and exotic class of molecules consisting of a Rydberg atom and one or more ground-state atoms [28]. The binding mechanism is based on the attractive interaction between the Rydberg electron and the ground-state atom. The corresponding bond lengths depend on the Rydberg principal quantum number and can reach thousands of Bohr radii, which is why they are called ultra-long-range Rydberg molecules (ULRM). At sufficiently high atomic densities, the Rydberg electron can even capture thousands of ground-state atoms simultaneously within its orbit and thereby form a Rydberg polaron [78–82]. Since the prediction of ULRM [28] and their experimental observation [42], the investigation of ULRM has become a research field involving a dozen research groups mostly located in the USA and in Germany. The main achievements of this research are presented in the course of this chapter.

Our investigations of ULRM can be summarized by three goals: Firstly, we want to unravel the impact of spin-dependent and spin-orbit dependent electron–atom scattering, which is their key binding mechanism, onto the structure and properties of ULRM. Secondly, we want to utilize this understanding to propose applications of ULRM in the context of collisions between Rydberg atoms and ground-state atoms as well as in the context of molecular charge transfer and ion formation. Here, the dynamics of ULRM play a significant role. Thirdly, we want to develop a comprehensive understanding of the transition from diatomic to polyatomic ULRM.

## 1.1 Ultra-long-range Rydberg molecules

The aforementioned prediction of ultra-long-range Rydberg molecules in 2000 [28] has a long history. When Eduardo Amaldi and Emilio Segrè investigated Rydberg alkaline atoms in the presence of perturbing noble gas atoms in the 1930s in Rome [7, 8], similar experiments were conducted by Christian Füchtbauer and coworkers in Rostock [83–85]. Due to the induced dipole interaction of the polarizable background medium, it was expected that a red shift of the atomic resonances would be observed. However, depending on the atomic species of the buffer gas, the experiments discovered both, red and blue shifts. Their respective strength depended additionally on the buffer gas density. Enrico Fermi was able to explain the experimental observations by taking into account the interaction of the Rydberg electron and the individual buffer gas atoms as a low-energy scattering process [86]. In this model, the frequency shift depends on the zero-energy  $s$ -wave scattering length of the electron–atom system as well as on the concentration of atoms. Since the scattering length depends on the atomic species and

can be both positive and negative, red and blue shifts can occur. Fermi's theory was in good agreement with the experiment and conversely allowed for the extraction of scattering lengths from the measured line shifts [85, 87].

With the advent of laser systems in the second half of the 20th century, the resolution of spectroscopic measurements was greatly increased, which enabled intense investigations of collisional processes of Rydberg atoms with ground-state atoms. This research focused on collisional line broadening and the variation of line profiles as well as on collisional transfer of Rydberg states such as  $n$ - or  $l$ -changing collisions [88–91]. The results of the experiments and the subsequent refining of the physical models was of great value for example in the application of experimental reconstruction of interatomic potentials, the development of wavelength standards, and the analysis of the composition of interstellar atmospheres [92, 93]. In this context, the scattering pseudo potential developed by Fermi proved to be a powerful tool, and was generalized by Alain Omont to be applicable to higher partial-wave interactions such as  $p$ -wave scattering [94].

The development of cooling techniques for atoms to reach the ultracold regime below criticality at the end of the 20th century meant another mile stone for control on the single-atom level [95, 96]. To prepare atoms close to their motional ground-state has intriguing consequences. In the year 2000, C. H. Greene, A. S. Dickinson, and H. R. Sadeghpour showed that the oscillatory probability density of the Rydberg electron can effectively act as a trap for the surrounding ground-state atoms and bind them to density maxima. The corresponding binding energies are in the GHz regime and can be as low as only several MHz, which is only sufficient for correspondingly cold atoms. The binding mechanism differs strongly from conventional covalent or ionic molecular bonds. This results in exotic properties, for instance oscillatory adiabatic potential energy surfaces (PES) and permanent electric dipole moments on the order of kilo debye even for homonuclear molecules, impressively surpassing the dipole moments of ground-state molecules that typically range from zero to ten debye. In this context, we need to distinguish ultra-long-range Rydberg molecules from another type of Rydberg molecules that possess tightly bound nuclei just like ground-state molecules, but highly excited electronic states, and are not within the scope of this thesis.

ULRM were experimentally confirmed in 2008 by the group of Tilman Pfau in Stuttgart [42] and have since then quickly developed into a research field of their own, providing numerous fascinating discoveries which will be further detailed throughout this chapter. Highlights include the control of molecular properties, such as dipole moments or alignment, via weak external magnetic or electric fields [97–102], as well as the emergence of polyatomic ULRM [43, 79, 103–108]. With sufficient atomic densities, a single Rydberg atom can trap many ground-state atoms within its orbit and we can witness a few-to-many-body transition to a polaron state [80, 81, 109, 110]. Extending the Rydberg orbit beyond the atomic ensemble allows for the controlled preparation of an ultracold ionic impurity immersed in the ultracold gas of ground-state atoms [111]. The major applications of ULRM include probing spacial correlations in ultracold atomic gases [112–114] and the characterization of low-energy electron–atom collisions [115–118]. They are also objected to electromagnetically induced transparency [119]. Furthermore, ULRM have been proposed as candidates for the production of ultracold negative ions [120] and other classes of exotic molecules via ion-pair dressing [121] and Rydberg dressing [122]. They can also be utilized to study the ion–atom interaction [123–127]. The atomic species in which ULRM have been produced so far are rubidium [42–44, 128, 129], cesium [130, 131], and strontium [132–134], including fermionic strontium [135]. Recently, also hetero-nuclear ULRM were observed in gases of two distinct strontium isotopes [136] and in a mixed gas of cesium and potassium [137]. ULRM are not constrained to be excited only from ultracold atomic gases, but for low principal quantum numbers, they can also be excited from tightly bound molecules such as

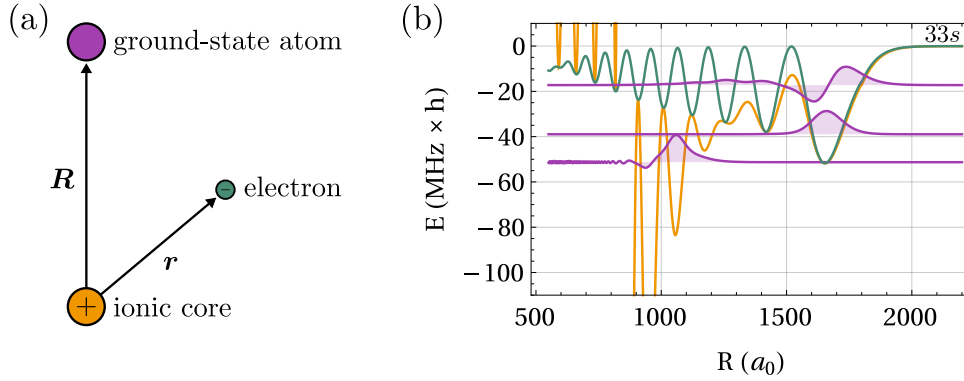


**Figure 1.1:** (a) Sketch of a diatomic  $^{87}\text{Rb}(33s)$  ultra-long-range Rydberg molecule and (b) the corresponding Born-Oppenheimer potential energy surface. The interaction between the Rydberg electron and the ground-state atom is modeled via  $s$ -wave scattering (green) or via  $s$ - and  $p$ -wave scattering (orange). Vibrational wave functions (purple) are shifted according to their binding energy. The energetically lowest one has finite amplitude at small nuclear distances and is bound by quantum reflection.

$\text{Rb}_2$  [138, 139]. The history and achievements of the field of ULRM are well documented in several reviews [140–142]. Additional reviews have a special focus on field control of ULRM [143] or on ULRM in dense gases [144]. There exist also summaries of experiments performed in particular research groups [145, 146]. Early reviews sometimes cover yet a third class of Rydberg molecules: Macrodimers are molecular states of two Rydberg atoms bound by attractive dipolar interaction [147–153] and will not be covered within this thesis.

## 1.2 Diatomic Rydberg molecules

The basic structure of a diatomic ULRM is shown in Fig. 1.1(a). It consists of a ground-state atom and a Rydberg atom, which itself consists of an ionic core and an excited valence electron. The electron interacts with the ground-state atom, which is sometimes also referred to as *perturber*. The spectrum of the Rydberg atom is described by the Rydberg formula  $E_{nl} = -1/2(n-\mu_l)^2$  (in atomic units), which depends on the principal quantum number  $n$  and the orbital angular momentum  $l$  of the electron.  $\mu_l$  is the  $l$ -dependent quantum defect that describes deviations of the hydrogenic spectrum due to the interaction of the electron with the inner shell electrons of the ionic core. In general, only low- $l$  states possess a substantial quantum defect as the core is shielded from penetration of the electron by the centrifugal-potential barrier produced by the angular momentum. In that sense, we distinguish the degenerate hydrogenlike high- $l$  states and the energetically isolated low- $l$  states. In  $^{87}\text{Rb}$ , which is the main species that we focus on, the Rydberg spectrum can be approximated by  $\mu_0 = 3.13$ ,  $\mu_1 = 2.65$ ,  $\mu_2 = 1.34$ ,  $\mu_3 = 0.0165$ , and  $\mu_{l>3} = 0$  [154–157].

For large internuclear distances  $R$  beyond the classical turning point of the Rydberg electron in the Coulomb potential, where  $R > 2n^2$ , the adiabatic Born-Oppenheimer potential energy surfaces (PES) become flat and asymptotically connect to the Rydberg energies. For small internuclear distances  $R < 100 a_0$ , where  $a_0 = 5.3 \times 10^{-11}$  m is the Bohr radius, the PES are dominated by the interaction between the ionic core and the polarizable ground-state atom, which leads to a steep descent of the PES.

At intermediate distances, when the ground-state atom overlaps with the electronic cloud of

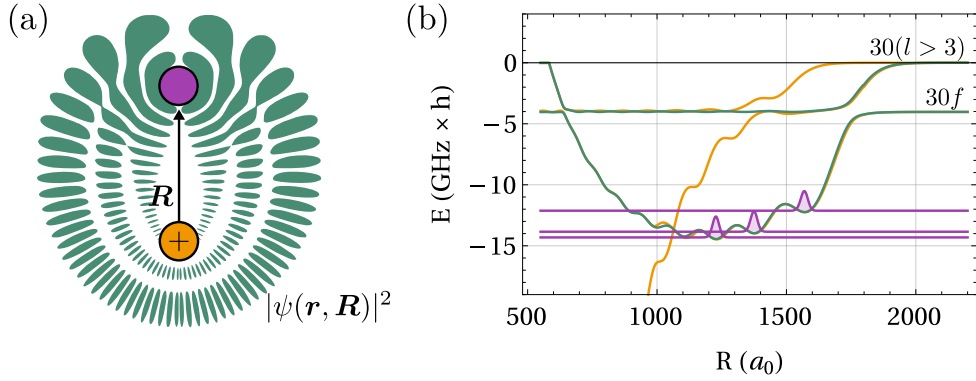


**Figure 1.2:** (a) Sketch of a diatomic  $^{87}\text{Rb}(30l)$  trilobite Rydberg molecule and its electronic density as well as (b) the corresponding Born-Oppenheimer PES. The potential of the  $30f$  state with small quantum defect is also shown. The interaction between the Rydberg electron and the ground-state atom is modeled via  $s$ -wave scattering (green) or via  $s$ - and  $p$ -wave interaction (orange). Some vibrational wave functions (purple) are localized to the potential wells.

the Rydberg atom, the scattering interaction of the electron with the neutral perturber modifies the Rydberg energy. This can be seen for the  $^{87}\text{Rb}(33s)$  state in Fig. 1.2. Here, the low-energy electron–atom interaction is modeled via  $s$ -wave scattering (green) or via  $s$ - and  $p$ -wave scattering (orange). In the case of pure  $s$ -wave scattering, the PES is proportional to an energy dependent  $s$ -wave scattering length, for which the energy of the Rydberg electron is approximated semiclassically, and to the electronic density, which leads to the characteristic oscillatory character. The potential wells can trap the ground-state atom and exemplary vibrational eigenstates are shown in purple and shifted according to their binding energy. The corresponding electronic state is to a good approximation isotropic, however, the scattering interaction can lead to small admixtures of high- $l$  states, which in turn leads to a finite permanent electric dipole moment on the order of one debye. Accordingly, the denotation  $l$ -state *ULRM* only implies that the potential asymptotically connects to the Rydberg- $l$  state, however, does not imply pure electronic- $l$  character.

Modeling the electron–atom interaction via both  $s$ - and  $p$ -wave scattering modifies the PES at small internuclear distances due to a shape resonance in the  $p$ -wave interaction. This is a general feature of electron interaction with alkaline atoms [158–163]. The resonance corresponds to a quasibound negative-ion state above the negative-ion threshold stabilized by the angular-momentum barrier. It leads to a steep potential drop, visible in Fig. 1.1(b) at approximately  $R = 900 a_0$ , that acts effectively as a potential barrier for the vibrational states and leads to the formation of vibrational resonances. They are characterized by a finite amplitude of the wave function at small internuclear distances. Illustratively, the vibrational resonances are bound by internal quantum reflection. An example of this is the energetically lowest vibrational state shown in Fig. 1.1(b). This implies an additional decay channel for the molecule via associative ionization. Here, the vibrational wave packet collides with the ionic core forming a tightly bound molecule and subsequently ionizing the Rydberg electron which obtains the excess kinetic energy of the collision [164–167].

Rydberg molecules with high- $l$  electronic character differ distinctly in their structure. Generally, the molecular system can minimize its total energy by maximizing the electronic density at the location of the ground-state atom. When the molecule is correlated to the degenerate manifold of high- $l$  states, a superposition of all available hydrogenic states is formed leading to

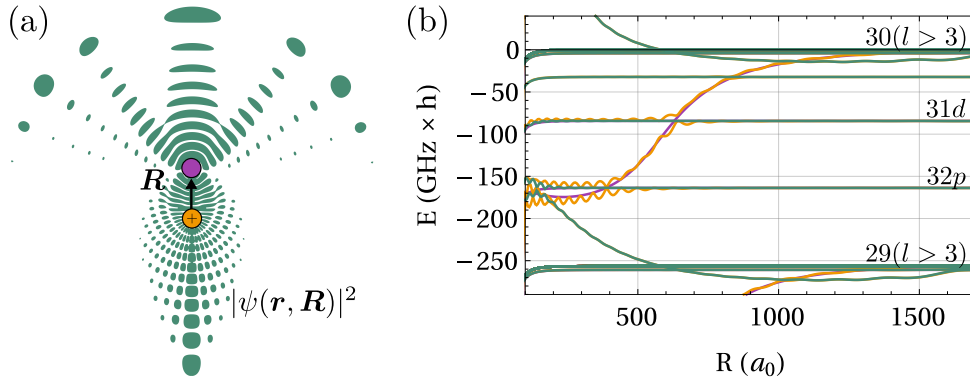


**Figure 1.3:** (a) Sketch of a diatomic  $^{87}\text{Rb}(30l)$  butterfly Rydberg molecule and its electronic density as well as (b) the corresponding Born-Oppenheimer potential energy surfaces. The interaction between the Rydberg electron and the ground-state atom is modeled via  $s$ -wave scattering (green) or via  $s$ - and  $p$ -wave interaction for the  $\Sigma$ - (orange) or  $\Pi$ -symmetry (purple). The butterfly potential cuts through the quantum defect states and stabilizes close to the  $32p$  asymptote above the degenerate  $29l$  manifold.

the paradigmatic trilobite wave function illustrated in Fig. 1.2(a), which resembles the shape of a trilobite fossil. Due to this property, trilobite molecules are polar and possess huge permanent electric dipole moments on the order of kilo debye, which is unique for homonuclear molecules. The corresponding PES are approximately one hundred times deeper than the PES corresponding to low- $l$  molecules and support vibrational states with several  $\text{GHz} \times h$  binding energies. This is shown in part (b) of Fig. 1.2 in green and purple, respectively. The trilobite PES crosses the PES associated to the  $f$  state that possesses a small quantum defect. This however, does not influence the deeply-bound vibrational states.

In the case of high- $l$  ULRM, modeling the electron–atom interaction via both  $s$ - and  $p$ -wave scattering modifies the PES only marginally. However, a third class of PES emerges corresponding to butterfly molecules. In Fig. 1.2, it is shown in orange and crosses the trilobite PES at approximately  $R = 1100 a_0$ . Similarly as in the case of low- $l$  molecules, this allows the molecule to decay via associative ionization, while the vibrational structure remains practically unaffected. The full butterfly PES is visualized in Fig. 1.3 for molecular  $\Sigma$  (orange) and  $\Pi$  symmetry (purple). Due to the resonant character of the  $p$ -wave interaction, the PES are comparably steep and cross the energetically detuned quantum defect states. They are stabilized only in the vicinity of the degenerate manifold corresponding to  $n - 1$ . Vibrational states have much smaller bond lengths than the trilobite molecules, here  $R < 500 a_0$ , while the dipole moment remains comparable.

### 1.2.1 Experimental observations

All three types of ULRM, i.e. the low  $l$ , the trilobite, and the butterfly molecule, have been observed experimentally [42, 102, 131]. The first to be realized were  $s$ -state ULRM, where the principal quantum number ranged from  $n = 34$  to 40. The molecules were created by two-photon photoassociation from an ultracold sample of  $^{87}\text{Rb}$  ground-state atoms trapped in a magnetic, Ioffe-Prichard trap in a fully spin stretched state. Subsequently a small electric field ionizes the molecules and they can be detected via ion detection. Molecular lifetimes were on the order of tens of  $\mu\text{s}$  [42, 128] and, therefore, lower than the parent Rydberg atomic

lifetimes [168]. Further investigations [129] revealed two main decay mechanisms that lead to the reduction in lifetimes: molecule–atom collisions, where the collision rate is proportional to the atomic density of the underlying ultracold gas, and inward penetration of the bound atomic pair due to the crossing of the  $s$ -state PES and the butterfly PES.

The molecular dipole moments have been quantified via Stark spectroscopy in weak electric fields. The permanent electric dipole moment is demonstrated by the observed linear Stark shift. In the case of  $s$ -state molecules, it is on the order of one debye and can be attributed to a small admixture of trilobite character to the otherwise isotropic  $s$  state [44]. In homonuclear molecules, the existence of such a permanent dipole moment is prohibited due to parity and exchange symmetry of the molecule and implies quadratic Stark shifts. However, in the case of ULRM, the electronic  $^3\Sigma_g$  and  $^3\Sigma_u$  are practically degenerate and the rotational splitting is on the order ten  $\text{kHz} \times h$ , while the experimentally relevant field strengths are on the order of  $\text{V/cm}$ . Therefore, different parity states are indistinguishable with the experimental resolutions and possess a finite permanent dipole moment [169].

Following this first series of experiments with  $s$ -state ULRM in Rubidium, also the atomic species cesium [130] and strontium [132, 133] have been studied as well as  $p$ -state [112] and  $d$ -state molecules [100, 115]. The atomic species used plays a substantial role in determining the molecular structure. Strontium, being an earth-alkaline element, does not possess a  $p$ -wave shape resonance. Therefore, the molecular lifetimes are comparable to those of their parent Rydberg atoms [134]. In cesium, the quantum defect of the  $s$  state  $\mu_0^{\text{Cs}}$  is almost integer and, therefore, the  $s$  state lies energetically close to a hydrogenic manifold. This leads to a crossing of the  $s$ -state PES with the trilobite PES. The trilobite states are high-angular-momentum states and, therefore, not accessible via one- or two-photon transitions due to angular momentum conservation. Due to the crossing of PES in cesium, trilobite ULRM possess increased admixture of  $s$ -state character. This insight has been exploited to excite trilobite ULRM with huge permanent electric dipole moments on the order of 2 kilo debye [131]. In a similar spirit, the energetic adjacency of butterfly ULRM and the  $p$  state in rubidium has been exploited to excite butterfly molecules via one-photon transitions [102]. Here, the crossing of the butterfly PES with the  $25p$ -state PES was used to excite molecules with permanent electric dipole moments on the order of 500 debye. Their bond lengths have been deduced from ro-vibrational splittings of the aligned molecule in an electric field.

### 1.2.2 Theoretical description

The essential features of both low- and high- $l$  ULRM are accurately modeled within the Born-Oppenheimer approximation [170] by the simple electronic Hamiltonian

$$H = H_0(\mathbf{r}) + V(\mathbf{r}, \mathbf{R}), \quad (1.1)$$

where  $\mathbf{r}$  is the position of the Rydberg electron and  $\mathbf{R}$  is the internuclear axis.  $H_0$  describes the Rydberg electron in the potential of the ionic core. In atomic units, its eigenenergies are given by the Rydberg formula  $E_{nl} = -1/2(n-\mu_l)^2$ , where  $n$  is the principal quantum number and  $l$  is the orbital angular momentum. The interactions of the Rydberg electron with the inner-shell electrons, electron correlation and exchange, are accounted for by the angular-momentum-dependent quantum defect  $\mu_l$ . It rapidly decreases with  $l$  due to the angular momentum barrier, which suppresses the electron's overlap with the ionic core. The corresponding electronic eigenfunctions  $\phi_{nlm}(\mathbf{r})$  depend additionally on the magnetic quantum number  $m$ . For high  $l$  with vanishing quantum defects, the radial part of  $\phi_{nlm}(\mathbf{r})$  can be expressed via hydrogenic wave functions in terms of Laguerre polynomials. For finite quantum defects, the long-range behav-

ior ( $R > 50 a_0$ ) of the radial part of  $\phi_{nlm}(\mathbf{r})$  is well described by appropriately phase-shifted Coulomb wave functions.

In a similar spirit, the interaction between the Rydberg electron and the ground-state atom can be modeled via the phase shift of a free electron that scatters off a neutral ground-state atom. In the low-energy limit, this leads to a Fermi-type, zero-range pseudo potential [28, 86, 94, 171]

$$V(\mathbf{r}, \mathbf{R}) = 2\pi a_s[k(R)]\delta(\mathbf{r} - \mathbf{R}) + 6\pi a_p^3[k(R)]\nabla_{\mathbf{r}}\delta(\mathbf{r} - \mathbf{R})\nabla_{\mathbf{r}}. \quad (1.2)$$

Here, the first term corresponds to  $s$ -wave scattering and the second term to  $p$ -wave scattering. When evaluating matrix elements of  $V$ , the differential operator  $\nabla_{\mathbf{r}}$  before the  $\delta$  function in the second term acts on the bra, while the other acts on the ket. The strengths of the respective interaction depends on the low-energy scattering lengths  $a_s[k]$  and volume  $a_p^3[k]$  that are linked to the phase shifts  $\delta_s[k]$  and  $\delta_p[k]$  of a the electron with wave number  $k$  via  $a_s[k] = -\tan \delta_s[k]/k$  and  $a_p^3[k] = -\tan \delta_p[k]/k^3$ . The electron's wave number  $k$  at the position of the ground-state atom is determined in a semiclassical approximation via its kinetic energy  $k^2/2 - 1/R = E_{nl}$ . The phase shifts  $\delta_s[k]$  and  $\delta_p[k]$  are required as input for the interaction potential and can be obtained from two-active-electron models [161, 172–176]. Analytical low-energy expansions are based on modified effective-range theory [172, 177, 178]. Here, we employ the zero-energy scattering length  $a_s[0] = -15.2 a_0$  observed in our high precision experiment [[3]] and a linear expansion  $a_s[k] = a_s[0] + \pi/3 \alpha k$ , where  $\alpha = 319.2$  a.u. [179] is the polarizability of an  $^{87}\text{Rb}$  ground-state atom. The pseudo potential formalism applies also to ULRM consisting of complex multichannel Rydberg atoms such as calcium or silicon [180].

The Hamiltonian  $H$  can be solved analytically by nondegenerate perturbation theory for the energetically isolated quantum defect states and by degenerate perturbation theory for high- $l$  states. Alternative approaches to the electronic structure rely on exact diagonalization within a finite set of basis states  $\phi_{nlm}(\mathbf{r})$  [28, 171], on Green's function methods [174, 181, 182], which can additionally be combined with  $R$ -matrix methods [183, 184], or by local frame transformation [185]. Within perturbation theory the PES of low- $l$  molecules with a global  $\Sigma$  symmetry reads

$$E_i^\Sigma(R) = -\frac{1}{2(n - \mu_0)^2} - \frac{\alpha}{2R^4} + 2\pi a_s[k(R)]|\phi_{nl0}(R)|^2 + 6\pi a_p^3[k(R)]|\nabla_R \phi_{nl0}(R)|^2, \quad (1.3)$$

where  $\nabla_R$  denotes the derivative solely in the direction of  $R$ . The second term takes into account the interaction between the ionic core and the polarizable ground-state atom, which only contributes to the PES at relatively small distances  $R < 100 a_0$ . Its impact, however, has been verified experimentally in an ultracold gas, after exciting a Rydberg atom to high principal quantum number  $n = 190$ , such that the size of the Rydberg orbit exceeds the typical internuclear separation between ground-state atoms [111]. At large internuclear distances when the kinetic energy of the Rydberg atom is small,  $p$ -wave interactions are of minor importance and the PES are proportional to the Rydberg electron's density (compare Fig. 1.1(b) for  $R > 1500 a_0$ ). This peculiarity may be exploited to imprint images of electronic orbitals onto a BEC [186, 187]. For smaller separations when the kinetic energy of the Rydberg electron approaches the energy of the shape resonance, which is approximately 25 meV in  $^{87}\text{Rb}$ , the last term in Eq. 1.3 formally diverges and the underlying perturbation theory breaks down. However, including couplings to adjacent Rydberg manifolds stabilizes the PES due to strong level repulsion such that the PES behave regularly and do not diverge. The fact that these PES are indeed trustworthy and provide the correct structure of ULRM can be understood by comparing to approximately derived PES within the semiclassical Borodin-Kazansky (BK) model developed in the context of collisional broadening [188]

$$E_i^{(BK)}(R) = -\frac{1}{2n^2} + \frac{1}{2} \left( n - \frac{\delta_l[k(R)]}{\pi} \right)^{-2}, \quad (1.4)$$

which depends only the phase shifts  $\delta_l[k(R)]$ . The BK-PES agree in overall shape and magnitude with those of the Fermi model, but lack the oscillatory behavior of the electronic density. They confirm that the PES converge adequately by level repulsion once the coupling to adjacent Rydberg states is included.

The analytic expression for the trilobite PES neglecting  $p$ -wave interactions reads [28]

$$E_t(R) = -\frac{1}{2n^2} - \frac{\alpha}{2R^4} + 2\pi a_s[k(R)] \sum_{l=4}^{n-1} |\phi_{nl0}(R)|^2 \quad (1.5)$$

and the corresponding electronic wave function

$$\psi_t(\mathbf{r}, \mathbf{R}) = \frac{1}{\mathcal{N}} \sum_{l=4}^{n-1} \sum_{m=l}^l \phi_{nlm}^*(\mathbf{R}) \phi_{nlm}(\mathbf{r}), \quad (1.6)$$

where  $\mathcal{N} = \sqrt{\sum_l |\phi_{nl0}(R)|^2}$  is a normalization constant. The nodal structure of Eq. 1.6 visible in Fig. 1.2(a) can again be understood semiclassically [189, 190]. In the classical region of  $|\psi_t(\mathbf{r}, \mathbf{R})|^2$ , within the classical turning points, the density can be obtained from interfering electron trajectories on Kepler ellipses.  $E_t(R)$  has a local minimum when the trajectories satisfy the Einstein-Brillouin-Keller quantization conditions, which imply an integer number of nodes  $n_\epsilon$  and  $n_\nu$  of the density along two elliptical directions. It is actually possible to realize the electronic wave function even without the presence of a ground-state atom via application of a specific sequence of electric and magnetic field pulses [191].

Once the solutions of the electronic Hamiltonian, i.e. the PES, are determined, the corresponding vibrational spectrum can be obtained numerically employing for example finite difference methods, a more general discrete variable representation, or shooting integration schemes. Exemplary vibrational eigenstates  $\chi_\nu(R)$  are shown in Figs. 1.1(b) and 1.2(b) in purple. The quantum reflection states can be obtained similarly as conventional shape resonances bound by the angular momentum barrier, however, employing inward scattering as opposed to outward scattering [43, 192]. The spectral line strength of a vibrational state  $\chi_\nu(R)$  can be estimated via the nuclear Franck-Condon factor  $\Gamma_\nu$ . When the initial state of a ground-state atom in the ultracold atomic ensemble is assumed to be isotropic, i.e. the probability to find an atom anywhere in the gas is the same, the factor reads

$$\Gamma_\nu \propto \left| \int dR R^2 \chi_\nu(R) \right|^2. \quad (1.7)$$

This accounts for the fact that vibrational states with approximate grade (ungrade) symmetry correspond to strong (weak) experimental signal. Furthermore, assuming the vibrational state to be well localized to single potential wells of the PES, the Franck-Condon factor becomes proportional to the pair correlation function  $g^{(2)}(R)$  of the atomic gas. This has been utilized to dynamically monitor the Mott insulator–superfluid phase transition in an optical lattice [112] and to distinguish Bose from Fermi gases [113, 114].

### 1.3 Polyatomic Rydberg molecules

ULRM are typically photoassociated from ultracold ensembles of trapped atoms. Depending on the atomic density  $\rho$  and the principal quantum number  $n$ , the average interatomic distance can be much smaller than the size of a Rydberg atom. The number of ground-state atoms  $N$  within a Rydberg volume increases rapidly  $N \sim \rho n^6$  and the Rydberg atom may bind several

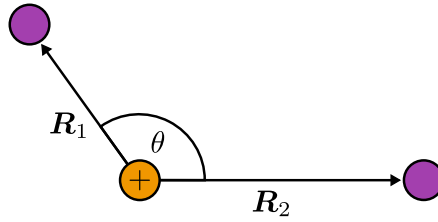


**Figure 1.4:** Sketch of a triatomic ultra-long-range Rydberg molecule with internuclear axes  $\mathbf{R}_1$  and  $\mathbf{R}_2$ , respectively, as well as the internuclear angle  $\theta$  between them.

ground-state atoms to form a polyatomic ULRM. The electronic Hamiltonian [Eq. (1.1)] can be generalized to include  $N$  ground-state atoms with coordinates  $\mathbf{R}_i$  relative to the ionic core of the Rydberg atom

$$H = H_0(\mathbf{r}) + \sum_{i=1}^N V(\mathbf{r}, \mathbf{R}_i). \quad (1.8)$$

Similarly to diatomic ULRM, polyatomic ULRM can be categorized according to the angular momentum of the Rydberg electron. Early theoretical studies of Eq. (1.8) focused on tri-, tetra-, and penta-atomic, high- $l$  ULRM [103]. Interestingly, ULRM can form *Borromean* states, which is a stable trimer with repulsive underlying two-body interaction such that no stable dimer exists [104]. Subsequent experiments, however, focused on low- $l$  ULRM since they are straight-forwardly accessible via one- or two-photon excitation. A different class of polyatomic ULRM arises, when a Rydberg atom binds a molecule. In the case of hetero-nuclear molecules, dipole interaction contributes significantly to the molecular structure. This has been studied for example in K-Rb [193–199].

Polyatomic  $s$ -state ULRM possess a shell-structure in which ground-state atoms occupy vibrational modes of the diatomic system. Therefore, the binding energies of polyatomic ground-state molecules are integer multiples of the dimer energies [43, 79, 81]. This is a consequence of isotropy of the electronic state. As  $N$  increases, the few-body regime of polyatomic ULRM characterized by individual molecular spectral lines transitions to a many-body regime, in which the Rydberg electron interacts with up to thousands of ground-state atoms [78] and which is characterized by a single collisionally broadened spectral line. In the mean-field limit, this is the scenario originally studied by Amaldi and Segre [7, 8] as well as independently by Füchtbauer [83–85] and interpreted by Fermi [86]. Assuming an energy independent  $s$ -wave scattering length, the mean energy shift is then given as

$$\Delta E = 2\pi a_s[0]\rho. \quad (1.9)$$

Generalized version of this formula, including energy-dependent scattering lengths,  $p$ -wave interaction, and inhomogeneous densities  $\rho$ , have been employed to successfully model the spectral response of Rydberg impurities in dense BEC [78, 109, 200]. Some aspects of the line shapes can only be explained by beyond-mean-field considerations and can be attributed to an emerging Rydberg *polaron* [80–82]. In the limit of large principal quantum numbers, when the Rydberg orbit exceeds the size of the atomic cloud and the Rydberg electron spends most of its time outside the gas, an ionic impurity can be realized [111, 125].

The anisotropy of Rydberg  $l > 0$ -states, complicates the structure of the corresponding polyatomic ULRM, but leads also to richer physical properties. Specifically, molecules with finite electronic angular momentum, become angle dependent and do not only depend on the

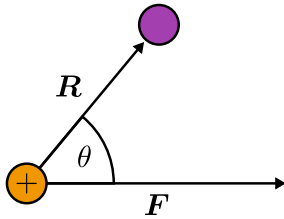


**Figure 1.5:** Sketch of a diatomic ultra-long-range Rydberg molecule in an external field. Here,  $\theta$  describes the angle between the internuclear axis  $\mathbf{R}$  and the external field axis  $\mathbf{F}$ .

internuclear distances  $R_i$ , but also on the relative angle  $\theta$ , as illustrated in Fig. 1.4 for a triatomic molecule. Due to the increased number of nuclear degrees of freedom, theoretical investigations of the PES focused mostly on randomly distributed ground-state atoms [106, 107, 200] or specific molecular geometries such as linear, planar, or cubic configurations [103, 104, 106]. More general studies of the vibrational structure of triatomic ULRM revealed that to a good approximation bending and stretching modes of the molecule can be adiabatically separated [105]. This is a consequence of the large internuclear distances in ULRM that causes bending to happen on a much longer time scale than stretching. The inherent anisotropy of  $p$ -state ULRM leads to linear equilibrium geometries of the trimer and causes the binding energies to be nonadditive as opposed to  $s$ -state ULRM. For the latter, however, the admixture of trilobite character in the PES can also cause anisotropy of the underlying electronic state. Within this thesis, we study the electronic and vibrational structure of high- $l$  triatomic ULRM. The corresponding outlines are provided in Sec. 2.3 for the cases of trilobite and butterfly molecules.

## 1.4 External fields

One of the features of ULRM that originally sparked the motivation to study them are their large permanent electric dipole moments that originate in their huge size and make them extremely susceptible to electric fields. Furthermore, the general sensitivity of the parent Rydberg atoms to external fields is inherited by the molecules. Control over the orientation  $\langle \cos \theta \rangle$  and alignment  $\langle \cos^2 \theta \rangle$  of ULRM can be achieved in weak electric and magnetic fields with field strengths on the order of tens of V/cm or tens of gauss, respectively. Here,  $\theta$  is the angle between the internuclear axis and the direction of the external field as illustrated in Fig. 1.5. This degree of control is unprecedented in conventional ground-state molecules.

In electric fields  $F < 1$  V/cm, the electronic structure of the molecule can be assumed to be unaltered and the field-free PES discussed previously are still applicable as well as the vibrational states. In this case, the electric field couples only to the molecules' dipole moment and affects the rotational spectrum [201]. Experimental observation of these spectra for butterfly molecules showed equidistant energy levels corresponding to a pendular state model. Going to zero field, an adiabatic transition to a rotational spectrum corresponding to freely rotating rigid rotors was obtained [102]. The large dipole moments, that can actually exceed the classical limit  $R$  due to the extend of the Rydberg orbital beyond the perturber, gave rise to the proposition to realize a chain of butterfly ULRM with anisotropic long-range interaction [202]. Tuning of the internuclear angle  $\theta$  via a weak external field allows for a blockade of simultaneous excitation of neighboring molecules analogously to the Rydberg blockade. Whereas in atoms this effect is induced by isotropic Van-der-Wals interactions, in ULRM the long-range interactions are of anisotropic dipolar character due to the automatically present molecular dipole moments.

Once the external fields exceed few V/cm or few gauss, respectively, they affect the electronic structure of the molecule and they have to be accounted for in the total electronic Hamiltonian. The magnetic part consists of a linear, paramagnetic term and a quadratic, diamagnetic term [203]

$$H_B = \frac{1}{2} \mathbf{B} \hat{\mathbf{l}} + \frac{1}{8} (B^2 r^2 - |\mathbf{B} \cdot \mathbf{r}|^2), \quad (1.10)$$

where  $\mathbf{B}$  is the magnetic field vector,  $\hat{\mathbf{l}}$  is the orbital angular momentum operator, and  $\mathbf{r}$  is the electronic coordinate. The electric field term is of linear order

$$H_F = \mathbf{F} \mathbf{r}, \quad (1.11)$$

with the electric field vector  $\mathbf{F}$ . For diatomic molecules, the resulting PES depend on the internuclear distance  $R$  and the relative angle  $\theta$  between the field and the internuclear axis. Hence, a rotational degree of freedom is converted into a vibrational one.

In magnetic fields, the topology of the PES undergo a qualitative change when the Zeeman splitting between magnetic states becomes comparable to the molecular binding energy. This has been studied for trilobite ULRM in the case of  $n = 35$ , the critical field strength is on the order of  $B \sim 500$  gauss. Fields below this threshold essentially conserve the overall shape of the radial trilobite PES and additionally confine the molecule to a perpendicular configuration  $\theta \sim \pi/2$ . Above the threshold, the trilobite PES splits into  $2l + 1$  Zeeman levels with equal magnetic quantum number  $m$ . The energetically lowest potential corresponds to the circular electronic state  $|m| = l$  and the vibrational states are confined in a two-dimensional harmonic potential perpendicular to the field axis [97].

In electric fields, trilobite ULRM are confined to linear configurations  $\theta \sim \pi$  and the molecular dipole moment allows for tuning the relative depth of adjacent potential wells of the trilobite PES [98]. When the linear Stark shift exceeds the molecular binding energy, the trilobite PES splits into  $n - 1 - l_{\min}$  Stark levels, where  $l_{\min}$  accounts for the number of orbital angular momentum states that are split off the degenerate, hydrogenic manifold due to their finite quantum defect. Employing both electric and magnetic fields in a parallel configuration allows for continuously tuning the molecular equilibrium configuration as a function of relative fields strengths  $F$  and  $B$  [99].

For the energetically isolated low- $l$  ULRM, the external field lifts the degeneracy of different magnetic states  $m$  and the presence of the ground-state atom only weakly perturbs each individual state. This mechanism opens fascinating possibilities to control the topology of the PES and to create molecules that have completely different geometries. In the presence of a magnetic field, the  $m = 0$  orbital of the electron of a  $d$ -state molecule, provides two distinct local minima in the two-dimensional PES allowing molecules to be aligned either axially or perpendicular to the field axis with different binding energies. A series of vibrational states corresponding to each configuration was identified experimentally and is in good agreement with theoretical predictions [100]. With additional electric fields, a superposition of different electronic orbitals can be formed and the geometry can be tuned continuously from axial to toroidal configurations [101]. For polyatomic ULRM subjected to external fields, even richer opportunities of control are expected. For instance, in addition to the external configuration, the internal angular arrangement of the nuclei can be tuned [142, 204].

## 1.5 Spin interactions

The energy scale of the electronic PES and the corresponding vibrational spectra is comparable to the fine structure of the Rydberg atom as well as to the hyperfine structure of the ground-state

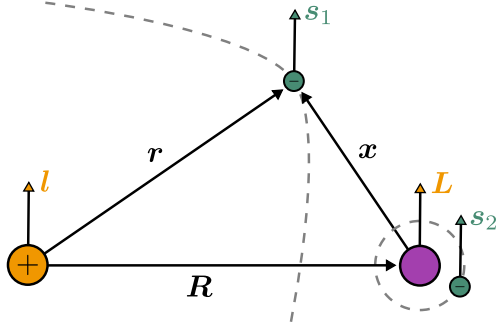


**Figure 1.6:** Angular momenta in a diatomic ultra-long-range Rydberg molecule. Both valence electrons have a spin,  $\mathbf{s}_1$  and  $\mathbf{s}_2$ , respectively. Depending on the frame of reference, the Rydberg electron has orbital angular momentum  $\mathbf{l} = -i\mathbf{r} \times \nabla$  or  $\mathbf{L} = -i\mathbf{x} \times \nabla$ . The nuclei may possess additional nuclear spin (not depicted).

atom. For the accurate description of experimental high resolution spectra of ULRM, therefore, the electronic spin structure needs to be accounted for. The relevant angular momenta are illustrated in Fig. 1.6.

The fine structure of the Rydberg atom is determined by the coupling of the spin  $\mathbf{s}_1$  of the Rydberg electron to its orbital angular momentum  $\mathbf{l}$  to form the total angular momentum  $\mathbf{j} = \mathbf{s}_1 + \mathbf{l}$ . The fine structure splitting scales as  $n^{-3}$ , similarly as the energy difference between adjacent Rydberg  $n$  manifolds and decreases rapidly with  $l$ . Therefore, its dominant impact is only on the quantum defect states and it does not alter the structure of the trilobite and butterfly states. The hyperfine structure of the Rydberg atom is typically negligible as it is proportional to the electronic wave function's amplitude at the ionic core which decays quickly with  $n$  [205]. However, for the ground-state atom it is relevant. Here, the spin  $\mathbf{s}_2$  of the ground-state atom's valence electron couples to the nuclear spin  $\mathbf{i}$  to form the total spin  $\mathbf{f} = \mathbf{s}_2 + \mathbf{i}$ .  $^{87}\text{Rb}$  has two hyperfine levels  $f = 1$  and  $f = 2$  which are separated by  $\Delta E_h = 6.834 \text{ GHz}$ . While asymptotically, for large internuclear separations both  $j$  and  $f$  are conserved, the scattering interaction of the Rydberg electron and the ground-state atom causes mixing of the two and only the total projection of these angular momenta onto the internuclear axis  $\Omega = m_j + m_f$  is a conserved quantity of the molecular system.

The first predictions of ULRM employed only a single scattering channel each for  $s$ -wave interaction [28] and  $p$ -wave interaction [171, 181], respectively. Denoting the orbital angular momentum of the Rydberg electron with respect to the ground-state atom by  $\mathbf{L} = -i\mathbf{x} \times \nabla$ , where  $\mathbf{x} = \mathbf{R} - \mathbf{r}$  is the vector between the Rydberg electron and the ground-state atom, these two channels correspond to  $L = 0$  and  $L = 1$  respectively. The scattering length  $a_s[k]$  for the  $s$ -wave channel and the scattering volume  $a_p^3[k]$  for the  $p$ -wave channel are associated to triplet scattering such that  $S = 1$  and  $\mathbf{S} = \mathbf{s}_1 + \mathbf{s}_2$  is the total electronic spin. Triplet scattering is typically much stronger than singlet scattering  $S = 0$ . In  $^{87}\text{Rb}$ , for instance, the zero-energy  $s$ -wave triplet scattering length  $a_s^S[0] = -15.2 a_0$ , while for singlet scattering it is only  $a_s^{S=0}[0] \approx 0.5 a_0$ .

It was soon realized, however, that singlet scattering can have a crucial impact on the molecular binding when the fine structure of the Rydberg atom and the hyperfine structure of the ground-state atom are included in the electronic Hamiltonian [115, 192]. Due to the interplay of these interactions, in general the total electronic spin  $S$  is not a conserved quantity anymore, and the low- $l$  ULRM are further divided into two classes characterized by  $S$ . The first class

is unaffected by the singlet channel and bound purely by triplet scattering. Hence, for this class of molecules, the predictions are not changed by including singlet scattering. The second class of low- $l$  molecules, however, is characterized by mixed singlet and triplet scattering. Correspondingly, the associated PES exhibit potential wells less deep than in the pure triplet case and the vibrational binding energies are smaller. This can be exploited as the vibrational spectra of both classes of molecules provide access to both types of scattering. This has been utilized for precision spectroscopy of  $s$ -wave phase shifts [116, 117] as well as  $p$ -wave phase shifts [118]. Furthermore, ULRM in a mixed singlet-triplet state contain contributions from both hyperfine states  $f$ . Therefore, excitation of these molecules can be used to induce remote spin flips of ground-state atoms [206] and offers another opportunity to excite high- $l$  trilobite molecules which have strong admixture of an adjacent low- $l$  hyperfine-mixed state via a two-photon transition [207]. Notably, due to electronic-configuration mixing also molecules with negative permanent electric dipole moments can be achieved, when the participating Rydberg wave functions destructively interfere in the vicinity of the ground-state atom [208].

In the case of triplet  $p$ -wave scattering, the electronic spin  $S = 1$  and the orbital angular momentum  $L = 1$  are additionally coupled by spin-orbit interaction and split into three sub-channels  $J \in \{0, 1, 2\}$  characterized by the total angular momentum  $\mathbf{J} = \mathbf{S} + \mathbf{L}$  in the frame of the ground-state atom [174]. Each of these channels corresponds to a quasibound negative-ion state that energetically splits by their fine structure. Hence, the  $p$ -wave shape resonance occurs at slightly varying energy depending on  $J$ . The splitting is on the order of meV and slightly larger in  $\text{Cs}^-$  than in  $\text{Rb}^-$ . Nevertheless, so far only the  $J = 1$  shape resonance was confirmed in  $\text{Cs}^-$  via photodetachment spectroscopy [209, 210]. For ULRM, only recently have theoretical methods been developed to account for the full spin structure including the Rydberg fine structure, the ground-state hyperfine structure, and the negative ion fine structure [211, 212]. The interaction can in this case be given in terms of the channels  $\beta = (S, L, J)$  in the frame of the negative ion

$$V(\mathbf{r}, \mathbf{R}) = \sum_{\beta} |\beta\rangle \frac{(2L+1)^2}{2} a_{\beta}[k(R)] \frac{\delta(x)}{x^{2(L+1)}} \langle\beta|, \quad (1.12)$$

where every channel is characterized by a corresponding scattering length or volume  $a_{\beta}[k]$  and  $x = |\mathbf{r} - \mathbf{R}|$  is the distance between the Rydberg electron and the ground-state atom. In Sec. 2.1, we provide outlines of our investigations of ULRM employing the full spin structure [Eq. (1.12)] with and without the presence of external magnetic fields [Eq. (1.10)]. A highlight here is the experimental confirmation of spin-orbit coupling in ULRM and a precision spectroscopy of the ionic resonances in  $^{87}\text{Rb}$ .

In polyatomic ULRM, the inclusion of the full spin structure results in a high degree of control over the molecular geometry and over the strength of the induced three-body interactions between the three nuclei. This is particularly interesting as the two ground-state atoms are in this case noninteracting and the three-body force is mediated by the Rydberg electron [108].

## 1.6 Quantum vibrational dynamics

So far, both the theoretical as well as the experimental investigations of ULRM have been focused on their electronic and vibrational structure. With ongoing progression towards higher experimental resolution and the development of ultracold-gas microscopy [167, 213], studying the dynamical properties of ULRM will soon be possible. Dynamical processes of ULRM may also lead to a better understanding of collisions between Rydberg atoms and ground-state atoms at ultracold temperatures [164–167]. According to the BO approximation, the adiabatic electronic PES serve as input for the vibrational Schrödinger equation, its time-independent

form needs to be solved for predictions of the experimental spectra of ULRM. To solve the time-dependent Schrödinger equation, many methods have been developed and refined throughout the past decades. Here, we want to give a brief overview of the multiconfigurational time-dependent Hartree (MCTDH) method [214–217]. MCTDH was originally developed as a tool for *ab initio* wave-packet propagation with a large number of degrees of freedom in the scope of quantum-molecular dynamics. It proved a powerful tool also for more general applications and is for instance used to study the dynamics of ultracold atomic gases [218–220]. We choose MCTDH to study the dynamics of ULRM because it allows straight-forwardly for the incorporation of not only a single PES, but multiple coupled PES on which the ULRM will experience beyond-BO physics [221, 222].

The key idea of MCTDH is to variationally optimize both the basis functions and the corresponding coefficients at each time step which combines the benefits of numerical precision and low computational cost as compared to other methods where e.g. only the coefficients are time dependent. The vibrational wave function depending on  $f$  degrees of freedom  $q_1, \dots, q_f$  is expanded as

$$\chi(q_1, \dots, q_f, t) = \sum_{i_1}^{n_1} \dots \sum_{i_f}^{n_f} c_{i_1 \dots i_f}(t) \prod_{d=1}^f \varphi_{i_d}^{(d)}(q_d, t). \quad (1.13)$$

$n_1, \dots, n_f$  are the numbers of basis functions to represent each degree of freedom (DOF) in terms of the time-dependent single particle function (SPF)  $\varphi_{i_d}^{(d)}$  for the  $d$ -th DOF.  $c_{i_1 \dots i_f}$  is a time-dependent coefficient. The wave-function representation [Eq. (1.13)] is not unique as both the coefficients and the SPFs are time-dependent. Therefore additional constraints on the SPF have to be imposed, which can be utilized to achieve orthonormality of the SPF:

$$\langle \varphi_i^{(d)} | \varphi_j^{(d)} \rangle = \delta_{ij} \quad \text{and} \quad \langle \varphi_i^{(d)} | \dot{\varphi}_j^{(d)} \rangle = 0. \quad (1.14)$$

The equations of motion are obtained via the Dirac-Frenckel variational principle [223, 224]. Notably, a degree of freedom, say  $q_j$  can also represent an electronic state. Then  $q_j \in \{1, \dots, \sigma\}$  takes only discrete values of up to  $\sigma$  considered electronic states. This *single-set formulation* does not change the equations of motion, however, each electronic degree of freedom is represented by the same set of SPF. Alternatively, one can turn to the *multi-set formulation*, where the wave function  $\chi$  is expanded in a set of electronic states and each state function is yet again expanded according to Eq. (1.13) such that for every electronic DOF a different set of SPF is employed [225].

Within this thesis, we present two articles employing MCTDH to study the dynamics of ULRM, the outlines of which are given in Sec. 2.2. One covers the dynamics of a diatomic trilobite molecules exposed to weak external electric fields. The other covers the nonadiabatic transitions of diatomic low-angular-momentum molecules with small quantum defect.



# Chapter 2

## Outline of the scientific contributions

In this chapter, we provide an overview of the scientific contributions presented in this dissertation. More detailed explanations may be found in the manuscripts provided in the next chapter.

### 2.1 Spin interactions in low- $l$ molecules

Published in a series of four articles, we investigate the impact of spin interactions on the structure of low- $l$  ULRM with and without exposure to weak external magnetic fields. Firstly, in  $d$ -state ULRM with a focus on the  $s$ -wave scattering regime. Secondly, in  $s$ -state ULRM with a focus on the  $p$ -wave regime. Thirdly, the predictions of the second article are observed in an experimental collaboration. And finally, in another experimental collaboration, we study  $p$ -state ULRM.

#### 2.1.1 Spin-interaction effects for ultralong-range Rydberg molecules in a magnetic field

Studying the consequences of electronic spin-spin interaction in the presence of weak external magnetic fields is motivated by the fact that in experimental settings, weak magnetic fields are practically always present as a byproduct of magneto-optical trapping of the ultracold quantum gas. Beyond that, magnetic fields offer the possibility to control and analyze the molecular orientation and alignment. In order to achieve a detailed understanding of the role of electronic spin, we focus first on the regime of dominant  $s$ -wave interaction in [[1]], before we study the effects in the regime of strong  $p$ -wave interaction in [[2]], where additional spin-orbit interaction plays a crucial role.

In a previous collaboration between our theory group and the experimental group of Tilman Pfau in Stuttgart, the structure of  $^{87}\text{Rb}$  ULRM in  $d$ -states was studied [100]. The equilibrium configuration of a  $d$ -state molecule can be oriented both, parallel and perpendicular, with respect to the magnetic field axis. This can be understood pictorially from the shape of the  $d$ -state electronic orbital which is aligned by the magnetic field along its axis and, therefore, inhibits local maxima of electronic density in these two configurations. So far, the system has been described without taking spin-dependent interactions into account. The quantitative agreement between theory and experiment in [100] confirmed the existence of both molecular configurations. Our work aims to explore quantitative corrections of binding energies and orientation angles resulting from spin interactions as well as to examine novel opportunities for molecular field control. To this end, we determine and analyze the BO PES as a function of field strength and deduce the energies and wave functions of bound vibrational states. We adopt the electronic Hamiltonian developed in [212], which for the scattering interaction between the Rydberg electron and the ground-state atom employs the pseudo potential with spin-dependent

*s*- and *p*-wave interactions. Since we address vibrational states in the outer potential wells, however, *p*-wave scattering is only of minor importance.

We consider weak homogeneous magnetic fields on the order of few up to a hundred gauss. In this regime of field strength, it is sufficient to consider the paramagnetic Zeeman term, in which the magnetic field  $\mathbf{B}$  couples linearly to the electronic spins of the Rydberg atom  $\mathbf{s}_1$  and the ground-state atom  $\mathbf{s}_2$ , as well as to the orbital angular momentum  $\mathbf{l}$  of the Rydberg electron. In the alkali ground-state atom, the orbital angular momentum is zero. Depending on the field strength, the associated Zeeman splitting  $\Delta E_z$  ranges up to approximately  $1 \text{ GHz} \times h$ . This can be compared to the energy scale of other competing interactions in the system, namely the molecular binding energy  $\Delta E_b$ , which for the considered principal quantum numbers around  $n = 40$  constitutes approximately  $30 \text{ MHz} \times h$ , the fine structure splitting of the Rydberg atom  $\Delta E_{fs} \sim 200 \text{ MHz} \times h$ , and the hyperfine splitting of the ground-state atom  $\Delta E_{hf} \sim 7 \text{ GHz} \times h$ . Based on this hierarchy, we distinguish three relevant regimes: the *s*-wave regime  $\Delta E_z < \Delta E_b$ , the fine structure regime  $\Delta E_b < \Delta E_z < \Delta E_{fs}$ , and the Zeeman regime  $\Delta E_{fs} < \Delta E_z < \Delta E_{hf}$ .

The experiment [100] was carried out in the fine structure regime, which our work also emphasizes on. In this regime, electronic states can be characterized by the approximately conserved quantities of the total angular momentum of the Rydberg electron  $j$  and its projection on the internuclear axis  $m_j$  as well as the total nuclear spin of the ground-state atom  $f$  and its projection on the internuclear axis  $m_f$ . Individual PES are separated by a Zeeman shift and can be associated to combination of these quantum numbers. Assuming spin-independent scattering, the topology of the PES depends only on  $j$  and  $m_j$  but not on  $f$  and  $m_f$ . Hence, for each combination of  $j$  and  $m_j$ , up to a constant Zeeman shift, there exist identical copies of the PES associated to different  $f$  and  $m_f$ . However, this changes drastically, when spin-dependent scattering is taken into account. In this case, the magnetic quantum numbers  $m_j$  and  $m_f$  control the admixture of singlet or triplet character in the electronic configuration. Since the triplet interaction is much stronger than the singlet interaction, this determines the depth of the potential wells of the corresponding PES and, hence, determines also the molecular alignment. This allows for tuning the molecular properties by experimentally addressing molecules with different magnetic quantum numbers  $m_f$  and  $m_j$ , which can be accomplished e.g. via adjusting the laser polarization. The maximally polarized *d*-state molecule with magnetic quantum numbers  $m_j = 5/2$  and  $m_f = 2$  is a pure electronic triplet state, hence, well described neglecting singlet interaction. However, e.g. in *d*-state molecules with magnetic quantum numbers  $m_j = 1/2$  and  $m_f = 2$ , the contribution of singlet interaction is significantly decreasing the depth of the potential wells of the corresponding PES and leads to a correction of binding energies which is consistent with the deviations observed in [100].

In the *s*-wave regime, the Zeeman splitting is too small for the magnetic quantum numbers to be conserved. Therefore, the PES, which can be associated to these quantum numbers asymptotically, strongly mix, experience numerous avoided crossings, and possess rather complex topologies. This results in rich spatial structures for molecular states, such as double or triple wells perpendicular to the field axis. This is also the case in the Zeeman regime. However, here, the magnetic field is strong enough to mix Rydberg states with different total angular momentum  $j = 3/2$  and  $j = 5/2$ . We demonstrate that this allows for continuous tuning of the molecular equilibrium angle by bringing PES of different  $j$  and  $m_j$  close to degeneracy.

The results obtained in our theoretical study of molecular equilibrium configurations in magnetic fields are readily applicable in state-of-the-art experiments. The strong coupling of the PES suggests interesting dynamical processes. Magnetic field control will also offer tunable molecular geometries in polyatomic settings, leading to exotic molecular shapes.

### 2.1.2 Alignment of $s$ -state Rydberg molecules in magnetic fields

In [[2]], we extend our investigations on spin interactions in the presence of weak external magnetic fields. While [[1]] was focused on molecules which are bound dominantly by  $s$ -wave interaction, here, we investigate molecules with smaller principal quantum number  $n < 30$  and smaller internuclear separation, where  $p$ -wave interaction is strong. In this regime, additionally to spin-spin interactions, spin-orbit interaction will be present, when both the total electron spin  $\mathbf{S}$  of the Rydberg electron and the valence electron of the ground-state atom and the orbital angular momentum  $\mathbf{L}$  of the Rydberg electron with respect to the ground-state atom are nonzero.

We demonstrate that the presence of spin-orbit coupling gives rise to an unconventional alignment mechanism in weak magnetic fields that applies to all types of ULRM, specifically also to  $s$ -state molecules. This is surprising, since the conventional alignment mechanism is restricted to ULRM where  $l > 0$ , the atomic orbitals of which are anisotropic and can be oriented with respect to the magnetic field axis. For the isotropic  $s$ -state ULRM, this is impossible. Vice versa, the experimental confirmation of such an alignment in  $s$ -state molecules would, therefore, provide clear evidence for the presence of spin-orbit coupling in the electron-atom scattering process. To measure and quantify this effect is desirable because it enables access to the closely related fine structure states of the corresponding negative ion, in this case  $\text{Rb}^-$ . These states are hardly accessible in conventional electron-atom scattering experiments [210, 226, 227] and it has been debated whether they are excited bound states or resonance states [158, 159, 161, 162]. Clear experimental evidence in the case of Rubidium was still missing.

Pictorially, the alignment process can be understood in two steps. Firstly, the magnetic field orients the electronic spin  $\mathbf{S} = \mathbf{s}_1 + \mathbf{s}_2$  along the field axis. Secondly, the coupling of spacial and spin degrees of freedom due to  $\mathbf{L} \cdot \mathbf{S}$  interaction favors certain orientations of the internuclear axis relative to  $\mathbf{S}$ , while penalizing others and can, consequently, lead to alignment of the molecule. A significant effect requires strong  $p$ -wave ( $L = 1$ ) interaction and can only be achieved in ULRM that support vibrational states in inner wells of the radial PES close to the crossing of the butterfly curve induced by the  $p$ -wave shape resonance.

We focus on  $^{87}\text{Rb}$   $s$ -state ULRM with principal quantum number  $n = 28$  at a magnetic field strength  $B = 10$  G. The Hamiltonian includes fine and hyperfine structure corrections to account for the experimental resolution [117]. Angular cuts of the PES, where the radius  $R$  is fixed to the radial equilibrium position of the inner most well, possess a pronounced angular structure with minima at  $\theta = 0, \pi/2$ , and  $\pi$ . When the  $\mathbf{L} \cdot \mathbf{S}$  coupling is switched off in the simulation, the angular dependence of the PES disappears, which allows one to clearly attribute the effect to the presence of spin-orbit interaction. Beyond that, we develop a perturbative model, which only considers a small subset of the original Hilbert space, specifically neglecting all orbital angular momentum states  $l > 0$ . The perturbative model is in good agreement with the full simulation, displaying that the angular dependence is not caused by admixture of nonzero angular momentum.

Employing a finite difference method, we determine the vibrational eigenstates supported by the two-dimensional PES and, hence, are able to quantify the orientation and alignment of the molecules. We find well localized states that can feature alignments up to  $\langle \cos^2 \theta \rangle = 0.94$ . Additionally, there exist toroidal states, where the molecular axis is perpendicular to the field axis, where  $\langle \cos^2 \theta \rangle = 0.04$ , but  $\langle \cos \theta \rangle \sim 1$ . The most deeply bound vibrational states are well described within the harmonic approximation and feature an energy spacing on the order of  $1 \text{ MHz} \times h$ , which is resolvable by state-of-the-art experiments. Observation of a series of discrete, oriented vibrational states would not only provide a clear indication for the presence of  $\mathbf{L} \cdot \mathbf{S}$  coupling, but additionally enable to determine the coupling strength based on the level

spacing. This coupling will also lead to quantitative corrections in spectra of ULRM where  $l > 0$ , however,  $s$  states provide a particular clean environment for studying this effect due to their isotropy. Furthermore, knowing the coupling strength allows for deduction of the spectral position of the shape resonances of  $\text{Rb}^-$  attributed to each  $J = |\mathbf{L} + \mathbf{S}|$ .

### 2.1.3 Precision spectroscopy of negative-ion resonances in ultralong-range Rydberg molecules

In a joint experimental and theoretical effort collaborating with the group of Tilman Pfau in Stuttgart [[3]], we experimentally observe the alignment of diatomic  $s$ -state ULRM in magnetic fields, which was theoretically predicted in [[2]]. The measurements provide clear evidence for the presence of  $\mathbf{L} \cdot \mathbf{S}$  coupling in  $^{87}\text{Rb}$  ULRM. We extract the low-energy  $p$ -wave triplet scattering phase shifts corresponding to the channels  $^3P_J$ , where  $J \in \{0, 1, 2\}$  and  $J = |\mathbf{L} + \mathbf{S}|$ , from the spectroscopic data. This includes information of the short-lived  $\text{Rb}^-$   $p$ -wave shape resonances lying approximately 25 meV above the electron detachment limit of  $\text{Rb}^-$ . Our work provides the first experimental determination of the fine structure splitting of these levels at the energies  $E_r^{J=(0,1,2)} = (24.4, 25.5, 27.7)$  meV.

Experimentally, we address molecular vibrational states via two-photon spectroscopy of a fully spin-stretched ultracold atomic gas held in a magnetic quadrupole trap. Molecules are detected via field ionization and subsequent ion detection. We focus on vibrational states that localize in the inner wells of the PES close to the crossing with the butterfly curve. This maximizes the impact of  $p$ -wave scattering as the semiclassical kinetic energy of the Rydberg electron in the Coulomb potential becomes comparable to the resonance energies  $E_r^J$ . Due to mixing of the total magnetic quantum number of the molecular system  $\Omega$  in small magnetic fields, which was studied in [[1]], it is not possible to address only a single PES even from a fully polarized atomic ensemble. Hence, at a field strength of  $B = 2.2$  G, we observe a characteristic doublet structure. At a larger field strength of  $B = 15$  G, where  $\Omega$  is approximately conserved, we observe a series of narrow spectral peaks, which correspond to pendular states bound in a single, angle-dependent PES. Here, the molecule is directed perpendicular to the magnetic field axis. Addressing other PES, for example by providing different laser polarization, allows for the photoassociation of molecules oriented parallel to the magnetic field axis.

To deduce the shape-resonance energies from the observed spectral line shapes, high accuracy of the underlying PES is necessary. We achieve this by first focusing on specific maximally polarized molecular states that are not affected by mixing of different hyperfine states  $F = 1$  and  $F = 2$ , as well as by singlet scattering  $S = 0$ . To determine the PES, this allows for the employment of Green's function methods taking into account triplet  $s$ - and  $p$ -wave scattering [228–231], which are not exposed to the convergence issues inherent to pseudo potential methods with a truncated-basis diagonalization [232, 233]. Current Green's function methods are limited to neglect the electronic spin structure and external fields.

In contrast to previous works, we do not use *ab initio* phase shift data. Instead, we employ a model potential for the electron–atom interaction, where short-range physics are encoded via a free model parameter [234]. This allows us to reproduce *ab initio* data and additionally provides the possibility to vary the phase shifts consistently over a wide range of electron energies. We then optimize the agreement between the experimentally obtained spectra and the theoretically predicted vibrational level structure for molecules with principal quantum numbers  $n \in \{31, \dots, 37\}$  in a regime, which is only weakly exposed to  $\mathbf{L} \cdot \mathbf{S}$  coupling. We retrieve the zero-energy  $s$ -wave scattering length  $a(0) = -15.2 a_0$  and the average resonance energy  $E_r^{\text{avg}} = 26.6$  meV.

In a second step, we employ the truncated-basis diagonalization to determine PES that take

into account  $\mathbf{L} \cdot \mathbf{S}$  coupling and magnetic fields. Systematic errors are minimized by adjusting the size of the employed basis set to match the PES that can be compared to those obtained from the Green's function approach. Then, we introduce the fine structure of the  $p$ -wave phase shifts, which is fitted according to the experimentally observed spectra in the regime, which is strongly affected by  $\mathbf{L} \cdot \mathbf{S}$  coupling and has been excluded from the first fitting process. To reproduce the measured line shapes, we take into account dipole transition elements and vibrational Franck-Condon factors.

The retrieved  $p$ -wave phase shifts contain the information on the resonance energies  $E_r^J$ . They are approximately 20% larger than theoretically predicted [161], which is consistent with the deviations that have been found in photodetachment experiments of  $\text{Cs}^-$ . This provides prospects for tuning and updating the model potentials of the underlying relativistic electron structure calculations. Additionally, we display the unprecedented resolution ULRM are able provide in order to study electron-atom scattering.

#### 2.1.4 Observation of spin-orbit-dependent electron scattering using long-range Rydberg molecules

In a second collaboration between theory and experiment with the group of Johannes Hecker-Denschlag in Ulm [[4]], we further investigate the impact of spin-dependent electron scattering on the vibrational structure of diatomic  $^{87}\text{Rb}$  ULRM in the  $16p$  state. Previous studies of the spin interaction in ULRM were focused on dimers bound in the outer potential well which are, hence, not subjected to strong  $p$ -wave interaction [115–117, 192]. In contrast, in this work, we study the regime of strong  $p$ -wave interaction, where also the relativistic effect of spin-orbit coupling is expected to play a role. For this purpose, low principal quantum numbers  $n$  are beneficial because potential wells that are strongly influenced by  $p$ -wave interaction due to their proximity to the crossing butterfly potentials lie at relatively large internuclear separations and support spectroscopically available vibrational states. A drawback of experiments at such low principal quantum number are the correspondingly large required ionization field strength and the difficult subsequent ion detection. Therefore, in [[5]], we detect ULRM via spontaneous decay into  $\text{Rb}^+$  and  $\text{Rb}_2^+$  ions. The optical dipole trap containing the ultracold atomic cloud is superimposed by a Paul trap, which confines the ions [235]. Molecules are excited via a one-photon transition and dominantly decay into ions subsequently. In the Paul trap, the ions undergo a micromotion, which induces collisional atom loss in the ultracold gas, which in turn can be detected via absorption imaging [236, 237].

We discover that the vibrational spectrum in this regime shows a substructure of lines in the form of singlet, doublet, or triplet peaks with internal splittings on the order of  $100 \text{ MHz} \times h$ . These structures appear as ladders of around ten multiplets with approximately constant energy spacing between  $1.3$  and  $1.8 \text{ GHz} \times h$ . The multiplet structures are correlated to the hyperfine state of the underlying atomic ensemble from which the molecules are photoassociated and which can experimentally be prepared in either a pure  $F = 1$  or a pure  $F = 2$  state. The singlets appear in the  $F = 1$  spectrum, the triplets appear in the  $F = 2$  spectrum, and the doublets appear in both revealing the mixed hyperfine character of the corresponding vibrational states. Similar spin flip excitations without multiplet substructure have previously been observed in [206].

As a theoretical model, we employ the pseudo potential Hamiltonian for ULRM that includes all spin degrees of freedom and corresponding interactions [212]. In a similar fashion as in the previous work [[3]], we optimize the size of the underlying basis set used for the diagonalization of the Hamiltonian such that the PES of the fully polarized states matches those obtained by a Green's function model that neglects spin interactions. We also use the phaseshifts obtained

in [[3]]. In fact, the such determined PES reflect the multiplet structure of the experimental spectra. We find three bundles of PES that are degenerate at large internuclear distances when the electron–atom interaction is dominated by  $s$ -wave scattering. However, for smaller internuclear distances closer to the crossing with the butterfly curve, where  $p$ -wave interaction dominates, the curves in each bundle split to form a singlet of  $F = 1$  character, a triplet of  $F = 2$  character, and a doublet of mixed hyperfine character. Each of the curves forms a well that supports a ladder of states matching the experiment.

The multiplet structure and its correlation to the hyperfine state can be understood in a perturbative model that includes the combined electronic and nuclear spin  $\mathbf{N} = \mathbf{S} + \mathbf{I}$ . However, we identify two possible physical origins of the splitting mechanism. This can be, first, the  $\mathbf{L} \cdot \mathbf{S}$  coupling, and second, the fact that the singlet and triplet  $p$ -wave scattering couple differently to the spin-up and the spin-down component of the Rydberg electron. In the regime that we consider, the first mechanism is dominant, the splitting of which exceeds the other effect by ten orders of magnitude.

Uncertainties in this study arise from the sensitivity of the determined PES to the employed basis size and the underlying phaseshift data, which could be supported by consistently studying also neighboring principal quantum numbers. However, unlike in the regime studied in [[3]], the resulting PES do not show a comparable degree of regular behavior when varying  $n$ , which complicates such studies from a theoretical perspective. Furthermore, since the observed vibrational states localize in the close vicinity of the crossing with the butterfly PES, one may have to consider beyond Born-Oppenheimer couplings to other electronic states.

## 2.2 Chemical and dynamical processes in high- $l$ molecules

A series of three articles is dedicated to push the field of ULRM in new directions. Firstly, an application of a uniquely investigated high- $l$  molecule to produce pairs of oppositely charged ultracold ions. Secondly, the prediction of a synthetic conical intersection in the PES of the trilobite and  $f$  state molecules unique to diatomic molecules. Here, the tunable Rydberg energy acts as an effective molecular parameter. And thirdly, a first investigation of wave-packet dynamics of trilobite molecules exposed to a weak external electric field with perspectives for molecular control and novel geometries.

### 2.2.1 An ultracold heavy Rydberg system formed from ultra-long-range molecules bound in a stairwell potential

In [[5]], we utilize our understanding of the structure of ULRM governed by spin interactions, to propose a specific type of molecule as an initial state for the creation of a heavy Rydberg system [238, 239]. A heavy Rydberg system is a bound pair of oppositely charged ions [240, 241] with sufficient internuclear separation to prevent rapid mutual neutralization [242]. It can be regarded as the molecular analogue of an atomic Rydberg state [243], however, the electron is replaced by the negatively charged anion [244, 245], which drastically changes the atomic properties, e.g. increasing the reduced mass by 6 orders of magnitude. ULRM offer the unique possibility to create HRS from an ultracold atomic gas [238, 246], whereas previous experiments have been focused on tightly bound molecules as initial states severely limiting the available internuclear distances and lifetimes [247–251].

The proposed ULRM initial state has not been studied previously and its binding mechanism is based on singlet  $p$ -wave scattering which leads to a unique structure of the PES resembling a stairwell which increases in energy for increasing internuclear distance, nonetheless, offering localized vibrational states due to its oscillatory character. The electronic state is of mixed

high- $l$  character similar to the trilobite or butterfly states, but can be conveniently addressed experimentally via a three photon transition to a Rydberg- $f$  state that is slightly red detuned off the hydrogenic manifold and crossing, thus, mixing with the stairwell potential.

The singlet  $p$ -wave nature of the ULRM allows for large electronic-dipole-transition elements to the anionic  $^1S_0$  state, which can be realized by an infra-red laser. The resulting HRS can be probed spectroscopically over a wide range of HRS principal quantum numbers. As an example, we focus on a Rydberg molecule bound in the stairwell potential connected to the  $^{87}\text{Rb}(24f)$ -Rydberg state, which leads to internuclear separations of approximately  $500 a_0$  and corresponding HRS principal quantum numbers  $\nu \approx 5200$ . Within an energy window of approximately  $500 \text{ GHz} \times h$ , there are as many as 100 vibrational HRS states for each rotational angular momentum state  $\Lambda$ . Due to the isotropy of the underlying ultracold gas of atoms from which the ULRM and HRS are excited, we expect dominant spectroscopic signals for a series of zero-angular momentum states. However, for imperfect isotropy, also series of nonzero  $\Lambda$  are possible, which allows for a measurement of the quantum defects of the HRS with the perspective to understand the short-range interaction of the ionic pair as the underlying model potentials can be benchmarked to reproduce the defects.

The HRS wave functions have a density maximum at the classical turning point of the Coulombic potential. Due to the low- $\Lambda$  character of the final HRS, the achievable Franck-Condon factors between the ULRM and HRS are limited, which is the main factor limiting the transition strength. We estimate the Rabi frequency of the transition to approximately 1 MHz. This is the same order of magnitude as the overall three-photon coupling for the ULRM production. Overall we find sufficient coupling strength for the branching ratio to be favorable towards the production of HRS as the lifetime of the Rydberg molecules is only limited by the lifetime of the Rydberg atom. The HRS can be detected by photodissociation and subsequent ion detection.

The prospect to produce HRS in an ultracold gas of atoms is intriguing in several respects. It offers a high degree of control over the formation and spectroscopy of HRS at internuclear distances for which the main decay channel of mutual neutralization is greatly suppressed [242]. Reactions of anions and cations, leading to neutralization, are important for the ionization balance of various cold astrophysical plasmas [252]. HRS may be used as a source for ultracold negative ions, which cannot be laser cooled due to the lack of cooling transitions requiring at least two bound states and, so far, only few atomic species have been identified which offer prospects to be cooled [253–256]. Increased production rates of HRS from ultracold atoms, may lead to the formation of two-component, strongly coupled plasmas, where, uniquely, negative and positive particles have the same mass.

### 2.2.2 Synthetic dimension-induced conical intersections in Rydberg molecules

In [[6]], we identify conical intersections (CI) in the potential energy surfaces of diatomic ULRM. We circumvent the von Neuman-Wigner theorem by employing the principal quantum number  $n$  of the Rydberg atom as a synthetic dimensions and find CI in the resulting two-dimensional PES. The CI has observable consequences for the collisional dynamics of Rydberg atoms interacting with ground-state atoms. In the vicinity of the CI, the rate for  $l$ -changing collisions is strongly suppressed independently of the temperature of the ultracold gas.

CI, points where adiabatic potential energy surfaces become degenerate, are responsible for many fascinating effects, including strong vibronic coupling and other processes beyond the Born-Oppenheimer approximation [221, 222, 225]. CI occur frequently in large molecules with many vibrational degrees of freedom and are responsible for ultrafast radiationless decay mechanisms on the femtosecond time scale [257–260]. A certain degree of tunability of CI can be

achieved using optical fields [261, 262] and they have been suggested to occur in interacting Rydberg atoms [263] and Rydberg ions [264].

In diatomic systems governed by a single vibrational parameter, the internuclear distance  $R$ , conical intersections are prohibited by the von Neumann-Wigner noncrossing rule [265, 266]. Recently, the concept of synthetic dimensions has sparked attention in several contexts, such as quantum simulation, artificial gauge fields, and photonics, as they can apparently raise the dimensionality of a system by mimicking real degrees of freedom. Synthetic dimensions have been realized in optical lattices [267, 268], and have applications in the study of artificial gauge fields [269], quantum simulation [270], photonics [271], and recently also in the context of Rydberg atoms [272].

In our manuscript, we employ the principle quantum number  $n$  of a Rydberg atom as a synthetic parameter to extend the potential energy curve of a diatomic system consisting of the Rydberg atom itself and an additional ground-state atom to a two-dimensional surface in the coordinate space of  $R$  and  $n$ . Besides supporting bound states of ULRM, at continuum energies these potentials govern the collisional processes between the two atoms. We identify conical intersections which, despite depending on this synthetic coordinate, have a clear observable consequence: A pronounced and temperature-independent suppression of angular-momentum-changing collisions, which otherwise occur rapidly in ultracold gas collisions. We unravel the underlying mechanism behind this effect by employing a beyond Born-Oppenheimer treatment. We predict the rates of these collisions for the alkaline atomic species.

Specifically, we use  $n$  to tune the electronic orbitals of Rydberg states  $|nl_0\rangle$  with a small quantum defect  $\mu_{l_0}$  on the order of  $\delta_s/\pi$ . Thus, we effectively tune the interaction of that state with a ground-state atom mediated by the Rydberg electron. At points, where the probability density of the Rydberg electron vanishes due to the nodal structure of its wave function, the interaction of the two atoms, mediated by the electron, equally vanishes. If one of these points coincides with an avoided crossing of the corresponding PES, a CI emerges. Far away from the CI, the nuclear dynamics across the PES is strictly adiabatic at ultracold temperatures and an atom initially prepared in the state  $|nl_0\rangle$  follows its adiabatic potential to pick up angular momentum forming a trilobite state. At high temperatures and corresponding high mean velocity, the atom may hop across the avoided crossing and remain in the state  $|nl_0\rangle$ . In the vicinity of the CI, the nuclear dynamics becomes dominantly diabatic and the  $l$ -changing process is strongly suppressed. The occurrence of the CI depends sensitively on the interactions strength expressed via the zero-energy scattering length of the electron-atom  $s$ -wave interaction and the quantum defect  $\mu_{l_0}$  of the initial state  $|nl_0\rangle$ . In our paper, we highlight results for rubidium, where  $l_0 = 3$ . In cesium, CI may be encountered with both the  $s$ -state and the  $f$ -state. In sodium, it is the  $d$ -state. Strontium is not expected to exhibit CI due to an unfortunate combination of quantum defects and  $s$ -wave scattering length.

Our work paves the way for further study of fundamental nonadiabatic processes in the well-controlled environments typical of ultracold Rydberg gases. The results are additionally of high relevance to the production of so-called circular Rydberg atoms [273–278], which have been identified as promising tools in the context of quantum computation and simulation. Recently, similar  $n$ - and  $l$ -changing process have sparked attention in the context of chemical reactions of ULRM [164–167]. Furthermore, the high sensitivity of the results to the underlying atomic properties, such as the quantum defects of the Rydberg atom and the electron-atom scattering length, provides a new means to extract high-precision measurements of these quantities with the experimental framework already available in state-of-the-art ultracold quantum gas experiments.

### 2.2.3 Electric field-induced wave-packet dynamics and geometrical rearrangement of trilobite Rydberg molecules

In [[7]], we investigate the quantum wave-packet dynamics of ULRM in a trilobite state bound by pure  $s$ -wave interaction. The molecule is exposed to a weak external electric field which breaks the spherical molecular symmetry and introduces an additional vibrational degree of freedom. We perturbatively deduce an analytic expression for the two-dimensional PES which is valid for field strengths up to 500 V/m in the case of  $n = 30$ . The field-free trilobite is oscillatory, exhibiting several potential wells which can support bound, localized vibrational states. Pictorially, this situation resembles to some extent a lattice; however, in this case, the relative energies of the potential wells differ. In the presence of the electric field, the PES contains a term that depends on the electric field strength, which is proportional to the molecular dipole moment. As the Rydberg electron maximizes its density at the location of the ground-state atom to account for the attractive scattering potential, the dipole moment increases with the internuclear distance  $R$ . Therefore, the potential wells at larger  $R$ , are more strongly influenced by the electric field and the overall lattice structure of the potential can be tilted depending on the electric field strength. Importantly, the tilt depends on the molecule's orientation. Large  $R$  are preferred for anti-parallel orientation with respect to the electric field, whereas small  $R$  are preferred for parallel orientation.

For the quantum wave-packet propagation, we employ the *ab initio* multiconfigurational time-dependent Hartree method [214–217]. The dynamics are triggered by quenches of the electric field. This includes different scenarios: Firstly, the molecule is prepared the field-free vibrational ground-state, i.e. radially localized to a single potential well and rotationally isotropic. At  $t = 0$ , the field is switched on and the wave packet evolves on the 2D-PES. Secondly, the molecule is prepared in the vibrational ground-state in the presence of the electric field. Depending on the field strength, the radial location may therefore differ from the field-free case. Rotationally, the wave packet is confined around the equilibrium position. Here, we choose the field to be directed anti-parallel to the  $z$  axis, therefore the equilibrium position is  $\theta = 0$ . At  $t = 0$ , the direction of the field is inverted, i.e. parallel to the  $z$  axis, and additionally, the field strength may be changed. Thirdly, starting from the first scenario, the field is periodically switched on and off.

The quench protocol dictates the character of the subsequent dynamics. In the first scenario, we observe a pendular motion of the angular one-body density (OBD). The initially isotropic wave-packet localizes in the vicinity of the equilibrium position  $\theta = \pi$  in the presence of the electric field and oscillates between these two configurations. The period of this motion is determined by the electric field strength and scales as  $F^{-1/2}$ . Contrarily, in the second scenario, where the angular wave-packet is initially localized at  $\theta = 0$ , we observe a rotational motion covering all angles, the period of which scales similarly as in the previous scenario. In both cases, after few periods, corrections to the overall character of the dynamics emerge due to the coupling to the radial degree of freedom. The radial OBD experiences a stretching oscillation with a period matching the one from the angular motion. Here, the stretch corresponds to the angular velocity of the wave packet. Additionally, a dipole oscillation on a much shorter time scale occurs. Here, only the amplitude depends on the field strength, but the period does not. This can be attributed to a slight shift of the equilibrium position of the potential well. In the first scenario, the dynamics are furthermore accompanied by a breathing oscillation. All these radial dynamics can be classified as intra-well dynamics as they occur within the initially populated potential well. Increasing the field strength above  $F = 325$  V/m, such that the radial equilibrium position shifts to the adjacent potential well, the radial dynamics drastically changes character and large-amplitude inter-well oscillations occur covering a wide range of

internuclear distances  $800 a_0 < R < 1700 a_0$ . After few oscillations, the wave packet blurs out and as many as five potential wells become populated, while the angular OBD is also evenly distributed with additional fluctuations.

Employing periodic sequences of quenches allows even more control over the molecular dynamics. Projecting the radial wave packet onto vibrational eigenstates of the field-free trilobite PES reveals that the number of states participating in the dynamics can be tuned by the waiting time between quenches. We find for example a sequence such that the molecule is in a superposition of two eigenstates localized to adjacent radial potential wells, the equilibrium positions of which differ by hundred of angstrom. To our knowledge, this is the first time that such a molecular configuration is proposed.

In our work, we focus on the molecular dynamics on a single PES. Within our employed method, it is straightforward to extend the setup to a number of coupled PES and investigate dynamics beyond the BO approximation. Including  $p$ -wave interactions into the electronic Hamiltonian provides a decay mechanism of the trilobite molecule for associative ionization via a coupling to the resonant butterfly PES, while having negligible impact on the trilobite structure. Therefore our works provides an avenue to study chemical reactions of ULRM.

## 2.3 Structure of triatomic high- $l$ molecules

In a series of two articles, we investigate the structure of triatomic trilobite and butterfly molecules and deduce intuitive building principles starting with a diatomic molecule to obtain stable trimers.

### 2.3.1 Building principle of triatomic trilobite Rydberg molecules

In [[8]], the structure of triatomic molecules that consist of two ground-state atoms and a Rydberg atom in an excited, high-angular-momentum, trilobite state is analyzed. In contrast to dimers, which possess only a single vibrational degree of freedom, the trimer is described by the two internuclear distances of the ground-state atoms to the Rydberg core  $R_1$  and  $R_2$ , as well as by the angle  $\theta$  between the two internuclear axes. The three vibrational modes corresponding to these degrees of freedom are symmetric stretching, where  $R_1 = R_2$ , asymmetric stretching, where  $R_1 - R_2 = \text{constant}$ , and bending, where  $\theta$  oscillates.

Previous studies of low- $l$  trimers revealed that the angular structure of the underlying PES and the resulting equilibrium bond angles are dictated by the angular momentum of the Rydberg atom:  $s$  trimers are almost isotropic,  $p$  trimers are linear ( $\theta = 0$  and  $\pi$ ), and  $d$  trimers are either linear or perpendicular ( $\theta = 0, \pi/2$  and  $\pi$ ). For the high- $l$  trilobite states and the correspondingly large Hilbert space of degenerate hydrogenic wave functions, we expect to find a rich angular structure and a multitude of equilibrium angles that we aim to derive and understand in [[6]].

Our employed model considers only  $s$ -wave interaction and neglects corrections due to fine and hyperfine structure. This allows one to derive the PES analytically. We obtain two PES labeled  $E_{\pm}(R_1, R_2, \theta)$  that are closely related to the trilobite orbital  $\phi(\mathbf{r}, \mathbf{R}_i)$ , when only the  $i$ -th ground-state atom is present. The trimer state is subjected to a coupling proportional to  $|\phi(R_1, R_2)|^2$ , which corresponds to the probability density of the trilobite orbital corresponding to one ground-state atom evaluated at the position of the other ground-state atom and is, therefore, symmetric with respect to atom exchange  $|\phi(R_1, R_2)|^2 = |\phi(R_2, R_1)|^2$ . Strong coupling leads to deviations of the trimer PES  $E_{\pm}$  from the dimer PES and, therefore, the energetically lower PES  $E_-$  can support trimers that are lower in energy than the dimers.

Hence, we deduce a straight-forward building principle for trilobite trimers: Considering a stable diatomic trilobite molecule with electronic orbital  $\phi(\mathbf{r}, \mathbf{R}_1)$ , placing the other ground-state atom in a local maximum of the electronic density results in a stable trilobite trimer. Due to the elliptically-shaped nodal pattern of the dimer densities, a plethora of angular equilibrium angles emerges. Furthermore, strong couplings  $|\phi(R_1, R_2)|^2$  allow for the stabilization of trimers at bond lengths in which dimers are unstable. A special case of this effect was studied in linear neon trimers [104].

We employ a finite difference method to determine vibrational states of the triatomic trilobite molecule. Due to the large number of local minima, we pick a few exemplary geometries to illustrate the trimer's properties. Here, we focus on bent geometries, which have not been studied previously. A typical geometry is a small, but finite bending angle  $\theta$  and two distinct internuclear distances  $R_1$  and  $R_2$ , which resembles a check mark ( $\checkmark$ ). We find several bound states that localize around the potential minimum. The energetic spacing of stretching and bending modes is comparable and on the order of  $100 \text{ MHz} \times h$ . This is in contrast to low- $l$  trimers, the less confined bending motion of which typically decouples from the stretching motion allowing for an adiabatic separation of the two degrees of freedom [105].

The investigated trilobite trimers are a paradigm example of an induced three-body force, which, in our case, couples two noninteracting ground-state atoms via the mutual interaction with the Rydberg electron. Three-body interactions have been applied in Rydberg systems to realize three-qubit gates for quantum computing, which may speed up certain quantum algorithms and are frequently used for quantum error corrections [279, 280].

### 2.3.2 Triatomic butterfly molecules

In [[9]], we extend our investigations of triatomic ULRM to butterfly molecules bound by resonant  $p$ -wave scattering. Similarly to trilobite molecules, the butterflies exist in a hybridized electronic state consisting of a superposition of a large number of degenerate, hydrogenic, high-angular-momentum states. The trimers can be divided into *even* and *odd* molecules depending on their parity under reflection of the electronic wave function through the molecular plane.

In our model Hamiltonian, we consider  $s$ - and  $p$ -wave interaction of the Rydberg electron and the ground-state atoms, but neglect corrections due to fine and hyperfine structure. This Hamiltonian can be conveniently expanded in a basis of *dimer orbitals* that are known analytically: the trilobite orbital and three butterfly orbitals, each for a component of the vectorial  $p$ -wave operator corresponding to the derivatives of the electronic wave function in spherical coordinates. As each of the three components lead to a characteristic dimer orbital, these are referred to as  $R$ -,  $\theta$ -, and  $\phi$ -butterfly, respectively. The trilobite states are energetically decoupled from the butterfly states and can, to a good approximation, be studied independently, which was done in [[6]]. Due to the parity symmetry of the molecular system, the remaining  $6 \times 6$  Hamiltonian has block-diagonal form and consists of a  $2 \times 2$ -block for the odd parity states and a  $4 \times 4$ -block for the even parity states.

The resonant nature of the  $p$ -wave interaction causes the scattering volume to diverge and the butterfly PES are only constrained to finite values via coupling to additional Rydberg manifolds. Furthermore, since the PES cover energetically almost the entire region between adjacent manifolds, also the coupling to low- $l$  Rydberg states, detuned from the hydrogenic manifold by a noninteger quantum defect, becomes important. We therefore diagonalize the electronic Hamiltonian in a basis including three Rydberg manifolds and the quantum defects for  $s$ ,  $p$ , and  $d$  states. Spectroscopic experiments in this regime [102], [[4]], along with more accurate theoretical approaches [174, 212], have shown that the finite-basis-set diagonalization of the pseudo potential remains a good approximation.

The odd parity molecules can be understood from the simple structure of the block Hamiltonian, which allowed us to analytically express the trimer PES  $E_{\pm}^{odd}(R_1, R_2, \theta)$  in terms of the dimer PES of the  $\phi$ -butterfly corresponding to the magnetic quantum numbers  $m = \pm 1$  and featuring a smooth functional behavior in  $R$  as well as a single global minimum. Similar to the trilobite PES studied in [[6]], the odd butterfly trimer PES possess a coupling term that depends on the density of the dimer orbital evaluated at the position of the remaining ground-state atom, which introduces an oscillatory behavior for the trimer PES. However, the coupling scales as  $\propto 1/\sin^4 \theta$  and, therefore, the trimer PES depend very sharply on the bending angle and stable trimers are only found near the linear geometry  $\theta = \pi$ .

In contrast to the relative simplicity of the odd trimer PES, the even trimer PES  $E_{\pm}^{even}(R_1, R_2, \theta)$  are highly complex, varying rapidly as a function of all coordinates, particularly of  $\theta$ . Nevertheless, the rather straight forward building principle developed for trilobite trimers in [[6]], can be generalized to be applicable also to the even butterfly trimers. While in the case of trilobite trimers, the second ground-state atom has to be placed in a local density maximum of the dimer orbital in order to achieve a stable trimer, in the case of the butterfly, the second ground-state atom has to be placed at a point of a *locally steepest gradient* of the wave function of the dimer orbital. This gradient can be with respect to  $R$  or with respect to  $\theta$  for either of the  $R$ - or  $\theta$ -butterfly dimer orbitals. If more of these couplings elements can be maximized at the same time, the deeper the corresponding local trimer minimum.

We analyze, additionally, the vibrational spectra of the butterfly trimers by aid of combined discrete variable and finite difference methods. To an excellent approximation, states belonging to the same bond lengths  $R_1 = R_2$  are well described by harmonic ladders with spacings of approximately  $400 \text{ MHz} \times h$  for asymmetric stretching,  $1.2 \text{ GHz} \times h$  for symmetric stretching, and  $2.5 \text{ GHz} \times h$  for bending modes. The order of these modes differs from triatomic low- $l$  Rydberg molecules, which are less tightly bound in  $\theta$  and the corresponding bending modes have much smaller energy spacing [105]. It also differs from triatomic trilobite molecules, where the energy spacing of bending and stretching modes is almost equal [[6]].

Interesting experimental applications for high- $l$  Rydberg trimers may be based on the large dipole moments these molecules offer, which allows for a large degree of field control. Even linear trimers will possess nonzero dipole moments due to either asymmetric bond length or mixing of  $R$ - and  $\theta$ -dimer orbitals. The mixing of symmetric and asymmetric stretch modes in the excitation spectrum also offers compelling opportunities for dynamical properties and nonadiabatic physics.

## 2.4 Review

We published a review article on the history and current status of the field of ULRM.

### 2.4.1 Ultralong-range Rydberg molecules

In [[10]], we review the experimental and theoretical contributions on ULRM, which since their prediction in 2000 [28] and subsequent observation in 2008 [42] have become a vibrant area of research. Our aim is to give an overview of the development of the field, while a special emphasis is put on specific aspects of ULRM, which have recently sparked a lot of attention. These are, firstly, control of molecular properties such as orientation, alignment, or dipole moments via weak external magnetic or electric fields. Secondly, polyatomic ULRM with specific studies on the structure of few body molecules constituted of not only one but several ground-state atoms and the emergence of many-body phenomena like Rydberg molecular polarons. Thirdly,

probing of spatial correlations in ultracold atomic ensembles. Finally, characterization of low-energy electron–atom collisions.

We start with a historical reflection on the field of Rydberg atoms interacting with neutral ground-state atoms. This was begun in the 1930s with experiments in Rome and Rostock studying the spectra of Rydberg atoms in the presence of a perturbing buffer gas consisting of different noble gas atomic species. These experiments led to the development of the theoretical pseudo-potential method to account for the scattering of the Rydberg electron with the neutral atoms by Enrico Fermi. This very description in terms of the low-energy *s*-wave scattering along with the spectroscopic structure of Rydberg atoms dictated by the quantum defects of low-angular-momentum states gives rise to the prediction of ULRM at ultracold temperatures.

The basic molecular properties are reviewed. In the energetically isolated low-*l* Rydberg states, the *s*-wave scattering interaction leads to the formation of oscillatory adiabatic PES that can trap individual ground-state atoms at large internuclear distances. The corresponding electronic states are isotropic except for tiny admixtures of high-*l* states that lead to a finite, but small permanent electric dipole moment. These type of ultra-long-range Rydberg molecules are termed *unpolar*. In contrast, in the degenerate manifold of high-*l* states the scattering interaction leads to a super position of all electronic states leading to the *polar* trilobite molecules with large permanent electric dipole moments on the order of kilo debye. Including also *p*-wave interaction in the model leads to the emergence of another class of polar high-*l* molecules called butterfly.

All three classes of ULRM have been observed experimentally. Experiments are typically conducted in alkali atoms like rubidium and cesium. But ULRM have also been observed in the earth-alkali element strontium and have been predicted for species with more complex electronic structure. In the original observation [42], the detection of ULRM was based on two-photon laser excitation for photoassociation of the molecule and subsequent ionization of the Rydberg electron by an electric field. The ion detection rates at specific laser energies can than be linked to vibrational states of ULRM. Lifetimes of ULRM are typically shorter than that of the parent Rydberg atom mainly due to two decay-mechanisms: Molecule–atom collisions at a rate proportional to the atomic density and tunneling to smaller internuclear distances due to crossings between the *s*-state and the butterfly PES leading to tightly bound molecular ions, e.g.  $\text{Rb}_2^+$ .

Emphasis is put on the theoretical description of ULRM which becomes increasingly refined to meet the increasing resolution of experimental observations. Along with the fine structure of the Rydberg atom and the hyperfine structure of the ground-state atom, the total electronic state of the Rydberg atom and the valence electron of the ground-state atom dictates the scattering process.

We highlight key observations like the transition from few-body spectra with individual molecular peaks for ULRM that bind up to five ground-state atoms to an overall shift of the Rydberg line in a high-density environment. In triatomic molecules the Rydberg electron can mediate an effective three-body interaction between ground-state atoms that are otherwise noninteracting. In external fields, the electronic orbital can be aligned to control molecular geometry. Spin interaction effects can be exploited to perform a spin flip of the hyperfine state of the ground-state atom.

Perspectives on ULRM research are given: Field control could be used to create molecules with tunable bond length or polyatomic molecules with unusual geometries. We point limitations of the current theoretical tools for the description of ULRM. Experimental resolution has reached a level where the convergence issues of the pseudo-potential diagonalization in a finite basis set have to be considered. We recommend the development of a generalization of the more accurate Green’s function method that accounts for fine and hyperfine structure of the Rydberg

and ground-state atom, respectively. Finally, prospects for studies of wave-packet dynamics in the oscillatory PES are given such as large amplitude oscillations of coherent states in the trilobite potential. Here, damping and loss rates contain information on decay channels.

# Chapter 3

## Publications



### 3.1 Spin-interaction effects for ultralong-range Rydberg molecules in a magnetic field

## Spin-interaction effects for ultralong-range Rydberg molecules in a magnetic field

Frederic Hummel,<sup>1,\*</sup> Christian Fey,<sup>1</sup> and Peter Schmelcher<sup>1,2</sup>

<sup>1</sup>Zentrum für Optische Quantentechnologien, Universität Hamburg, Luruper Chaussee 149, 22761 Hamburg, Germany

<sup>2</sup>The Hamburg Centre for Ultrafast Imaging, Universität Hamburg, Luruper Chaussee 149, 22761 Hamburg, Germany



(Received 23 November 2017; published 23 April 2018)

We investigate the fine and spin structure of ultralong-range Rydberg molecules exposed to a homogeneous magnetic field. Each molecule consists of a  $^{87}\text{Rb}$  Rydberg atom the outer electron of which interacts via spin-dependent  $s$ - and  $p$ -wave scattering with a polarizable  $^{87}\text{Rb}$  ground-state atom. Our model includes also the hyperfine structure of the ground-state atom as well as spin-orbit couplings of the Rydberg and ground-state atom. We focus on  $d$ -Rydberg states and principal quantum numbers  $n$  in the vicinity of 40. The electronic structure and vibrational states are determined in the framework of the Born-Oppenheimer approximation for varying field strengths ranging from a few up to hundred Gauss. The results show that the interplay between the scattering interactions and the spin couplings gives rise to a large variety of molecular states in different spin configurations as well as in different spatial arrangements that can be tuned by the magnetic field. This includes relatively regularly shaped energy surfaces in a regime where the Zeeman splitting is large compared to the scattering interaction but small compared to the Rydberg fine structure, as well as more complex structures for both weaker and stronger fields. We quantify the impact of spin couplings by comparing the extended theory to a spin-independent model.

DOI: [10.1103/PhysRevA.97.043422](https://doi.org/10.1103/PhysRevA.97.043422)

### I. INTRODUCTION

Ultralong-range Rydberg molecules (ULRM) comprising a Rydberg and a ground-state atom possess huge bond lengths and can exhibit correspondingly large permanent electric dipole moments. In cold or ultracold atomic clouds, molecular bound states can be formed with an underlying oscillatory potential landscape that is induced by scattering of the Rydberg electron off the neutral ground-state atom. Pictorially speaking, the potential-energy surfaces (PES) due to which molecules form reflect the spatial variation of the density of the electronic Rydberg wave function. ULRM were theoretically predicted in 2000 [1] and come in different classes such as nonpolar molecules with low angular momenta  $l \leq 3$  and polar molecules for high angular momenta  $l > 3$ , which are called trilobite. Both of these species have been found in corresponding spectroscopic experiments [2–4]. The electronic scattering process is modeled by a Fermi-type pseudopotential for  $s$ -wave scattering [5]. The generalization to include  $p$ -wave scattering [6] leads to a novel type of molecules, named butterfly states [7], the existence of which has also been confirmed experimentally [8,9]. Both trilobites and butterflies share the property of a strong localization of the electronic wave function around the ground-state atom, possible through a mixing of the quasidegenerate high angular momentum  $l > 3$  states and allowing for a strong binding on the order of gigahertz. Opposite to this, low angular momentum states  $l \leq 3$  possess binding energies on the order of several megahertz. They are energetically detuned from the hydrogenic manifold due to their noninteger quantum defect, an effect that originates from

the interaction of the Rydberg electron with the core electrons of the Rydberg atom. Thus, both localization and dipole moments are much weaker compared to polar molecules.

For large principal quantum numbers  $n \gtrsim 45$ , and depending on the density of the cold atomic gas, polyatomic molecules become possible, when a single Rydberg electron binds several ground-state atoms [10–14]. ULRM have proven a valuable tool in a variety of settings from probing electron scattering resonances [15] to occupancies of atomic lattices [16] and observation of ultracold chemical reactions [17,18].

Looking at ULRM in some more detail, i.e., for a higher resolution, further relevant interactions include spin-dependent  $s$ -wave and  $p$ -wave scattering in combination with the hyperfine structure of the ground-state atom [19]. These were very recently observed experimentally in rubidium [20,21] and cesium ULRM [22]. An actual spin transfer process from the Rydberg atom to the ground-state atom has been observed in Ref. [23]. For strontium with vanishing nuclear spin, the corresponding couplings are less prominent, but even these species have been detected [24,25].

The effects of spin-orbit coupling in the electron-neutral interaction of the Rydberg electron and the ground-state atom were treated in an alternative theoretical approach using Green's-function techniques [26]. However, in this treatment the inclusion of the hyperfine structure remains unclear. Only very recently efforts have been made to incorporate the latter into the pseudopotential approach [27,28].

As a matter of fact, the electronic Rydberg wave function is very sensitive to external static or time-dependent fields. Thus, the density and consequently the potential-energy surface can be tuned to support certain molecular equilibrium geometries using only weak magnetic or electric fields. Indeed, the impact of magnetic and electric fields has been studied both

\*frederic.hummel@physnet.uni-hamburg.de

theoretically [29,30] and experimentally [31,32], including the case of combined electric and magnetic fields [33].

In the present paper we go one step further and combine a detailed theoretical description of ULRM including the effects of spin couplings with the application of external homogeneous magnetic fields. Specifically, we will focus on  $l = 2$ , i.e.,  $d$ -state Rydberg molecules, including also higher partial wave interactions. Three regimes of magnetic-field strength relative to other relevant interaction strengths emerge. In the intermediate regime, the PES are regularly shaped and effects of mixed singlet and triplet scattering are visible. For weaker fields, PES of different angular momenta projection states strongly mix, influencing and distorting the shapes of individual potential wells as well as the overall PES. For stronger fields, PES of different total angular momenta states of the Rydberg electron mix, leading to a tunable molecular orientation relative to the magnetic field.

This paper is organized as follows. Section II provides the theoretical framework for the description of ultralong-range Rydberg molecules. In Sec. III we briefly recapitulate the PES for the Hamiltonian developed in Ref. [28], which is here modified by the inclusion of additional magnetic fields. In Sec. IV we present the results for  $d$ -state molecules in a homogeneous magnetic field, which are organized into an intermediate- (Sec. IV A), a weak- (Sec. IV B), and a strong-field regime (Sec. IV C). Section V contains our conclusions.

## II. THEORETICAL DESCRIPTION OF RYDBERG MOLECULES

We consider a system of two rubidium atoms, one in a Rydberg state and the second one in its ground state at position  $\vec{R}$  relative to the ionic core of the Rydberg atom as depicted in Fig. 1. In the Born-Oppenheimer approximation

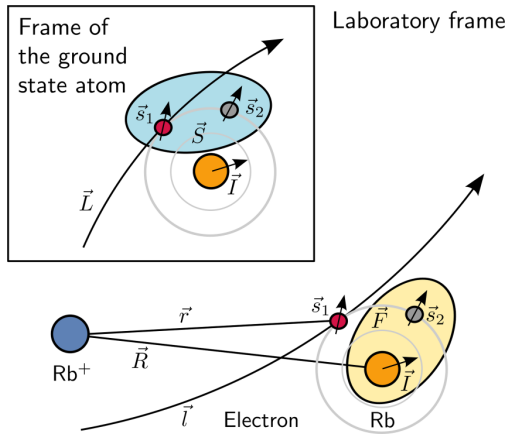


FIG. 1. Sketch of the molecular system. The Rydberg electron at position  $\vec{r}$  relative to the rubidium core carries an orbital angular momentum  $\vec{l}$  and spin  $\vec{s}_1$ . The neutral ground-state atom at position  $\vec{R}$  carries a nuclear spin  $\vec{I}$  which interacts with the spin  $\vec{s}_2$  of its valence electron to form a hyperfine state characterized by the quantum number  $F$ . Upon contact of the two systems (in the inset box) the total electronic spin  $\vec{S} = \vec{s}_1 + \vec{s}_2$  interacts with the angular momentum of the Rydberg electron relative to the ground-state atom  $\vec{L}$ .

the electronic motion is described by the time-independent Schrödinger equation

$$\hat{H}(\vec{r}; \vec{R})\Psi_i(\vec{r}; \vec{R}) = \epsilon_i(\vec{R})\Psi_i(\vec{r}; \vec{R}) \quad (1)$$

for the electronic wave functions  $\Psi_i(\vec{r}; \vec{R})$ .  $\epsilon_i(\vec{R})$  are the adiabatic potential-energy surfaces which depend parametrically on the relative vector  $\vec{R}$ . In atomic units the electronic Hamiltonian is of the form [28]

$$\hat{H}(\vec{r}; \vec{R}) = \hat{H}_{\text{Ryd}}(\vec{r}) + \hat{H}_{\text{HF}} + \hat{V}_P(\vec{R}, \vec{r}) - \frac{\alpha}{2R^4} + \hat{H}_B. \quad (2)$$

Here,  $\hat{H}_{\text{Ryd}}(\vec{r})$  is the Hamiltonian of the Rydberg atom including its spin-orbit coupling. Its eigenfunctions are

$$\Psi_{nljm_j}(\vec{r}) = \sum_{m_l, m_1} C_{lm_l, s_1 m_1}^{jm_j} \frac{1}{r} f_{nlj}(r) Y_{lm_l}(\hat{r}) \chi_{m_1}^{s_1}, \quad (3)$$

where  $C_{lm_l, s_1 m_1}^{jm_j}$  is a Clebsch-Gordan coefficient,  $f_{nlj}(r)$  is a Whitaker function,  $Y_{lm_l}(\hat{r})$  is a spherical harmonic, and  $\chi_{m_1}^{s_1}$  is the Rydberg electron's spin wave function, with the Rydberg electron's spin  $s_1$  and its projection quantum number  $m_1$ . Whitaker functions approximate the radial solution of the Hamiltonian by means of the asymptotic energy

$$E_{nlj} = -\frac{1}{2[n - \mu(n, l, j)]^2}, \quad (4)$$

where  $\mu(n, l, j)$  are the noninteger nonzero quantum defects for  $l \leq 3$ . The quantum defects take into account the scattering of the Rydberg electron from the Rydberg core and inner shell electrons, leading to an effective energy shift of the Rydberg state. Thus,  $f_{nlj}(r)$  is a good approximation for distances larger than a few Bohr radii. For higher angular momentum the quantum defect is negligible and the Whitaker functions coincide with hydrogenic eigenfunctions. We obtain the quantum defect from experimental data of atomic spectroscopy [34]. Employing the good quantum numbers  $|nljm_j\rangle$  of the Rydberg electronic wave function in the absence of a perturbing ground-state atom diagonalizes  $\hat{H}_{\text{Ryd}}(\vec{r})$ . These are the principal quantum number  $n$ , the orbital angular momentum  $l$ , the total angular momentum  $j$  including spin, and its projection onto the internuclear axis  $m_j$ .

The Hamiltonian of the ground-state atom contains the hyperfine interaction of its nuclear and electronic spins:

$$\hat{H}_{\text{HF}} = A \hat{I} \cdot \hat{s}_2, \quad (5)$$

with a hyperfine coupling for Rb(5s) of  $A = 3.417$  GHz. As a basis we choose here  $|s_2 m_2 I m_I\rangle$ , with the valence electron spin  $s_2$  and the  $z$  component of its magnetic quantum number  $m_2$  as well as the nuclear spin  $I$  and its projection onto the  $z$  axis  $m_I$ . For rubidium the nuclear spin is given by  $I = 3/2$ . Due to the coupling to the total nuclear spin  $F = I \pm s_2$ ,  $\hat{H}_{\text{HF}}$  is not diagonal in this basis.

The Fermi-like pseudopotential  $\hat{V}_P(\vec{R}, \vec{r})$  models the interaction of the Rydberg electron and the neutral ground-state atom [5,6], generalized to include all scattering channels up to  $p$  wave, which means spectroscopically that we account for  $^{2S+1}L_J = ^1S_0, ^3S_1, ^1P_1$ , and  $^3P_{0,1,2}$ . These channels arise because the Rydberg electron and the valence electron of the ground-state atom form a singlet or triplet state  $S$ , which interacts via spin-orbit coupling with the electronic orbital

angular momentum  $L$  relative to the ground-state atom to form the total angular momentum  $J$  relative to the ground-state atom. Each scattering channel can be associated with a scattering length or volume  $a(S, L, J, k)$ , which is modeled using the phase shifts presented in Ref. [26], which depend on the collision energy of the scattering partners. The collision energy is approximated via the semiclassical electronic momentum  $k(R) = \sqrt{2/R - 1/n_h^2}$ , where  $n_h$  is the principal quantum number of the closest upper hydrogenic manifold. To properly evaluate the scattering, the electronic wave functions have to be expanded as spherical waves around the position of the ground-state atom. Equivalently this can be thought of as a frame transformation onto the scattering center such that a diagonal scattering matrix is obtained. The pseudopotential is proportional to the scattering length and volume associated with each scattering channel:

$$\hat{V}_P(\vec{R}, \vec{r}) = \sum_{\beta} \frac{(2L+1)}{2} a(S, L, J, k) \frac{\delta(x)}{x^{2(L+1)}} |\beta\rangle \langle \beta|. \quad (6)$$

Here,  $x = |\vec{r} - \vec{R}|$  is the relative distance between the Rydberg electron and the ground-state atom and  $\beta = (S, L, J, M_J)$  labels angular momentum quantum numbers in the frame of the ground-state atom, with the projection of total angular momentum  $M_J$  of the Rydberg electron and valence electron pair relative to the ground-state atom. Note that the above representation includes the change of basis from the unperturbed Rydberg atom to the ground-state atom. This is described more elaborately in Ref. [28]. Asymptotically, when the ground-state atom is sufficiently far from the Rydberg electron, the PES can be classified by the Rydberg electron's angular momentum relative to the ionic core  $j$  and the total spin  $F$  of the ground-state atom.  $\alpha/2R^4$  is the polarization potential induced by the ionic core of the Rydberg atom, with polarizability  $\alpha = 319.2$  a.u.

Lastly,  $\hat{H}_B$  describes the impact of the magnetic field, which we assume to be homogeneous. It couples to all angular momenta and spins of the system. For sufficiently weak fields only the paramagnetic or Zeeman terms are important such that

$$\hat{H}_B = \frac{\vec{B}}{2} \cdot (\hat{J} + \hat{s}_1 + 2\hat{s}_2). \quad (7)$$

Since the coupling to the nuclear spin of the ground-state atom is suppressed by  $1/M$ , where  $M$  is the nuclear mass, it can be safely neglected. The quadratic Zeeman effect is suppressed for the principle quantum numbers and field strengths considered in this paper. The ratio of quadratic and linear effect scales with  $n^4 B$ , where  $B$  is given in units of  $2.35 \times 10^9$  G [35]. We choose the magnetic field to be parallel to the  $z$  axis  $\vec{B} = B\hat{e}_z$ . Due to the azimuthal molecular symmetry corresponding to rotations of the internuclear axis around the  $z$  axis, the internuclear axis can without loss of generality be chosen as

$$\vec{R} = R(\sin\theta \hat{e}_x + \cos\theta \hat{e}_z). \quad (8)$$

$\hat{H}(\vec{r}; \vec{R})$  is diagonalized for a truncated basis set  $|nljm_j m_2 m_1\rangle$  ( $l$  and  $s_2$  are constant and therefore neglected here), where  $n$  and  $l$  are fixed to a single value (unless indicated otherwise),  $j = l \pm 1/2$ , and all other quantum numbers are covered completely.  $\vec{R}$  is discretized on a spatial grid, thus obtaining

$\epsilon_i(\vec{R}) = \epsilon_i(R, \theta)$ , which is then used in the stationary vibrational Schrödinger equation

$$[\vec{P}^2/M + \epsilon_i(\vec{R})]\Phi_\nu(\vec{R}) = E_\nu \Phi_\nu(\vec{R}), \quad (9)$$

with the vibrational energies  $E_\nu$ , eigenfunctions  $\Phi_\nu(\vec{R})$ , and the mass of Rubidium  $M$ . This set of partial differential equations is solved via a two-dimensional (2D) finite difference method in cylindrical coordinates [33] to obtain the molecular vibrational states and energies crucial for the determination of the binding properties. Beyond this, they are of course of immediate relevance to the analysis of observational spectroscopic data.

### III. FIELD-FREE POTENTIAL-ENERGY CURVES

Before considering the impact of magnetic fields, let us first recapitulate the PES of the field-free Hamiltonian, which have previously been discussed in Refs. [27,28]. In this case, the PES depend only on the internuclear distance  $R$ :  $\epsilon_i(\vec{R}) \rightarrow \epsilon_i(R)$  and without loss of generality we can choose the internuclear axis to be the  $z$  axis. The projection of the total spin  $\Omega = m_j + m_2 + m_1$  onto the internuclear axis is an exact conserved quantum number of the molecular system [28].

Figure 2 shows the PES and the Rydberg electron's angular momentum  $l$  for principal quantum number  $n = 43$ . Most of the PES come in pairs of total spin  $F = 2$  and 1 with an energy gap of approximately 7 GHz, due to the hyperfine splitting for rubidium in its ground state. This behavior is exact within our

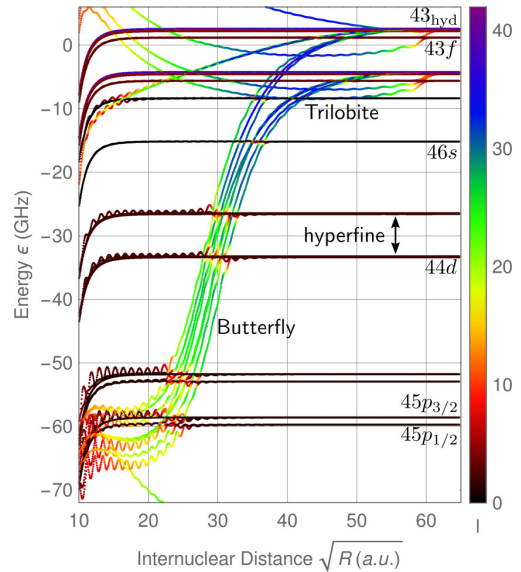


FIG. 2. Complete manifold of the  $n = 43$ ,  $\Omega = 1/2$  PES with nearby quantum defect split states of low angular momentum in field-free space. The internuclear axis is chosen to coincide with the  $z$  axis. Each PES for a given angular momentum  $l$  splits into two hyperfine states  $F = 2$  and 1. The PES of  $p$  states are additionally substantially spin-orbit split. At the top of the figure is the high  $l$  hydrogenic manifold from which the trilobite PES emerge. PES cutting through the entire spectrum stem from the  $p$ -wave resonant scattering and are referred to as butterfly states. The colorcode indicates the angular momentum  $l$  character of the PES.

model and most prominent for large distances  $R$ , where the two atoms do not interact. Coming from large distances  $R$ , the PES belonging to the high angular momentum polar states [1] deviate from the hyperfine split hydrogenic manifold close to zero energy by approximately 4 GHz and can be explained by pure  $s$ -wave scattering. These trilobite curves are crossed by  $l = 3f$  states with a small quantum defect. For lower energies we encounter the PES of the  $s$ ,  $d$ , and  $p$  state, respectively. The  $p$  state comprises slightly different quantum defects for  $j = 3/2$  and  $1/2$  due to spin-orbit effects, introducing an additional visible splitting. For the  $d$  state this splitting is smaller and practically not visible on the energy scale of Fig. 2. The curves originating in the hydrogenic manifold and cutting through all other PES are the butterfly curves. Their steepness originates from a resonance of the  $p$ -wave scattering, when the phase shift is  $\pi/2$  for certain electronic kinetic energies. Here, multiple curves are visible for each hyperfine state, which is due to the spin-orbit interaction of the scattering partners. In the proximity of the Rydberg core  $\sqrt{R} \lesssim 15$ , the polarization potential becomes dominant. Figure 2 was derived by diagonalizing  $H(\vec{r}; \vec{R})$  for discrete values of the internuclear distance  $R$  and using a truncated basis set including hydrogenic manifolds with principal quantum numbers  $\{n - 2, \dots, n + 1\}$ , where  $n = 43$ . Since for scattering of the Rydberg electron off the ground-state atom only partial waves up to  $p$  wave (i.e.,  $L \leq 1$ ) are included, only states with  $|m_j| \leq 3/2$  will be perturbed.  $H(\vec{r}; \vec{R})$  is block diagonal in  $\Omega$  and  $\Omega = 1/2$  is shown in Fig. 2.

The spherical symmetry of the PES in the diatomic case can be broken when several ground-state atoms are located in the vicinity of the Rydberg atom and polyatomic bound states are possible. For the triatomic case, this is studied in Ref. [13]. In our paper, the presence of a magnetic field causes the breaking of the spherical symmetry.

#### IV. D-STATE RYDBERG MOLECULES IN A HOMOGENEOUS MAGNETIC FIELD

In the following, we focus on  $d$ -state Rydberg molecules i.e., with an angular momentum of  $l = 2$  carried by the Rydberg electron. Therefore, we restrict the basis set also to  $l = 2$ . Diagonalizing an entire hydrogenic manifold is not feasible here, since all total angular momentum projection states have to be taken into account to obtain converged results. However, since the  $l < 3$  states are detuned from the hydrogenic manifold due to their quantum defects,  $l$  is very accurately approximated to be a good quantum number of the molecular system in the vicinity of the outermost potential well. When a magnetic field is present the  $(2j + 1) \times (2F + 1)$ -fold degeneracy of each potential-energy surface in the separate atom limit  $R \rightarrow \infty$  is lifted. The asymptotic energy splitting (due to the anomalous Zeeman effect) is given by

$$\Delta\epsilon = B \left[ m_j \left( 1 + \frac{(-1)^{l+1/2-j}}{1+2l} \right) + m_F \frac{(-1)^{2-F}}{2} \right]. \quad (10)$$

We can distinguish between three regimes of magnetic-field strength when compared to other interactions, which are discussed in detail in this section.

(I) The  $s$ -wave regime for weak magnetic fields, where the Zeeman splitting is small compared to the effects of the  $s$ -wave

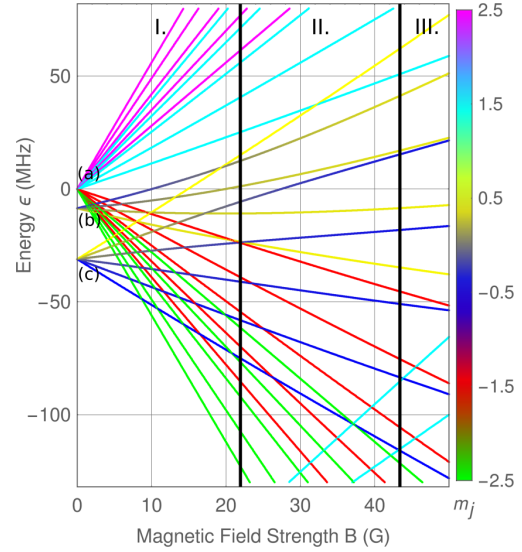


FIG. 3. Energies of the  $38d$  states for  $F = 2$  and  $j = 5/2$  with varying magnetic-field strength and for a fixed internuclear distance  $R = 2530$  a.u. This corresponds to the radial position of the outermost potential well. The magnetic field is aligned parallel to the internuclear axis. The colorcode indicates the Rydberg electronic total angular momentum projection  $m_j$ . Each color of equal  $m_j$  appears fivefold due to the five  $m_F$  states for  $F = 2$ .  $|m_j| > 1/2$  states do not couple to the ground-state atom positioned on the  $z$  axis, hence the associated curves linearly emerge from zero energy for absent fields (a).  $|m_j| \leq 1/2$  states are perturbed by the ground-state atom (b, c). Three regimes of magnetic-field strengths are identifiable with different dominant interactions, namely,  $s$ -wave scattering (I), fine structure (II), and Zeeman splitting (III).

scattering. In this regime  $m_j$  and  $m_F$  mixing dominates the shape of the PES.

(II) The fine-structure regime for intermediate magnetic fields, where the Zeeman splitting is tuned to exceed the  $s$ -wave scattering interaction, but is smaller than the spin-orbit splitting. In this regime  $m_j$  and  $m_F$  are approximately good quantum numbers.

(III) The Zeeman regime for strong magnetic fields, where the Zeeman splitting is comparable or larger than the fine-structure splitting. In this case, the shapes of the PES are strongly tunable since states of different Rydberg electronic angular momenta  $j$  mix.

This distinction into the three regimes I, II, and III is shown in Fig. 3. Before we enter into the discussion of the case of the presence of a magnetic field, let us elucidate the zero-field case for  $d$ -state Rydberg molecules: At the position of the outermost potential well, which for the  $38d$  state lies at  $R = 2530$  a.u., three values for the energy for  $F = 2$  and  $j = 5/2$ -states are possible.

(a) Zero energy, i.e., there is no coupling of the Rydberg electron to the ground-state atom. Since the internuclear axis coincides with the  $z$  axis, these states carry  $|m_j| > 1/2$ . The absence of the coupling can be understood in terms of the spherical harmonics for  $l = 2$  and  $m_l = \{-l, \dots, l\}$ , which introduce the probability to find the electron at a given angle

relative to the  $z$  axis. Only  $m_l = 0$  states have a nonzero probability on the  $z$  axis. Via the Clebsch-Gordan coefficients,  $m_l = 0$  states can only contribute to  $m_j = \pm 1/2$ .

(b) Slightly lowered energy for states with  $|m_j| < 1/2$ , corresponding to a shallow potential well at  $R = 2530$ . This can be understood in terms of the scattering lengths of the associated spin-dependent  $s$ -wave scattering, which is negative for triplet scattering and comparatively small for singlet scattering. The shallow potential well emerges for antiparallel spin alignment of the scattering partners, namely, the Rydberg electron and the valence electron of the ground-state atom. Note that  $m_l = \pm 1/2$  dominantly contributes to  $m_j = \pm 1/2$ . Antiparallel spin alignment corresponds to a mixed singlet-triplet state, therefore the potential depth cannot be maximal.

(c) Strongly lowered energy for states with  $|m_j| < 1/2$ , corresponding to a deep potential well and to maximal triplet character, i.e., dominantly parallel alignment of the scattering partners.

This  $s$ -wave induced energy splitting is complemented by a Zeeman splitting, when a magnetic field is present. For  $|m_j| \leq 1/2$  mixing of  $m_j$  and  $m_F$  states emerges. When the internuclear axis is rotated relative to the magnetic-field axis (not shown in Fig. 3) also other  $m_j$  states start to mix due to the mixing of orbital  $m_l$  states to account for the spatial position of the Rydberg electron.

For intermediate fields the mixing of states with either different  $m_j$  or  $m_F$  is suppressed and states of equal  $m_j$  appear in sets of consecutive, decreasing  $m_F$ . For stronger fields the Zeeman splitting exceeds the fine structure and  $j$  mixing emerges.

#### A. The fine-structure regime for intermediate magnetic fields

We start the discussion of our results with the intermediate regime due to its immediate link to the existing literature. A special case in this regime excluding all spin and spin-orbit interactions was under investigation in Ref. [31]. There, only triplet scattering  $^3S_1$  and  $^3P_0$  was assumed for every channel. In this section, we focus on  $n = 44$  to match the experimental study [31]. Furthermore, we investigate  $n = 38$  for the other regimes below, since a lower principle quantum number leads to deeper potential-energy wells and therefore allows us to achieve a better localization of vibrational states in different angular configurations. Figure 4 shows the PES of the  $F = 2$  and  $44d$  state for a magnetic field of  $B = 13.55$  G and fixed orientation angle  $\theta = 0$ . The PES are characterized by a colorcode according to the total angular momentum projection of the Rydberg electron  $m_j$ . In principle, due to the magnetic field and electronic scattering, states of different spin can mix. However, in the intermediate regime the energetic separation of different spin states exceeds the effects of the scattering. Therefore,  $m_j$  and  $m_F$  are approximately good quantum numbers in this regime. Particularly,  $\Omega$  is approximately conserved also for nonzero  $\theta$ . For all other regimes we consider in the paper,  $\Omega$  is conserved only for  $\theta = 0$ . For the given magnetic field in Fig. 4, the Zeeman splitting is visible for  $j = 3/2$  and  $5/2$  which are energetically clearly separated. Each color appears fivefold due to the five possible  $m_F$  states. As described in earlier parts of Sec. IV, for the given orientation angle  $\theta = 0$ , only PES of  $m_j = \pm 1/2$  states interact with the ground-state

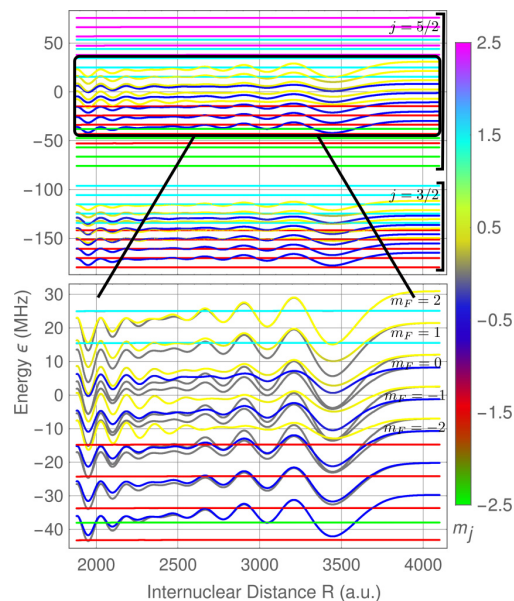


FIG. 4. Energies of the radial PES for  $44d$  states with  $F = 2$ ,  $\theta = 0$ , and a magnetic field of  $B = 13.55$  G. The  $j$  and  $F$  sublevel degeneracy with respect to  $m_j$  and  $m_F$  is lifted when a magnetic field is present.  $m_j$  is indicated by a colorcode. The  $j = 3/2$  PES are split up into 20 curves, where five carry the same  $m_j$  and four carry the same  $m_F$ . The energetically higher  $j = 5/2$  PES are analogously split up  $5 \times 6$  times. For  $\theta = 0$  only states with  $|m_j| \leq 1/2$  couple to the ground-state atom via  $s$ -wave interaction and form oscillating PES (bottom). Here, PES from a theory where the electron-neutral atom scattering is assumed to be spin independent are indicated in gray and deviate significantly.

atom. In contrast to the field-free case, where the PES of  $m_j = \pm 1/2$  states comprise either a deep or a shallow outermost potential well, for intermediate field strength this distinction obliterates. The outermost well varies in depth for different  $m_F$ . For  $m_j = 1/2$  it deepens for increasing  $m_F$  and vice versa for  $m_j = -1/2$ , as visible in the lower part of Fig. 4. For intermediate fields, the energies of the  $m_j$  and  $m_F$  states are not degenerate anymore, and the variation of the potential depth can be directly associated with the spin alignment of the Rydberg and valence electron of the ground-state atom: In  $m_j = 1/2$  ( $m_j = -1/2$ ) states, the dominant electronic spin contribution is  $m_l = 1/2$  ( $m_l = -1/2$ ). Simultaneously, the  $m_F = 2$  state is a pure electronic  $m_2 = 1/2$  state, therefore resulting in maximal triplet (mixed) character. The contribution of  $m_2 = 1/2$  gradually decreases for decreasing  $m_F$ , such that  $m_F = -2$  is a pure electronic  $m_2 = -1/2$  state. The shallower wells mirror the change from a triplet-dominant character to a mixed-state-dominant character. In a model where the electron-neutral ground-state atom scattering is assumed to be spin independent the outermost potential wells possess a constant depth. In Fig. 4 the associated PES to the latter model are shown in gray.

Under variation of  $\theta$ , more features of the PES become apparent and are presented in Fig. 5, where  $\theta$  is varied and the internuclear distance is fixed to the position of the outermost

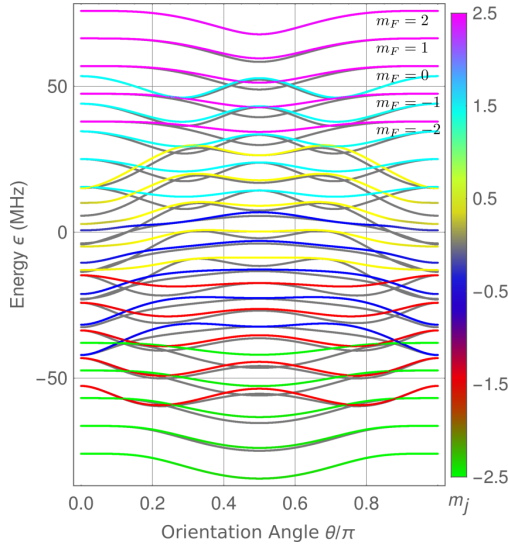


FIG. 5. Radial cuts of the PES for  $44d$  states with  $F = 2$ ,  $j = 5/2$ ,  $R = 3452$  a.u., and a magnetic field of  $B = 13.55$  G with varying angle  $\theta$  between the internuclear axis and the magnetic field. Each equally colored potential-energy surface of constant  $m_j$  carries a different nuclear spin projection  $-2 < m_F < 2$  and exhibits potential wells which support molecular states/geometries for different angles  $\theta$ . For  $m_j > 0$  ( $m_j < 0$ ), the depth of the potential wells decreases for decreasing (increasing)  $m_F$ . The gray PES are derived upon neglecting the spin dependence in the electron-neutral atom scattering. In this case, the depth of the potential wells is constant for equal  $m_j$ .

potential well  $R = 3452$  a.u. The potential wells emerge approximately for three different angular positions. These are  $\theta = 0$  and  $\pi$  for  $m_j = \pm 1/2$  states,  $\theta = \pi/4$  and  $3\pi/4$  for  $m_j = \pm 3/2$  states, and  $\theta = \pi/2$  for  $m_j = \pm 5/2$  states. This can be understood in terms of the above-mentioned spherical harmonics for  $l = 2$  and  $m_l = \{-l, \dots, l\}$ , which have angular positions of maximal electronic density at the orientation angles  $\theta = 0$  for  $m_l = 0$ ,  $\theta = \pi/4$  for  $m_l = \pm 1$ , and  $\theta = \pi/2$  for  $m_l = \pm 2$  and contribute to  $m_j$  states accordingly. Equally to the feature seen in Fig. 4, the depth of the potential wells decreases for decreasing (increasing)  $m_F$  when  $m_j > 0$  ( $m_j < 0$ ), whereas for the spin-independent model the depth is constant. These deviations are particularly interesting, as the  $m_j = 5/2$ ,  $m_F = 2$  state (upper most pink PES in Fig. 5) and  $m_j = 1/2$ ,  $m_F = 2$  state (upper most yellow PES in Fig. 5) were investigated in Ref. [31]. While the PES for the  $m_j = 5/2$ ,  $m_F = 2$  state are practically identical in the spin-independent model used in Ref. [31] and the spin-dependent model used in this paper, the PES for the  $m_j = 1/2$ ,  $m_F = 2$  state are narrower around the molecular ground state at  $\theta = 0$ . A full two-dimensional image of the latter particular PES is depicted in Fig. 6, along with the four energetically lowest vibrational states and binding energies. The narrower potential well leads to an increased energy spacing of bound vibrational states. In fact, discrepancies between the energetic separation of experimental and theoretical states have been observed in Ref. [31]. Our results may explain these discrepancies and attribute them to the included spin couplings. We were able

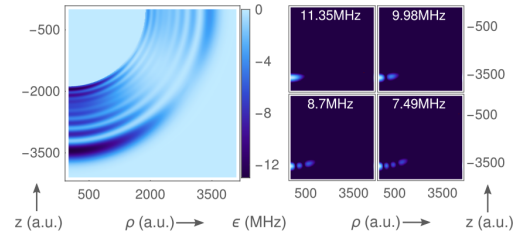


FIG. 6. 2D PES for the  $44d$  state with  $F = 2$ ,  $m_F = 2$ ,  $j = 5/2$ , and  $m_j = 1/2$  in cylindrical coordinates (left). It supports several molecular vibrational excitations; the four energetically lowest states are shown, along with their binding energies (right, logarithmic color scaling).

to reduce the relative energetic deviation from the spectrum from around 10% in the spin-independent model to less than 5% when spin couplings are included, and the average relative energy spacing of the vibrational states from 4 to 2%.

### B. The $s$ -wave regime for weak magnetic fields

When the magnetic Zeeman splitting of states of different total angular momentum projection  $m_j$  and total nuclear spin projection  $m_F$  is weak compared to the effect of the interaction with the ground-state atom, the PES may strongly influence each other allowing for avoided crossings which lead to molecular vibrational eigenstates for new geometries and spin states. The emerging complex patterns are depicted in Figs. 7 and 8. As an example, we focus on a Rydberg atom in the  $38d$  state in a magnetic field  $B = 8$  G. Although an overall pattern as in the intermediate regime is still visible, namely, that potential wells become shallower as  $m_F$  decreases (increases) for  $m_j > 0$  ( $m_j < 0$ ), the PES acquire novel features due to their interaction with energetically close-by PES. States with  $m_j = 5/2$ , which comprise a stable molecular geometry when the internuclear axis is perpendicular to the magnetic field in the intermediate regime, gain a richer structure with double ( $m_F = 1$ ) and triple ( $m_F = 0$ ) wells around  $\theta = \pi/2$ . This is also true for states of  $m_j = 3/2$  with local minima at  $\theta = \pi/4$  and  $3\pi/4$ . As seen in Fig. 7, the richer potential well structure leads to novel vibrational states with varying equilibrium positions and degree of localization.

Additionally, for  $m_j = \pm 1/2$  states, the typical structure of groups of PES with the same  $m_j$  and decreasing  $m_F$  breaks down in the weak-field regime. This succession is disrupted by the  $s$ -wave interaction and can be explained in terms of the strong influence of the singlet and triplet  $S$  state which governs the scattering. This is also visible in Fig. 3 panel I. However, the general shape and depth of the potential wells is not influenced much by this effect.

Opposite to this, the energetically lowest potential-energy surface of  $j = 5/2$  shown in Fig. 8 exhibits a surprisingly deep potential well at angular position  $\theta = \pi/2$ . Pictorially speaking, this potential-energy surface inherits the features of the  $m_j$  state, that minimizes the energy at a given orientation angle:  $m_j = -1/2$  for  $\theta \approx 0$ ,  $m_j = -3/2$  for  $\theta \approx \pi/4$ , and  $m_j = -5/2$  for  $\theta \approx \pi/2$ . This effect makes the arising potential well twice as deep as it would be without  $m_j$  mixing. Thus,

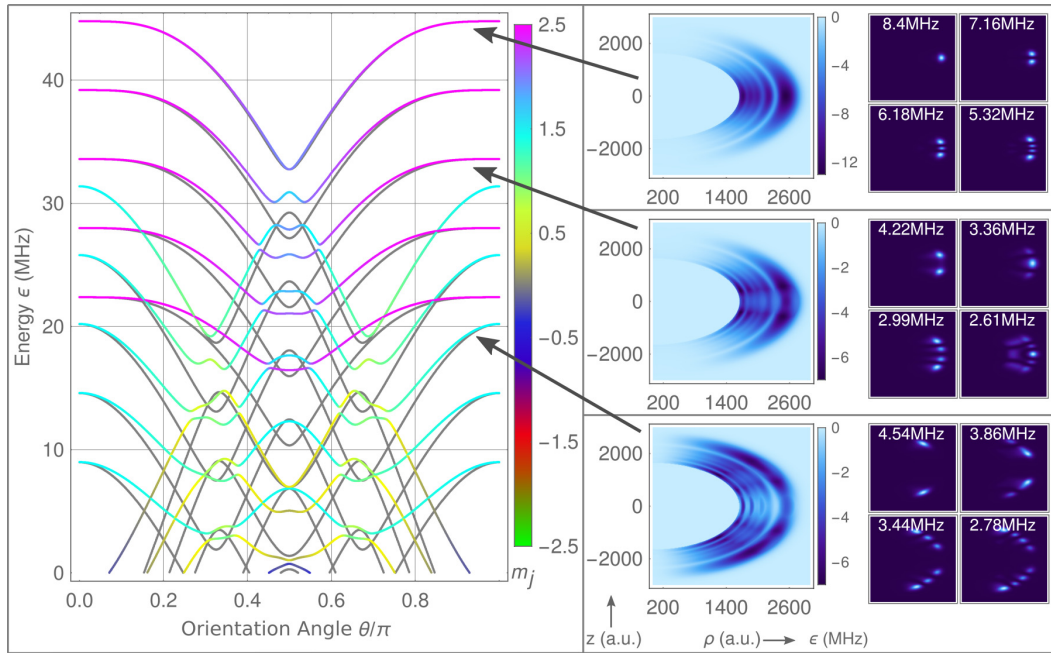


FIG. 7. Angular dependence of the PES for  $38d$  states with  $F = 2$ ,  $j = 5/2$ ,  $R = 2530$  a.u., and a magnetic field  $B = 8$  G—upper part of the spectrum (left). Spin-independent scattering is shown in gray, while a colorcode indicates the  $m_j$  state for the model where spin couplings are included. On the right, full 2D PES in cylindrical coordinates are shown for selected states, namely, those dominated by their  $(m_j = 5/2, m_F = 2)$  character which exhibits a single potential well,  $(m_j = 5/2, m_F = 0)$  character with a triple potential well, and  $(m_j = 3/2, m_F = 0)$  character (from top to bottom), each accompanied by the normalized densities of the four lowest vibrational molecular states (axes to scale of the 2D PES), which show a variety of geometric alignments.

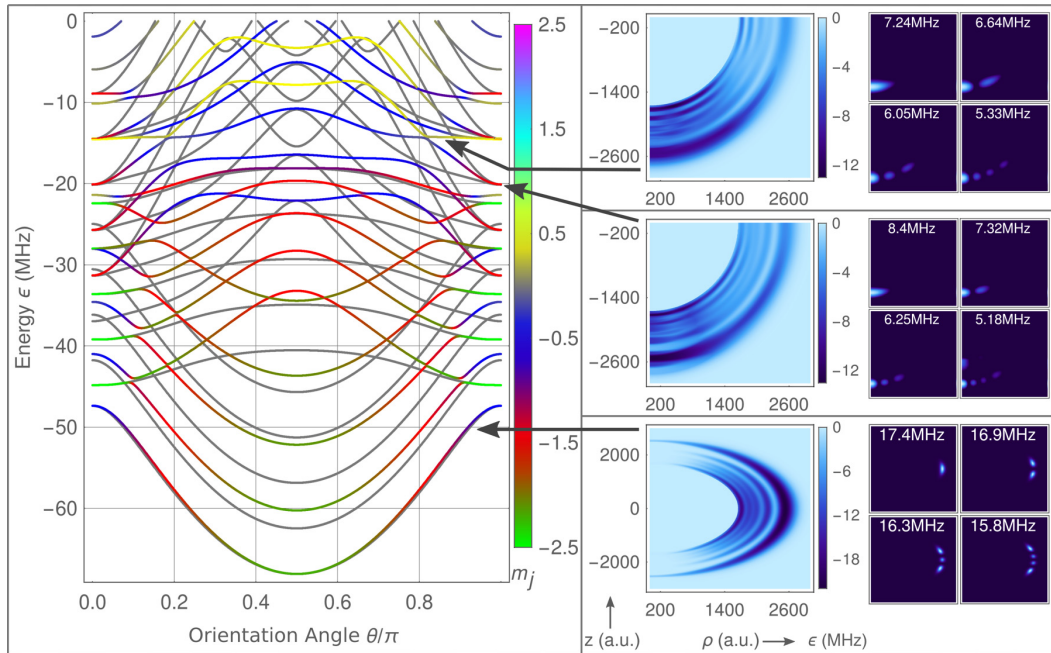


FIG. 8. Angular dependence of the PES for  $38d$  states with  $F = 2$ ,  $j = 5/2$ ,  $R = 2530$  a.u., and a magnetic field  $B = 8$  G—lower part of the spectrum (left). The focus here is on states dominated by  $(m_j = 1/2, m_F = -2)$ ,  $(m_j = -1/2, m_F = 0)$ , and  $(m_j = -5/2, m_F = -2)$  character. Exemplarily, their full PES in cylindrical coordinates are shown (right). The latter displays a multitude of excitations (axes to scale of the 2D PES) purely in angular direction, while in the former case only faint angular excitations are present (logarithmic color scaling in the two upper plots).

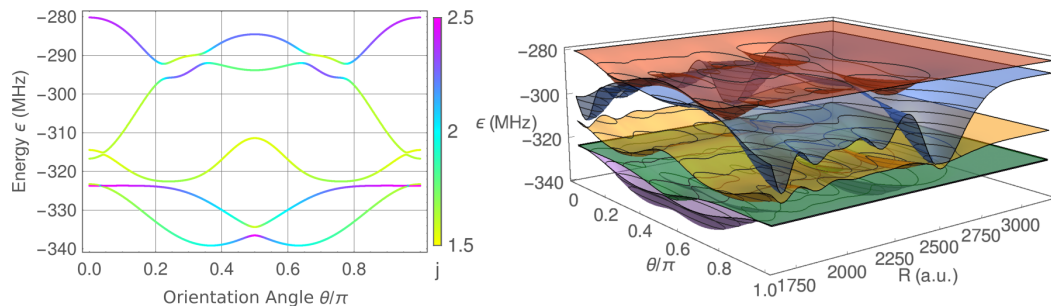


FIG. 9. Left: Angular dependence of the PES for  $38d$  states in a magnetic field  $B = 93$  G at  $R = 2530$  a.u. Due to the large field only a small subset of PES is shown. The color indicates the  $j$  character of the PES, which strongly mixes in this regime of field strength. The spin-orbit separation is overcome and energetically close PES influence each other, resulting in molecular states at various orientation angles  $\theta$  (lowest and uppermost curve) and with tunable depth at the most common well positions  $\theta = 0$  (second uppermost curve) or  $\theta = \pi/2$  (not visible here). Right: Full 2D surfaces of the same PES.

molecular states are relatively deeply bound with vibrational excitations purely in the angular direction.

### C. The Zeeman regime for strong magnetic field

For a Zeeman splitting that exceeds the spin-orbit splitting, even more complex PES emerge due to mixing of states with different total angular momentum  $j$  (compare Fig. 9). Here, the magnetic field can be used to energetically connect PES of desired angular momentum projections. In the regime of intermediate magnetic fields (II), with its typical fanlike structure for varying field (see Fig. 3), the energetic distance between PES within the same fan can never vanish, since the  $s$ -wave interaction has too little influence on the shape of the PES. Thus, for increasing fields, the relative impact that PES in the same fan have on each other can only decrease. In contrast to this, in the strong-field regime, the magnetic field can be used to combine states (and PES) from different  $j$  almost arbitrarily, since they span another fan. This results in avoided crossings which allow PES with exotic shapes. Since for different  $m_j$  the curves have potential wells at different orientation angles  $\theta$ , the emergent  $m_j$  mixing makes the angular position of the resulting potential wells tunable, so that molecules can form in desired geometric configuration relative to the magnetic field. Additionally, by combining curves with different  $j$ , but equal  $m_j = 0$ , the depth of the potential well at  $\theta = 0$  can be increased. This is also possible when combining  $j = 5/2, m_j = \pm 5/2$  states with  $j = 3/2, m_j = \pm 3/2$  states, the associated PES of which both comprise a potential well at  $\theta = \pi/2$ . In Fig. 9, all of the above-mentioned effects are visible as well as a global view on the two-dimensional PES.

## V. CONCLUSION

We have explored the impact of a homogeneous magnetic field on ultralong-range Rydberg molecules exemplarily for  $d$  states. In contrast to previous works, all relevant spin couplings up to  $p$ -wave interactions have been taken into account, including the spin-orbit coupling of the interaction between the ground-state atom and the Rydberg electron. The magnetic field couples (otherwise isolated) potential-energy surfaces and a rich landscape of surfaces emerges. We were able to identify three regimes of magnetic-field strength relative to the strength of the  $s$ -wave interaction and the spin-orbit splitting of the

Rydberg atom. These three regimes were analyzed regarding equilibrium positions, binding energies, and molecular orientation relative to the magnetic field, quantities that are in principle accessible in experiments. Additionally to the known orientations of  $d$ -state molecules, which are  $\theta = 0, \pi/4$ , and  $\pi/2$ , the magnetic field in combination with spin couplings gives rise to novel equilibrium configurations at intermediate angles. This is accomplished by controlling the mixing of the angular momentum and spin quantum numbers  $j, m_j$ , and  $m_F$ . The arising PES of these mixed states comprise complex structures and are strongly tunable. Hence, via the controllable spin content of a molecular state its molecular geometry can be tailored and both properties are strongly intertwined. Parallel as well as perpendicularly aligned ULRM with  $l = 2$  and  $m_F = 2$  have already been observed experimentally [31]. Their orientations were determined, however, only indirectly by identifying peaks in the experimental spectrum with vibrational energies of oriented molecular states from theoretical computations. By the same means, new orientation angles proposed in this paper can be confirmed experimentally. An alternative option for a more direct experimental measurement would be to drive microwave transitions between vibrational molecular states. The corresponding Franck-Condon factors of these transitions contain information of the spatial arrangement of the vibrational states and therefore depend directly on the relative molecular orientations.

The strong coupling of the PES suggests interesting dynamical processes. In a polyatomic setting the magnetic field could make the molecular geometry tunable, leading to exotic molecular shapes. This paper can be extended to Rydberg molecules consisting of cesium and strontium as well as to  $p$ -state molecules in magnetic fields. Here,  $p$ -wave interaction plays a significant role and the effect of  $^3P_J$  splitting is more prominent than for  $d$ -state molecules.

## ACKNOWLEDGMENTS

The authors would like to thank Matthew T. Eiles for fruitful discussions. F.H. and P.S. acknowledge support from the Deutsche Forschungsgemeinschaft within the priority program DFG SPP 1929 (GiRyd). C.F. gratefully acknowledges a scholarship by the Studienstiftung des deutschen Volkes.

- [1] C. H. Greene, A. S. Dickinson, and H. R. Sadeghpour, *Phys. Rev. Lett.* **85**, 2458 (2000).
- [2] V. Bendkowsky, B. Butscher, J. Nipper, J. P. Shaffer, R. Löw, and T. Pfau, *Nature (London)* **458**, 1005 (2009).
- [3] W. Li, T. Pohl, J. M. Rost, S. T. Rittenhouse, H. R. Sadeghpour, J. Nipper, B. Butscher, J. B. Balewski, V. Bendkowsky, R. Löw, and T. Pfau, *Science* **334**, 1110 (2011).
- [4] D. Booth, S. T. Rittenhouse, J. Yang, H. R. Sadeghpour, and J. P. Shaffer, *Science* **348**, 99 (2015).
- [5] E. Fermi, *Il Nuovo Cimento* **11**, 157 (1934).
- [6] A. Omont, *J. de Phys.* **38**, 1343 (1977).
- [7] E. L. Hamilton, C. H. Greene, and H. R. Sadeghpour, *J. Phys. B* **35**, L199 (2002).
- [8] V. Bendkowsky, B. Butscher, J. Nipper, J. B. Balewski, J. P. Shaffer, R. Löw, T. Pfau, W. Li, J. Stanojevic, T. Pohl, and J. M. Rost, *Phys. Rev. Lett.* **105**, 163201 (2010).
- [9] T. Niederprüm, O. Thomas, T. Eichert, C. Lippe, J. Pérez-Ríos, C. H. Greene, and H. Ott, *Nat. Commun.* **7**, 12820 (2016).
- [10] I. C. H. Liu and J. M. Rost, *Eur. Phys. J. D* **40**, 65 (2006).
- [11] I. C. H. Liu, J. Stanojevic, and J. M. Rost, *Phys. Rev. Lett.* **102**, 173001 (2009).
- [12] A. Gaj, A. T. Krupp, J. B. Balewski, R. Löw, S. Hofferberth, and T. Pfau, *Nat. Commun.* **5**, 5546 (2014).
- [13] C. Fey, M. Kurz, and P. Schmelcher, *Phys. Rev. A* **94**, 012516 (2016).
- [14] M. T. Eiles, J. Pérez-Ríos, F. Robicheaux, and C. H. Greene, *J. Phys. B* **49**, 114005 (2016).
- [15] M. Schlagmüller, T. C. Liebisch, H. Nguyen, G. Lohead, F. Engel, F. Böttcher, K. M. Westphal, K. S. Kleinbach, R. Löw, S. Hofferberth, T. Pfau, J. Pérez-Ríos, and C. H. Greene, *Phys. Rev. Lett.* **116**, 053001 (2016).
- [16] T. Manthey, T. Niederprüm, O. Thomas, and H. Ott, *New J. Phys.* **17**, 103024 (2015).
- [17] T. Niederprüm, O. Thomas, T. Manthey, T. M. Weber, and H. Ott, *Phys. Rev. Lett.* **115**, 013003 (2015).
- [18] M. Schlagmüller, T. C. Liebisch, F. Engel, K. S. Kleinbach, F. Böttcher, U. Hermann, K. M. Westphal, A. Gaj, R. Löw, S. Hofferberth, T. Pfau, J. Pérez-Ríos, and C. H. Greene, *Phys. Rev. X* **6**, 031020 (2016).
- [19] D. A. Anderson, S. A. Miller, and G. Raithel, *Phys. Rev. Lett.* **112**, 163201 (2014).
- [20] D. A. Anderson, S. A. Miller, and G. Raithel, *Phys. Rev. A* **90**, 062518 (2014).
- [21] F. Böttcher, A. Gaj, K. M. Westphal, M. Schlagmüller, K. S. Kleinbach, R. Löw, T. C. Liebisch, T. Pfau, and S. Hofferberth, *Phys. Rev. A* **93**, 032512 (2016).
- [22] H. Saßmannshausen, F. Merkt, and J. Deiglmayr, *Phys. Rev. Lett.* **114**, 133201 (2015).
- [23] T. Niederprüm, O. Thomas, T. Eichert, and H. Ott, *Phys. Rev. Lett.* **117**, 123002 (2016).
- [24] F. Camargo, J. D. Whalen, R. Ding, H. R. Sadeghpour, S. Yoshida, J. Burgdörfer, F. B. Dunning, and T. C. Killian, *Phys. Rev. A* **93**, 022702 (2016).
- [25] J. D. Whalen, F. Camargo, R. Ding, T. C. Killian, F. B. Dunning, J. Pérez-Ríos, S. Yoshida, and J. Burgdörfer, *Phys. Rev. A* **96**, 042702 (2017).
- [26] A. A. Khuskivadze, M. I. Chibisov, and I. I. Fabrikant, *Phys. Rev. A* **66**, 042709 (2002).
- [27] S. Markson, S. T. Rittenhouse, R. Schmidt, J. P. Shaffer, and H. R. Sadeghpour, *Chem. Phys. Chem.* **17**, 3683 (2016).
- [28] M. T. Eiles and C. H. Greene, *Phys. Rev. A* **95**, 042515 (2017).
- [29] I. Lesanovsky, P. Schmelcher, and H. R. Sadeghpour, *J. Phys. B* **39**, L69 (2006).
- [30] M. Kurz and P. Schmelcher, *Phys. Rev. A* **88**, 022501 (2013).
- [31] A. T. Krupp, A. Gaj, J. B. Balewski, P. Ilzhöfer, S. Hofferberth, R. Löw, T. Pfau, M. Kurz, and P. Schmelcher, *Phys. Rev. Lett.* **112**, 143008 (2014).
- [32] A. Gaj, A. T. Krupp, P. Ilzhöfer, R. Löw, S. Hofferberth, and T. Pfau, *Phys. Rev. Lett.* **115**, 023001 (2015).
- [33] M. Kurz and P. Schmelcher, *J. Phys. B* **47**, 165101 (2014).
- [34] P. Goy, J. M. Raimond, G. Vitrant, and S. Haroche, *Phys. Rev. A* **26**, 2733 (1982).
- [35] T. Gallagher, *Rydberg Atoms*, Cambridge Monographs on Atomic, Molecular, and Chemical Physics (Cambridge University, Cambridge, England, 2005), p. 143.

## 3.2 Alignment of s-state Rydberg molecules in magnetic fields

## Alignment of $s$ -state Rydberg molecules in magnetic fields

Frederic Hummel,<sup>1,\*</sup> Christian Fey,<sup>1</sup> and Peter Schmelcher<sup>1,2</sup>

<sup>1</sup>Zentrum für Optische Quantentechnologien, Universität Hamburg, Luruper Chaussee 149, 22761 Hamburg, Germany

<sup>2</sup>Hamburg Centre for Ultrafast Imaging, Universität Hamburg, Luruper Chaussee 149, 22761 Hamburg, Germany



(Received 6 September 2018; published 1 February 2019)

We unravel some peculiar properties of ultra-long-range Rydberg molecules formed by an  $s$ -state  $^{87}\text{Rb}$  Rydberg atom and a corresponding ground-state atom whose electronic orbitals are spherically symmetric and therefore should not be influenced by the presence of weak magnetic fields. However, the electron-atom interaction, which establishes the molecular bond, is under certain conditions subject to a sizable spin-orbit coupling and, hence, sensitive to the magnetic field. This mechanism can be harnessed to counterintuitively align the  $s$ -state molecules with respect to the field axis. We demonstrate this by analyzing the angular-dependent Born-Oppenheimer potential energy surfaces and the supported vibrational molecular states. Our predictions open interesting possibilities for accessing the physics of relativistic electron-atom scattering experimentally.

DOI: [10.1103/PhysRevA.99.023401](https://doi.org/10.1103/PhysRevA.99.023401)

### I. INTRODUCTION

The extraordinary properties of ultra-long-range Rydberg molecules (ULRM) such as their enormous size and large permanent electric dipole moments (PEDM) have stirred increasing interest in their study. Two main molecular species can be distinguished: nonpolar molecules with low electronic angular momentum, e.g.,  $s$ -state or  $d$ -state ULRM, and polar ones with high angular momentum. The latter are called trilobite and butterfly molecules after their electronic wave function shaped by  $s$ - and  $p$ -wave interactions with the ground-state atom [1–3].

In recent years, a multitude of spectroscopic experiments have probed ULRM from their first detection in rubidium [4], cesium [5], and strontium [6], their coherent excitation [7], lifetime measurements [8–10], the observation of PEDM [11,12] and angular momentum couplings [13], to proving the existence of polymers [14,15] and controlling ULRM in external fields [16–18]. Additionally, several applications have been proposed and implemented such as probing lattice gases via ULRM [19] and performing remote spin flips [20], as well as the study of ultracold chemical reactions [21] and electromagnetically induced transparency [22]. Moreover, they provide the possibility to realize Rydberg and ionic impurities in Bose-Einstein condensates [23–29] and to study ion-atom interaction [30,31] as well as to employ optical Feshbach resonances in order to tune atom-atom interaction [32,33].

The molecular binding originates from  $s$ - and  $p$ -wave scattering of the Rydberg electron off a neutral ground-state atom [34,35]. Therefore, ULRM serve as a unique tool to characterize electronic scattering channels [36,37] and resonances at very low electronic energies [38,39]. Specifically, they provide an excellent platform for experimentally

testing *ab initio* calculations of  $s$ - and  $p$ -wave scattering phase shifts [40–43]. In particular, in rubidium and cesium the electron-neutral scattering possesses a  $p$ -wave shape resonance, which can be understood as a short-lived, metastable, anionic state of the electron-neutral system [44–46]. A higher level theory that takes relativistic spin-orbit coupling of the two valence electron's spin with their angular momentum relative to the ground-state atom's core into account has been provided [47–49].

In this paper, we demonstrate that the relativistic spin-orbit interaction paired with a weak magnetic field gives rise to the surprising feature of alignment of  $s$ -state ULRM. For  $d$ -state ULRM, alignment in magnetic fields has been demonstrated and stems from the nonzero orbital angular momentum of the electronic state [16,50]. However, for  $s$ -state, i.e., zero angular momentum, ULRM such an alignment process is unexpected, due to the isotropy of the electronic state, since  $l$  mixing is strongly suppressed for nonpolar ULRM (see the appendix). Indeed, for  $s$ -state ULRM, the alignment originates from the interaction of the electronic spin degrees of freedom with the spatial degrees of freedom within the  $p$ -wave scattering. A pictorial illustration of the mechanism is presented in Fig. 1: In a first step, the magnetic field couples to the electronic spins and tends to align them. In a second step, the spin-orbit coupling modifies the electron-atom interaction in an angular-dependent fashion.

We analyze this alignment by determining the angular-dependent Born-Oppenheimer potential energy surfaces (PES) as well as energies and wave functions of bound vibrational states. To provide a more intuitive physical picture of the underlying mechanism, we present an approach that considers the presence of  $p$ -wave shape resonances and the magnetic field perturbatively and reproduces the polar potential energy curves of the underlying *ab initio* calculations. We focus here on rubidium molecules. However, our approach applies also to ULRM of other atomic species that possess a  $p$ -wave shape resonance such as cesium.

\*frederic.hummel@physnet.uni-hamburg.de

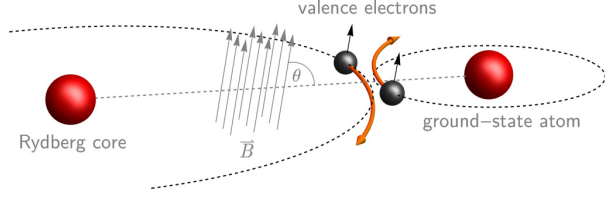


FIG. 1. Pictorial representation of the alignment mechanism of the Rydberg electron and the ground-state atom. The magnetic field (gray arrows) tends to orient the electronic spins (black arrows). Because of spin-orbit interaction, the relative angle with regard to the internuclear axis  $\theta$  influences the scattering process (orange arrows) and leads, consequently, to angular-dependent potential energy surfaces.

## II. SETUP AND INTERACTIONS

Our diatomic ULRM consists of a Rydberg and a ground-state rubidium atom. The closed-shell core electrons of the Rydberg atom are taken into account by quantum defects of the Rydberg energy levels obtained by experimental observation [51,52]. The polarizable ground-state atom with hyperfine structure [53] at relative position  $\vec{R}$  to the Rydberg core acts as a perturber to the Rydberg electron's wave function (see Fig. 2 for a sketch including all relevant spin degrees of freedom). The interaction of the ground-state atom with the Rydberg electron can be described via a generalized Fermi pseudopotential (we use atomic units unless stated otherwise),

$$V(\vec{R}, \vec{r}) = \sum_{\beta} \frac{(2L+1)}{2} a(2S+1L_J, k) \frac{\delta(x)}{x^{2(L+1)}} |\beta\rangle \langle \beta|, \quad (1)$$

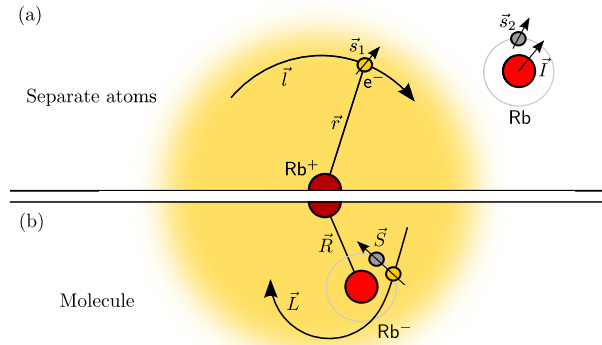


FIG. 2. Sketch of the molecule and its spin degrees of freedom in two different representations. In panel (a), the ground-state atom with nuclear spin  $\vec{I}$  and electronic spin  $\vec{s}_2$  is located outside the electronic cloud of the Rydberg atom (yellow shading). The Rydberg atom's core is located in the center and the Rydberg electron at position  $\vec{r}$  carries orbital angular momentum  $\vec{l}$  and spin  $\vec{s}_1$ . In panel (b), the ground-state atom is located inside the cloud at position  $\vec{R}$ . Here, the electronic spins are coupled to the total electronic spin  $\vec{S}$  which again couples to the electron pair's angular momentum relative to the ground-state atom's core  $\vec{L}$ .

which takes into account partial waves up to  $p$ -wave interactions that are proportional to the respective spin-dependent scattering lengths [47,49]. This includes six scattering channels labeled with angular momentum quantum numbers in the frame of the ground-state atom,  $^{2S+1}L_J = \{^1S_0, ^3S_1, ^1P_1, ^3P_0, ^3P_1, ^3P_2\}$ , where  $S$  is the total spin of the valence electron pair,  $L$  is the electron pair's orbital angular momentum relative to the ground-state atom,  $J$  is the total electronic angular momentum arising from  $\vec{L} \cdot \vec{S}$  coupling, and  $M_J$  is the total electronic angular momentum projection onto the internuclear axis. The scattering states are labeled as  $|\beta\rangle = |(L, S)J, M_J\rangle$ ,  $x = |\vec{r} - \vec{R}|$  is the distance between the Rydberg electron and the neutral ground-state atom, and  $a(^{2S+1}L_J, k)$  is the energy-dependent scattering length associated to the respective channel. The wave number  $k$  is approximated via the semiclassical electron energy  $\frac{1}{2}k^2(R) = \frac{1}{R} - \frac{1}{2n_h^2}$ , where  $R$  is the distance between the two atoms and  $n_h$  is the principal quantum number of the closest hydrogenic manifold. Although the contact potential in (1) leads to formally ill-behaved solutions, it approximates the electron-atom interaction reasonably well, when employed in a restricted basis set approach [26,54,55], in very good agreement with experiments [4]. Alternative approaches are based on finite-range pseudopotentials, Green's function methods, or  $R$ -matrix techniques [2,47,56]. The ground-state atom's hyperfine structure is considered via  $H_{\text{HF}} = A\vec{s}_2 \cdot \vec{I}$ , where  $\vec{s}_2$  is the ground-state atom's electronic spin,  $\vec{I}$  is its nuclear spin, with  $I = \frac{3}{2}$  for rubidium, and  $A = 3.417$  GHz is rubidium's hyperfine constant. The effect of a magnetic field is included via the corresponding Zeeman term and couples linearly to the electronic angular momenta

$$H_B = \vec{B} \cdot (\vec{S} + \vec{I}/2), \quad (2)$$

where  $\vec{B}$  is given in units of  $2.35 \times 10^9$  Gauss and  $l$  is the Rydberg electrons's orbital angular momentum relative to the Rydberg core, which is nonzero for states other than the  $s$  state.

The combined electronic Hamiltonian  $H = H_{\text{Ryd}} + V + H_{\text{HF}} + H_B$  [49,50] is diagonalized within the Born-Oppenheimer approximation, yielding the adiabatic PES, which depend parametrically on the distance between the Rydberg core and the ground-state atom. Indeed, due to the azimuthal molecular symmetry corresponding to rotations around the magnetic field axis, the PES depend only on the internuclear distance  $R$  and the polar angle  $\theta$  between the magnetic field axis and the internuclear axis. Our basis includes the closest hydrogenic manifold, which lies energetically above the considered  $s$  state (Fig. 3), with all Rydberg electronic angular momentum states that have a maximal projection onto the internuclear axis of  $m_{\text{max}} = 3/2$ , and all ground-state atomic hyperfine states. Further increase of  $m_{\text{max}}$  has only minor influence on our results (see the appendix, cf. [57]).

## III. RESULTS

Figure 3 depicts a radial cut of the PES for rubidium 28s ( $s$ PES) and  $F = 2$  in a magnetic field of  $B = 10$  G that is aligned parallel to the internuclear axis. The presence of the

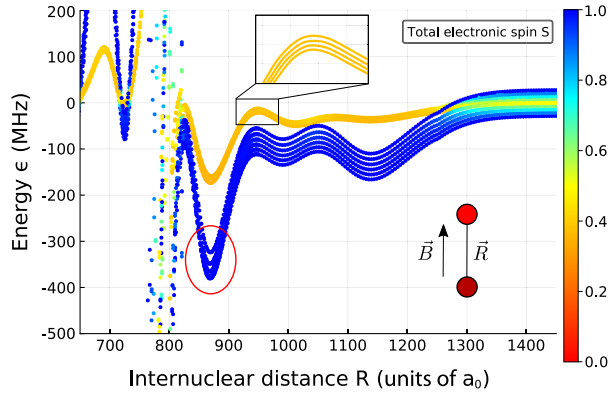


FIG. 3. Radial cut of the PES for a rubidium  $28s$  state in a magnetic field of  $B = 10$  G parallel to the internuclear axis ( $\theta = 0$ ) for the ground-state atom in a hyperfine  $F = 2$  state. The color code indicates the expected total electronic spin. A pure triplet curve with sixfold multiplicity is visible as well as a mixed singlet-triplet curve with fourfold multiplicity (inset). In the deepest potential well around  $R = 870 a_0$  (see encircled region), which lies close to the  $p$ -wave shape resonance, the Zeeman splitting is not equidistant.

neutral ground-state atom in the Rydberg electronic cloud leads to an oscillatory potential curve typical for ULRM. Illustratively speaking, the emerging potential wells act as traps for the neutral ground-state atom and lead to radially localized bound states between the Rydberg atom and the ground-state atom, thus forming a molecule. At distances  $R \approx 800 a_0$ , where  $a_0$  is the Bohr radius, the kinetic energy of the Rydberg electron matches the energy of the  $p$ -wave shape resonances, which leads to a steep crossing of the butterfly PES. Sufficiently far from the resonance, the PES can be characterized by their total electronic spin character, which is shown in Fig. 3 as a color code. Deep potential wells occur when the electronic spins are aligned to a triplet state ( $S = 1$ ), and shallow wells when the spins are antialigned in a mixed singlet-triplet state. The presence of the magnetic field splits the otherwise degenerate curves and reveals their multiplicity, which in the case of the  $F = 2$  hyperfine state is six for the triplet curve and four for the mixed curve.

Typically within a region of  $100 a_0$  around the crossing with the butterfly curve (at  $R \approx 800 a_0$ ), we find a significant dependence of the sPES on the polar angle  $\theta$ . An angular cut of the sPES at the radial position of the deepest potential well at  $R = 870 a_0$  is shown in gray in Fig. 4(a). The emerging angular potential wells are deep enough to support aligned molecular states for which three equilibrium angles are possible. Both the energetically lowest and highest visible sPES allow for molecules oriented perpendicular to the magnetic field axis ( $\theta = \frac{\pi}{2}$ ), whereas all other visible sPES allow for parallel and antiparallel alignment ( $\theta = \{0, \pi\}$ ). The second lowest visible sPES shown in gray in Fig. 4(a) constitutes an exception to this and is mostly flat, not allowing any alignment. The angular dependence of the sPES is only present if the spin-orbit interaction is included in the description and the  $p$ -wave interaction is sufficiently strong. When choosing equal scattering lengths for all three triplet  $p$ -wave channels and therefore effectively eliminating the relativistic spin-orbit

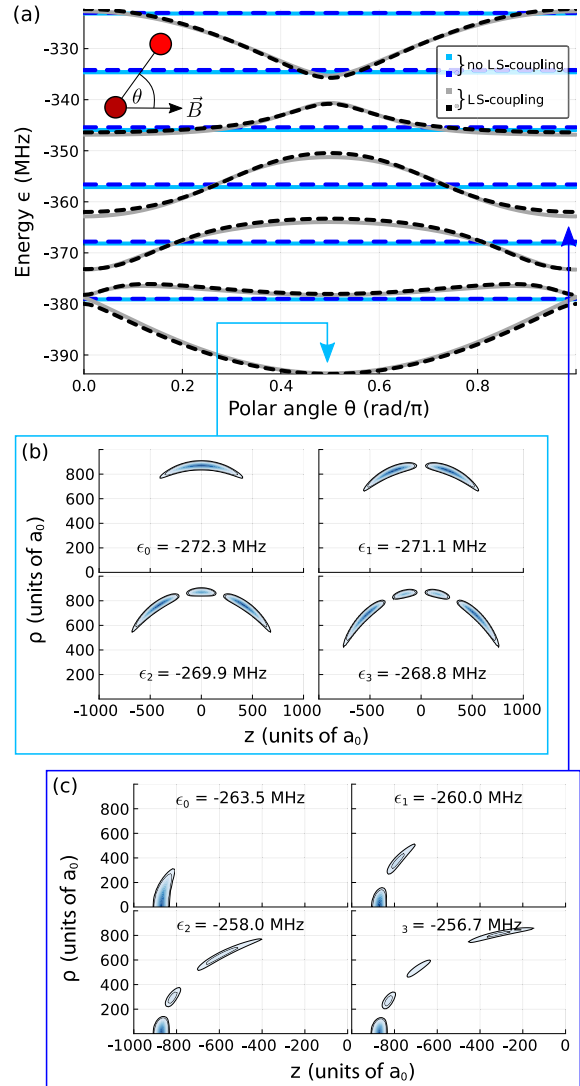


FIG. 4. (a) Angular cut of the PES for a rubidium  $28s$  state in a magnetic field of  $B = 10$  G at the radial position  $R = 870 a_0$  matching the position of the potential well close to the  $p$ -wave shape resonance (see Fig. 3). The numerical result within exact diagonalization of the electronic Hamiltonian (light blue and gray lines) is compared to a reduced model only taking the six relevant states of the  $K = 5/2$  multiplet into account (blue and black dashed lines). Both approaches are considered with equal (light blue, blue) and distinguishable (gray, black) triplet  $p$ -wave scattering lengths. [(b), (c)] Probability densities in cylindrical coordinates of vibrational states  $u(\rho, z)$  supported by the  $m_F = -2$  and  $m_F = 0$  dominated states, respectively. The ground-state atom localizes in the perpendicular (parallel) configuration relative to the magnetic field axis. The eigenstate energy  $\epsilon_v$  is provided relative to the unperturbed  $28s, F = 2$  atomic energy. The vibrational ground state features an alignment of  $\langle \cos^2 \theta \rangle = 0.04$  (b) and  $0.98$  (c).

coupling in the scattering event, the polar-angle dependence vanishes, which is shown in light blue.

To describe vibrational states belonging to the PES, it is beneficial to introduce cylindrical coordinates, i.e.,

$\vec{R} = \rho(\cos\phi \hat{e}_x + \sin\phi \hat{e}_y) + z \hat{e}_z$ , with the  $z$  axis pointing along the direction of the  $\vec{B}$  field. In this case, stationary states can be expressed as  $\chi(\vec{R}) = u(\rho, z)\exp(-i\mu\phi)/\sqrt{\rho}$  with a good azimuthal angular momentum quantum number  $\mu$ . The states  $u(\rho, z)$  are governed by the Hamiltonian [16,50]

$$H_{\text{vib}} = -\frac{1}{M}(\partial_\rho^2 + \partial_z^2) + \frac{\mu^2 - 1/4}{M\rho^2} + \epsilon_i(\rho, z), \quad (3)$$

where  $M$  is the atomic mass of  $^{87}\text{Rb}$  and  $\epsilon_i(\rho, z)$  are the PES. We focus exclusively on  $\mu = 0$  and obtain the eigenstates of (3) via a two-dimensional finite difference method. For the energetically lowest curve in Fig. 4(a), which represents the spin-polarized  $F = 2$ ,  $m_F = -2$  state, the probability densities of the vibrational ground state and the first three excited states are provided in Fig. 4(b). They exhibit an energy spacing of 1 MHz and the vibrational ground state features an alignment of  $\langle \cos^2\theta \rangle = 0.04$ . The third gray curve from the bottom in Fig. 4(a) corresponds to an  $s$  state dominated by  $F = 2$ ,  $m_F = 0$  contributions and possesses potential wells around  $\theta = 0$  and  $\theta = \pi$ . The probability densities of the corresponding vibrational states can be seen in Fig. 4(c) and exhibit an energy spacing of 2 MHz, while the vibrational ground state features an alignment of  $\langle \cos^2\theta \rangle = 0.98$ .

#### IV. DISCUSSION

In order to develop a more intuitive picture of our alignment mechanism, we reduce the complexity of the electronic Hamiltonian by means of a perturbative approach. To reproduce the angular cuts of the PES, it is sufficient to restrict the Hilbert space to a subspace with  $l = 0$  and a constant quantum number  $K = |\vec{S} + \vec{I}| = |\vec{s}_1 + \vec{F}|$ . For  $s$ -state ULRM,  $K$  represents the molecular system's total angular momentum and is approximately conserved (up to admixture of  $l > 0$  states). This is reflected by the multiplicity of the PES in Fig. 3. The extreme values for  $K = \{\frac{1}{2}, \frac{5}{2}\}$  correspond to pure triplet ( $S = 1$ ) states, whereas  $K = \frac{3}{2}$  states have mixed singlet and triplet character. In this subspace, the Hamiltonian reads

$$H(\theta) = c_s + c_p \sum_{J=0}^2 V_p(J) + H_B, \quad (4)$$

where  $c_s$  and  $c_p$  are parameters which are adjusted to reproduce the results of the field-free exact diagonalization.  $c_s$  corresponds to the overall offset due to the dominant  $s$ -wave interaction and  $c_p$  controls the admixture of the  $p$ -wave interaction. The  $p$ -wave interactions  $V_p(J)$  depend on the total electronic angular momentum  $J$  relative to the ground-state atom at  $\vec{R}$ , while  $H_B$  couples the electronic spins to the  $\vec{B}$ -field axis. The resulting PES will, however, only depend on the relative angle  $\theta$  between  $\vec{R}$  and  $\vec{B}$ . Without loss of generality we can therefore specify  $\vec{R} = R\hat{e}_z$  and  $\vec{B} = B(\cos\theta \hat{e}_z + \sin\theta \hat{e}_x)$ . In the  $l = 0$  subspace, the  $p$ -wave interaction terms in (1) simplify then to

$$V_p(J) = a(^3P_J, k) \sum_{M_S} |C_{10,1M_S}^{JM_S}|^2 |M_S\rangle \langle M_S|, \quad (5)$$

where  $M_S$  are the three possible projections of  $S = 1$  onto the internuclear  $z$  axis and  $C_{LM_L, SM_S}^{JM_S}$  is a Clebsch-Gordan coefficient describing the coupling of  $\vec{S}$  and  $\vec{L}$  to  $\vec{J}$ . The impact of the magnetic field on  $s$  states reduces from (2) to

$$H_B = B(S_z \cos\theta + S_x \sin\theta), \quad (6)$$

with the spin matrices for  $z$  and  $x$  direction  $S_{z,x}$ . The simple structure of (5) and (6) reveals the nature of the alignment mechanism: If the scattering lengths for the  $p$ -wave channel  $a(^3P_J, k)$  are equal, the generator of rotations  $\theta$  in (6), here  $S_y$ , commutes with  $V_p$ , and the eigenvalues of  $H(\theta)$  are independent of  $\theta$ . However, in the case of different  $p$ -wave triplet scattering lengths an angular dependence emerges. To compare the model (4) to the full Hamiltonian, we diagonalize the matrix  $\langle KM_K | H(\theta) | KM_K \rangle$ , where  $M_K$  is the projection of  $K$  onto the internuclear axis.

Figure 4(a) shows the sPES of the model in the case of  $K = 5/2$  for a magnetic field of  $B = 10$  G, which corresponds the curves circled in red in Fig. 3. For distinguishable (equal) scattering lengths, shown in black (blue), the model recovers the results of the exact diagonalization, which are shown in gray (light blue). For larger magnetic fields, when  $H(\theta)$  is dominated by  $H_B$ , the different PES separate further while the depth of the potential wells does not increase. For smaller magnetic fields, when  $H(\theta)$  is dominated by  $V_p(J)$ , the PES are structured in pairs of equal absolute total angular momentum projection  $|M_K|$ . The  $\theta$ -dependent influence of the interaction matrices  $V_p(J)$ , which represent the three different triplet  $p$ -wave scattering channels, on the eigenvalues of  $H(\theta)$  corresponds to the physical picture that the spin-orbit interaction introduces a spatial degree of freedom and consequently angular anisotropy to the otherwise isotropic molecular system.

#### V. CONCLUSION

We predict the possibility of molecular alignment of  $s$ -state ultra-long-range Rydberg molecules in a homogeneous magnetic field. In contrast to  $d$ -state ULRM that can be aligned in magnetic fields due to the nonzero orbital angular momentum of the Rydberg state, the alignment of  $s$ -state ULRM has a completely different origin. We attribute the effect to the interplay of a magnetic field and the spin-orbit coupling of the electron-atom interaction. For the alignment to occur in  $s$  states, it needs both the  $\vec{L} \cdot \vec{S}$ - and the strong  $p$ -wave interaction. The alignment mechanism can be interpreted by means of a reduced interaction model in a comparably low-dimensional Hilbert space. This novel degree of control of the otherwise isotropic  $s$  states of ULRM is clearly within reach of current experimental efforts. Although signatures in measured electric dipole moments of butterfly ULRM indicate the presence of  $\vec{L} \cdot \vec{S}$  couplings in ULRM [26], a clear experimental confirmation is still missing. An experimental observation of the here proposed alignment of  $s$ -state ULRM would be perfectly suited for such a purpose.

Beyond this work, it would be beneficial to study the influence of higher angular momentum states on the alignment, for instance in trilobites or  $p$ -state molecules, with

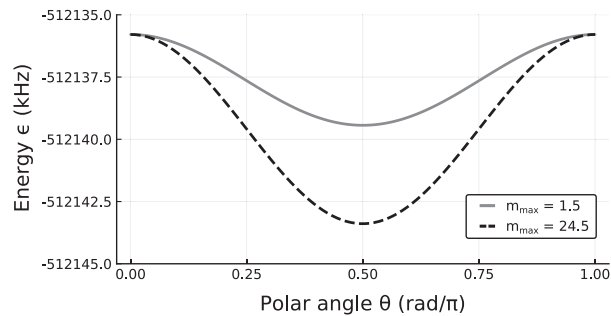


FIG. 5. The same setup as in Fig. 4(a) neglecting hyperfine structure and  $\vec{L} \cdot \vec{S}$  coupling. The results for different maximal total angular momentum projections of the Rydberg electron  $m_{\max}$  are shown. The inclusion of more projection states makes the angular dependency more pronounced. The maximal energetic difference of different polar angles between the internuclear axis and the magnetic field is on the order of a few kHz.

the butterfly molecules being a prominent candidate to show effects of spin-orbit interaction. Furthermore, similar effects should occur in polyatomic ULRM and are expected to lead to novel forms of angular dependent three-body interactions. ULRM are an exceptionally suitable environment to experimentally study low-energy electronic scattering. In particular, the study of spin-orbit interaction effects provides unique possibilities to experimentally characterize relativistic electron-atom  $p$ -wave scattering and its underlying resonances.

## ACKNOWLEDGMENTS

F.H. and P.S. acknowledge support from the German Research Foundation within the priority program “Giant Interactions in Rydberg Systems” (SPP 1929 GiRyd). C.F. gratefully acknowledges a scholarship from the Studienstiftung des deutschen Volkes.

## APPENDIX: $l$ MIXING OF MOLECULAR STATES

In general, the interaction of the Rydberg electron with the ground-state atom leads to  $l$  mixing. However, due to the noninteger quantum defect of atomic states with low orbital angular momentum  $l < 3$  and resulting energetical detuning off the degenerate hydrogenic manifold, this process is strongly suppressed for Rydberg  $s$  states discussed here. To quantitatively examine the impact of  $l$  mixing on the alignment process, we neglect the hyperfine structure of the ground-state atom in the absence of  $\vec{L} \cdot \vec{S}$  coupling. This approach makes it numerically feasible to consider all total angular momentum projection quantum numbers of the Rydberg electron  $m_j$  up to  $m_{\max} = n - 1 + \frac{1}{2} = 24.5$ . Figure 5 shows an angular cut of the derived PES for the  $28s + 5s$  molecule for such a calculation (black, dashed line) at the radial position of the inner potential well shown in Fig. 3 at  $R = 870 a_0$  and compares it to a calculation where  $m_{\max} = 1.5$  (gray, solid line). While the inclusion of all projection states makes the effect more pronounced, an angular dependence is visible on the scale of a few kHz, which is four orders of magnitude smaller than the effect of the spin-orbit coupling of the scattering interaction studied in this paper, which is on the scale of tens of MHz.

- [1] C. H. Greene, A. S. Dickinson, and H. R. Sadeghpour, *Phys. Rev. Lett.* **85**, 2458 (2000).
- [2] E. L. Hamilton, C. H. Greene, and H. R. Sadeghpour, *J. Phys. B* **35**, L199 (2002).
- [3] M. I. Chibisov, A. A. Khuskivadze, and I. I. Fabrikant, *J. Phys. B* **35**, L193 (2002).
- [4] V. Bendkowsky, B. Butscher, J. Nipper, J. P. Shaffer, R. Löw, and T. Pfau, *Nature (London)* **458**, 1005 (2009).
- [5] J. Tallant, S. T. Rittenhouse, D. Booth, H. R. Sadeghpour, and J. P. Shaffer, *Phys. Rev. Lett.* **109**, 173202 (2012).
- [6] B. J. DeSalvo, J. A. Aman, F. B. Dunning, T. C. Killian, H. R. Sadeghpour, S. Yoshida, and J. Burgdörfer, *Phys. Rev. A* **92**, 031403(R) (2015).
- [7] B. Butscher, J. Nipper, J. B. Balewski, L. Kukota, V. Bendkowsky, R. Löw, and T. Pfau, *Nat. Phys.* **6**, 970 (2010).
- [8] B. Butscher, V. Bendkowsky, J. Nipper, J. B. Balewski, L. Kukota, R. Löw, T. Pfau, W. Li, T. Pohl, and J. M. Rost, *J. Phys. B* **44**, 184004 (2011).
- [9] F. Camargo, J. D. Whalen, R. Ding, H. R. Sadeghpour, S. Yoshida, J. Burgdörfer, F. B. Dunning, and T. C. Killian, *Phys. Rev. A* **93**, 022702 (2016).
- [10] J. D. Whalen, F. Camargo, R. Ding, T. C. Killian, F. B. Dunning, J. Pérez-Ríos, S. Yoshida, and J. Burgdörfer, *Phys. Rev. A* **96**, 042702 (2017).
- [11] W. Li, T. Pohl, J. M. Rost, S. T. Rittenhouse, H. R. Sadeghpour, J. Nipper, B. Butscher, J. B. Balewski, V. Bendkowsky, R. Löw, and T. Pfau, *Science* **334**, 1110 (2011).
- [12] D. Booth, S. T. Rittenhouse, J. Yang, H. R. Sadeghpour, and J. P. Shaffer, *Science* **348**, 99 (2015).
- [13] D. A. Anderson, S. A. Miller, and G. Raithel, *Phys. Rev. Lett.* **112**, 163201 (2014).
- [14] V. Bendkowsky, B. Butscher, J. Nipper, J. B. Balewski, J. P. Shaffer, R. Löw, T. Pfau, W. Li, J. Stanojevic, T. Pohl, and J. M. Rost, *Phys. Rev. Lett.* **105**, 163201 (2010).
- [15] A. Gaj, A. T. Krupp, J. B. Balewski, R. Löw, S. Hofferberth, and T. Pfau, *Nat. Commun.* **5**, 4546 (2014).
- [16] A. T. Krupp, A. Gaj, J. B. Balewski, P. Ilzhöfer, S. Hofferberth, R. Löw, T. Pfau, M. Kurz, and P. Schmelcher, *Phys. Rev. Lett.* **112**, 143008 (2014).
- [17] A. Gaj, A. T. Krupp, P. Ilzhöfer, R. Löw, S. Hofferberth, and T. Pfau, *Phys. Rev. Lett.* **115**, 023001 (2015).
- [18] T. Niederprüm, O. Thomas, T. Eichert, C. Lippe, J. Pérez-Ríos, C. H. Greene, and H. Ott, *Nat. Commun.* **7**, 12820 (2016).
- [19] T. Manthey, T. Niederprüm, O. Thomas, and H. Ott, *New J. Phys.* **17**, 103024 (2015).
- [20] T. Niederprüm, O. Thomas, T. Eichert, and H. Ott, *Phys. Rev. Lett.* **117**, 123002 (2016).

- [21] M. Schlagmüller, T. C. Liebisch, F. Engel, K. S. Kleinbach, F. Böttcher, U. Hermann, K. M. Westphal, A. Gaj, R. Löw, S. Hofferberth, T. Pfau, J. Pérez-Ríos, and C. H. Greene, *Phys. Rev. X* **6**, 031020 (2016).
- [22] I. Mirgorodskiy, F. Christaller, C. Braun, A. Paris-Mandoki, C. Tresp, and S. Hofferberth, *Phys. Rev. A* **96**, 011402(R) (2017).
- [23] J. B. Balewski, A. T. Krupp, A. Gaj, D. Peter, H. P. Büchler, R. Löw, S. Hofferberth, and T. Pfau, *Nature (London)* **502**, 664 (2013).
- [24] J. Wang, M. Gacesa, and R. Côté, *Phys. Rev. Lett.* **114**, 243003 (2015).
- [25] F. Camargo, R. Schmidt, J. D. Whalen, R. Ding, G. Woehl, S. Yoshida, J. Burgdörfer, F. B. Dunning, H. R. Sadeghpour, E. Demler, and T. C. Killian, *Phys. Rev. Lett.* **120**, 083401 (2018).
- [26] M. T. Eiles, J. Pérez-Ríos, F. Robicheaux, and C. H. Greene, *J. Phys. B* **49**, 114005 (2016).
- [27] R. Schmidt, H. R. Sadeghpour, and E. Demler, *Phys. Rev. Lett.* **116**, 105302 (2016).
- [28] R. Schmidt, J. D. Whalen, R. Ding, F. Camargo, G. Woehl, S. Yoshida, J. Burgdörfer, F. B. Dunning, E. Demler, H. R. Sadeghpour, and T. C. Killian, *Phys. Rev. A* **97**, 022707 (2018).
- [29] K. S. Kleinbach, F. Engel, T. Dieterle, R. Löw, T. Pfau, and F. Meinert, *Phys. Rev. Lett.* **120**, 193401 (2018).
- [30] T. Schmid, C. Veit, N. Zuber, R. Löw, T. Pfau, M. Tarana, and M. Tomza, *Phys. Rev. Lett.* **120**, 153401 (2018).
- [31] F. Engel, T. Dieterle, T. Schmid, C. Tomschitz, C. Veit, N. Zuber, R. Löw, T. Pfau, and F. Meinert, *Phys. Rev. Lett.* **121**, 193401 (2018).
- [32] N. Sándor, R. González-Férez, P. S. Julienne, and G. Pupillo, *Phys. Rev. A* **96**, 032719 (2017).
- [33] O. Thomas, C. Lippe, T. Eichert, and H. Ott, *Nat. Commun.* **9**, 2238 (2018).
- [34] E. Fermi, *Nuovo Cimento* **11**, 157 (1934).
- [35] A. Omont, *J. Phys. (Paris)* **38**, 1343 (1977).
- [36] H. Saßmannshausen, F. Merkt, and J. Deiglmayr, *Phys. Rev. Lett.* **114**, 133201 (2015).
- [37] F. Böttcher, A. Gaj, K. M. Westphal, M. Schlagmüller, K. S. Kleinbach, R. Löw, T. C. Liebisch, T. Pfau, and S. Hofferberth, *Phys. Rev. A* **93**, 032512 (2016).
- [38] M. Schlagmüller, T. C. Liebisch, H. Nguyen, G. Lothead, F. Engel, F. Böttcher, K. M. Westphal, K. S. Kleinbach, R. Löw, S. Hofferberth, T. Pfau, J. Pérez-Ríos, and C. H. Greene, *Phys. Rev. Lett.* **116**, 053001 (2016).
- [39] J. L. MacLennan, Y.-J. Chen, and G. Raithel, [arXiv:1808.05136](https://arxiv.org/abs/1808.05136).
- [40] I. I. Fabrikant, *J. Phys. B* **19**, 1527 (1986).
- [41] C. Bahrim and U. Thumm, *Phys. Rev. A* **61**, 022722 (2000).
- [42] C. Bahrim, U. Thumm, and I. I. Fabrikant, *Phys. Rev. A* **63**, 042710 (2001).
- [43] M. T. Eiles, *Phys. Rev. A* **98**, 042706 (2018).
- [44] A. R. Johnston and P. D. Burrow, *J. Phys. B* **15**, L745 (1982).
- [45] A. R. Johnston and P. D. Burrow, *Phys. Rev. A* **51**, 406 (1995).
- [46] M. Scheer, J. Thøgersen, R. C. Bilodeau, C. A. Brodie, H. K. Haugen, H. H. Andersen, P. Kristensen, and T. Andersen, *Phys. Rev. Lett.* **80**, 684 (1998).
- [47] A. A. Khuskivadze, M. I. Chibisov, and I. I. Fabrikant, *Phys. Rev. A* **66**, 042709 (2002).
- [48] S. Markson, S. T. Rittenhouse, R. Schmidt, J. P. Shaffer, and H. R. Sadeghpour, *Chem. Phys. Chem.* **17**, 3683 (2016).
- [49] M. T. Eiles and C. H. Greene, *Phys. Rev. A* **95**, 042515 (2017).
- [50] F. Hummel, C. Fey, and P. Schmelcher, *Phys. Rev. A* **97**, 043422 (2018).
- [51] W. Li, I. Mourachko, M. W. Noel, and T. F. Gallagher, *Phys. Rev. A* **67**, 052502 (2003).
- [52] J. Han, Y. Jamil, D. V. L. Norum, P. J. Tanner, and T. F. Gallagher, *Phys. Rev. A* **74**, 054502 (2006).
- [53] E. Arimondo, M. Inguscio, and P. Violino, *Rev. Mod. Phys.* **49**, 31 (1977).
- [54] N. Y. Du and C. H. Greene, *Phys. Rev. A* **36**, 971 (1987).
- [55] C. Fey, M. Kurz, P. Schmelcher, S. T. Rittenhouse, and H. R. Sadeghpour, *New J. Phys.* **17**, 055010 (2015).
- [56] M. Tarana and R. Čurík, *Phys. Rev. A* **93**, 012515 (2016).
- [57] K. S. Kleinbach, F. Meinert, F. Engel, W. J. Kwon, R. Löw, T. Pfau, and G. Raithel, *Phys. Rev. Lett.* **118**, 223001 (2017).



### 3.3 Precision spectroscopy of negative-ion resonances in ultralong-range Rydberg molecules

## Precision Spectroscopy of Negative-Ion Resonances in Ultralong-Range Rydberg Molecules

F. Engel,<sup>1</sup> T. Dieterle,<sup>1</sup> F. Hummel,<sup>2</sup> C. Fey,<sup>2</sup> P. Schmelcher,<sup>2,3</sup> R. Löw,<sup>1</sup> T. Pfau,<sup>1</sup> and F. Meinert<sup>1</sup>

<sup>1</sup>*Physikalisches Institut and Center for Integrated Quantum Science and Technology, Universität Stuttgart, Pfaffenwaldring 57, 70569 Stuttgart, Germany*

<sup>2</sup>*Zentrum für optische Quantentechnologien, Fachbereich Physik, Universität Hamburg, 22761 Hamburg, Germany*

<sup>3</sup>*The Hamburg Centre for Ultrafast Imaging, Universität Hamburg, 22761 Hamburg, Germany*



(Received 17 April 2019; published 16 August 2019)

The level structure of negative ions near the electron detachment limit dictates the low-energy scattering of an electron with the parent neutral atom. We demonstrate that a single ultracold atom bound inside a Rydberg orbit forming an ultralong-range Rydberg molecule provides an atomic-scale system that is highly sensitive to electron-neutral scattering and thus allows for detailed insights into the underlying near-threshold anion states. Our measurements reveal the so-far unobserved fine structure of the  $^3P_J$  triplet of  $\text{Rb}^-$  and allows us to extract parameters of the associated  $p$ -wave scattering resonances that deviate from previous theoretical estimates. Moreover, we observe a novel alignment mechanism for Rydberg molecules mediated by spin-orbit coupling in the negative ion.

DOI: [10.1103/PhysRevLett.123.073003](https://doi.org/10.1103/PhysRevLett.123.073003)

Negative ions constitute remarkable objects that have been studied intensively over the past decades [1,2]. In contrast to neutral atoms or positively charged ions, anions are much more weakly bound by shallow and short-range potentials and typically feature only few bound states. As a consequence, they have been proven ideal model systems for investigating the role of electron-electron correlations on their level structure [2]. More recently, the observation of excited opposite-parity bound states [3] has triggered renewed interest in high-resolution negative-ion spectroscopy [4–6] motivated by prospects to realize laser cooling for trapped anions [7,8].

The fine details of the interaction potentials that determine negative-ion bound states also dictate the very low-energy quantum scattering of their neutral parent atom with a free electron [9–11]. Particularly, broad scattering resonances can arise when the associated negative-ion system hosts a short-lived transient state, bound by a centrifugal barrier and located just a few meV above the electron detachment limit. Accessing details of these underlying anion states such as relativistic fine-structure effects experimentally, however, is challenged by their short lifetime, low energy [12], or by selection rules in photodetachment studies starting from the negative-ion ground state [13]. In this Letter, we demonstrate a completely different route to investigate these systems by devising an ultrasensitive microscopic scattering laboratory provided by an ultralong-range Rydberg molecule (ULRM) [14–17]. ULRMs consist of a Rydberg atom that binds to a neutral ground-state atom inside the electron orbit via frequent low-energy scattering of the latter with the quasifree Rydberg electron.

Here, we exploit ULRMs at an unprecedented quantitative level and demonstrate their potential to perform precise spectroscopy of negative-ion resonances at the example of the quasibound  $^3P_J$  state of  $\text{Rb}^-$ . To this end, we identify previously unobserved molecular states, which are dominated by resonant electron-atom  $p$ -wave scattering, and thereby allow us to reveal the presence of relativistic spin-orbit coupling leading to a fine-structure triplet ( $J \in \{0, 1, 2\}$ ). The latter was predicted theoretically for the heavy alkali metals  $\text{Rb}^-$ ,  $\text{Cs}^-$ , and  $\text{Fr}^-$ , but so far remained experimentally inaccessible [10,18]. Moreover, we observe that the presence of spin-orbit interaction aligns the ULRM even for spherically symmetric Rydberg  $S$  states [19]. Our approach holds intriguing perspectives for high-resolution probing of more complex perturbers such as molecules or clusters [20,21].

An ULRM naturally provides a highly adjustable atomic-scale system for precise studies of electron-neutral scattering at collision energies in the meV regime [16,22]. Apart from the capability to achieve very low scattering energies unfeasible to realize with free electrons, the high precision arises from the resonating Rydberg electron wave confined in the Coulomb potential, and the resulting narrow Rydberg states. Consider now the presence of a single neutral ground-state atom inside the Rydberg orbit at a distance  $R$  from the Rydberg core. Quantum scattering of the electron off the perturber gives rise to a phase shift imparted on the electron wave function, which is detectable via a slight shift of the Rydberg electron resonance energy.

Here, we focus on ultralong-range dimers consisting of a single  $^{87}\text{Rb}$  ground-state atom inside the orbit of  $nS_{1/2}$   $\text{Rb}$

Rydberg states ( $n = 31, \dots, 37$ ). For values of  $R$  comparable to the size of the Rydberg orbit, the semiclassical electron momentum  $k$  is sufficiently small so that  $s$ -wave scattering, as quantified by an energy-dependent (triplet) scattering length  $a_s^T(k)$ , dominates. This gives rise to a smoothly varying potential energy of the system as a function of  $R$  that reflects the nodal structure of the Rydberg electron wave function (see Fig. 1) [14,15,23]. For smaller values of  $R$  the electron momentum increases and  $p$ -wave scattering can become relevant. Importantly, the  $p$ -wave contribution is enhanced by a shape resonance arising from the presence of the  $\text{Rb}^-({}^3P)$  state [24,25], which *ab initio* theoretical predictions locate about 23 meV above the  $\text{Rb-}e^-$  threshold [10,18]. The resonant  $p$ -wave contribution leads to deep potential energy minima with decreasing  $R$  when the electron kinetic energy approaches the  ${}^3P$  resonance. The motion of the perturber atom is dictated by the resulting potential energy curve (PEC) and quantized due to the strong radial confinement associated with the potential wells, leading to discrete vibrational dimer states. In Fig. 1, the resulting lowest lying vibrational wave functions are indicated for the  $s$ -wave ( $p$ -wave) dominated wells at  $R = 1450a_0$  ( $R = 890a_0$ ).

Let us now turn to the internal spin structure of the system and in particular the consequence of spin-orbit coupling in the  $\text{Rb}^-({}^3P_J)$  state. In general, the latter gives rise to three (overlapping) anion states and consequently to a splitting of the single shape resonance into a triplet. A theoretical treatment of this spin-orbit coupling in the

context of ULRMs has been provided in Refs. [15,26,27]. For the PEC in Fig. 1, the spin-orbit interaction leads to a splitting of the deep  $p$ -wave dominated potential well into three substates, while the  $s$ -wave dominated outer part of the PEC is essentially unaffected. The splitting is due to three different  $p$ -wave scattering channels associated with the ( ${}^3P_J$ ) states, which are quantified by respective (triplet) scattering lengths  $a_{p,J}^T(k)$ . Each of the three split PECs is twofold degenerate and can be associated with a different projection of the total angular momentum on the internuclear axis  $|\Omega| = |m_F + m_j|$  [26]. Here,  $m_j$  and  $m_F$  denote magnetic quantum numbers for the Rydberg electron spin and the ground-state atom hyperfine level, respectively. We focus on the experimentally relevant PECs for  $F = 2$ .

According to the above considerations, the potential detection of spin-orbit interaction in the ( ${}^3P_J$ ) negative-ion system requires investigation of deeply bound dimer states with sufficient resonant  $p$ -wave scattering character. In a first set of experiments, we aim to identify and study these candidates via extensive molecular spectroscopy. To this end, we perform Rydberg spectroscopy incorporating field ionization and subsequent ion detection starting from an ultracold ( $1.5 \mu\text{K}$ ) ensemble of typically  $4.5 \times 10^6$   ${}^{87}\text{Rb}$  atoms prepared in the fully spin-stretched  $|F = 2, m_F = 2\rangle$  hyperfine state and held in a magnetic quadrupole trap. In the trap, the atoms experience a homogeneous magnetic offset field set to  $B = 2.2$  G. We address  $nS_{1/2}$  Rydberg states via two-photon spectroscopy involving the intermediate  $6P_{3/2}$  state at typical intermediate detunings between  $+80$  and  $+400$  MHz, and laser polarizations set to address the Zeeman sublevel  $m_j = 1/2$ .

An exemplary spectrum of the ULRMs below the  $|35S_{1/2}, m_j = 1/2; F = 2, m_F = 2\rangle$  asymptote is shown in Fig. 2(a). The strongest molecular line at  $-22.6$  MHz corresponds to the  $s$ -wave dominated dimer ( $D$ ) [16]. Additional lines with smaller binding energy are excited dimers bound by quantum reflection [28], previously studied in [22]. For larger binding energies, we observe two comparatively broad and so-far unexplored resonances labeled A and B, which we attribute to the two deeply bound dimer states depicted in Fig. 1 for  $n = 31$ . Four remaining resonances are attributed to trimer states with binding energies that match the sum of dimer lines [22]. Specifically, these comprise the simplest trimer formed by two atoms in the  $s$ -wave dimer state ( $T$ ), a trimer formed by one atom in the  $s$ -wave dimer and one in the dimer state B ( $B + D$ ), as well as trimers formed when one perturber resides in the strongest excited dimer state ( $B + D^*$  and  $D + D^*$ ).

In order to investigate the role of spin-orbit coupling on the deeply bound dimer A, we have taken spectra as shown in Fig. 2(a) for a range of principal quantum numbers. The measured binding energies for the states D, A, and B are

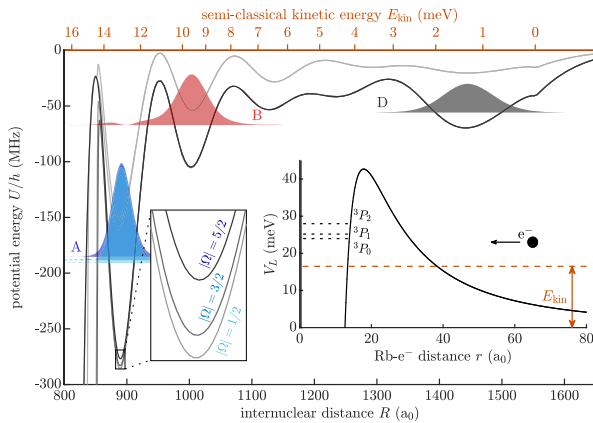


FIG. 1. Anion spectroscopy in ULRMs. Molecular potential energy for the  $31S$  Rydberg level owing to (triplet)  $\text{Rb-}e^-$  scattering as a function of internuclear distance  $R$  (black line). Vibrational wave functions for the molecular states A (blue), B (red), and D (black) are denoted by shaded areas. The  $p$ -wave dominated well ( $R = 890a_0$ ) is split due to the  $\text{Rb}^-$  fine-structure triplet  ${}^3P_J$ . For completeness, the gray line shows the shallow PEC originating from mixed singlet-triplet scattering (not accessed in this work). Inset: Long-range centrifugal barrier leading to the  ${}^3P_J$  states (dotted lines) of  $\text{Rb}^-$  above the electron detachment limit ( $V_L = 0$ ).

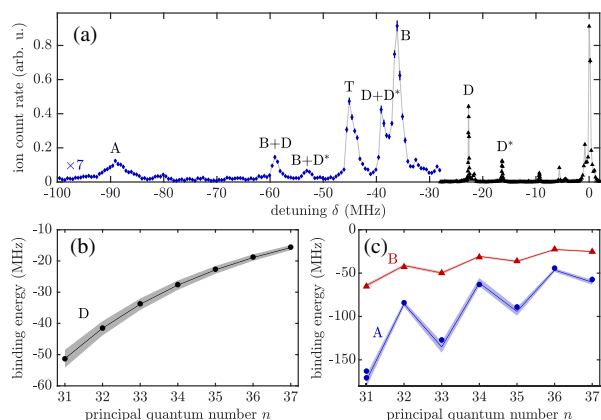


FIG. 2. ULRM spectroscopy for extracting  $s$ - and  $p$ -wave scattering lengths. (a) Ion signal as a function of detuning  $\delta$  from the atomic Rydberg line  $|35S_{1/2}, m_j = 1/2\rangle$ . Deeply bound molecular states are magnified for better visibility. Solid lines connect the data points to guide the eye. (b) Binding energy of the outermost dimer  $D$  as a function of  $n$ . (c) Binding energies of the deeply bound dimers  $A$  (circles) and  $B$  (triangles) as a function of  $n$ . Solid lines show results from a Green's function calculation with fitted  $s$ - and  $p$ -wave scattering lengths (see the text). The shaded areas mark small variations on the scattering lengths as described in the text. Error bars in (a) and all other spectra denote one standard deviation. Error bars for the measured binding energies in (b) and (c) are smaller than the data points.

depicted in Figs. 2(b) and 2(c). For the  $s$ -wave dominated dimer, we observe the well-known monotonic decrease of the binding energy with  $n$  [16]. The deeply bound states  $A$  and  $B$ , however, show a qualitatively different behavior characterized by a strong alternation of their energy with  $n$ . Note that state  $B$  appears as a single resonance for all  $n$ . The same holds for state  $A$  except for  $n = 31$ . Here, we observe a doublet structure split by  $\approx 8$  MHz.

In a next step, we perform numerical simulations based on a Fermi model, which allow us to extract triplet  $s$ - and  $p$ -wave scattering lengths from our data. To this end, we combine advantages from two different methods for simulating PECs, i.e., Green's function calculus and Hamiltonian diagonalization on a finite basis set. Briefly, the Green's function approach intrinsically provides converged results accounting for all Rydberg levels but lacks the possibility to include the full molecular spin structure [15]. Full diagonalization allows us to include all relevant spin degrees of freedom [26,27,39], but exhibits uncertainties originating from the chosen size of the basis set [40]. We stress that it is the combination of both methods that permits conclusions on a precise quantitative level by adapting the employed basis set as outlined in the following.

The starting point is the comparatively simple spin configuration investigated in our experiment, i.e., ULRMs associated with the  $|35S_{1/2}, m_j = 1/2; F = 2, m_F = 2\rangle$  asymptote. For negligible spin-orbit interaction,

these molecules are described by a single (triplet)  $s$ - and  $p$ -wave scattering channel [22]. Importantly, in that case complications due to atomic hyperfine structure or Rydberg fine structure do not play a role [41,42]. The PEC and the associated vibrational molecular states are then obtained from Green's function calculations. First, we have computed the molecular states  $D$ ,  $A$ , and  $B$  using  $s$ - and  $p$ -wave scattering length data from *ab initio* calculations [10,18] and found rather poor agreement with the data in Fig. 2(c), particularly for the  $p$ -wave dominated state  $A$ . Second, we adapted the  $s$ - and  $p$ -wave scattering lengths  $[a_s^T(k)$  and  $a_p^T(k)]$  that enter the calculations, aiming for improved agreement between experiment and simulation results. For this, we employ a comparatively simple model potential to compute the  $k$ -dependent scattering lengths, consisting of a long-range polarization potential and a short-range adjustable hard wall [27,28,43]. Moreover, note that the  $s$ - and  $p$ -wave channel can be adjusted independently by exploiting that the binding energy of the  $s$ -wave dominated dimer ( $D$ ) is essentially unaffected by the  $p$ -wave channel.

The molecular binding energies computed with the adjusted scattering lengths are depicted with solid lines in Figs. 2(b) and 2(c). We obtain a zero-energy  $s$ -wave scattering length  $a_s^T(0) = -15.2a_0$  and a value for the  $p$ -wave shape-resonance position  $E_r^{\text{avg}} = 26.6$  meV [44]. In order to estimate uncertainties for these values, the range of binding energies obtained from slight changes of the scattering lengths is indicated by shaded regions. Those correspond to variations in  $a_s^T(0)$  of  $\pm 0.5a_0$  and  $E_r^{\text{avg}}$  of  $\pm 0.2$  meV. Note that the ( $J$ -averaged) resonance position predicted in Ref. [10] based on a two active-electron model to account for electron correlations is about 20% smaller. Similar discrepancy has been found in photodetachment experiments of  $\text{Cs}^-$  [10,13]. For  $a_s^T(0)$ , the obtained value lies between previous theoretical estimates ( $-13a_0$  [10],  $-16.9a_0$  [45]).

While the Green's function calculation allows us to predict the observed molecular binding energies, it does not explain the measured doublet structure of the  $p$ -wave dominated state  $A$  for  $n = 31$ . In the following, we investigate this state in more detail and demonstrate that the level splitting is directly related to the fine structure of the  $^3P_J$  negative-ion resonance. High-resolution spectroscopy of the observed doublet is shown in Fig. 3 for three increasing values of the magnetic field  $B$ . We observe a strong qualitative change in the spectral shape when changing the magnetic field from about 2 to 15 G. While the doublet is observed for comparatively small fields (triangles), a single resonance modulated by a characteristic narrow substructure appears for higher values of  $B$  (diamonds).

To explain this observation, we now include the full molecular spin structure into our calculation of PECs via diagonalization of the system Hamiltonian on a finite basis set [26–28]. Here, the fine structure of the anion enters the computation via three  $J$ -dependent  $p$ -wave scattering

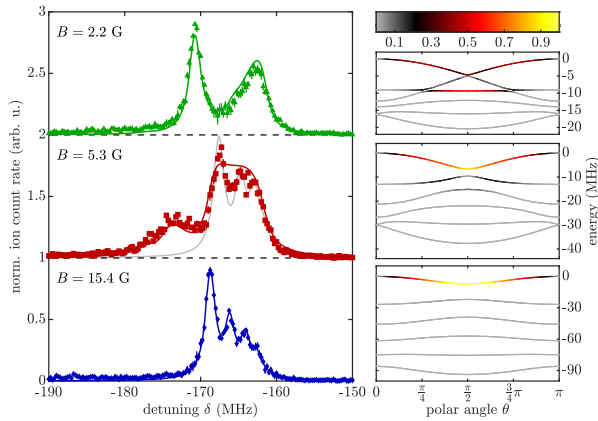


FIG. 3. Spin-orbit interaction and molecular alignment. (Left) Spectra of the  $p$ -wave dominated molecular state  $A$  with  $n = 31$  and for magnetic fields  $B$  as indicated. Zero detuning corresponds to the atomic Rydberg line  $|31S_{1/2}, m_j = 1/2\rangle$ . Solid lines are simulated line shapes based on the  $\theta$ -dependent PECs [28]. (Right) Angular dependence of the PECs evaluated at the minimum of the potential well in which state  $A$  is localized ( $R = 890a_0$ ). Energies are referenced to the maximum of the uppermost PEC. The three plots are computed for the magnetic field present in the corresponding measurement, i.e., for increasing values of  $B$  from top to bottom. Coloring encodes the projection onto  $m_j = 1/2$  and  $m_F = 2$  (see the text).

channels, quantified by their corresponding scattering lengths  $a_{p,J}^T(k)$ . We calculate the scattering lengths using the short-range parameters obtained above from the data in Fig. 2, but now add standard  $LS$  interaction to our model potential [28], which delivers the  $J$ -dependent  $a_{p,J}^T(k)$  and the corresponding shape-resonance positions  $E_r^J$ . Evidently, our approach yields values for  $E_r^J$  that fulfil Landé's interval rule, as expected for pure Russell-Saunders coupling [10]. Importantly, we can largely reduce the aforementioned uncertainties arising from the choice of the basis set by switching off the anion fine structure in the calculation and then adapting the basis set to match the previous Green's function results, yielding four hydrogenic Rydberg manifolds with  $n - 5$  to  $n - 2$  [28].

While the PECs shown in Fig. 1 are computed for a field-free situation, the magnetic field present in the experiment renders the situation even richer. Specifically, the Zeeman energy of the electron spins lifts the pairwise degeneracy of the three  $|\Omega\rangle$  states. Furthermore, when the effect of spin orbit coupling is sufficiently strong, the PECs obtain additional angular dependence as a result of an angular-dependent mixing of the three  $p$ -wave scattering channels [19]. Computed PECs for the values of  $B$  set in the experiment are shown in Fig. 3 (right column). For  $B = 2.2$  G, our laser excitation scheme couples only to the upper two PECs as indicated by the coloring, which denotes the absolute square of the projection of the

electronic molecular state onto  $|m_j = 1/2; F = 2, m_F = 2\rangle$  weighted by the solid angle  $\sin(\theta)$ . Note that for negligible spin-orbit interaction, the PECs are independent of  $\theta$  and one only couples to the highest energy state ( $\Omega = +5/2$ ). The observed doublet is thus a direct consequence of the  $^3P_J$  fine structure.

With increasing  $B$  the Zeeman shift separates the  $\theta$ -dependent PECs and only the curve with  $\Omega = +5/2$  can be addressed. Moreover, the increasing angular confinement finally aligns the molecule, leading to a series of discrete pendular states. This transition from a doublet to a single relevant PEC that exhibits a pendular-state substructure (Fig. 3,  $B = 15.4$  G) is in excellent agreement with the experimental observation. For a quantitative comparison, the spectra are compared to simulated line shapes using a semiclassical sampling approach based on the relevant PECs in the case of unresolved pendular states ( $B = 2.2$  G and  $B = 5.3$  G) and a rigid-rotor model when individual pendular states are observed ( $B = 15.4$  G) [28]. Deviations for  $B = 5.3$  G in the spectral part associated with the uppermost PEC are due to the onset of strong molecular alignment, as seen by comparison to the rigid-rotor model prediction based on that PEC (gray line). Moreover, the excellent agreement between theory and experiment allows for extracting the fine-structure splitting of the  $^3P_J$  anion state [28]. For the fitted results shown in Fig. 3, we obtain  $E_r^{J=(0,1,2)} = (24.4, 25.5, 27.7)$  meV, respectively. Apart from the systematically larger value of the measured  $E_r^{\text{avg}}$

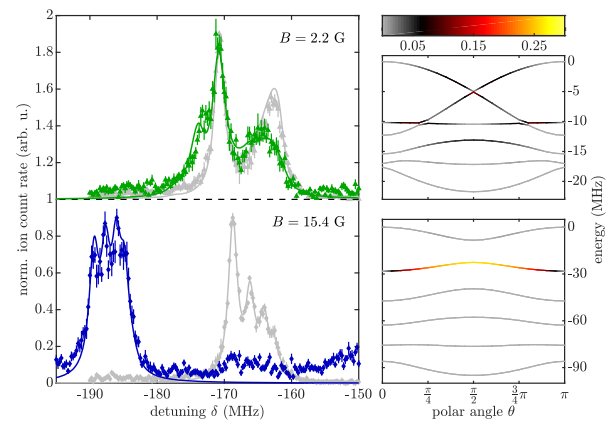


FIG. 4. Spin character of the spin-orbit affected ULRM. (Left) Spectra of the  $p$ -wave dominated molecular state  $A$  for  $n = 31$  with laser polarization set to address the  $m_j = -1/2$  atomic Rydberg state and for magnetic fields  $B$  as indicated. Gray data sets show the corresponding spectra for  $m_j = 1/2$  reprinted from Fig. 3 for comparison. Zero detuning corresponds to the atomic Rydberg line  $|31S_{1/2}, m_j = 1/2\rangle$ . Solid lines are simulated line shapes based on the  $\theta$ -dependent PECs. (Right) Angular dependence of the corresponding PECs similar to the ones shown in Fig. 3. Coloring now encodes the projection onto  $m_j = -1/2$  and  $m_F = 2$ .

discussed above, the obtained fine-structure splitting is in good agreement with the predictions in Ref. [10].

Finally, we investigate the spin character of the PECs in the presence of spin-orbit coupling by changing the laser polarization to couple to the  $|31S_{1/2}, m_j = -1/2\rangle$  Rydberg level. Measured spectra of the molecular state  $A$  are shown in Fig. 4 for two different settings of the magnetic field. For the low-field data ( $B = 2.2$  G) the spectrum only slightly changes due to a small shift of the excitation strength to smaller energies. Note that this is again an effect of spin-orbit interaction, which strongly mixes the spin character of the  $\theta$ -dependent PECs. For larger values of  $B$ , this spin mixing is less pronounced and our excitation scheme mostly couples to the second highest energy state ( $\Omega = +3/2$ ). This is reflected in the experiment data for  $B = 15.4$  G, showing a pronounced Zeeman shift of resolved pendular states. Again, we find excellent agreement with simulated line shapes.

In conclusion, we have exploited ULRMs for precise measurements on a quasibound negative-ion resonance. A careful analysis of measured binding energies allowed us to extract  $s$ - and  $p$ -wave scattering lengths and pinpoint the positions of the  $p$ -wave shape resonances associated with the  $^3P_J$  fine-structure triplet of  $\text{Rb}^-$ . We expect that the obtained scattering data will form the basis for future experiments on evermore delicate aspects of ULRMs, comprising few-body effects [46,47], molecular dynamics, or more complex spin couplings [41]. These prospects also call for developing Green's function calculations including all molecular spins. Moverover, our results allow for refining sophisticated predictions for low-energy electron-neutral scattering [10,15,18]. The presented technique for measuring fine details of near-threshold negative-ion resonances can further be transferred to benchmark other atomic and potentially also molecular systems featuring intriguing low-energy scattering properties [11,48,49].

We thank M. Eiles for numerous discussions and W. Li for assistance with the Green's function calculations. We acknowledge support from Deutsche Forschungsgemeinschaft [Grants No. PF 381/13-1, No. PF 381/17-1, and No. SCHM 885/30-1, the latter two being part of the SPP 1929 (GiRyd)]. F. M. acknowledges support from the Carl-Zeiss Foundation and is indebted to the Baden-Württemberg-Stiftung for the financial support by the Eliteprogramm for Postdocs.

- 
- [1] T. Andersen, *Phys. Rep.* **394**, 157 (2004).  
 [2] D. J. Pegg, *Rep. Prog. Phys.* **67**, 857 (2004).  
 [3] R. C. Bilodeau and H. K. Haugen, *Phys. Rev. Lett.* **85**, 534 (2000).  
 [4] U. Warring, M. Amoretti, C. Canali, A. Fischer, R. Heyne, J. O. Meier, Ch. Morhard, and A. Kellerbauer, *Phys. Rev. Lett.* **102**, 043001 (2009).

- [5] C. W. Walter, N. D. Gibson, D. J. Matyas, C. Crocker, K. A. Dungan, B. R. Matola, and J. Rohlén, *Phys. Rev. Lett.* **113**, 063001 (2014).  
 [6] E. Jordan, G. Cerchiari, S. Fritzsche, and A. Kellerbauer, *Phys. Rev. Lett.* **115**, 113001 (2015).  
 [7] A. Kellerbauer and J. Walz, *New J. Phys.* **8**, 45 (2006).  
 [8] L. Pan and D. R. Beck, *Phys. Rev. A* **82**, 014501 (2010).  
 [9] S. J. Buckman and C. W. Clark, *Rev. Mod. Phys.* **66**, 539 (1994).  
 [10] C. Bahrim and U. Thumm, *Phys. Rev. A* **61**, 022722 (2000).  
 [11] K. Bartschat and H. R. Sadeghpour, *J. Phys. B* **36**, L9 (2003).  
 [12] D. H. Lee, W. D. Brandon, D. Hanstorp, and D. J. Pegg, *Phys. Rev. A* **53**, R633(R) (1996).  
 [13] M. Scheer, J. Thøgersen, R. C. Bilodeau, C. A. Brodie, H. K. Haugen, H. H. Andersen, P. Kristensen, and T. Andersen, *Phys. Rev. Lett.* **80**, 684 (1998).  
 [14] C. H. Greene, A. S. Dickinson, and H. R. Sadeghpour, *Phys. Rev. Lett.* **85**, 2458 (2000).  
 [15] A. A. Khuskivadze, M. I. Chibisov, and I. I. Fabrikant, *Phys. Rev. A* **66**, 042709 (2002).  
 [16] V. Bendkowsky, B. Butscher, J. Nipper, J. P. Shaffer, R. Löw, and T. Pfau, *Nature (London)* **458**, 1005 (2009).  
 [17] J. P. Shaffer, S. T. Rittenhouse, and H. R. Sadeghpour, *Nat. Commun.* **9**, 1965 (2018).  
 [18] C. Bahrim, U. Thumm, and I. I. Fabrikant, *Phys. Rev. A* **63**, 042710 (2001).  
 [19] F. Hummel, C. Fey, and P. Schmelcher, *Phys. Rev. A* **99**, 023401 (2019).  
 [20] S. T. Rittenhouse and H. R. Sadeghpour, *Phys. Rev. Lett.* **104**, 243002 (2010).  
 [21] M. T. Eiles and C. H. Greene, *Phys. Rev. Lett.* **115**, 193201 (2015).  
 [22] V. Bendkowsky, B. Butscher, J. Nipper, J. B. Balewski, J. P. Shaffer, R. Löw, T. Pfau, W. Li, J. Stanojevic, T. Pohl, and J. M. Rost, *Phys. Rev. Lett.* **105**, 163201 (2010).  
 [23] M. Jungen and V. Staemmler, *J. Phys. B* **21**, 463 (1988).  
 [24] E. L. Hamilton, C. H. Greene, and H. R. Sadeghpour, *J. Phys. B* **35**, L199 (2002).  
 [25] T. Niederprüm, O. Thomas, T. Eichert, C. Lippe, J. Pérez-Ríos, C. H. Greene, and H. Ott, *Nat. Commun.* **7**, 12820 (2016).  
 [26] M. T. Eiles and C. H. Greene, *Phys. Rev. A* **95**, 042515 (2017).  
 [27] S. Markson, S. T. Rittenhouse, R. Schmidt, J. Shaffer, and H. R. Sadeghpour, *Chem. Phys. Chem.* **17**, 3683 (2016).  
 [28] See Supplemental Material at <http://link.aps.org/supplemental/10.1103/PhysRevLett.123.073003> for details on the excited dimer states, modeling and fitting of the scattering lengths, and calculation of PECs and line shapes, which includes Refs. [29–38].  
 [29] F. Hummel, C. Fey, and P. Schmelcher, *Phys. Rev. A* **97**, 043422 (2018).  
 [30] W. Li, I. Mourachko, M. W. Noel, and T. F. Gallagher, *Phys. Rev. A* **67**, 052502 (2003).  
 [31] J. Han, Y. Jamil, D. V. L. Norum, P. J. Tanner, and T. F. Gallagher, *Phys. Rev. A* **74**, 054502 (2006).  
 [32] J. E. Sansonetti, *J. Phys. Chem. Ref. Data* **35**, 301 (2006).

- 
- [33] E. Arimondo, M. Inguscio, and P. Violino, *Rev. Mod. Phys.* **49**, 31 (1977).
- [34] L. Hostler and R. H. Pratt, *Phys. Rev. Lett.* **10**, 469 (1963).
- [35] V. A. Davidkyn, B. A. Zon, N. L. Manakov, and L. P. Rapoport, *Zh. Eksp. Teor. Fiz.* **60**, 124 (1971) [*Sov. Phys. JETP* **33**, 70 (1971)].
- [36] A. Omont, *J. Phys.* **38**, 1343 (1977).
- [37] S. P. Andreev, B. M. Karnakov, V. D. Mur, and V. A. Polunin, *Zh. Eksp. Teor. Fiz.* **86**, 866 (1984) [*Sov. Phys. JETP* **59**, 506 (1984)].
- [38] S. P. Andreev, B. M. Karnakov, and V. D. Mur, *Theor. Math. Phys.* **64**, 838 (1985).
- [39] D. A. Anderson, S. A. Miller, and G. Raithel, *Phys. Rev. A* **90**, 062518 (2014).
- [40] C. Fey, M. Kurz, P. Schmelcher, S. T. Rittenhouse, and H. R. Sadeghpour, *New J. Phys.* **17**, 055010 (2015).
- [41] M. Deiß, S. Haze, J. Wolf, L. Wang, F. Meinert, C. Fey, F. Hummel, P. Schmelcher, and J. Hecker Denschlag, *arXiv*: 1901.08792.
- [42] F. Böttcher, A. Gaj, K. M. Westphal, M. Schlagmüller, K. S. Kleinbach, R. Löw, T. C. Liebisch, T. Pfau, and S. Hofferberth, *Phys. Rev. A* **93**, 032512 (2016).
- [43] R. G. Parsons and V. F. Weisskopf, *Z. Phys.* **202**, 492 (1967).
- [44] In Ref. [22], the smaller value for the  $p$ -wave resonance position was concluded from spectroscopy of the weakly bound quantum reflection states, which are less sensitive to the resonance than the states  $A$  and  $B$ . Additionally, and in contrast to this work, an effective range approximation was employed to model the scattering length.
- [45] I. I. Fabrikant, *J. Phys. B* **19**, 1527 (1986).
- [46] M. T. Eiles, J. Pérez-Ríos, F. Robicheaux, and C. H. Greene, *J. Phys. B* **49**, 114005 (2016).
- [47] C. Fey, J. Yang, S. T. Rittenhouse, F. Munkes, M. Baluktsian, P. Schmelcher, H. R. Sadeghpour, and J. P. Shaffer, *Phys. Rev. Lett.* **122**, 103001 (2019).
- [48] M. Tarana and R. Čurík, *Phys. Rev. A* **99**, 012708 (2019).
- [49] H. Hotop, M.-W. Ruf, M. Allan, and I. I. Fabrikant, *Adv. At. Mol. Opt. Phys.* **49**, 85 (2003).

## SUPPLEMENTARY MATERIAL: PRECISION SPECTROSCOPY OF NEGATIVE-ION RESONANCES IN RYDBERG MOLECULES

### Excited dimers bound by internal quantum reflection

In the main article, we have demonstrated that the measured binding energies of the molecular states D, A, and B allow for precise fitting of the  $k$ -dependent (triplet)  $s$ - and  $p$ -wave scattering lengths. Here, we discuss the vibrationally excited dimer states which are formed by internal quantum reflection at the steep drop of the PEC caused by the  $p$ -wave shape resonance [1]. These states lie energetically above the vibrational ground-state dimer D. Fig. 5 depicts the relevant part of the spectrum presented in Fig. 2 of the main article. In total, we identify five excited dimer states lying energetically between state D at  $\delta = -22.6$  MHz and the atomic Rydberg line ( $\delta = 0$ ). Note that three of the resonances ( $\delta = -21.7$  MHz,  $\delta = -4.5$  MHz, and  $\delta = -0.8$  MHz) were not resolved in earlier work [1]. All the observed states are predicted by our Green's function calculations (black circles) using the adapted  $a_s^T(k)$  and  $a_p^T(k)$  obtained from the fitting procedure to the data of Fig. 2 (b) and (c). The good quantitative agreement provides additional support for the obtained scattering lengths. Small residual deviations could be explained by the neglected spin-orbit coupling in the Green's function calculation.

### Model for computing electron-neutral scattering lengths

For the calculation of the energy-dependent (triplet)  $s$ - and  $p$ -wave electron-neutral scattering lengths, we employ a comparatively simple model potential describing the Rb- $e^-$  interaction (in atomic units)

$$V_L(r) = -\alpha/(2r^4) + L(L+1)/(2\mu_e r^2). \quad (1)$$

Here,  $\alpha$  denotes the Rb ground-state polarizability,  $r$  is the distance of the electron from the Rb core,  $\mu_e$  the reduced mass, and the angular momentum  $L = 0$  ( $L = 1$ ) for the  $s$ -wave ( $p$ -wave) scattering channel. The short-range details are captured by an inner hard-wall at an adaptable distance  $r_0$ . Solving the radial Schrödinger equation for a range of momenta  $k$  yields  $s$ - and  $p$ -wave (triplet) scattering phase shifts  $\delta_s^T(k)$  and  $\delta_p^T(k)$ , respectively. The scattering lengths are then given by  $a_s^T(k) = -\tan(\delta_s^T(k))/k$  and  $a_p^T(k) = -\tan(\delta_p^T(k))/k^3$ . Spin-orbit interaction in the  $p$ -wave scattering channel is modeled by adding standard  $LS$ -coupling

$$V_{L,S}(r) = -\beta \frac{dV_0(r)/dr}{2c^2 r} \vec{L} \cdot \vec{S}. \quad (2)$$

For triplet scattering, the total electron spin  $S = 1$ . Consequently, Eq. 2 gives rise to three  $p$ -wave scattering channels with total angular momentum  $\vec{J} = \vec{L} + \vec{S}$  ( $J \in$

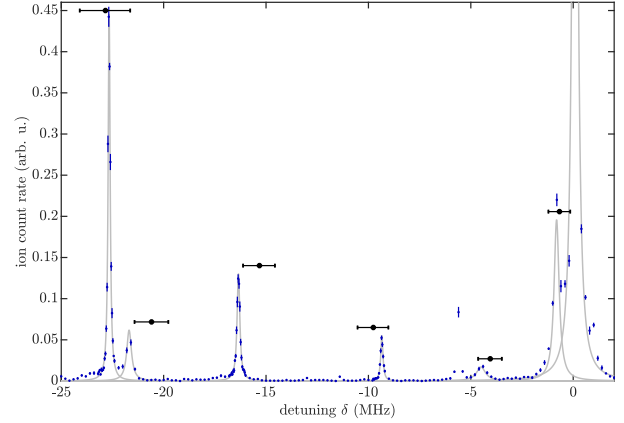


FIG. 5: ULRM spectroscopy of excited dimer states bound by quantum reflection for  $n = 35$ . Shown are the data presented in Fig. 2 of the main article with focus on the spectral region between the  $s$ -wave dominated dimer (D) at  $\delta = -22.6$  MHz and the atomic Rydberg line  $|35S_{1/2}, m_j = 1/2\rangle$  at  $\delta = 0$ . The solid line is a fit to the data using a sum of multiple Lorentzians. The signal at  $\delta = -5.6$  MHz stems from weak residual coupling to the Zeeman-shifted  $|35S_{1/2}, m_j = -1/2\rangle$  atomic Rydberg line and is excluded from the fit. Black circles are predicted molecular states from Green's function calculations with our fitted  $s$ - and  $p$ -wave scattering lengths, i.e. not accounting for spin-orbit coupling. Error bars are derived from the same variations in the scattering lengths used to obtain the shaded regions in Fig. 2.

$\{0, 1, 2\}$ ). Including Eq. 2 into the computation of scattering phase shifts and scattering lengths yields  $J$ -dependent results  $\delta_{p,J}^T(k)$  and  $a_{p,J}^T(k)$ . Each channel exhibits a shape-resonance associated with the corresponding Rb $^-$  ( $^3P_J$ ) negative-ion resonance. The resonance position  $E_r^J$  is defined as the inflection point of  $a_{p,J}^T(k)$ . We use the parameter  $\beta \approx 1.0$  in our fitting procedure to fine tune the strength of the spin-orbit coupling for matching the observed line shapes in Fig. 3 and Fig. 4 of the main article.

Before adjusting the short-range hard wall position  $r_0$  to fit the scattering lengths to the experimental data, we have verified that our model potential reproduces the full  $k$ -dependence of predicted  $s$ - and  $p$ -wave phase shifts [2, 3]. Moreover, the functional  $k$ -dependence is found insensitive to the precise value of  $\alpha$ , i.e. for a small variation of  $\alpha$  one finds a slightly shifted  $r_0$  which produces the same phase shifts.

The phase shifts obtained in this work by fitting to the experimental data (see below) are shown in Fig. 6, and are compared to previous theoretical predictions.

### Fitting the $k$ -dependent scattering lengths to the data

Our procedure to fit the scattering lengths  $a_s^T(k)$  and  $a_p^T(k)$  to the measured binding energies shown in Fig. 2 of the main article exploits the different sensitivity of the

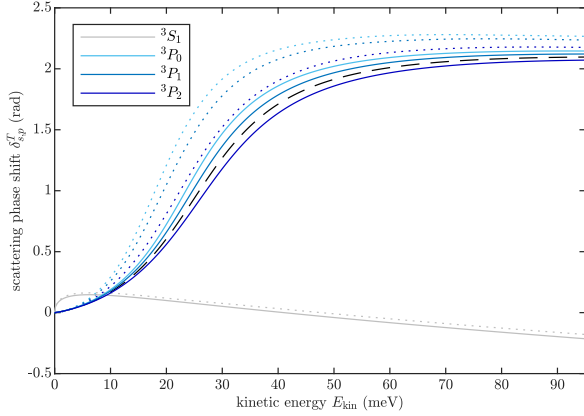


FIG. 6: Rb- $e^-$  scattering phase shifts for triplet  $s$ - and  $p$ -wave scattering. The solid lines show the data for  $\delta_s^T$  and  $\delta_{p,J}^T$  as a function of collision energy  $E_{\text{kin}} = k^2/2$  obtained in this work by fitting to the measured molecular states. The dashed line denotes the  $p$ -wave phase shift in the absence of spin-orbit coupling used in the Green's function calculations. For comparison, the dotted lines show the predicted phase shifts reported in Refs. [2, 3].

investigated molecular states to the  $s$ - and  $p$ -wave scattering channel. Starting with the  $s$ -wave dominated dimer (D) allows for adjusting  $a_s^T(k)$  largely independent of  $a_p^T(k)$ . The  $k$ -dependent scattering length is adjusted by small variations of the hard inner wall  $r_0$  aiming for minimizing the deviation between experiment and theory. Having fixed  $a_s^T(k)$ , we continue adjusting  $a_p^T(k)$  in the same way, now minimizing deviations between measurement and calculated binding energies for the states A and B. For this, we consider all measured binding energies for state B but select a subset for state A, specifically  $n = 32, 34$ , and  $36$ . Those are the principal quantum numbers for which the state A is less bound (*cf.* Fig. 2(c)), and essentially unaffected by spin-orbit coupling. This allows us to model the data with the Green's function calculation. The shaded regions in Fig. 2(c) are obtained by small variations of  $r_0$ , which result in the bounds on  $a_s^T(0)$  and  $E_r^{\text{avg}}$  given in the main article.

### Calculation of molecular potential energy curves

#### Hamiltonian diagonalization approach

In the spirit of the Born-Oppenheimer approximation, we assume the nuclear motion of the molecule's constituents to be separable from the electronic motion of the Rydberg atom. Solving the stationary Schrödinger equation for the electronic degree's of freedom provides the potential energy curves (PECs) which are used as input for the vibrational Schrödinger equation. To calculate the PECs,

we employ the electronic Hamiltonian (in atomic units) [4]

$$H = H_R + H_G + H_B + V. \quad (3)$$

$H_R$  describes the dynamics of the Rydberg electron at position  $\vec{r}$  in the potential of the ionic core of the Rydberg atom, which is located at the coordinate origin. The electron has spin  $\vec{s}_1$  and angular momentum  $\vec{l}$ . Eigenstates of  $H_R$  are  $\phi_{nljm_j}(\vec{r})$  with eigenvalues  $E_{nlj}$ ,  $n$  being the principal quantum number and  $j = |\vec{l} + \vec{s}_1|$  the total angular momentum of the Rydberg electron. The energies  $E_{nlj}$  are taken from spectroscopic measurements [5–7] and are used as input to analytically determine the long-range behavior of  $\phi_{nljm_j}(\vec{r})$  in terms of appropriately phase shifted Coulomb wave functions.  $H_G = A \vec{I} \cdot \vec{s}_2$  represents the Hamiltonian of hyperfine interaction in the ground-state atom with the spin of the valence electron  $\vec{s}_2$ , the nuclear spin  $\vec{I}$ , and  $A = 3.417$  GHz [8]. Eigenstates of  $H_G$  are  $|Fm_F\rangle$ , where  $F = |\vec{I} + \vec{s}_2|$ .  $H_B = \vec{B} \cdot (\vec{s}_1 + \vec{s}_2 + \vec{l}/2)$  models the Zeeman coupling of the electronic angular momenta to the magnetic field, where  $\vec{B}$  is given in units of  $2.35 \times 10^9$  G.  $V$  describes the interaction between the Rydberg electron and the ground-state atom, which depends on the total electronic spin  $\vec{S} = \vec{s}_1 + \vec{s}_2$  as well as the orbital angular momentum  $\vec{L}$  of the Rydberg electron in the reference frame of the ground-state atom. We consider singlet ( $S = 0$ ) and triplet ( $S = 1$ ) interaction for the  $s$ -wave ( $L = 0$ ) and  $p$ -wave ( $L = 1$ ) channel. To this end, we employ a generalized Fermi pseudopotential [9]

$$V = \sum_{\beta} \frac{(2L+1)^2}{2} a_{(s;p,J)}^{(T;S)}(k) \frac{\delta(X)}{X^{2(L+1)}} |\beta\rangle \langle \beta|. \quad (4)$$

Here,  $X = |\vec{r} - \vec{R}|$  is the distance between the Rydberg electron and the ground-state atom and  $\beta$  is a multi index that defines projectors onto the different interaction channels  $|\beta\rangle = |(LS)JM_J\rangle$ , with  $\vec{J} = \vec{L} + \vec{S}$  being the total angular momentum of the two electrons with respect to the ground-state atom's core and  $M_J$  the corresponding magnetic quantum number. The scattering lengths  $a_{(s;p,J)}^{(T;S)}(k)$  are derived from the respective phase shifts as discussed above. Note that the upper indices  $T$  and  $S$  denote triplet and singlet scattering and the latter is not to be confused with the total electron spin. The wave number is calculated via the semi-classical relation  $k = \sqrt{2/R - 2E^*}$  given in terms of the energy  $E^*$  of the asymptotic atomic level  $nS_{1/2}$  that we are interested in.

Note that  $V$  neither commutes with  $H_R$ ,  $H_G$ , nor with  $H_B$ , however, in the absence of a magnetic field, a good quantum number to discriminate the PECs is  $\Omega = m_l + m_1 + m_2 + m_I$ , which corresponds to the projection of the total angular momentum of the (non-rotating) molecular system onto the internuclear axis. Here,  $m_l, m_1, m_2, m_I$  are the magnetic quantum numbers of  $l, s_1, s_2, I$ , respectively.

Considering the symmetries of a dimer in a magnetic field leads to two relevant spatial degrees of freedom: The internuclear distance  $R$ , and the relative angle between the magnetic field axis and the internuclear axis  $\theta$ . Without loss of generality, we fix the internuclear axis to be the  $z$ -axis such that  $\vec{R} = R\hat{e}_z$  and consider rotations of the magnetic field vector around the  $y$ -axis such that  $\vec{B} = B(\cos\theta\hat{e}_z + \sin\theta\hat{e}_x)$ .

We obtain PECs by diagonalizing  $H$  in a finite basis set. As stated in the main article, quantitative uncertainties in the PECs arising from the choice of the basis set are largely reduced by switching off the fine structure in the triplet scattering channel and then comparing the results to the Green's function calculations. Specifically, we find optimal matching of the two methods using a basis set which comprises in total four manifolds of electronic Rydberg states with principal quantum numbers such that two hydrogenic manifolds lie energetically below and two above the  $nS_{1/2}$  state we are interested in. Further, all total angular momenta  $j$  are considered, while the projections  $m_j$  are truncated to neglect  $|m_j| > 3/2$  which do not interact with the ground-state atom. The basis  $|Fm_F\rangle$  is considered completely.

Additionally to the eigenvalues of  $H$  constituting the PECs, by aid of the associated eigenvectors  $|\Psi_\epsilon(R, \theta)\rangle$ , we obtain the squared electronic dipole transition elements  $|d(R, \theta)|^2 = \langle \Psi_\epsilon(R, \theta) | \hat{P} | \Psi_\epsilon(R, \theta) \rangle$ , with  $\hat{P} = |m_j; F, m_F\rangle \langle m_j; F, m_F|$ , which are used for the simulation of the measured spectral line shapes (see below).

#### Green's function approach

Due to the mentioned convergence issues, which are inherent to the above presented diagonalization scheme in the

truncated Hilbert space [9, 10], we also derive PECs employing alternative Green's function methods [1, 3]. These Green's function methods make use of the analytically known Coulomb Green's function  $G_c(\vec{r}, \vec{r}', E)$  [11], which satisfies  $(-\Delta/2 - 1/r - E)G_c(\vec{r}, \vec{r}', E) = \delta(\vec{r} - \vec{r}')$ , where  $E$  is the energy. Based on this Coulomb Green's function, one can construct a Green's function  $G(\vec{r}, \vec{r}', E)$  for the Rydberg electron that incorporates quantum defects  $\Delta_l$  characteristic for the Rydberg atom as  $G(\vec{r}, \vec{r}', E) = G_c(\vec{r}, \vec{r}', E) + G_{qd}(\vec{r}, \vec{r}', E)$  [12].

Green's function approaches are more accurate than the truncated diagonalization in the sense that, firstly, the Green's function contains information on all bound and continuum states of the system and, secondly, it allows for a proper handling of the singular  $\delta$ -interaction in the pseudopotential. On the other hand Green's function methods typically neglect certain spin-interaction effects such as the fine structure of the Rydberg atom and the hyperfine structure of the ground-state atom and their coupling by the electron scattering, which is in many cases essential for a correct interpretation of spectroscopic results but has so far only been included in the framework of truncated-diagonalization schemes [9].

However, for the Rydberg  $S$ -state investigated in the experiment, the Rydberg fine structure is only of minor importance. Furthermore, the molecular states investigated in this work are essentially pure  $F = 2$  and pure triplet ( $S = 1$ ) states and are not affected by mixing between  $S = 0$  and  $S = 1$  states. For this reason a Green's function approach that neglects the fine structure of the Rydberg atom and takes only triplet scattering into account is well suited to describe the investigated molecular states.

---

An appropriate pseudopotential for the electron-atom interaction is in this case given by [13, 14]

$$V = 2\pi a_s^T(k)\delta(\vec{R} - \vec{r}) + 6\pi a_p^T(k)\overleftarrow{\nabla}_{\vec{r}} \cdot \delta(\vec{R} - \vec{r})\overrightarrow{\nabla}_{\vec{r}}. \quad (5)$$

The Coulomb Green's function can be written as [11]

$$G_C(\vec{r}, \vec{r}', E) = \frac{\Gamma(1 - n^*)}{\pi n^*(\xi - \eta)} \left[ M'_{n^*, 1/2}(\eta) W_{n^*, 1/2}(\xi) - M_{n^*, 1/2}(\eta) W'_{n^*, 1/2}(\xi) \right] \quad (6)$$

with  $E = -1/(2n^*)$ ,  $\xi = (r + r' + |\vec{r} - \vec{r}'|)/n^*$ ,  $\eta = (r + r' - |\vec{r} - \vec{r}'|)/n^*$  and the Whittaker functions  $W_{n^*, l+1/2}(\xi)$  and  $M_{n^*, l+1/2}(x)$ . The correction term that incorporates the quantum defects is given by [12]

$$G_{qd}(\vec{r}, \vec{r}', E) = \sum_{lm} \frac{\Gamma(l+1-n^*) \sin\pi(\Delta_l+l)}{\Gamma(l+1+n^*) \sin\pi(\Delta_l+n^*)} \frac{n^*}{rr'} W_{n^*, l+\frac{1}{2}}\left(\frac{2r}{n^*}\right) W_{n^*, l+\frac{1}{2}}\left(\frac{2r'}{n^*}\right) Y_{lm}(\hat{r}) Y_{lm}^*(\hat{r}'). \quad (7)$$

We use quantum defects  $\Delta_0 = 3.1314$ ,  $\Delta_1 = 2.65$ ,  $\Delta_2 = 1.35$ ,  $\Delta_3 = 0.02$  and  $\Delta_l = 0$  for  $l \geq 4$ .

Our approach to derive an equation that determines the PECs based on the Green's function follows Refs. [15, 16]. First we express the electron wave function with energy  $E$  close to the position of the ground-state atom asymptotically as

$$\psi(\vec{X}) = \sum_{L=0}^1 \sum_{M=-L}^L c_{LM}(E) \left[ X^{-L-1} Y_{LM}(\hat{X}) + \dots + B_L(E) \left( X^L Y_{LM}(\hat{X}) + \dots \right) \right] \quad (8)$$

where  $\vec{X} = \vec{r} - \vec{R}$ ,  $X$  is small,  $c_{LM}(E)$  are energy-dependent coefficients and  $B_L(E) = [(2L+1)a_L(E)]$  is linked to the energy-dependent scattering length and volume  $a_0(E) = a_s^T(k)$  and  $a_1(E) = a_p^T(k)$ , respectively, where  $k^2/2 - 1/R = E$ . To determine the energy-dependent coefficients  $c_{LM}(E)$  the above wave function needs to be matched to a solution valid at large  $X$ . This solution can be expressed in terms of the Green's function. Using the Lippmann Schwinger equation,  $\Psi(\vec{r}) = -\int d^3r' G(\vec{r}, \vec{r}', E) V \psi(\vec{r}')$ , and the expression for the potential  $V$ , Eq. (5), we obtain

$$\Psi(\vec{r}) = -2\pi a_s^T(k) G(\vec{r}, \vec{R}, E) \Psi(\vec{R}) - 6\pi a_p^T(k) \vec{\nabla}_{\vec{R}} G(\vec{r}, \vec{R}, E) \cdot \vec{\nabla}_{\vec{R}} \Psi(\vec{R}). \quad (9)$$

The expressions  $\Psi(\vec{R})$  and  $\vec{\nabla}_{\vec{R}} \Psi(\vec{R})$  can be viewed as energy-dependent coefficients that need to be determined by matching (9) to (8) in the limit  $X \rightarrow 0$ . An alternative approach to derive an equation similar to (9) that does not make use of the pseudopotential is provided in [16].

To simplify the notation we assume, without loss of generality, that  $\vec{R} = R\vec{e}_z$ . Due to the cylindrical symmetry, the magnetic quantum number  $M = m$  is in this case conserved. Since we are interested in Rydberg  $S$ -states we focus on the symmetry subspace  $M = m = 0$ . In that case, all cartesian components of  $\vec{\nabla}_{\vec{R}} \Psi(\vec{R})$  except for the  $z$ -component vanish. Hence, equation (9) becomes

$$\psi(\vec{X}) = 2\pi \tilde{c}_{00}(E) G(\vec{r}, \vec{R}, E) + 2\pi \tilde{c}_{10}(E) \left. \frac{\partial}{\partial z'} G(\vec{r}, \vec{r}', E) \right|_{\vec{r}'=\vec{R}}, \quad (10)$$

where  $\tilde{c}_{00}(E)$  and  $\tilde{c}_{10}(E)$  are energy-dependent coefficients that replace corresponding prefactors in (9).

To match (10) to (8) for small  $X$ , we need to expand the expression of the Green's function in (10) for small  $X$ . This leads to [16]

$$2\pi G(\vec{r}, \vec{R}, E) = X^{-1} Y_{00}(\hat{X}) + \dots + \sum_{L'=0}^1 A_{0L'}(E) \left( X^{L'} Y_{L'0}(\hat{X}) + \dots \right) \quad (11)$$

and

$$2\pi \left. \frac{\partial}{\partial z'} G(\vec{r}, \vec{r}', E) \right|_{\vec{r}'=\vec{R}} = X^{-2} Y_{10}(\hat{X}) + \dots + \sum_{L'=0}^1 A_{1L'}(E) \left( X^{L'} Y_{L'0}(\hat{X}) + \dots \right) \quad (12)$$

with four energy-dependent coefficients  $A_{LL'}(E)$  that satisfy  $A_{LL'}(E) = A_{L'L}(E)$ . Matching the irregular parts (divergent for small  $X$ ) of (10) and (8) immediately yields  $\tilde{c}_{LM}(E) = c_{LM}(E)$ , while matching the regular parts yields the system of equations  $B_L c_{L0} = \sum_{L'=0}^1 A_{L'L}(E) c_{L'0}$ . Non trivial solutions exist only if the determinant of this system vanishes. This implies

$$-A_{10}(E)^2 + A_{11}(E) + (1/a_s^T(k) + A_{00}(E)) (1/(3a_p^T(k)) + A_{11}(E)) = 0. \quad (13)$$

This equation is the central result of the Green's function approach. The coefficients  $A_{LL'}$  depend not only on the energy  $E$  but implicitly also on the position of the ground-state atom  $\vec{R}$ . Using a numerical root-finding algorithm that provides solutions  $E$  of (13) as a function of  $\vec{R}$  yields the PECs. Knowledge of the coefficients  $A_{LL'}$  is crucial for this purpose. We find

$$A_{00} = 2\pi \left. \frac{\partial}{\partial X} X G(\vec{R} + X\vec{e}_z, \vec{R}, E) \right|_{X=0}, \quad (14)$$

$$A_{10} = 2\pi \left. \frac{\partial}{\partial(X \cos \theta)} G(\vec{R} + X(\cos \theta \vec{e}_z + \sin \theta \vec{e}_x), \vec{R}, E) \right|_{\theta=0, X=0}, \quad (15)$$

and

$$A_{11} = \frac{\pi}{3} \left. \frac{\partial^3}{\partial X^3} X^2 \frac{\partial}{\partial z'} G(\vec{R} + X\vec{e}_z, z'\vec{e}_z, E) \right|_{z'=R, X=0}. \quad (16)$$

### Modeling of the spectral line shapes

In order to simulate the spectral line shape of the molecular state A (*cf.* Figs. 3 and 4), we use the angular-dependent

PECs  $V(\theta)$  shown in Figs. 3 and 4 of the main text, which are obtained by fixing the radial coordinate  $R$  to the position of the minimum  $R_0$  of the potential well in which state

A localizes. Then, we employ the rotational Hamiltonian

$$H_r = \frac{\hat{N}^2}{2\mu R_0^2} + V(\theta) \quad (17)$$

with the rotational angular momentum operator  $\hat{N}$  and the reduced mass  $\mu$  of the diatomic system. This is the Hamiltonian of a rigid rotor. This approach is justified due to the fact that in our case, the energy scale of radial excitation is much larger than the energy scale of angular excitation.  $H_r$  has eigenstates  $\chi_\nu(\theta)$  with eigenvalues  $E_\nu$  which can be obtained by diagonalizing  $H_r$  in a basis of Legendre polynomials such that  $\chi(\theta) = \sum_N c_N P_N(\cos\theta)$  or alternatively by employing standard methods such as finite difference or discrete variable representation.

Each eigenstate contributes to the observed line shape according to the Franck-Condon overlap  $\Gamma \propto |\int d\theta \sin\theta \chi_\nu(\theta) d(R_0, \theta) \chi_{\text{in}}(\theta)|^2$ , where the initial state  $\chi_{\text{in}}(\theta)$  is assumed to be isotropic, i.e. independent of  $\theta$ , and  $d(R_0, \theta)$  is the electronic dipole transition element derived from the solution of the electronic Hamiltonian  $H$  (see above). Note that only states with even  $\nu$  contribute. To compare the solution to experimental spectra, we use three fit parameters. First, we convolute eigenstates  $\chi_\nu(\theta)$  with a Lorentzian line shape of constant width, which reflects the lifetime of the radial quantum reflection state. Second, we allow for an overall frequency offset (blue-shift) accounting for the radial zero-point energy. Third, the amplitude of the obtained line shape is rescaled to match the experimental results.

The rigid rotor model provides an excellent description for a sufficiently large magnetic field, separating the angular PECs  $V(\theta)$  which are coupled by spin-orbit interaction. In that case the Born-Oppenheimer approximation holds and non-adiabatic electronic couplings are suppressed. This is the case for the largest applied magnetic field  $B = 15.4$  G. For intermediate field strength, i.e.  $B = 5.3$  G, we find that the rigid-rotor model provides only partial agreement. Specifically, the spectral part associated with the uppermost PEC is still modeled well (*cf.* Fig. 3, gray line), however, we find quantitative deviations for the region below  $-170$  MHz.

Therefore, we employ a sampling technique, which treats rotational degrees of freedom classically and is capable of reproducing the overall line shape for  $B = 5.3$  G and  $B = 2.2$  G. To this end, a random angle  $\theta$  is drawn from a distribution representing an isotropic gas  $p(\theta) = \sin\theta$  and the energy for this angle  $V(\theta)$  is weighted by the squared electronic dipole element  $|d(R_0, \theta)|^2$ . We repeat this step ten thousand times to obtain a histogram, which then serves as input for the same procedure introduced for the rigid-rotor model employing the three fit parameters, i.e. to account for the molecule's lifetime, the zero-point energy, and the experimental signal amplitude.

- 
- [1] V. Bendkowsky, B. Butscher, J. Nipper, J. B. Balewski, J. P. Shaffer, R. Löw, T. Pfau, W. Li, J. Stanojevic, T. Pohl, and J. M. Rost, *Phys. Rev. Lett.* **105**, 163201 (2010).
  - [2] C. Bahrim and U. Thumm, *Phys. Rev. A* **61**, 022722 (2000).
  - [3] A. A. Khuskivadze, M. I. Chibisov, and I. I. Fabrikant, *Phys. Rev. A* **66**, 042709 (2002).
  - [4] F. Hummel, C. Fey, and P. Schmelcher, *Phys. Rev. A*, **97**, 043422 (2017).
  - [5] W. Li, I. Mourachko, M. W. Noel, and T. F. Gallagher, *Phys. Rev. A*, **67**, 052502 (2003).
  - [6] J. Han, Y. Jamil, D. V. L. Norum, P. J. Tanner, and T. F. Gallagher, *Phys. Rev. A*, **74**, 054502 (2006).
  - [7] J. E. Sansonetti, *J. Phys. Chem. Ref. Data*, **35**, 301 (2006).
  - [8] E. Arimondo, M. Inguscio, and P. Violino, *Rev. Mod. Phys.* **49**, 31 (1977).
  - [9] M. T. Eiles and C. H. Greene, *Phys. Rev. A* **95**, 042515 (2017).
  - [10] C. Fey, M. Kurz, P. Schmelcher, S. T. Rittenhouse, and H. R. Sadeghpour, *New J. Phys.* **17**, 055010 (2015).
  - [11] L. Hostler, R. H. Pratt, *Phys. Rev. Lett.* **10**, 469 (1963).
  - [12] V. A. Davidkyn, B. A. Zon, N. L. Manakov, L. P. Rapoport, *Sov. Phys. JETP* **33**, 70 (1971).
  - [13] A. Omont, *J. Phys.* **38**, 1343 (1977).
  - [14] E. L. Hamilton, C. H. Greene, and H. R. Sadeghpour, *J. Phys. B: At. Mol. Opt. Phys.* **35** L199 (2002).
  - [15] S. P. Andreev, B. M. Karnakov, V. D. Mur, V. A. Polunin, *Sov. Phys. JETP* **59**, 506 (1984).
  - [16] S. P. Andreev, B. M. Karnakov, V. D. Mur, *Theor. Math. Phys.* **64**, 838 (1985).

### 3.4 Observation of spin-orbit-dependent electron scattering using long-range Rydberg molecules

## Observation of spin-orbit-dependent electron scattering using long-range Rydberg molecules

Markus Deiß,<sup>1</sup> Shinsuke Haze,<sup>1</sup> Joschka Wolf,<sup>1</sup> Limei Wang,<sup>1</sup> Florian Meinert,<sup>2</sup> Christian Fey,<sup>3</sup> Frederic Hummel,<sup>3</sup> Peter Schmelcher,<sup>3,4</sup> and Johannes Hecker Denschlag<sup>1</sup>

<sup>1</sup>*Institut für Quantenmaterie and Center for Integrated Quantum Science and Technology IQ<sup>ST</sup>, Universität Ulm, 89069 Ulm, Germany*

<sup>2</sup>*Physikalisches Institut and Center for Integrated Quantum Science and Technology IQ<sup>ST</sup>, Universität Stuttgart, 70569 Stuttgart, Germany*

<sup>3</sup>*Zentrum für optische Quantentechnologien, Universität Hamburg, Fachbereich Physik, 22761 Hamburg, Germany*

<sup>4</sup>*Hamburg Centre for Ultrafast Imaging, Universität Hamburg, 22761 Hamburg, Germany*



(Received 11 April 2019; revised manuscript received 17 October 2019; published 14 January 2020)

We present experimental evidence for spin-orbit interaction of an electron as it scatters from a neutral atom. The scattering process takes place within a Rb<sub>2</sub> ultralong-range Rydberg molecule, consisting of a Rydberg atomic core, a Rydberg electron, and a ground state atom. The spin-orbit interaction leads to characteristic level splittings of vibrational molecular lines which we directly observe via photoassociation spectroscopy. We benefit from the fact that molecular states dominated by resonant *p*-wave interaction are particularly sensitive to the spin-orbit interaction. Our work paves the way for studying novel spin dynamics in ultralong-range Rydberg molecules. Furthermore, it shows that the molecular setup can serve as a microlaboratory to perform precise scattering experiments in the low-energy regime of a few meV.

DOI: [10.1103/PhysRevResearch.2.013047](https://doi.org/10.1103/PhysRevResearch.2.013047)

### I. INTRODUCTION

Since their prediction almost 20 years ago [1] and boosted by their first observation [2], ultralong-range Rydberg molecules have become a research area of major interest (for reviews, see, e.g., [3–5]). Nevertheless, the spin substructure of these molecules is not fully understood yet. In particular, one fundamental unresolved question concerns the coupling between the total electronic spin  $\vec{S}$  and the relative orbital angular momentum  $\vec{L}_p$  of the Rydberg electron with respect to the ground state perturber atom. The role of this  $\vec{L}_p \cdot \vec{S}$  type spin-orbit interaction for the molecular system was predicted almost 20 years ago [6] and has remained a topic of active research until now [7,8]. From the experimental side, some preliminary indication for  $\vec{L}_p \cdot \vec{S}$  coupling has been found recently [9]; however, clear evidence has been lacking. It has escaped discovery although a variety of spectroscopic studies with impressive resolution were carried out, investigating Rydberg molecules for various atomic species (Rb, Cs, Sr) and different Rydberg orbitals (*S*, *P*, or *D*) [2,10–23].

Very recently, in parallel with our work reported here, *indirect* evidence for  $\vec{L}_p \cdot \vec{S}$  coupling has been found in the observation of specific pendular states in Rb<sub>2</sub> ultralong-range Rydberg molecules [24], an effect predicted shortly before in [25]. Here, we complete the evidence for  $\vec{L}_p \cdot \vec{S}$  interaction, as we spectroscopically *directly* observe the Rydberg molecular level splitting caused by it; in fact, we resolve the full fine

structure multiplet. For this, we investigate ultralong-range <sup>87</sup>Rb<sub>2</sub> Rydberg molecules consisting of a 5S<sub>1/2</sub> ground state atom and a 16P<sub>3/2</sub> Rydberg atom. The molecular bound states of interest are located in the second outermost well of the Born-Oppenheimer potential energy curve (PEC), which is significantly influenced by the *p*-wave shape resonance. The resonant *p*-wave interactions strongly increase the  $\vec{L}_p \cdot \vec{S}$ -induced level splittings of spin states so that they can be well resolved experimentally. For the molecular level spectroscopy, we carry out photoassociation in ultracold clouds of Rb ground state atoms, which can be prepared in different spin polarizations. We observe three vibrational ladders of the molecular Rydberg states. Each ladder has a characteristic line-multiplet substructure, which allows for unambiguous assignment of all spin states. Using model calculations on the basis of a pseudopotential Hamiltonian and including spin-spin and spin-orbit interactions [7], we are able to fully explain the observed spectra.

### II. MOLECULAR SYSTEM AND POTENTIAL ENERGY CURVES

The molecular system is sketched in Fig. 1. A ground state atom is located at position  $\vec{R}$  relative to the ionic core of a Rydberg atom. The Rydberg electron at position  $\vec{r}$  has spin  $\vec{s}_1$  and orbital angular momentum  $\vec{l}$  relative to the ionic core. Its total angular momentum is described by  $\vec{j} = \vec{l} + \vec{s}_1$ . The ground state atom possesses electronic spin  $\vec{s}_2$  and nuclear spin  $\vec{I}$  which are coupled by hyperfine interaction to form the total angular momentum  $\vec{F} = \vec{I} + \vec{s}_2$  [19–23,26]. In the reference frame of the ground state atom the Rydberg electron is located at position  $\vec{X} = \vec{r} - \vec{R}$  and has orbital angular momentum  $\vec{L}_p$ . Actually, we will be mainly interested in  $\vec{L}_p \cdot \vec{S}$  spin-orbit coupling, where  $\vec{S}$  is the total electronic spin  $\vec{S} = \vec{s}_1 + \vec{s}_2$ .

*Published by the American Physical Society under the terms of the Creative Commons Attribution 4.0 International license. Further distribution of this work must maintain attribution to the author(s) and the published article's title, journal citation, and DOI.*

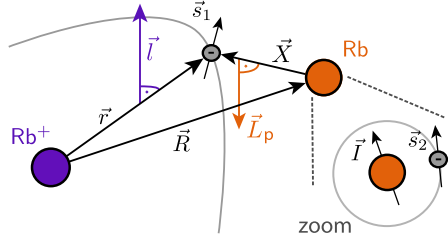


FIG. 1. Composition of the molecular system (see text).

Figure 2 shows the relevant PECs for our experiments. The ultralong-range Rydberg molecular states we investigate are bound in the second outermost wells at an internuclear distance of about  $260 a_0$ . Here,  $a_0$  is the Bohr radius. Figure 2(b) is a zoom onto these wells. On the left-hand side of the wells steep butterfly PECs [13,27,28] cross through that arise because of a  $p$ -wave shape resonance, where the Rydberg electron with angular momentum  $L_p = 1$  resonantly interacts with the Rb ground state atom. This resonance occurs at a collision energy  $E_r^{\text{avg}} = 26.6$  meV [24,29]. Due to the vicinity to the  $p$ -wave shape resonance the ultralong-range Rydberg molecular states in the second outermost wells experience strong  $p$ -wave interaction and are thus very sensitive to  $\vec{L}_p \cdot \vec{S}$  coupling.

For large distances  $R$ , the  $P$  state PECs have four asymptotes, corresponding to the combinations of the atomic Rydberg states  $16P_{3/2}$  and  $16P_{1/2}$  with hyperfine states  $F = 1$  and  $F = 2$  of the Rb ground state atom. The color coding in Fig. 2 shows the  $F$  content of the states (see also Fig. 8 of the Appendix for the electronic spin  $S$  content). As can be seen clearly in Fig. 2(b) some of the PECs exhibit  $F$  mixing. As we will discuss in more detail in Sec. IV this is especially due to the spin dependence of the  $p$ -wave interaction.

In order to formally label the PECs, it is convenient to use the quantum number  $N$  corresponding to the angular momentum  $\vec{N} = \vec{S} + \vec{I}$ . The spin-orbit interaction  $\vec{L}_p \cdot \vec{S}$  splits up each PEC characterized by  $N$ , according to its multiplicity  $N(N + 1)$  into different  $\Omega = -N, -N + 1, \dots, N$  states. Here,  $\Omega = m_l + m_s + m_i$  is the magnetic quantum number of the total angular momentum, and we have chosen the internuclear axis

as the quantization axis. In Fig. 2(b) only the splitting of the  $N = 3/2$  PEC into  $|\Omega| = 1/2$  and  $|\Omega| = 3/2$  is clearly visible. Because of rotational symmetry about the internuclear axis, the PECs for each pair of  $\pm\Omega$  are generally energetically degenerate. Therefore, for each  $N$ , energy splittings only arise between the  $(2N + 1)/2$  different  $|\Omega|$  components.

### III. EXPERIMENTS AND SPECTROSCOPIC RESULTS

The experiments are carried out in a hybrid atom-ion setup [30] consisting of a crossed optical dipole trap for an ultracold cloud of  $^{87}\text{Rb}$  ground state atoms and a linear Paul trap which we use in the detection of Rydberg molecules. The dipole trap operates at a wavelength of 1065 nm and has a potential depth of about  $20 \mu\text{K} \times k_B$ . The atomic sample is prepared either in the hyperfine state  $F = 1, m_F = -1$  or in the state  $F = 2, m_F = +2$ . It has a temperature of  $\approx 1 \mu\text{K}$ , and typically consists of about  $4 \times 10^6$  atoms. The cloud is Gaussian-shaped with a size of  $\sigma_{x,y,z} \approx (70, 10, 10) \mu\text{m}$  along the three directions of space.

The general procedure of our experiment is as follows (see also the illustration in Fig. 3). We measure photoassociation spectra by scanning the frequency of a narrow-linewidth laser in a steplike fashion at a wavelength of about 302 nm (for technical details on the photoassociation laser setup, see Appendix A 2). For each laser frequency we produce a cold cloud of Rb atoms and expose it for a well-defined time of typically a few hundred ms to the laser light. If the laser frequency is on resonance, photoassociation of  $5S_{1/2} - 16P_{3/2}$  Rb<sub>2</sub> Rydberg molecules takes place [see (i) Fig. 3]. We detect this production of dimers as follows. Because of various processes, such as photoionization, collisions, and ionization due to molecular relaxation, some of the Rydberg molecules decay into ions (ii). These ions are subsequently confined in the linear Paul trap which has a trap depth of about 1 eV. The Paul trap is centered on the optical dipole trap so that the ions are immersed in the atom cloud. The ions inflict loss on the atom cloud (iii) [31,32], which we measure via absorption imaging. Thus, by detecting atom loss, we infer the production of Rydberg molecules. In brief, the losses are due to micromotion-driven elastic collisions between atoms and ions, which expel atoms out of the shallow dipole trap. Even a

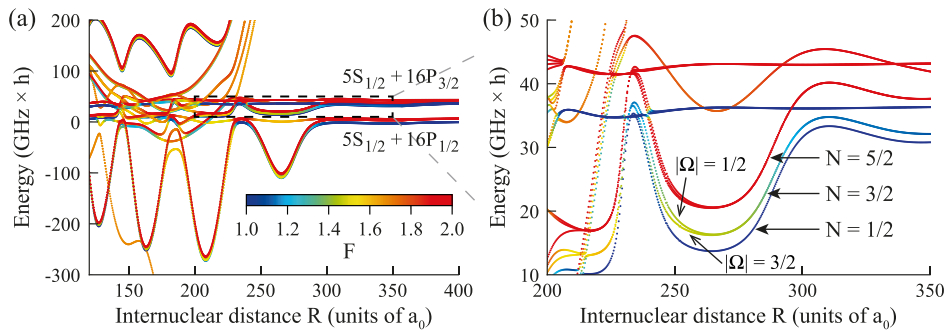


FIG. 2. (a) The molecular PECs correlated to the  $5S_{1/2} + 16P_j$  atomic asymptotes for  $j \in \{1/2, 3/2\}$  and different hyperfine states  $F \in \{1, 2\}$  of the  $5S_{1/2}$  atom. The color code represents the expectation value of the quantum number  $F$ . Calculations of PECs are described in Sec. IV A. (b) Zoom into the dashed rectangle in (a) indicating the region of interest for the present work.  $N$  and  $|\Omega|$  are quantum numbers which label the PECs. The  $N = 5/2, 3/2, 1/2$  branches are composed of a triplet, doublet, and singlet substructure of  $|\Omega|$  states, respectively.

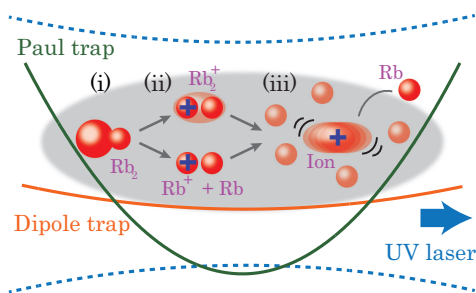


FIG. 3. Illustration of the experimental setup and scheme. The orange solid line indicates the dipole trap potential for the ultracold neutral atoms while the dark-green solid line represents the Paul trap potential for ions. (i) Inside the atom cloud (indicated by the gray shaded area)  $\text{Rb}_2$  Rydberg molecules are produced by means of the UV photoassociation laser (blue dashed lines and blue arrow). (ii) The molecules can decay into ions, where processes leading to  $\text{Rb}^+$  and  $\text{Rb}_2^+$  are possible (see, e.g., [33,34]). A resulting ion is captured by the Paul trap. (iii) The micromotion-driven ion elastically collides with Rb atoms leading to atom loss from the dipole trap.

single ion can lead to a significant loss signal. In general, the number of remaining atoms decreases with increasing number of ions.

In Fig. 4 two photoassociation spectra in the vicinity of the atomic  $16P$  Rydberg state are presented. We plot the normalized atom loss  $L = 1 - \tilde{N}/\tilde{N}_0$  as a function of the photoassociation laser frequency. Here,  $\tilde{N}$  and  $\tilde{N}_0$  are the remaining number of atoms after an experimental run when the photoassociation laser was turned on and off, respectively. The loss-signal strengths in Fig. 4 have a strongly nonlinear dependence on the number of trapped ions. While the largest loss signals correspond to hundreds of ions the smallest loss peaks are the result of only a few ions. For the measurements of Fig. 4 the frequency  $\nu$  of the photoassociation laser was scanned in steps of 20 MHz, and each data point represents a single run of the experiment. Scan (a) (blue data points) shows data for atoms prepared in the hyperfine state  $F = 1$ ,  $m_F = -1$ , while scan (b) (red data points) was obtained for atoms prepared in  $F = 2$ ,  $m_F = +2$ . For convenience, the two spectra are horizontally shifted relative to each other by twice the hyperfine splitting of the electronic ground state of  $^{87}\text{Rb}$ , i.e.,  $2 \times \nu_{\text{hfs}} = 2 \times 6.835$  GHz [35,36], to account for the frequency spacing of the  $F = 1 + F = 1$  and  $F = 2 + F = 2$  atomic asymptotes there. Then, signals for identical molecular levels line up in both data sets of Fig. 4. Besides the photoassociation resonances the spectra also include the  $16P_{3/2}$  and  $16P_{1/2}$  atomic Rydberg lines which are marked with arrows. A discussion of the atomic lines is given in Appendix A 3. In the following, we focus on the frequency range of  $10 \text{ GHz} < \Delta\nu < 40 \text{ GHz}$ , where we expect our molecular Rydberg states of interest [cf. Fig. 2(b)].

An analysis of our measured spectra shows that we observe three different vibrational ladders. The frequency spacings between vibrational lines for each ladder are approximately equidistant, typically ranging between 1.4 and 1.8 GHz. The first of the three ladders appears in spectrum (a), the second ladder appears in spectrum (b), and lines of the third ladder

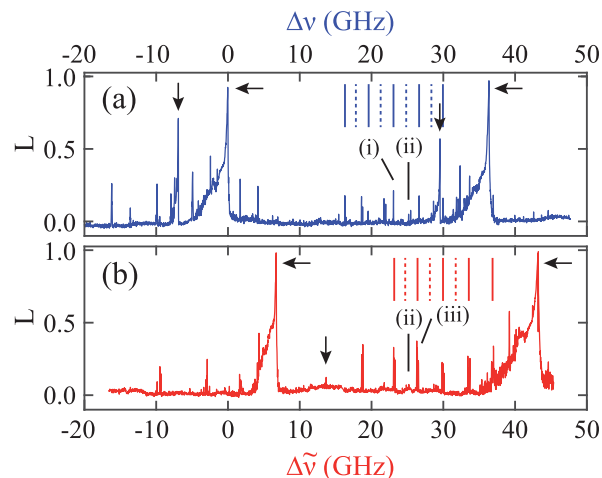


FIG. 4. Spectra measured for atomic samples initially prepared in the hyperfine state  $F = 1$  (a) and  $F = 2$  (b), respectively. Shown is the atom loss  $L$  as a function of the frequency  $\nu$  of the UV spectroscopy laser light. The frequency  $\nu$  is given in terms of  $\Delta\nu = \nu - \nu_0$  (a) and  $\Delta\tilde{\nu} = \nu - \nu_0 + 2 \times \nu_{\text{hfs}}$  (b), where  $\nu_0 = 991.55264$  THz is the resonance frequency for the  $16P_{1/2}$  atomic Rydberg line when starting with  $F = 1$  atoms. The data of (a) are obtained for a pulse duration of 125 ms of the spectroscopy light while for (b) 200 ms are used (the light intensities, micromotion energies, and ion-atom cloud interaction times are about the same for both scans). Horizontal and vertical black arrows mark resonances assigned to atomic transitions. The black solid lines with denotations (i), (ii), and (iii) point to line multiplets which are investigated in Fig. 6 with higher resolution. Vertical red solid (dashed) lines in (a) illustrate the frequency positions of observed strong (weak) three-line multiplets for  $F = 2$ , while vertical blue solid (dashed) lines in (b) mark strong (weak) single-line peaks for  $F = 1$ .

appear in both spectra (a) and (b). The positions of signals of the first and second ladder are marked in Fig. 4 as a progression of vertical solid and dashed lines, which indicate strong and weak transition lines, respectively. We note that not all of the experimentally observed lines are resolved in the two shown spectra (a) and (b). More refined scans over several small frequency ranges of interest revealed additional resonances (for more information on the methodology see Appendix A 4). A list of all observed lines can be found in Table II of the Appendix. Signals of the third ladder are in general comparatively weak and some of these are barely or not visible in Fig. 4. The signal marked with (ii) in (a) and (b) is an example of a line from the third ladder. The selectivity of each vibrational ladder for being observed exclusively in the spectra (a) or (b) (or in both) can be explained by the total angular momentum  $\vec{F}$  content of the PECs in Fig. 2(b). According to selection rules for electric dipole transitions, photoassociation does not intrinsically change the  $F$  quantum number of the Rb atom that stays in the ground state. For example, when starting from an ensemble of  $F = 1$  atoms only vibrational states in the potential wells with  $N = 1/2$  and  $N = 3/2$  can be reached because they exhibit some  $F = 1$  content. Specifically, the  $N = 1/2$  potential well is of pure  $F = 1$  character and the  $N = 3/2$  potential well is of mixed

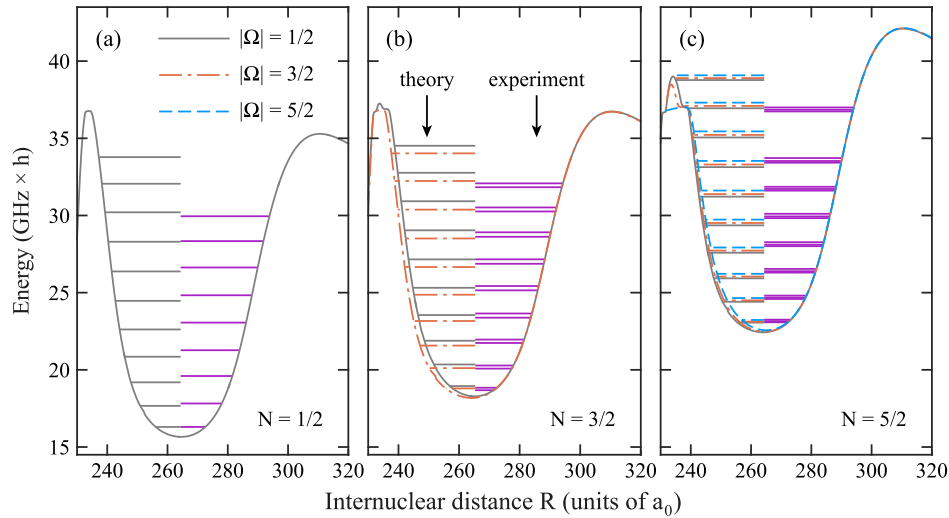


FIG. 5. Comparison of measured molecular term energies (purple horizontal lines) and calculated molecular term energies for  $N = 1/2$  (a),  $N = 3/2$  (b), and  $N = 5/2$  (c). The theoretical results for the different  $|\Omega|$  states are indicated by the line color and line style as given in the legend. Here, the predicted term energies and the PECs are shifted by  $1.94 \text{ GHz} \times h$  to higher energies as compared to Table II of the Appendix and Fig. 2(b), respectively, for better comparison to the experimental data. Then, the calculated position for the vibrational ground state of  $N = 1/2$  (which has even symmetry) coincides with the lowest observed singlet line at  $16.30 \text{ GHz} \times h$  (which is a strong signal). Such a shift is well within the uncertainty of a few  $\text{GHz} \times h$  of absolute energy determinations in the perturbative electronic structure calculations [7,37].

$F = 1$  and  $F = 2$  character. The vibrational ladder in the  $N = 5/2$  potential well, however, cannot be reached, because it has pure  $F = 2$  character. Similarly, with an ensemble of  $F = 2$  atoms only  $N = 3/2$  and  $N = 5/2$  vibrational states can be addressed due to their  $F = 2$  content, but not vibrational states of  $N = 1/2$ . Therefore, we can now assign the first ladder [ $F = 1$  ensemble, blue vertical lines in Fig. 4(a)] to the  $N = 1/2$  potential well, the second ladder [ $F = 2$  ensemble, red vertical lines in Fig. 4(b)] to the  $N = 5/2$  potential well, and the third ladder to the  $N = 3/2$  potential well. In Fig. 5 we show each measured vibrational ladder for its respective  $N$  state together with calculated molecular level energies (see Table II of the Appendix). The potential wells are the same as in Fig. 2(b), apart from a shift of  $1.94 \text{ GHz} \times h$  toward higher energies. The agreement between the measured and calculated vibrational ladders is quite good. The alternation of signal strength is observed for each vibrational ladder and can be explained by the Franck-Condon overlaps, which are in general larger for vibrational wave functions with even symmetry as compared to those with odd symmetry [15].

Figure 5 reveals that both in the experimental data as well as in the calculations, the vibrational ladders for  $N = 3/2$  and  $N = 5/2$  exhibit a substructure. For  $N = 3/2$  each vibrational level consists of a doublet and for  $N = 5/2$  each vibrational level consists of a triplet. In Fig. 6 we show measurements of these multiplets, which are obtained from high-resolution scans. Here, also a singlet line for  $N = 1/2$  is presented. The frequency position of each line multiplet [i.e., (i), (ii), and (iii)] is also indicated in the two overview spectra of Fig. 4. The lines in Fig. 6 are approximately Gaussian shaped and have typical linewidths (FWHM) of a few tens of MHz (see also Appendix A 5).

The splitting of the vibrational levels into the multiplets is mainly due to the spin-orbit interaction  $\vec{L}_p \cdot \vec{S}$ . More precisely, each  $N = 5/2$  vibrational level splits up into three spin components  $|\Omega| = \{1/2, 3/2, 5/2\}$ , and each  $N = 3/2$  vibrational level into a doublet corresponding to  $|\Omega| =$

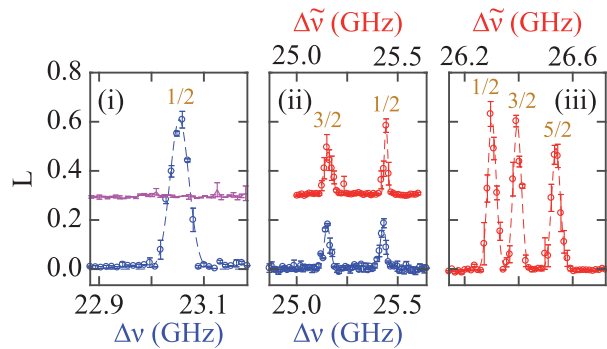


FIG. 6. Line multiplets observed for atomic samples initially prepared in the hyperfine state  $F = 1$  [blue data points for (i) and (ii)] and  $F = 2$  [red data points for (ii) and (iii)], respectively. The individual lines are labeled with the  $|\Omega|$  quantum number of the corresponding assigned molecular state (see also Fig. 5). In the left panel for the magenta data points the Paul trap was off during the spectroscopy pulse, and no loss signal is visible. Here, the pulse duration of the spectroscopy light was 200 ms for the  $F = 1$  data and 300 ms for the  $F = 2$  data. For better visibility the magenta data points and also the red data points in the center panel are shifted in the vertical direction by 0.3. The error bars represent the statistical uncertainty. Dashed blue and red lines are the results of Gaussian fits.

$\{1/2, 3/2\}$ . Since the  $N = 1/2$  levels only have  $|\Omega| = 1/2$  they do not split up. These multiplicities agree precisely with our experimental observations and confirm our assignment of the lines.

We now investigate the multiplet splittings in more detail. For the triplets of  $N = 5/2$ , the observed separation between adjacent lines is typically on the order of about 100 to 200 MHz. Overall, this is in good agreement with the predictions (see Table II of the Appendix); however there is a systematic increase of the discrepancy for increasing vibrational excitation. Furthermore, the ratio of the energy splittings between the  $|\Omega| = 1/2$  and  $3/2$  components and the  $|\Omega| = 3/2$  and  $5/2$  components is about 2 : 3 on average for the vibrational states, for both experiments and theory. Regarding the line doublets of  $N = 3/2$  we typically find splittings of a few hundred MHz. Also here, the discrepancy between measured and calculated splittings increases with vibrational excitation, up to about a factor of 2. In addition, we find that the spectroscopy signals for the  $N = 3/2$  ladder are in general weaker when working with an  $F = 2$  atomic ensemble as compared to an  $F = 1$  ensemble (except for the structure at  $\Delta\nu \sim 18.7$  GHz). In fact, some of the line doublets could only be detected for  $F = 1$ .

#### IV. THEORY

##### A. Potential energy curves

We determine the molecular PECs by using the electronic Hamiltonian

$$H = H_{\text{Ryd}} + H_g + V. \quad (1)$$

$H_{\text{Ryd}}$  describes the interaction of the Rydberg electron in the potential of the ionic  $\text{Rb}^+$  core, and has eigenstates  $\phi_{nljm_j}(\vec{r})$  with energies  $E_{nlj}$ . The energies  $E_{nlj}$  are taken from spectroscopic measurements [38,39] and are utilized as input to analytically determine the long-range behavior (larger than several Bohr radii  $a_0$ ) of  $\phi_{nljm_j}(\vec{r})$  in terms of appropriately phase-shifted Coulomb wave functions. Knowledge of the wave functions for smaller distances is not necessary for our purpose.  $H_g = A \vec{I} \cdot \vec{S}_2$  represents the Hamiltonian of hyperfine interaction in the ground state atom with eigenstates  $|Fm_F\rangle$ , where  $A = 3.417 \text{ GHz} \times h/\hbar^2$  [36]. The term  $V$  describes the interaction between the Rydberg electron and the ground state atom which is largely determined by the orbital angular momentum  $\vec{L}_p$  of the Rydberg electron in the reference frame of

the ground state atom. For  $L_p = 0$  there is  $s$ -wave interaction, while  $p$ -wave interaction is given for  $L_p = 1$ . We employ a generalized Fermi pseudopotential [7,40]

$$V = \sum_{\beta} \frac{(2L_p + 1)^2}{2} a(L_p, S, J, k) \frac{\delta(X)}{X^{2(L_p+1)}} |\beta\rangle\langle\beta| \quad (2)$$

(using atomic units). However, for convenience, we also show in Appendix A 8 how conventional representations of spin-spin and spin-orbit interactions can be derived from this approach, in general. Here,  $X = |\vec{r} - \vec{R}|$  is the absolute distance between the Rydberg electron and the ground state atom (see Fig. 1). The quantum number  $J$  corresponds to the angular momentum  $\vec{J} = \vec{L}_p + \vec{S}$ , for which the associated magnetic quantum number is denoted by  $M_J$ . Furthermore,  $\beta$  is a multi-index that defines projectors onto the different scattering channels  $|\beta\rangle = |L_p S J M_J\rangle$ . The interaction strength in each channel depends on the scattering lengths or volumes  $a(L_p, S, J, k) = -k^{-(2L_p+1)} \tan \delta(L_p, S, J, k)$ , where  $\delta(L_p, S, J, k)$  are phase shifts of an electron with wave number  $k$  that scatters off a  $^{87}\text{Rb}$  ground state atom. As a basis for our simulations we employ phase shift data from [24]. The wave number is calculated via the semiclassical relation  $k = \sqrt{2/R - 1/n_{\text{eff}}^2}$ . To compute the PECs we use the effective principle quantum number  $n_{\text{eff}} = 13.3447$ . Please note that neither  $\vec{F}$  nor  $\vec{j}$  are conserved quantities, since  $V$  neither commutes with  $H_{\text{Ryd}}$  nor with  $H_g$ .

In general, for our calculations the Hilbert space is restricted to a subset of Rydberg states in the spectral region of interest, as described in Appendix A 6. The PECs obtained by taking into account both  $s$ -wave and  $p$ -wave interactions in Eq. (1) are shown in Fig. 2. The relevant curves are characterized in Fig. 2(b) by  $N$  and  $|\Omega|$ .  $N$  provides the correct multiplicity; however, strictly speaking,  $N$  is not a good quantum number. Instead,  $\Omega$  represents a good quantum number, and it is appropriate to further discriminate the PECs. Please note that  $\Omega$  is not the projection quantum number of  $N$ .

##### B. Comparison of spin-spin and spin-orbit interactions

In the following, we investigate in detail the reasons for the splitting of the PECs with a given  $N$  quantum number into the various  $|\Omega|$  components. It will turn out that the  $\vec{L}_p \cdot \vec{S}$  interaction is by far the dominant mechanism. For our investigation, we introduce two control parameters  $\lambda_1$  and  $\lambda_2$ .

TABLE I. Overview of the scattering lengths or volumes  $a(L_p, S, J, k)$  that are modified via control parameters  $\lambda_1$  and  $\lambda_2$  in order to study the splitting mechanisms in Fig. 7. The scattering channels are given in terms of the quantum numbers  $L_p$  ( $L_p = 0$  :  $s$ -wave scattering;  $L_p = 1$  :  $p$ -wave scattering),  $S$  ( $S = 0$  : singlet scattering;  $S = 1$  : triplet scattering), and  $J = \{0, 1, 2\}$ .

Scattering channel			Parameter	Mapping
$L_p$	$S$	$J$		
0	0	0	$\lambda_1$	$a(0, 0, 0, k) \mapsto \lambda_1 a(0, 0, 0, k) + (1 - \lambda_1) a(0, 1, 1, k)$
0	1	1		$a(0, 1, 1, k) \mapsto a(0, 1, 1, k)$
1	0	1	$\lambda_1$	$a(1, 0, 1, k) \mapsto \lambda_1 a(1, 0, 1, k) + (1 - \lambda_1) a(1, 1, J_{\text{avg}}, k)$
1	1	0	$\lambda_2$	$a(1, 1, 0, k) \mapsto \lambda_2 a(1, 1, 0, k) + (1 - \lambda_2) a(1, 1, J_{\text{avg}}, k)$
1	1	1	$\lambda_2$	$a(1, 1, 1, k) \mapsto \lambda_2 a(1, 1, 1, k) + (1 - \lambda_2) a(1, 1, J_{\text{avg}}, k)$
1	1	2	$\lambda_2$	$a(1, 1, 2, k) \mapsto \lambda_2 a(1, 1, 2, k) + (1 - \lambda_2) a(1, 1, J_{\text{avg}}, k)$

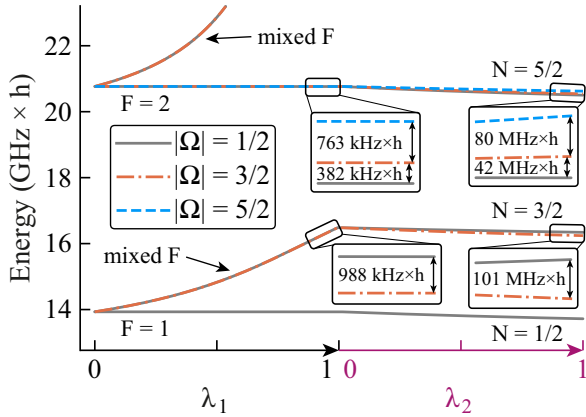


FIG. 7. Values of the molecular PECs at an internuclear distance  $R = 265 a_0$  as a function of the interaction control parameters  $\lambda_1$  and  $\lambda_2$  (see also Table I). On the left, where  $\lambda_1 = \lambda_2 = 0$ , interaction is identical for singlet and triplet states.  $s$ -wave and  $p$ -wave interactions are, however, not identical. When going to the right  $\lambda_1$  and  $\lambda_2$  are subsequently turned on. Parameter  $\lambda_1$  modifies the singlet  $s$ -wave and  $p$ -wave scattering and introduces a splitting of the lines in two respects. First, branches of mixed  $F$  character separate from branches of pure  $F$  character. Second, the  $|\Omega|$  components within these branches slightly split off from each other. Parameter  $\lambda_2$  introduces a  $\vec{L}_p \cdot \vec{S}$  type of interaction. This enhances the  $|\Omega|$  splittings by about two orders of magnitude.

These allow for relative tuning of different scattering channels by modifying the scattering lengths or volumes  $a(L_p, S, J, k)$ , which helps us to gain insight about the role of relevant interactions. The mapping is summarized in Table I. We analyze the impact of the individual control parameters on the PECs for an internuclear distance of  $265 a_0$ , which roughly corresponds to the locations of the minima of the potential wells in Fig. 2(b). This choice is motivated by the positions of the barycenters of the vibrational wave functions. The results are shown in Fig. 7.

When  $\lambda_1 = \lambda_2 = 0$ , the electron-atom interaction  $V$  is insensitive to the total electronic spin  $\vec{S}$  and the interaction can be simplified to [1,27,41]

$$V = 2\pi a_s(k)\delta(\vec{R} - \vec{r}) + 6\pi a_p(k)\vec{\nabla}_{\vec{r}} \cdot \delta(\vec{R} - \vec{r})\vec{\nabla}_{\vec{r}} \quad (3)$$

with  $a_s(k) = a(0, 1, 1, k)$ ,  $a_p(k) = a(1, 1, J_{\text{avg}}, k)$ , and  $\vec{R} = R\hat{e}_z$ . The phase shift for  $J_{\text{avg}}$  corresponds to the situation in which the  $\vec{L}_p \cdot \vec{S}$  coupling is neglected. For the resonance energy  $E_r^{\text{avg}}$  associated with this phase shift we use the value  $E_r^{\text{avg}} = 26.6$  meV taken from [24]. Figure 7 shows that for this case there is no splitting of the PECs for both the  $F = 1$  and the  $F = 2$  branch.

We now let  $\lambda_1 > 0$ , while keeping  $\lambda_2 = 0$ . The parameter  $\lambda_1$  introduces a difference in the singlet and triplet scattering lengths or volumes. As a consequence, typically, a splitting of each of the  $F = 1, 2$  branches occurs; i.e., a separation of states with mixed  $F$  character from those with pure  $F = 1, 2$  character is obtained. The energy differences between pure and mixed  $F$  states change as a function of the internuclear distance (see Fig. 10 of the Appendix). For the specific choice

of  $R = 265 a_0$  these are on the order of several  $\text{GHz} \times h$  for  $\lambda_1 = 1$  in Fig. 7. Additionally, the parameter  $\lambda_1$  lifts the energetic degeneracy of the different  $|\Omega|$  components for the individual  $F$  branches. However, the introduced splittings of the  $|\Omega|$  states are below  $1 \text{ MHz} \times h$  for  $R = 265 a_0$ , and therefore very small. Further information on the separation of  $F$  branches and the impact of  $\lambda_1$  on  $|\Omega|$  components is given in Appendix A 7.

For the regime  $\lambda_1 = 1, \lambda_2 > 0$  the full interaction introduced in Eq. (2) is realized by including the  $J$  dependency of the  $p$ -wave triplet scattering. The physical origin of the  $J$  dependency is  $\vec{L}_p \cdot \vec{S}$  spin-orbit coupling. Each  $J$  channel ( $J = \{0, 1, 2\}$ ) is associated with a characteristic energy  $E_r^J$  where the  $p$ -wave shape resonance occurs. For our scattering phase shifts these values are  $E_r^{J=(0,1,2)} = (24.4, 25.5, 27.7)$  meV, respectively [24]. We note that the energies  $E_r^J$  follow the Landé interval rule. Thus, electronic triplet states of different  $J$  experience different interaction strength for any given internuclear separation. Figure 7 shows that this leads to additional, strikingly large splittings of the  $|\Omega|$  components, on the order of tens of  $\text{MHz} \times h$  for the  $F = 2$  branch and up to about  $100 \text{ MHz} \times h$  for the lower mixed  $F$  branch. This is by about 2 orders of magnitude larger than the splitting due to  $\lambda_1$  spin-spin interaction. Therefore, we conclude that the shapes of the observed multiplet substructures are almost entirely determined by  $\vec{L}_p \cdot \vec{S}$  spin-orbit interaction.

We note that in general, the  $|\Omega|$  splittings depend on the internuclear distance  $R$  due to the energy dependence of the scattering lengths or volumes  $a(L_p, S, J, k)$  as well as the spatial variation of the Rydberg electron wave function. This can be seen, e.g., in the PECs of Fig. 2(b). For example, when considering the  $N = 3/2$  doublet, within the potential wells, for smaller values of  $R$  (i.e., closer to the  $p$ -wave shape resonance) the  $|\Omega| = 1/2$  and  $|\Omega| = 3/2$  states are farther energetically separated from each other than for higher values of  $R$ . This is due to the fact that resonant  $p$ -wave interactions amplify the effect of  $\vec{L}_p \cdot \vec{S}$  coupling. In order to check for consistency we have varied the internuclear separation around the value of  $R = 265 a_0$  used for Fig. 7. A corresponding analysis reveals that the ratios of  $|\Omega|$  splittings introduced by parameters  $\lambda_1$  and  $\lambda_2$  are robust; i.e., over the whole potential wells of Fig. 2(b)  $\vec{L}_p \cdot \vec{S}$  coupling still remains the dominant interaction that energetically separates the  $|\Omega|$  components. Only when going to the left of the barriers very close to the  $p$ -wave shape resonance (e.g., at an internuclear distance of about  $220 a_0$ ) does the relative impact of the parameter  $\lambda_1$  increase significantly.

## V. CONCLUSIONS AND OUTLOOK

In conclusion, we find evidence for spin-orbit dependent-scattering of an electron from a neutral atom. The scattering takes place within an ultralong-range Rydberg molecule which represents a microlaboratory for low-energy scattering experiments. We observe the spin-orbit interaction directly and quantitatively in terms of bound state level splittings of the ultralong-range Rydberg molecule. These level splittings are particularly large in the chosen parameter regime close to a  $p$ -wave shape resonance which enhances the effect of spin-orbit coupling on the molecular structure. Model calculations

agree well with our experimental data and allow for assigning all relevant spin states to observed levels.

Having obtained a good understanding of the complex spin couplings and level structures of the ultralong-range Rydberg molecules, it is now possible to study interesting spin and wave packet dynamics in these systems. In fact, for  $\text{Rb}_2$  molecules having principal quantum numbers in the vicinity of  $n = 16$ , our calculations predict that the level crossings of the butterfly state with the  $P$  state curves will give rise to nontrivially coupled potential energy landscapes where, e.g., nonadiabaticity effects (such as the breakdown of the Born-Oppenheimer approximation) and interesting tunneling effects can be studied. The ultralong-range Rydberg molecule will then become an even more versatile microlaboratory for fundamental quantum dynamics aspects [42,43].

In addition, the presented observation and interpretation of spin structures sets a basis for further high-precision Rydberg spectroscopic studies. These will allow for testing the limits of the theoretical understanding and modeling of the Rydberg system, in general. In fact, it might turn out that the effective pseudopotential approach is not adequate to fully describe all relevant interactions, as it suffers from limited accuracy due to convergence issues [7,37]. Precision spectroscopy data will therefore spark increased efforts, e.g., in the development of appropriate  $R$ -matrix methods [44] or the inclusion of spin interactions in Green's function approaches, to obtain a consistent theoretical treatment.

Finally, our results on spin-spin and spin-orbit coupling are helpful for current research activities regarding polyatomic many-body systems (see, e.g., [45–49]) due to the fundamental importance of pairwise interactions between two atoms.

#### ACKNOWLEDGMENTS

We thank Herwig Ott for valuable discussions. This work was supported by the German Research Foundation (DFG) within the priority program ‘‘Giant Interactions in Rydberg Systems’’ [DFG SPP 1929 GiRyd (Projects No. HE 6195/3-1, No. PF 381/17-1, and No. SCHM 885/30-1)], and under DFG Project No. PF 381/13-1. M.D. acknowledges support from Universitat Ulm and Ulmer Universitatsgesellschaft (UUG) through a Forschungsbonus grant. F.M. acknowledges support from the Carl Zeiss Foundation and is indebted to the Baden-Wurttemberg Stiftung for financial support by the Eliteprogramm for postdocs.

#### APPENDIX

##### 1. Electronic spin character of the potential energy curves

Figure 8 shows the same PECs as Fig. 2 of the main text; however, the color coding gives the expectation value of the total spin  $S$ . Interestingly, the PECs differ quite substantially in their  $S$  spin character despite the fact that the hyperfine character  $F$  is nearly constant for a given set of curves that belong to the same  $N$ .

We note that the cusps in the outer wells of the PECs around  $R = 360 a_0$ , which are visible, e.g., in Figs. 8 and 10, occur due to the nonanalytic behavior of the wave number  $k$  close to the classical turning point, where  $k$  becomes zero.

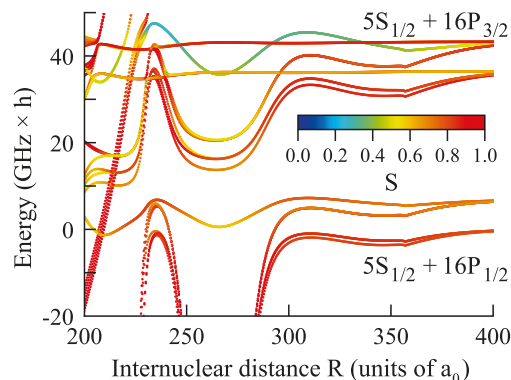


FIG. 8. The molecular PECs correlated to the  $5S_{1/2} + 16P_j$  atomic asymptotes for  $j \in \{1/2, 3/2\}$  and different hyperfine states  $F \in \{1, 2\}$  of the  $5S_{1/2}$  atom. Here, the color code represents the expectation value of the quantum number  $S$  of the total electronic spin.

##### 2. Photoassociation setup

The photoassociation laser operates at wavelengths of around 302 nm. The laser light is generated by a frequency-doubled cw dye laser with a narrow short-time linewidth of a few hundred kilohertz. The laser is frequency-stabilized to a wavelength meter (High Finesse WS7) which is repeatedly calibrated to an atomic  $^{87}\text{Rb}$  reference signal at a wavelength of 780 nm in intervals of hours. We achieve a shot-to-shot frequency stability of below  $\pm 10$  MHz for the 302 nm light.

A multimode optical fiber is used to transfer the UV light to the experimental table. At the location of the atoms the spectroscopy beam has a waist ( $1/e^2$  radius) of about 1.5 mm and the power is typically in the range of 4 to 10 mW. The light pulse has a rectangular shape and the atoms are exposed to the laser radiation for a duration on the order of 0.1 to 1 s.

##### 3. Atomic lines

The strong resonance lines marked with horizontal black arrows in the spectra (a) and (b) of Fig. 4 correspond to the atomic transitions toward  $16P_{1/2}$  and  $16P_{3/2}$ . Here, the atom loss of the atomic cloud is close to 100%. The  $16P_{1/2}$  line is located at  $\Delta\nu = 0$  in (a) and at  $\Delta\tilde{\nu} \approx \nu_{\text{hfs}} = 6.835$  GHz in (b) which corresponds to the ground state hyperfine splitting. For the excited Rydberg  $P$  state the hyperfine splitting can be neglected. The asymmetric tail on the red side of each atomic resonance line arises from the Stark effect due to the electric fields of both the Paul trap and the trapped ions (see also [50–52]). The strong resonance lines marked with vertical black arrows in the spectra (a) and (b) of Fig. 4 also correspond to transitions toward the atomic  $16P_{1/2}$  and  $16P_{3/2}$  states. These lines are shifted by about  $\pm \nu_{\text{hfs}}$  relative to the atomic resonance lines marked with horizontal black arrows. Apparently, each of the prepared  $F = 1$  ( $F = 2$ ) samples is not 100% pure but contains a fraction of atoms in the other spin state  $F = 2$  ( $F = 1$ ), respectively. Although these admixed fractions are possibly on the percent level or less they still can give rise to large signals due to the nonlinear behavior of the atomic loss, as discussed in the main text.

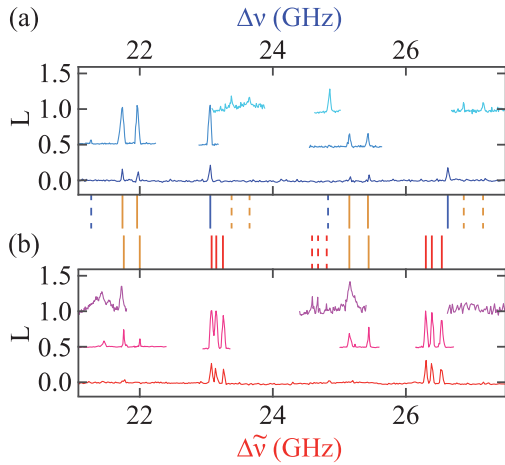


FIG. 9. Measured series of line multiplets for atomic samples initially prepared in the hyperfine state  $F = 1$  (a) and  $F = 2$  (b). The blue and red data curves in (a) and (b), respectively, are the same as in Fig. 4. All other spectra are obtained for individually optimized experimental parameters to locally increase the signal-to-noise ratio. For better visibility, light blue (cyan) data in (a) are shifted in the vertical direction by 0.5 (1.0), as well as the magenta (purple) data in (b). Blue and orange (red and orange) vertical lines at the bottom of plot (a) [at the top of plot (b)] indicate the frequency positions of measured resonances belonging to line singlets and line doublets (line triplets and line doublets) in (a) and (b), respectively. Orange color corresponds to light gray in gray-scale versions. The alternating signal strength behavior for each multiplet series is illustrated by the line style, where solid (dashed) lines represent strong (weak) signals.

#### 4. Mining of experimental data

In general, we have various parameters available to tune signal strengths for the detection of ultralong-range Rydberg molecules. These are the intensity and pulse duration of the spectroscopy light, but also the ionic micromotion energy and the time for interaction between trapped ions and neutral atoms. Figure 9 shows qualitatively how signals change when we vary these parameters, as indicated by different line colors and scan ranges. The dark blue data in (a) and the red data in (b) are zooms into Figs. 4(a) and 4(b), respectively. Additional resonance lines which are not visible in these two spectra can be revealed after individual parameter optimization. The blue, orange, and red vertical lines represent the center frequency positions of the measured resonances of line singlets, line doublets, and line triplets. Solid and dashed vertical lines mark strong and weak signals, respectively. They alternate between adjacent vibrational states for each of the three observed ladders. Within the given frequency range we observe almost the complete series of expected resonances for each multiplet structure. Only the weak line doublets for  $F = 2$  are missing in Fig. 9(b) (see purple data scan at around  $\Delta\tilde{\nu} = 27$  GHz). An overview of all observed (and calculated) molecular level positions is provided in Table II.

#### 5. Linewidths of molecular signals

The measured linewidths of several tens of MHz are more than 1 order of magnitude larger than expected from the

natural lifetimes of the molecular states. These natural lifetimes should be on the order of that of the atomic  $16P_{3/2}$  Rydberg state, for which a value of about  $4 \mu\text{s}$  is predicted [53]. The observed large linewidths of the molecular lines might be explained by the uncertainty of the UV photoassociation laser of about  $\pm 10$  MHz and due to the Stark effect. In our experimental scheme an ion trap is used and therefore dc and ac position-dependent electric fields are present. A detailed analysis of electric dipole moments and a simulation of the impact of the Stark effect on linewidths of molecular signals needs to be done in future work. Finally, we note that also limitations in the lifetime arising from the ionization of molecules subsequent to their formation can play a role.

#### 6. Restricting the Hilbert space for numerical calculations

The Hamiltonian  $H$  is constructed in a finite basis set that includes the  $15S$ ,  $16S$ ,  $17S$ ,  $14P$ ,  $15P$ ,  $16P$ ,  $13D$ ,  $14D$ , and  $15D$  states, and the hydrogenic states with higher orbital angular momenta  $l \geq 3$  with principle quantum numbers  $n = 12$ ,  $n = 13$ , and  $n = 14$ . All these states are considered with all possible total angular momenta  $j$ , while the projections  $m_j$  are truncated to include  $|m_j| \leq 3/2$ . According to the choice of the molecular axis lying on the  $z$  axis, states with  $|m_j| > 3/2$  do not interact with the ground state atom. Additionally, the nuclear and electronic spins of the ground state atom are taken into account completely ( $m_l = \{\pm 1/2, \pm 3/2\}$  and  $m_{s_2} = \pm 1/2$ ). Note that placing the perturber onto the  $z$  axis significantly reduces the basis set. Since the scattering interaction  $V$  vastly exceeds the Zeeman energy for any magnetic fields occurring due to the experimental setup, the atomic orbitals align along the internuclear axis. This is different, however, when the interaction with an external field is comparable to or larger than the scattering interaction [14]. Alternative approaches to derive the PECs that circumvent a finite basis set are Green's function methods employed for example in [6,28]. However, these approaches do not incorporate spin interactions that are crucial for the interpretation of our results. Nevertheless, we used a Green's function approach and a reduced spin model which neglects fine and hyperfine structure to find the optimal basis size. The corresponding basis was then employed for the full model calculations.

#### 7. Discussion of splitting mechanisms

In order to recall the molecular setup, the inset of Fig. 10 shows the electronic  $16P$  orbital of the Rydberg atom, which overlaps with the ground state atom at distance  $R$ . To a first approximation the interaction between the ground state atom and the Rydberg electron can be modeled by a short-range,  $s$ -wave Fermi-type pseudopotential. In Fig. 10 the Born-Oppenheimer PECs are shown, when the  $p$ -wave interaction is neglected in Eq. (1), i.e.,  $a(L_p = 1, S, J, k) = 0$ . Using this simplified situation aids convenient discussion in the following.

The oscillatory behavior of the PECs in Fig. 10 reflects the radial wave function of the Rydberg electron. Here, the separation of states with mixed  $F$  character from those with pure  $F = 1, 2$  character as a function of the internuclear distance  $R$  can directly be seen for  $R \lesssim 370 a_0$ . Each asymptote breaks up into two oscillatory PECs, marked with A and B. There is an additional, nonoscillatory PEC, marked with C, for each  $P_{3/2}$

TABLE II. Measured and calculated molecular energy level positions. The subscripts  $e$  and  $t$  denote experimental and theoretical results, respectively.  $\Delta\nu_e$  and  $\Delta\tilde{\nu}_e$  are measured resonance frequencies, while  $\Delta\nu_t$  corresponds to computed term frequencies (referenced to the calculated  $5S_{1/2} + 16P_{1/2}$  dissociation threshold). The subscript  $s$  indicates splittings between  $|\Omega|$  states within individual multiplet structures and the subscript  $v$  is used to mark vibrational splittings for a given  $|\Omega|$  quantum number. Signal strengths of measured and calculated resonance lines are classified as weak ( $w$ ) or strong ( $s$ ). Not-observed lines are labeled with “n.o.” Values of  $\Delta\nu_e$  and  $\Delta\tilde{\nu}_e$  indicated by (\*) characterize experimental signals which might come from different molecular states than considered here. These signals are not taken into account for Fig. 5. The resonance at  $\Delta\tilde{\nu}_e = 31.86$  GHz marked with (\*\*) is rather broad and expected to consist of an  $N = 5/2$  and an  $N = 3/2$  molecular line which cannot be resolved. Therefore, we give this frequency for the corresponding lines of the double as well as the triple line pattern.

Experiment ( $F = 1$ )				Experiment ( $F = 2$ )				Theory				
$\Delta\nu_e$ (GHz)	$\delta\nu_{s,e}$ (GHz)	$\delta\nu_{v,e}$ (GHz)	Signal strength	$\Delta\tilde{\nu}_e$ (GHz)	$\delta\tilde{\nu}_{s,e}$ (GHz)	$\delta\tilde{\nu}_{v,e}$ (GHz)	Signal strength	$ \Omega $	$\Delta\nu_t$ (GHz)	$\delta\nu_{s,t}$ (GHz)	$\delta\nu_{v,t}$ (GHz)	Signal strength
Vibrational ladder of single lines ( $N = 1/2$ , pure triplet)												
16.30			$s$					0.5	14.36			$s$
17.82	1.52		$w$					0.5	15.73	1.37		$w$
19.60	1.78		$s$					0.5	17.25	1.52		$s$
21.27	1.67		$w$					0.5	18.91	1.66		$w$
23.06	1.79		$s$					0.5	20.67	1.76		$s$
24.83	1.77		$w$					0.5	22.53	1.86		$w$
26.63	1.80		$s$					0.5	24.43	1.90		$s$
28.34	1.71		$w$					0.5	26.36	1.93		$w$
29.95	1.61		$s$					0.5	28.27	1.91		$s$
31.38*	1.43		$w$					0.5	30.11	1.84		$w$
32.34*	0.96		$s$					0.5	31.84	1.73		$s$
Double-line pattern ( $N = 3/2$ , mixed singlet-triplet)												
18.68			$s$	18.64			$s$	1.5	16.86			$s$
18.84	0.16		$s$	18.80	0.16		$s$	0.5	17.01	0.15		$s$
20.08		1.40	$w$	20.12		1.48	$w$	1.5	18.17		1.31	$w$
20.28	0.20	1.44	$w$	20.32	0.20	1.52	$w$	0.5	18.41	0.24	1.40	$w$
21.74		1.66	$s$	21.76		1.64	$s$	1.5	19.63		1.46	$s$
21.96	0.22	1.68	$s$	22.00	0.24	1.68	$s$	0.5	19.95	0.32	1.54	$s$
23.38		1.64	$w$	n.o.				1.5	21.22		1.59	$w$
23.65	0.27	1.69	$w$	n.o.				0.5	21.61	0.39	1.66	$w$
25.15		1.77	$s$	25.15			$s$	1.5	22.93		1.71	$s$
25.43	0.28	1.78	$s$	25.44	0.29		$s$	0.5	23.37	0.44	1.76	$s$
26.87		1.72	$w$	n.o.				1.5	24.72		1.79	$w$
27.16	0.29	1.73	$w$	n.o.				0.5	25.21	0.49	1.84	$w$
28.62		1.75	$s$	28.65			$s$	1.5	26.57		1.85	$s$
28.91	0.29	1.75	$s$	28.93	0.28		$s$	0.5	27.10	0.53	1.89	$s$
30.26		1.64	$w$	n.o.				1.5	28.44		1.87	$w$
30.52	0.26	1.61	$w$	n.o.				0.5	28.98	0.54	1.88	$w$
31.83		1.57	$s$	31.86**			$s$	1.5	30.29		1.85	$s$
32.08	0.25	1.56	$s$	32.10	0.24		$s$	0.5	30.83	0.54	1.85	$s$
								1.5	32.08		1.79	$w$
								0.5	32.58	0.50	1.75	$w$
Triple-line pattern ( $N = 5/2$ , pure triplet)												
				21.36*			$w$					
				21.43*	0.07		$w$					
				21.54*	0.11		$w$					
				23.08		1.72	$s$	0.5	21.12			$s$
				23.15	0.07	1.72	$s$	1.5	21.18	0.06		$s$
				23.25	0.10	1.71	$s$	2.5	21.29	0.11		$s$
				24.59		1.51	$w$	0.5	22.47		1.35	$w$
				24.68	0.09	1.53	$w$	1.5	22.56	0.09	1.38	$w$
				24.81	0.13	1.56	$w$	2.5	22.71	0.15	1.42	$w$
				26.30		1.71	$s$	0.5	23.99		1.52	$s$
				26.39	0.09	1.71	$s$	1.5	24.10	0.11	1.54	$s$
				26.54	0.15	1.73	$s$	2.5	24.28	0.18	1.57	$s$
				28.01		1.71	$w$	0.5	25.65		1.66	$w$
				28.11	0.10	1.72	$w$	1.5	25.78	0.13	1.68	$w$
				28.27	0.16	1.73	$w$	2.5	25.98	0.20	1.70	$w$

TABLE II. (*Continued.*)

Experiment ( $F = 1$ )				Experiment ( $F = 2$ )				Theory				
$\Delta v_e$ (GHz)	$\delta v_{s,e}$ (GHz)	$\delta v_{v,e}$ (GHz)	Signal strength	$\Delta \tilde{v}_e$ (GHz)	$\delta \tilde{v}_{s,e}$ (GHz)	$\delta \tilde{v}_{v,e}$ (GHz)	Signal strength	$ \Omega $	$\Delta v_t$ (GHz)	$\delta v_{s,t}$ (GHz)	$\delta v_{v,t}$ (GHz)	Signal strength
Triple-line pattern ( $N = 5/2$ , pure triplet)												
				29.83		1.82	<i>s</i>	0.5	27.42		1.77	<i>s</i>
				29.94	0.11	1.83	<i>s</i>	1.5	27.57	0.15	1.79	<i>s</i>
				30.11	0.17	1.84	<i>s</i>	2.5	27.79	0.22	1.81	<i>s</i>
				31.61		1.78	<i>w</i>	0.5	29.28		1.86	<i>w</i>
				31.72	0.11	1.78	<i>w</i>	1.5	29.44	0.16	1.87	<i>w</i>
				31.86**	0.14	1.75	<i>w</i>	2.5	29.67	0.23	1.88	<i>w</i>
				33.42		1.81	<i>s</i>	0.5	31.19		1.91	<i>s</i>
				33.53	0.11	1.81	<i>s</i>	1.5	31.36	0.17	1.92	<i>s</i>
				33.72	0.19	1.86	<i>s</i>	2.5	31.59	0.23	1.92	<i>s</i>
				n.o.				0.5	33.11		1.92	<i>w</i>
				n.o.				1.5	33.28	0.17	1.92	<i>w</i>
				n.o.				2.5	33.51	0.23	1.92	<i>w</i>
				36.74			<i>s</i>	0.5	35.00		1.89	<i>s</i>
				36.85	0.11		<i>s</i>	1.5	35.16	0.16	1.88	<i>s</i>
				37.00	0.15		<i>s</i>	2.5	35.37	0.21	1.86	<i>s</i>
								0.5	36.83		1.83	<i>w</i>
								1.5	36.96	0.13	1.80	<i>w</i>
								2.5	37.14	0.18	1.77	<i>w</i>

asymptote. These C PECs correspond to Rydberg states with  $m_j = \pm 3/2$  which do not undergo  $s$ -wave interaction, because the ground state atom on the  $z$  axis is located at the node of the  $|m_l| = 1$  electronic orbital. The remaining interaction of the C PECs in Fig. 10 is then solely through the attractive  $1/R^4$  polarization potential due to the  $\text{Rb}^+$  ionic core.

In the literature [19,20,23,26] each pair of oscillatory PECs is subclassified into a “deeper” curve (A) and a “shallower” curve (B) which are sometimes also labeled “triplet” and “mixed,” respectively. However, the deeper curves are not pure triplet states due to Rydberg fine structure. We explain how this is possible with the following example. We consider the electronic state of a Rydberg atom in a  $P$  state with total orbital angular momentum  $j = 1/2$  and projection  $m_j = 1/2$  and a ground state atom in a polarized nuclear spin state  $F = 2$  and  $m_F = 2$ ,

$$\begin{pmatrix} \psi_{m_l=0,\uparrow}(\vec{r}) \\ \psi_{m_l=1,\downarrow}(\vec{r}) \end{pmatrix} \otimes |F = 2, m_F = 2\rangle. \quad (\text{A1})$$

In first-order perturbation theory (with respect to weak  $s$ - and  $p$ -wave interactions) this state must be an eigenstate of the Hamiltonian, as it is the only possible realization of an  $\Omega = 5/2$  state in the Hilbert subspace considered here. The spin-up component has  $m_l = 0$  and the spin-down component has  $m_l = 1$ . Together with the spin-stretched ground state atom, the spin-up component forms a pure spin triplet. Therefore, this component does not interact in the  $s$ -wave singlet channel. The spin-down component is a mixed singlet-triplet state. However, it still does not interact in the  $s$ -wave singlet channel because  $m_l = 1$  and hence the ground state atom is located at the node of the electronic wave function. Thus, despite the fact that the state of Eq. (A1) has a singlet component, it is insensitive to  $s$ -wave singlet interaction.

The state of Eq. (A1) is just one example for the many degenerate eigenstates associated with the deep PECs. The degeneracy of the deep and shallow PECs can be obtained with the help of the spin operator  $\vec{N}^2$ , where  $\vec{N} = \vec{S} + \vec{I} = \vec{s}_1 + \vec{F}$ . We note that  $\vec{N}^2$  does not commute with  $H_{\text{Ryd}}$  due to the Rydberg fine structure; however, it is still useful for labeling the scattering channels, as we show in the following. The basis states of a given  $F$  branch all have a form similar to that of the state of Eq. (A1). Within the vector space spanned by these basis states, we want to determine the dimension of the subspace that is susceptible to singlet  $s$ -wave interaction. Since the  $|m_l| = 1$  component of a basis state does not contribute to  $s$ -wave interaction, we only consider its  $m_l = 0$  component, of which the spin can be up or down. Thus, the problem can be reduced to determining the dimension of the formed  $S = 1$  subspace when coupling an electronic spin  $\vec{s}_1$  to the angular momentum  $F$  manifold where  $\vec{F} = \vec{I} + \vec{s}_2$ . For this, we divide up the resulting new manifold into subspaces with good quantum number  $N$ . Since  $\vec{N}^2$  commutes with both  $\vec{S}^2$  and  $\vec{F}^2$ , this will help us in sorting out the spin structure. We note, however, that  $\vec{S}^2$  and  $\vec{F}^2$  do not commute. For  $F = 2$ ,  $N$  can be  $N = 5/2$  or  $N = 3/2$ . Since the  $N = 5/2$  subspace must have  $S = 1$  it belongs to branch A. With the help of Wigner  $6j$  coefficients one can show that the  $N = 3/2$  subspace, however, contains states with singlet and triplet character and therefore belongs to branch B. Similarly, for  $F = 1$ , we have the subspaces  $N = 3/2$  and  $N = 1/2$ . Here,  $N = 1/2$  goes along with  $S = 1$  and thus belongs to branch A, whereas  $N = 3/2$  includes both  $S$  characters and belongs to branch B. As the difference in the singlet and triplet  $s$ -wave interactions becomes larger, the two  $N = 3/2$  manifolds of the  $F = 1$  and  $F = 2$  branches start mixing. The degree of  $F$  mixing depends on the relative strength of the differential singlet-triplet  $s$ -wave interaction and the hyperfine interaction

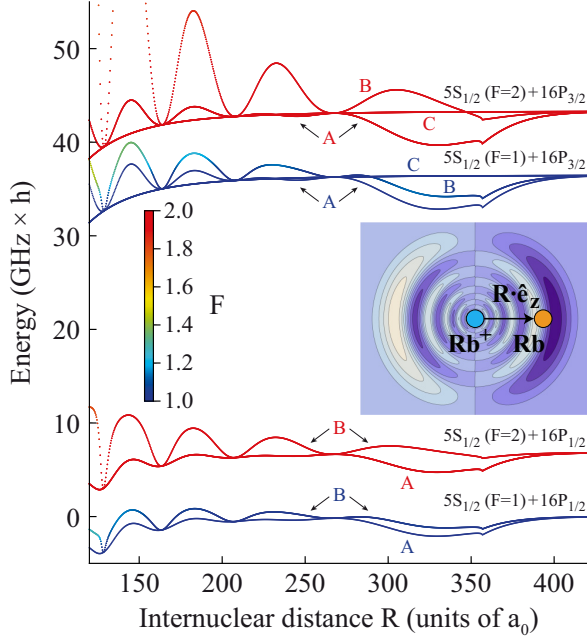


FIG. 10. The molecular Born-Oppenheimer potentials when  $s$ -wave interactions between the electron and the ground state atom are taken into account but  $p$ -wave interactions are neglected. The colors of the curves indicate the expectation value of the  $F$  quantum number of the ground state atom. From each atomic asymptote two oscillatory potentials emerge. They have  $|m_j| = 1/2$  and feature the nodes of the electronic wave function. The deeper PECs (marked with A) are associated with pure triplet scattering and the shallower PECs (marked with B) are associated with mixed singlet-triplet scattering. The PECs labeled with C have  $|m_j| > 1/2$  and do not show an oscillatory behavior. In the inset a sketch of an ultralong-range Rydberg molecule is shown. It consists of a  $\text{Rb}^+$  ionic core, an electronic Rydberg  $16P$  state orbital, and a ground state Rb atom which is located at position  $\vec{R} = R\hat{e}_z$  relative to the ionic core. The  $16P$  electronic orbital is given in a contour plot representation.

$H_g$ . The  $F$  mixing due to the presence of a singlet  $s$ -wave scattering channel is essential for the spin-flip effect observed in [22].  $N$  reproduces the multiplicities for the PECs, which are visible in Figs. 2(b) and 7. For the  $F = 2$  asymptote, the deep curve corresponds to  $N = 5/2$  and has six degenerate states of pure  $F = 2$  character. For the  $F = 1$  asymptote, the deep curve corresponds to  $N = 1/2$  and has two degenerate states of pure  $F = 1$  character. The shallow curves of both the  $F = 1$  and the  $F = 2$  asymptotes correspond to  $N = 3/2$  and have four degenerate states of mixed  $F = 1$  and  $F = 2$  character each. While this regime of interactions is sufficient to describe the PECs at the outer potential wells (in this case for  $R > 300 a_0$ ), additional  $p$ -wave related interactions become important for smaller internuclear separations, which are also relevant in the parameter regime of  $\lambda_1$ .

The difference between the singlet and triplet channels introduced via parameter  $\lambda_1$  affects in particular the spinor components with  $m_l = \pm 1$ , which only probe the  $p$ -wave

interaction but not the  $s$ -wave interaction. Although the state with  $\Omega = 5/2$  of Eq. (A1) is of pure triplet character in its  $m_l = 0$  component, it is of mixed singlet-triplet character in its  $m_l = 1$  component, as discussed before. As a consequence, it will experience a first-order level shift. States with a different  $|\Omega|$  have different mixing ratios and will exhibit different shifts. Therefore, the spin-selective  $p$ -wave interaction generally leads to a splitting of  $|\Omega|$  states. This splitting, however, arises only due to the Rydberg fine structure and is, hence, not visible in  $S$  state ultralong-range Rydberg molecules recently studied [25], since they do not exhibit such a kind of fine structure related to  $|m_l| = 1$ .

### 8. Alternative representation of spin-spin and spin-orbit interaction

The pseudopotential that models the interaction between the Rydberg electron and the ground state atom is given in Eq. (2) of the main text. Our aim is now to rewrite the given interaction potential in terms of operators such as  $\vec{s}_1 \cdot \vec{s}_2$  and  $\vec{L}_p \cdot \vec{S}$ , respectively.

First, we consider the example of pure  $s$ -wave scattering, i.e.,  $L_p = 0$  and therefore  $J = S$  and  $M_J = M_S$ . The corresponding expression of Eq. (2) is compared to the ansatz

$$V_{L_p=0} = [c_1 \hat{1} + c_2 \vec{s}_1 \cdot \vec{s}_2] \frac{\delta(X)}{2X^2} |L_p = 0\rangle \langle L_p = 0|. \quad (\text{A2})$$

For this, Eq. (A2) is represented as a  $4 \times 4$  matrix in the basis  $|S, M_S\rangle$ . From the comparison we find that both expressions are identical if  $c_1 = [a(0, 0, 0, k) + 3a(0, 1, 1, k)]/4$  and  $c_2 = a(0, 1, 1, k) - a(0, 0, 0, k)$ . As expected, there is no spin-spin coupling, i.e.,  $c_2 = 0$ , when the  $s$ -wave singlet and triplet scattering lengths or volumes  $a(0, 0, 0, k)$  and  $a(0, 1, 1, k)$  are equal. Furthermore,  $c_1$  corresponds to the averaged  $s$ -wave scattering length or volume.

Now, we turn to a treatment of spin-orbit coupling. Since spin-orbit interaction only takes place in the  $p$ -wave triplet channel only the subspace with  $L_p = 1$  and  $S = 1$  has to be considered in Eq. (2). The resulting expression is compared to the ansatz

$$V_{L_p=S=1} = [c_3 \hat{1} + c_4 \vec{L}_p \cdot \vec{S} + c_5 (\vec{L}_p \cdot \vec{S})^2] \times \frac{9\delta(X)}{2X^4} |L_p = 1, S = 1\rangle \langle L_p = 1, S = 1|, \quad (\text{A3})$$

which includes second-order spin-orbit interaction. We obtain

$$\begin{aligned} c_3 &= \frac{-a(1, 1, 0, k) + 3a(1, 1, 1, k) + a(1, 1, 2, k)}{3}, \\ c_4 &= \frac{-a(1, 1, 1, k) + a(1, 1, 2, k)}{2}, \\ c_5 &= \frac{2a(1, 1, 0, k) - 3a(1, 1, 1, k) + a(1, 1, 2, k)}{6}. \end{aligned} \quad (\text{A4})$$

The result implies that the  $\vec{L}_p \cdot \vec{S}$  coupling vanishes, i.e.,  $c_4 = c_5 = 0$ , only if all scattering volumes are equal, which agrees with our expectation. Our analysis shows that including the second-order spin-orbit interaction is particularly important for the description close to the  $p$ -wave shape resonance.

- [1] C. H. Greene, A. S. Dickinson, and H. R. Sadeghpour, *Phys. Rev. Lett.* **85**, 2458 (2000).
- [2] V. Bendkowsky, B. Butscher, J. Nipper, J. P. Shaffer, R. Löw, and T. Pfau, *Nature (London)* **458**, 1005 (2009).
- [3] J. P. Shaffer, S. T. Rittenhouse, and H. R. Sadeghpour, *Nat. Commun.* **9**, 1965 (2018).
- [4] C. Fey, F. Hummel, and P. Schmelcher, *Mol. Phys.* (2019), doi:10.1080/00268976.2019.1679401.
- [5] M. T. Eiles, *J. Phys. B: At. Mol. Opt. Phys.* **52**, 113001 (2019).
- [6] A. A. Khuskivadze, M. I. Chibisov, and I. I. Fabrikant, *Phys. Rev. A* **66**, 042709 (2002).
- [7] M. T. Eiles and C. H. Greene, *Phys. Rev. A* **95**, 042515 (2017).
- [8] S. Markson, S. T. Rittenhouse, R. Schmidt, J. P. Shaffer, and H. R. Sadeghpour, *Chem. Phys. Chem.* **17**, 3683 (2016).
- [9] O. Thomas, C. Lippe, T. Eichert, and H. Ott, *Nat. Commun.* **9**, 2238 (2018).
- [10] W. Li, T. Pohl, J. M. Rost, S. T. Rittenhouse, H. R. Sadeghpour, J. Nipper, B. Butscher, J. B. Balewski, V. Bendkowsky, R. Löw, and T. Pfau, *Science* **334**, 1110 (2011).
- [11] J. Tallant, S. T. Rittenhouse, D. Booth, H. R. Sadeghpour, and J. P. Shaffer, *Phys. Rev. Lett.* **109**, 173202 (2012).
- [12] D. Booth, S. T. Rittenhouse, J. Yang, H. R. Sadeghpour, and J. P. Shaffer, *Science* **348**, 99 (2015).
- [13] T. Niederprüm, O. Thomas, T. Eichert, C. Lippe, J. Pérez-Ríos, C. H. Greene, and H. Ott, *Nat. Commun.* **7**, 12820 (2016).
- [14] A. T. Krupp, A. Gaj, J. B. Balewski, P. Ilzhöfer, S. Hofferberth, R. Löw, T. Pfau, M. Kurz, and P. Schmelcher, *Phys. Rev. Lett.* **112**, 143008 (2014).
- [15] B. J. DeSalvo, J. A. Aman, F. B. Dunning, T. C. Killian, H. R. Sadeghpour, S. Yoshida, and J. Burgdörfer, *Phys. Rev. A* **92**, 031403(R) (2015).
- [16] M. A. Bellos, R. Carollo, J. Banerjee, E. E. Eyler, P. L. Gould, and W. C. Stwalley, *Phys. Rev. Lett.* **111**, 053001 (2013).
- [17] K. S. Kleinbach, F. Meinert, F. Engel, W. J. Kwon, R. Löw, T. Pfau, and G. Raithel, *Phys. Rev. Lett.* **118**, 223001 (2017).
- [18] V. Bendkowsky, B. Butscher, J. Nipper, J. P. Balewski, J. P. Shaffer, R. Löw, T. Pfau, W. Li, J. Stanojevic, T. Pohl, and J. M. Rost, *Phys. Rev. Lett.* **105**, 163201 (2010).
- [19] F. Böttcher, A. Gaj, K. M. Westphal, M. Schlagmüller, K. S. Kleinbach, R. Löw, T. C. Liebisch, T. Pfau, and S. Hofferberth, *Phys. Rev. A* **93**, 032512 (2016).
- [20] H. Saßmannshausen, F. Merkt, and J. Deiglmayr, *Phys. Rev. Lett.* **114**, 133201 (2015).
- [21] J. L. MacLennan, Y.-J. Chen, and G. Raithel, *Phys. Rev. A* **99**, 033407 (2019).
- [22] T. Niederprüm, O. Thomas, T. Eichert, and H. Ott, *Phys. Rev. Lett.* **117**, 123002 (2016).
- [23] D. A. Anderson, S. A. Miller, and G. Raithel, *Phys. Rev. Lett.* **112**, 163201 (2014).
- [24] F. Engel, T. Dieterle, F. Hummel, C. Fey, P. Schmelcher, R. Löw, T. Pfau, and F. Meinert, *Phys. Rev. Lett.* **123**, 073003 (2019).
- [25] F. Hummel, C. Fey, and P. Schmelcher, *Phys. Rev. A*, **99**, 023401 (2019).
- [26] D. A. Anderson, S. A. Miller, and G. Raithel, *Phys. Rev. A* **90**, 062518 (2014).
- [27] E. L. Hamilton, C. H. Greene, and H. R. Sadeghpour, *J. Phys. B: At. Mol. Opt. Phys.* **35**, L199 (2002).
- [28] M. I. Chibisov, A. A. Khuskivadze, and I. I. Fabrikant, *J. Phys. B: At. Mol. Opt. Phys.* **35**, L193 (2002).
- [29]  $E_r^{\text{ave}}$  represents an average value which follows the rule  $E_r^{\text{ave}} = [\sum_{J=0}^2 (2J+1)E_r^J] / [\sum_{J=0}^2 (2J+1)]$ . Here,  $E_r^J$  are the characteristic energies where the  $p$ -wave shape resonance occurs for the three individual channels  $J = \{0, 1, 2\}$  (see also the discussion in Sec. IV B).
- [30] S. Schmid, A. Härter, A. Frisch, S. Hoinka, and J. Hecker Denschlag, *Rev. Sci. Instrum.* **83**, 053108 (2012).
- [31] A. Härter, A. Krüchow, A. Brunner, and J. Hecker Denschlag, *Appl. Phys. Lett.* **102**, 221115 (2013).
- [32] J. Wolf, M. Deiß, A. Krüchow, E. Tiemann, B. P. Ruzic, Y. Wang, J. P. D’Incao, P. S. Julienne, and J. Hecker Denschlag, *Science* **358**, 921 (2017).
- [33] T. Niederprüm, O. Thomas, T. Manthey, T. M. Weber, and H. Ott, *Phys. Rev. Lett.* **115**, 013003 (2015).
- [34] M. Schlagmüller, T. C. Liebisch, F. Engel, K. S. Kleinbach, F. Böttcher, U. Hermann, K. M. Westphal, A. Gaj, R. Löw, S. Hofferberth, T. Pfau, J. Pérez-Ríos, and C. H. Greene, *Phys. Rev. X* **6**, 031020 (2016).
- [35] S. Bize, Y. Sortais, M. S. Santos, C. Mandache, A. Clairon, and C. Salomon, *Europhys. Lett.* **45**, 558 (1999).
- [36] E. Arimondo, M. Inguscio, and P. Violino, *Rev. Mod. Phys.* **49**, 31 (1977).
- [37] C. Fey, M. Kurz, P. Schmelcher, S. T. Rittenhouse, and H. R. Sadeghpour, *New J. Phys.* **17**, 055010 (2015).
- [38] W. Li, I. Mourachko, M. W. Noel, and T. F. Gallagher, *Phys. Rev. A* **67**, 052502 (2003).
- [39] J. Han, Y. Jamil, D. V. L. Norum, P. J. Tanner, and T. F. Gallagher, *Phys. Rev. A* **74**, 054502 (2006).
- [40] F. Hummel, C. Fey, and P. Schmelcher, *Phys. Rev. A* **97**, 043422 (2018).
- [41] The operator  $\overleftarrow{\nabla}_{\vec{r}} \cdot \delta(\vec{R} - \vec{r}) \overrightarrow{\nabla}_{\vec{r}}$  is a shorthand for  $\sum_{i,j} |\psi_i\rangle \langle \psi_j| \int d^3r \delta(\vec{R} - \vec{r}) [\overleftarrow{\nabla}_{\vec{r}} \psi_i^*(\vec{r})] \cdot [\overrightarrow{\nabla}_{\vec{r}} \psi_j(\vec{r})]$ , where the  $\{|\psi_i\rangle\}$  form an orthonormal basis of the Hilbert space and  $\psi_i(\vec{r}) \equiv \langle \vec{r} | \psi_i \rangle$ .
- [42] H. Köppel, W. Domcke, and L. S. Cederbaum, *Adv. Chem. Phys.* **57**, 59 (1984).
- [43] G. A. Worth and L. S. Cederbaum, *Annu. Rev. Phys. Chem.* **55**, 127 (2004).
- [44] M. Tarana and R. Čurík, *Phys. Rev. A* **93**, 012515 (2016).
- [45] C. Fey, M. Kurz, and P. Schmelcher, *Phys. Rev. A* **94**, 012516 (2016).
- [46] M. Schlagmüller, T. C. Liebisch, H. Nguyen, G. Lothead, F. Engel, F. Böttcher, K. M. Westphal, K. S. Kleinbach, R. Löw, S. Hofferberth, T. Pfau, J. Pérez-Ríos, and C. H. Greene, *Phys. Rev. Lett.* **116**, 053001 (2016).
- [47] M. T. Eiles, J. Pérez-Ríos, F. Robicheaux, and C. H. Greene, *J. Phys. B: At. Mol. Opt. Phys.* **49**, 114005 (2016).
- [48] R. Schmidt, H. R. Sadeghpour, and E. Demler, *Phys. Rev. Lett.* **116**, 105302 (2016).
- [49] Y. Ashida, T. Shi, R. Schmidt, H. R. Sadeghpour, J. I. Cirac, and E. Demler, *Phys. Rev. Lett.* **123**, 183001 (2019).
- [50] S. Haze, J. Wolf, M. Deiß, L. Wang, G. Raithel, and J. Hecker Denschlag, *arXiv:1901.11069*.
- [51] N. V. Ewald, T. Feldker, H. Hirzler, H. A. Fürst, and R. Gerritsma, *Phys. Rev. Lett.* **122**, 253401 (2019).
- [52] F. Engel, T. Dieterle, T. Schmid, C. Tomschitz, C. Veit, N. Zuber, R. Löw, T. Pfau, and F. Meinert, *Phys. Rev. Lett.* **121**, 193401 (2018).
- [53] C. E. Theodosiou, *Phys. Rev. A* **30**, 2881 (1984).



### 3.5 An ultracold heavy Rydberg system formed from ultra-long-range molecules bound in a stairwell potential

# New Journal of Physics

The open access journal at the forefront of physics

Deutsche Physikalische Gesellschaft  DPG  
IOP Institute of Physics

Published in partnership  
with: Deutsche Physikalische  
Gesellschaft and the Institute  
of Physics



## PAPER

# An ultracold heavy Rydberg system formed from ultra-long-range molecules bound in a stairwell potential

### OPEN ACCESS

RECEIVED  
27 January 2020

REVISED  
27 April 2020

ACCEPTED FOR PUBLICATION  
6 May 2020

PUBLISHED  
29 June 2020

F Hummel<sup>1,2</sup>, P Schmelcher<sup>1,3</sup> , H Ott<sup>4</sup>  and H R Sadeghpour<sup>2</sup> 

<sup>1</sup> Zentrum für Optische Quantentechnologien, Fachbereich Physik, Universität Hamburg, Luruper Chaussee 149, 22761 Hamburg, Germany

<sup>2</sup> ITAMP, Harvard-Smithsonian Center for Astrophysics, 60 Garden St., Cambridge, Massachusetts 02138, United States of America

<sup>3</sup> The Hamburg Centre for Ultrafast Imaging, Universität Hamburg, Luruper Chaussee 149, 22761 Hamburg, Germany

<sup>4</sup> Research Center OPTIMAS, Technische Universität Kaiserslautern, 67663 Kaiserslautern, Germany

E-mail: [frederic.hummel@physnet.uni-hamburg.de](mailto:frederic.hummel@physnet.uni-hamburg.de)

**Keywords:** ultra-long range Rydberg molecules, photoassociation, ultracold negative ions, heavy Rydberg systems

Original content from this work may be used under the terms of the [Creative Commons Attribution 4.0 licence](https://creativecommons.org/licenses/by/4.0/).

Any further distribution of this work must maintain attribution to the author(s) and the title of the work, journal citation and DOI.



## Abstract

We propose a scheme to realize a *heavy Rydberg system* (HRS), a bound pair of oppositely charged ions, from a gas of ultracold atoms. The intermediate step to achieve large internuclear separations is the creation of a unique class of ultra-long-range Rydberg molecules bound in a stairwell potential energy curve. Here, a ground-state atom is bound to a Rydberg atom in an oscillatory potential emerging due to attractive singlet p-wave electron scattering. The utility of our approach originates in the large electronic dipole transition element between the Rydberg and the ionic molecule, while the nuclear configuration of the ultracold gas is preserved. The Rabi coupling between the Rydberg molecule and the heavy Rydberg system is typically in the MHz range and the permanent electric dipole moments of the HRS can be as large as one kilo-Debye. We identify specific transitions which place the creation of the heavy Rydberg system within immediate reach of experimental realization.

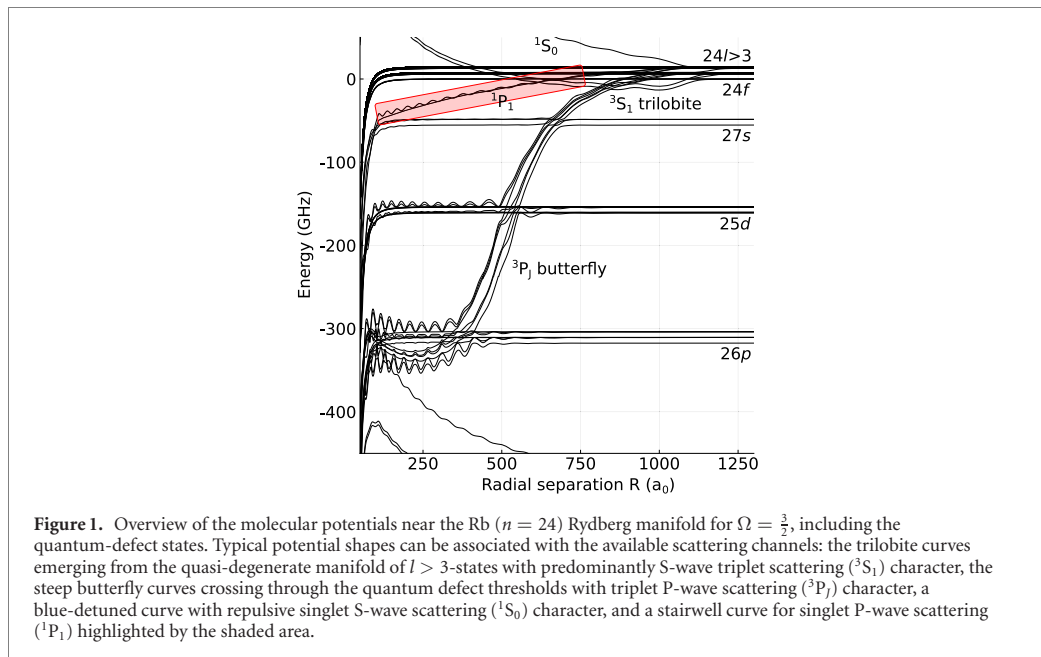
## 1. Introduction

A bound pair of oppositely charged ions can be viewed as the molecular analogue of an atomic Rydberg state in which the electron is replaced by the negatively charged anion, hence termed a heavy Rydberg system (HRS) [1, 2]. Such HRS do form in ionic molecules, such as alkali-halides [3], and whose vibrational energy spectra follow the Rydberg quantum defect formula,

$$E_\nu = -\frac{R_\infty}{\mu(\nu - \delta)^2}, \quad (1)$$

in atomic units, where  $E_\nu$  is the energy of the vibrational level  $\nu$ ,  $R_\infty$  is the Rydberg constant, and  $\delta$  is the quantum defect. In electronic Rydberg systems, the reduced mass  $\mu \approx m_e$ , where  $m_e$  is the electron mass, while for the homonuclear HRS,  $\mu = M/2$ , where  $M$  is the atomic mass.

Reactions of anions and cations, leading to neutralization, are important for the ionization balance of various cold astrophysical plasmas [4]. HRS are typically created from tightly bound molecules [2, 5–7] and long-range HRS have only been populated via excitation of complex resonances, which are required due to vanishing Franck–Condon overlaps with the vibrational states [8]. Excitation of HRS in an ultracold gas, which automatically provides the desired inter-atomic distances, was proposed recently via magnetic Feshbach resonances [1] or with field-control to couple covalent and ion-pair potentials [9]. Formation of HRS via coupling to covalent Rydberg states in the long range in an ultracold environment has several advantages: because these states may form away from the complicated short-range molecular interaction region, there's better control over their formation and spectroscopy; the decay channels which mainly consist of mutual neutralization into atomic species is greatly suppressed [10]; and the possibility that the



ion pair constituents are both at ultracold temperatures and therefore may lead to formation of a two-component strongly coupled plasma. Ultracold HRS may eventually serve as a source for production of ultracold negative ions, which are not amenable to laser cooling due to the fact that negative ions have typically a single bound state and hence no cooling transition exists. So far only few atomic species have been identified that offer prospects to cool them [11, 12].

In this work, we propose to utilize the excitation of a new class of ultra-long-range Rydberg molecules (which for brevity we refer to as Rydberg molecules from now on) as intermediate states for the preparation of the HRS states. The binding mechanism in a Rydberg molecule is mediated by the repeated scattering of a nearly-free Rydberg electron from a perturber ground-state atom [13–16]. The resulting molecular potentials capture the oscillatory character of the Rydberg electronic wave functions.

The electronic state of the anion–cation pair has the  ${}^1\Sigma$  singlet molecular symmetry for the alkali-metal cases. For the formation of URLM in a magneto-optical trap, it is possible to select different molecular symmetries, due to spin-dependent scattering of the Rydberg electron off the perturber [17–19], which was also experimentally demonstrated [20–25]. To maximize the transition strength to the anionic  ${}^1S_0$  state, a Rydberg molecular state has to be prepared that provides two properties: first, electronic density in the vicinity of the perturber. Second, electronic singlet P-wave ( ${}^1P_1$ ) character with respect to the perturber. To this end, we investigate a *stairwell* Rydberg molecular potential, that has not previously been studied and represents the singlet analogue of the butterfly potentials [26–28] (cf Figure 1). Similar to the butterfly potentials, the electronic state corresponding to Rydberg molecules formed in a well of this potential can be expressed as a superposition of high-angular momentum Rydberg wave functions. In order to gain spectroscopic access to this type of molecule, we exploit the fact that in  ${}^{87}\text{Rb}$ , the stairwell potential crosses and mixes with the Rydberg f-state, which is detuned slightly from the hydrogenic manifold due to a small quantum defect. Thus, molecules can be excited via a three-photon transition.

Specifically, we demonstrate the charge transfer process by exciting a Rydberg molecule red detuned off the  ${}^{87}\text{Rb}(24f)$  Rydberg state, which is formed on the stairwell potential due to attractive  ${}^1P_1$  scattering. An infra-red photon can then be used to drive a transition to the anionic  ${}^1S_0$  state. The resulting HRS molecular state is the vibrational analogue of highly excited, isotropic Rydberg electronic states and can be probed spectroscopically over a wide range of HRS principal quantum numbers  $5120 \lesssim \nu \lesssim 5250$ .

Before we discuss the results that provide specific experimental requirements for the realization of the proposed excitation scheme in section 3, in the following section 2, we introduce the methods used to theoretically derive the Rydberg molecular potential energy curves (PECs) and the vibrational structure of Rydberg molecules. Furthermore, we introduce the model for the HRS. Section 4 provides the conclusion.

## 2. Methodology

### 2.1. Ultra-long-range Rydberg molecule

Let us consider two rubidium atoms, one of which is excited to a Rydberg state. In the spirit of the Born–Oppenheimer approximation, we separate the nuclear from the electronic degrees of freedom, while the adiabatic electronic eigenstates and corresponding energies depend parametrically on the internuclear separation  $R$ . Solving the time-independent Schrödinger equation (SE) for the electronic problem provides the PECs which are used as input for the vibrational SE. We employ the electronic Hamiltonian (in atomic units) [19]

$$H_e = H_R + H_G + V_p + V_e. \quad (2)$$

$H_R$  describes the dynamics of the Rydberg electron at position  $\mathbf{r}$  in the potential of the ionic core at the origin. The electron has spin  $s_1$  and orbital  $l$  angular momentum. The eigenstates of  $H_R$ ,  $\phi_{nljm_j}(\mathbf{r})$ , depend on the principal quantum number  $n$ , orbital angular momentum  $l$ , and the total angular momentum  $j = |s_1 + l|$  with its projection onto the internuclear axis  $m_j$ . The eigenvalues are taken from spectroscopic measurements [29, 30] and are used to analytically express the long-range behavior of  $\phi_{nljm_j}(\mathbf{r})$  in terms of Whitaker functions.

The ground-state atom is considered in terms of its hyperfine interaction  $H_G = a\mathbf{I} \cdot \mathbf{s}_2$ , where  $\mathbf{I}$  is the nuclear spin,  $\mathbf{s}_2$  is the spin of the valence electron, and  $a$  is the hyperfine constant taken from [31]. Eigenstates of  $H_G$  are  $|F, m_F\rangle$ , where  $F = |\mathbf{I} + \mathbf{s}_2|$ . The ionic Rydberg core polarizes the ground-state atom, which is considered by  $V_p = -\frac{\alpha}{2R^4}$ , where the polarizability  $\alpha$  is taken from [32].

The interaction of the Rydberg electron and the ground-state atom is modeled by a Fermi-type pseudopotential [33], which has been generalized to include orbital angular momentum  $L$  of the Rydberg electron relative to the ground-state atom [34] up to P-wave interaction ( $L = 1$ ;  $L = 0$  corresponds to S-wave interaction) as well as the total electronic spin of the Rydberg electron and the valence electron  $\mathbf{S} = \mathbf{s}_1 + \mathbf{s}_2$  in terms of singlet ( $S = 0$ ) and triplet ( $S = 1$ ) scattering channels. For this contact interaction, we employ the potential [19]

$$V_e = \sum_{\beta} a_{SLJ}(k) \frac{(2L+1)^2}{2x^{2(L+1)}} \delta(x) |\beta\rangle \langle \beta|, \quad (3)$$

where  $x = |\mathbf{r} - \mathbf{R}|$  is the distance between the Rydberg electron and the ground-state atom and the sum is taken over available interaction channels defined by the multi index  $\beta$ , where  $|\beta\rangle = |(LS)JM_j\rangle$ . Here,  $J = |\mathbf{L} + \mathbf{S}|$  is the total angular momentum of the two electrons with respect to the ground-state atom's core and  $M_j$  its projection onto the internuclear axis. The spin and orbital angular momentum dependent scattering lengths and volumes  $a_{SLJ}(k)$  are derived from the respective phase shifts, which are taken from [24]. They are energy dependent and the wave number  $k$  is calculated via the semi-classical relation  $k = \sqrt{2/R - 2E^*}$ , where  $E^*$  is the asymptotic atomic energy of  $^{87}\text{Rb}(24f)$ . The only good quantum number of the Rydberg molecule is the projection of the total angular momentum onto the internuclear axis  $\Omega = m_j + m_F$ .

Without loss of generality, the internuclear axis is assumed to be the  $z$  axis. Solutions to the electronic problem and the PECs are obtained by diagonalizing  $H_e$  (2) in a finite basis that includes two hydrogenic manifolds, one of which lies energetically above the state of interest  $24f$  ( $n = 24$ ) and one lies below ( $n = 23$ ). All angular momenta  $j$  are considered, while projections  $|m_j| > \frac{3}{2}$  are neglected since they do not interact with the ground-state atom. The basis  $|Fm_F\rangle$  is included completely. The chosen basis set has proven to be sufficiently accurate despite the inherent convergence issues that stem from the non-local character of the contact scattering interaction [24, 35].

After solving the electronic problem, a specific molecular potential  $V_{\text{in}}(R)$  is used as input for the nuclear vibrational SE which is solved by standard one-dimensional finite difference methods. Since the energy spacing of vibrational states is on the order of few GHz, we neglect couplings to rotational degrees of freedom, the energetic scale of which is three orders of magnitude smaller for the given internuclear separations.

The vibrational ground-state in the given PEC  $V_{\text{in}}(R)$  is termed initial state  $\chi_{\text{in}}(R)$  for the creation of the heavy Rydberg system. This type of state is typically a Gaussian-like wave packet without nodes. Its center of mass is given by  $R_{\text{in}} = \langle \chi_{\text{in}} | R | \chi_{\text{in}} \rangle$ . The corresponding electronic wave function for this equilibrium position is termed  $\psi_{\text{in}}(\mathbf{r}; R_{\text{in}}) = \langle \mathbf{r} | \psi_{\text{in}} \rangle$ . The electronic spin character of the initial state is obtained by projecting the electronic wave function  $\sigma_S(R_{\text{in}}) = |\langle S | \psi_{\text{in}} \rangle|^2$ .

### 2.2. Heavy Rydberg system

To model the heavy Rydberg system, we employ the ionic potential

$$V_f = -E_{\text{ea}} - \frac{1}{R} - \frac{\alpha_p + \alpha_m}{2R^4}, \quad (4)$$

where  $E_{\text{ea}} = 117.5$  THz is the electron affinity of rubidium [36] and  $\alpha_{p/m} = 9.11/526 a_0^3$  is the polarizability of the positively/negatively charged rubidium ion [32, 37]. In general, the vibrational nuclear wave function can be expressed in terms of the hydrogenic wave functions  $|\chi_{\nu}^{\Lambda}\rangle$  with the appropriate reduced mass  $\mu$  and with principal quantum number  $\nu$  and angular momentum  $\Lambda$ , which correspond to vibrations and rotations, respectively:

$$|\chi_f\rangle = \sum_{\nu\Lambda} c_{\nu\Lambda} |\chi_{\nu}^{\Lambda}\rangle. \quad (5)$$

Here, up to normalization, the coefficient  $c_{\nu\Lambda}$  equals the nuclear Franck–Condon overlap  $\langle\chi_{\nu}^{\Lambda}|\chi_{\text{in}}\rangle$  of a specific vibrational-rotational state and the Rydberg molecular initial state  $|\chi_{\text{in}}\rangle$ . In our case, the range of available  $c_{\nu\Lambda}$  depends on the spectroscopic width of the transition from the Rydberg molecule to the HRS. Typically, by aid of a narrow-band laser, each level  $\nu$ , the energy of which is given by equation (1), can be addressed individually and the sum over  $\nu$  in equation (5) collapses to a specific value  $\nu'$ .

For the anion electronic wave function, we employ an Eckart wave function [38] with the functional form

$$\langle\mathbf{r}|\psi_f\rangle = N \cosh^{-2\lambda} \left( \frac{x}{r_0} \right) \sinh \left( \frac{x}{r_0} \right), \quad (6)$$

where  $N$  is a normalization constant,  $x = |\mathbf{r} - R_{\text{in}}\hat{\mathbf{e}}_z|$  is the distance of the electron to the position of the anion nucleus  $R_{\text{in}}$ , and  $\lambda = 1.35094$  and  $r_0 = 9.004786 a_0$  have been obtained to reproduce the electron affinity and the electron-atom S-wave scattering length of  $^{87}\text{Rb}$  [9].

### 3. Results and discussions

#### 3.1. Stairwell Rydberg molecular potential curve

To calculate the transition from the Rydberg molecule to the HRS, we determine the initial and final states of the respective systems, individually. The ultra-long-range dimer consists of a single  $^{87}\text{Rb}(5s)$  ground-state atom inside the orbit of a  $^{87}\text{Rb}(24f)$ -Rydberg state. In rubidium and other alkali metals, the f states have a small quantum defect  $\delta_f = 0.01637$  [30].

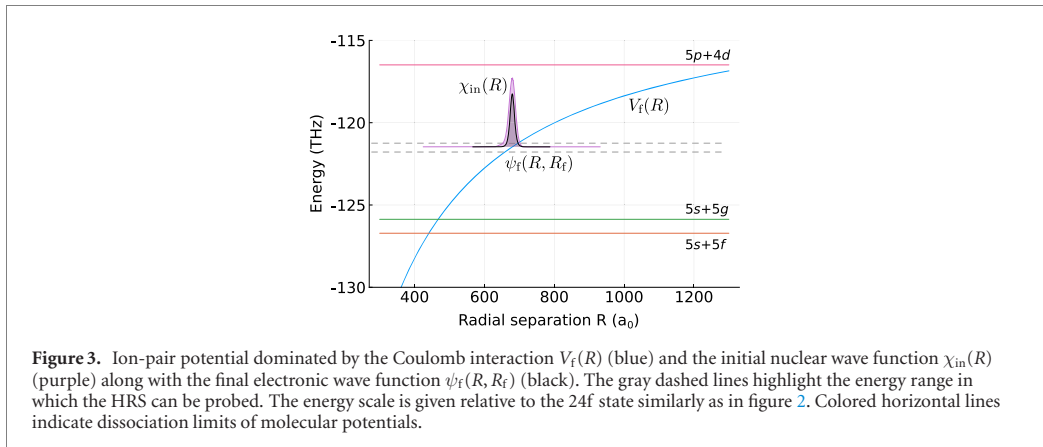
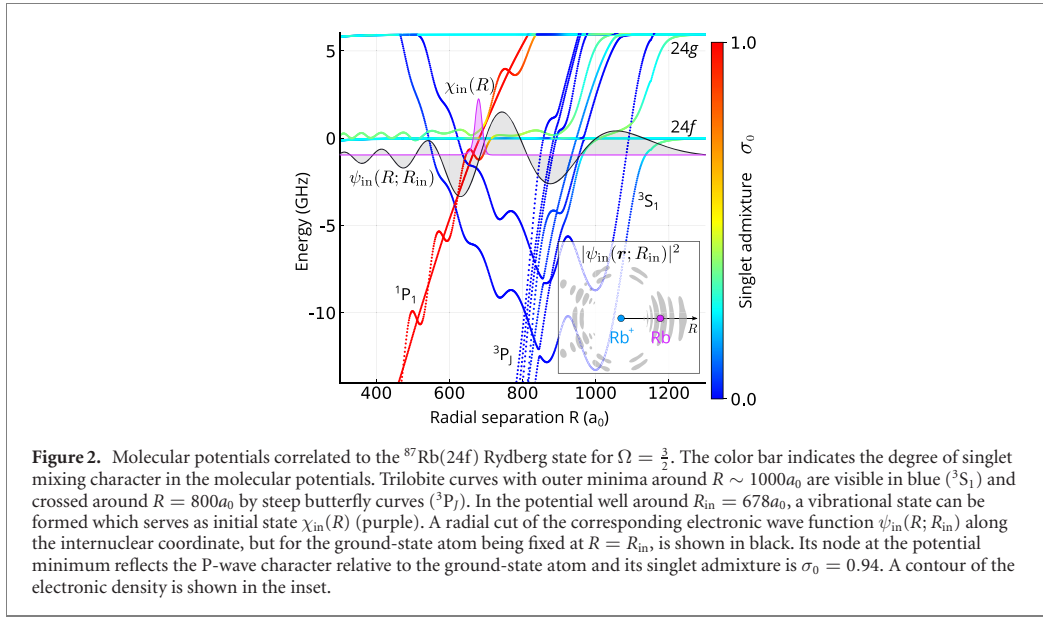
The molecular potentials in the region of the atomic  $n = 24$ -Rydberg state in the  $\Omega = \frac{3}{2}$  molecular symmetry are given in figure 1. At large internuclear distances, the potentials are flat and the energies reflect the atomic Rydberg energies. The multiplets of the quantum defect states arise from the Rydberg fine structure and ground-state hyperfine structure splittings. The zero energy on the vertical axes is set to the asymptotic atomic energy of the  $\text{Rb}(24f_{5/2})$  with the ground-state atom in a hyperfine state  $F = 1$ . The archetypal trilobite [39] and butterfly [28] molecules form potentials which detach from the hydrogenic manifold. Trilobite molecules form due to the attractive S-wave scattering length [13], while butterfly molecules form due to resonant P-wave scattering [26, 27]. In both cases, the corresponding total electronic state of the two participating valence electrons is a triplet state, hence the labeling  $^3S_1$  and  $^3P_J$ , respectively. Additionally, a different potential emerges from the degenerate manifold that corresponds also to the P-wave scattering, but in the electronic singlet channel ( $^1P_1$ ), here highlighted by the red box, and hereafter called the *stairwell* potential. This potential crosses the f electronic state, which in turn can be employed to access the molecular states. The stairwell potential is also present for  $\Omega = \frac{1}{2}$ , while for  $\Omega = \frac{5}{2}$ , only the non-oscillatory potential that does not support bound states remains.

A more detailed presentation of the PECs is shown in figure 2. The singlet character of the potentials is represented in color; red curves have mainly singlet, while blue curves have mainly triplet character. The  $^1P_1$  curve has an avoided crossing with the f state at around  $R = 700 a_0$  below which a potential well is visible. It supports vibrational states, the ground-state of which is visible in figure 2 as the purple curve and is labeled  $\chi_{\text{in}}(R)$ , for it serves as the initial vibrational state for the transition to the HRS. Its mean radial position and the minimum of the potential well lie at  $R_{\text{in}} = 678 a_0$ .

A radial cut of the electronic wave function  $\psi_{\text{in}}(R; R_{\text{in}})$  along the internuclear coordinate  $\mathbf{r} = R\hat{\mathbf{e}}_z$  corresponding to the fixed internuclear distance  $R_{\text{in}}$  is shown to scale as the black curve, for it serves as the initial electronic state for the transition to the HRS. Its P-wave character relative to the ground-state atom is reflected by the node at the potential minimum, where the gradient of the wave function is maximal. Additionally, the inset shows a contour of the full density of the electronic wave function and the nuclear positions therein. Significant electron density is localized in the vicinity of the ground-state atom, which is also visualized by the maximal amplitude of the wave function next to its node at the position of the ground-state atom.

#### 3.2. HRS potential curve

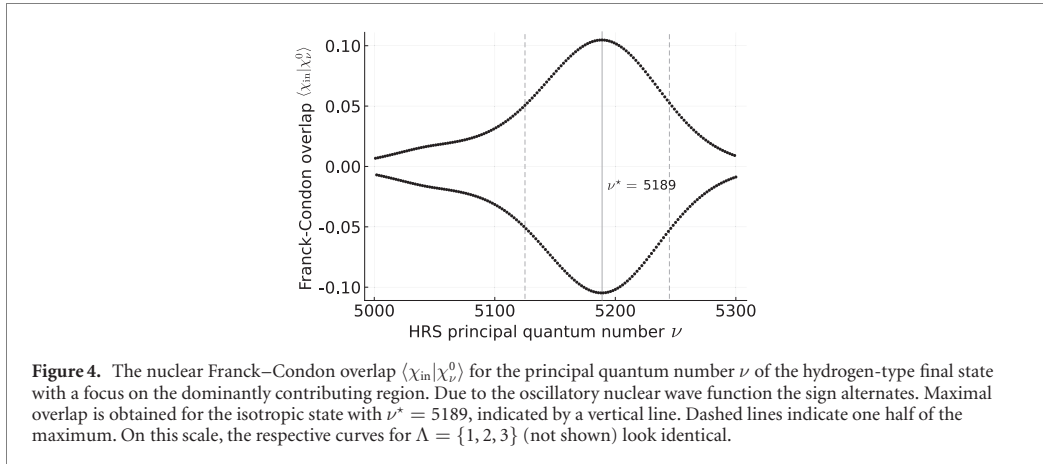
In the HRS, the excited electron is charge transferred to the ground-state atom to form a negative ion, which then interacts with the positive ion, through Coulomb and charge-atom polarization potentials. In



general, this potential is crossed by other molecular PEC corresponding to electronically low-lying excited molecular states in the dissociation limit. For internuclear separations  $R > 30 a_0$  these potentials are flat and lead to narrow avoided crossings with the Coulomb-like potential  $V_f(R)$  [9, 40]. Figure 3 shows the HRS potential  $V_f(R)$  (blue) in the region of interest along with the closest dissociation limits of the  $^{87}\text{Rb}$   $5s + 5f$ ,  $5s + 5g$ , and  $5p + 4d$  states (colored lines). Remote of the crossings, the energy levels of vibrational states in this potential are well described by the Rydberg formula given in equation (1). As a corollary to Coulombic three-body recombination, the mechanism which ‘recombines’ the ions here is called the mutual neutralization.

The anion electronic wave function localizes at the initial position of the ground-state atom  $R_{\text{in}}$ . A radial cut  $\psi_f(R, R_f)$  is shown in figure 3 as black curve while the initial vibrational wave function  $\chi_{\text{in}}(R)$  is shown in purple.

When the ultracold gas is prepared experimentally, we expect it to be homogeneous and isotropic. The electronic Rydberg transition to prepare the initial Rydberg molecule does not alter this isotropic nuclear configuration: due to the absence of external fields, no angular dependence is introduced by the Rydberg molecular potentials and the dimer depends only on the radial internuclear coordinate. The Franck–Condon transition from Rydberg molecule to HRS still maintains the isotropy and consequently only isotropic states  $|\chi_{\nu}^0\rangle$  contribute to the overlaps. From the given initial state  $|\chi_{\text{in}}\rangle$ , the range of available energy levels  $\nu$  is indicated by the gray dashed lines in figure 3 (compare discussion in section 3.3).



At  $R_{\text{in}}$ , where most of the initial gas atoms are found (largest Franck–Condon factor), the electronic dipole transition element is calculated,

$$\langle \psi_f | \hat{\epsilon} \mathbf{r} | \psi_{\text{in}} \rangle = 0.91 a_0, \quad (7)$$

which includes the contribution of the spin-mixing, given as  $\langle S = 0 | \psi_{\text{in}} \rangle = 0.96$ . Here,  $\hat{\epsilon}$  is the direction of the electric field imposed by the laser, linearly polarized parallel to the internuclear axis. This matrix element is sizable and on the order of a typical optical dipole transition, allowing for efficient coupling between the Rydberg molecule and the HRS.

### 3.3. Optimal Franck–Condon factors

Due to the spectroscopically resolvable energetic separation between vibrational levels in the HRS, each vibrational state  $|\chi_{\nu}^0\rangle$  can be addressed individually. Figure 4 shows the distribution of Franck–Condon overlaps  $\langle \chi_{\text{in}} | \chi_{\nu}^0 \rangle$  for a range of HRS principal quantum numbers  $\nu$ . The wave function of the given initial state  $\chi_{\text{in}}(R)$  is shown in figures 2 and 3. The dominant contribution with  $\langle \chi_{\text{in}} | \chi_{\nu^*}^0 \rangle = 0.105$  is achieved for the vibrational level  $\nu^* = 5189$  indicated in figure 4 by the vertical line. The energy difference between the initial and this state is  $E_{\nu^*} - E_{\text{in}} = 121.47$  THz, which translates to a laser wave length of  $\lambda = 2468$  nm in the near infra-red. Here,  $E_{\text{in}}$  is the energy of the Rydberg molecular vibrational ground state in the molecular potential  $V_{\text{in}}(R)$  and  $E_{\nu^*}$  is the energy of the HRS according to equation (1) omitting the quantum defect  $\delta$ . Deviations of this energy allow systematic determination of  $\delta$  for  $\Lambda = 0$ . We focus on levels where the Franck–Condon overlap exceeds half of the maximal value at  $\nu^*$  indicated in figure 4 by the dashed, vertical line. In an energy window of  $\sim 500$  GHz, around  $E_{\nu^*} - E_{\text{in}}$ , there are as many as 100 vibrational HRS states. The spacing between individual levels is approximately 3.6 to 3.9 GHz. For  $\nu^*$ , the binding energy in the ionic potential is 9.68 GHz. If it is possible to excite also rotational states  $\Lambda > 0$  from the ultracold gas, additional Rydberg series corresponding to each  $\Lambda$  will be observed. The distribution of Franck–Condon overlaps for  $\Lambda = \{1, 2, 3\}$  up to seven-digit precision is the same as for  $\Lambda = 0$ , shown in figure 4.

The dipole moment of the HRS can be given analytically  $\langle R \rangle = \langle \chi_{\nu}^{\Lambda} | R | \chi_{\nu}^{\Lambda} \rangle = [3\nu^2 - \Lambda(\Lambda + 1)]/2\mu$  [41] and for  $5120 \lesssim \nu \lesssim 5250$  and  $\Lambda = 0$  this results in  $500 a_0 \lesssim \langle R \rangle \lesssim 520 a_0$ .

In general, also f states with different principal quantum number can be employed as the initial states. We chose the 24f state due to the fact that the potential well in which the molecule forms is energetically close to the asymptotic f-state Rydberg energy, which guarantees sufficient f admixture to spectroscopically address the molecule by a three-photon transition. Additionally, another class of molecules correlated with the Rb(*mp*) Rydberg atoms can also serve as the initial state, the properties of which vary from the presented ones and are discussed in appendix A.

### 3.4. Experimental realization

The experimental generation of an HRS, as outlined above is promising. Both, the excitation of Rydberg f states as well as the coupling of the Rydberg molecule to the HRS can be achieved with the current state-of-the-art laser technology. For rubidium, the photoassociation of the Rydberg molecule requires a three photon scheme, involving, e.g., 776 nm, 780 nm and 1280 nm. All three wavelengths can be realized with tunable diode lasers and an overall three-photon coupling rate in the MHz range can be achieved.

Ultracold temperatures as realized by standard laser cooling and high atomic densities of  $10^{12}\text{cm}^{-3}$  or larger are advisable in order to have a large overlap of the ground state wave function with the Rydberg molecular vibrational wave function.

The second step, the coupling to the HRS, is equally feasible. The transition wavelength of 2468 nm requires either an OPO system or a DFB diode laser. Thereby, a laser power of a few mW is already sufficient: for a beam waist of 1 mm, a power of 1 mW, a Franck–Condon overlap of 0.1 and an electric dipole transition matrix element of  $1 ea_0$ , the Rabi frequency between the Rydberg molecule and the HRS amounts to about 1 MHz. This time scale is much faster than the lifetime of the Rydberg molecule, which is here only limited by the Rydberg atom, such that the branching ratio is favorable toward the production of an HRS.

The generation of an HRS could be done in a pump–probe type of experiment and the HRS could be detected by photodissociation followed by the detection of the negative ion. The latter can be identified by its time of flight to the detector.

#### 4. Conclusion

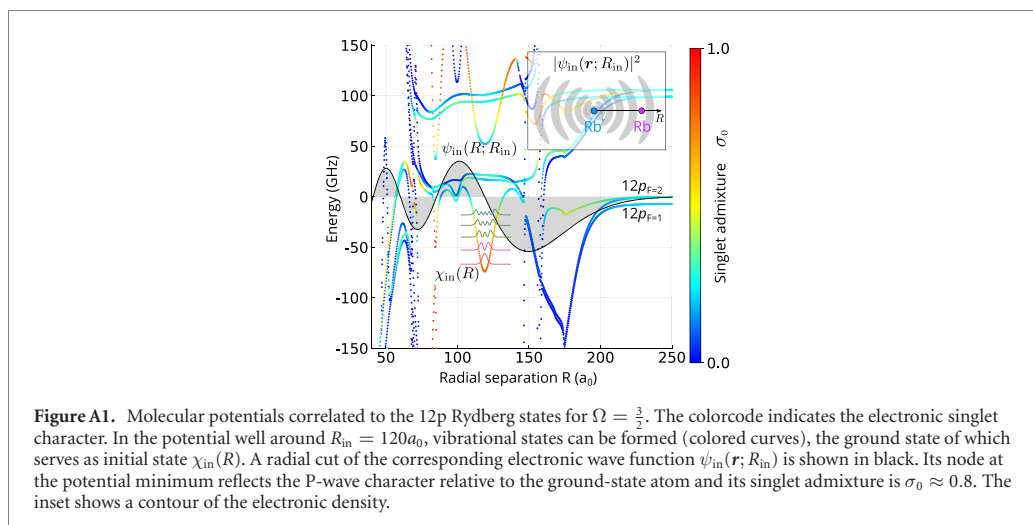
We show that ultra-long-range Rydberg molecules can be used to produce ultracold heavy Rydberg system i.e. a bound anion–cation pair. Due to the large internuclear separations inherent to Rydberg molecules, the resulting HRS can be probed over a wide range of large principal quantum numbers. To our knowledge, HRS have only been produced from tightly bound molecules, in which the Franck–Condon factor strongly constrains possible internuclear separations. In the proposed association scheme, we utilize a molecular potential that has not been studied previously and arises from weakly attractive singlet P-wave scattering. The resulting electronic states, similarly to the trilobite and butterfly states, are superpositions of high angular momentum states and, thus, have large densities in the vicinity of the ground-state atom which largely increases the electronic dipole transition element compared to other choices of initial states. Still, studying the plethora of Rydberg molecule potentials is still far from exhaustive and further efforts would be beneficial in order to explore other choices for the initial state. In this spirit, a recent work [42] has predicted that in cesium also p-state molecules with appropriate butterfly admixture provide a suitable initial state. Creation and study of ultracold HRS will lead to new insights on questions of molecular formation in dilute stellar gases and mutual neutralization processes. Furthermore, HRS serves as the precursor to the creation of equal mass strongly-coupled ultra-cold plasmas.

#### Acknowledgments

PS acknowledges financial support from the Deutsche Forschungsgemeinschaft within the priority program ‘Giant interactions in Rydberg systems’ [DFG SPP 1929 GiRyd project SCHM 885/30-1]. This work was financially supported within the PIER Hamburg-MIT/BOS Seed Projects with the Project ID: PHM-2019-06. FH is grateful to Matthew Eiles and Kevin Keiler for useful comments and enlightening discussions.

#### Appendix A. p-state molecules

In addition to the Rb(24f) Rydberg molecular potential energy stairwell curve for initiating the formation of HRS, we present here another example of an initial state, namely the Rb(12p) Rydberg molecule. The corresponding potentials are far detuned from the hydrogenic manifold (cf figure 1) and the stairwell potential is energetically not available. However, for this relatively low-lying Rydberg state, the semi-classical electron momentum  $k$  varies sufficiently quickly along the internuclear separation, that in the outer region of the electron orbit additionally to S-wave scattering, P-wave channels contribute to the overall shape of the resulting PECs. These potentials can be seen in figure A1. For large internuclear distances, flat curves are visible representing the atomic Rydberg levels occurring with a slight splitting in energies which depends on the hyperfine level of the ground-state atom. For internuclear distances between  $150 a_0 < R < 200 a_0$  the atomic energy is lowered due to the presence of attractive triplet S-wave scattering which reflects the electronic density. The relative depth of different visible curves arises due to varying singlet admixture of the corresponding electronic state, which is indicated by the colorcode. At  $R = 150 a_0$  crossings with steep butterfly curves occur, which are induced by a shape resonance in the P-wave scattering channel [26, 27]. For smaller internuclear distances  $100 a_0 < R < 150 a_0$  a potential well with a high singlet admixture is visible. The electronic wave function  $\psi_{\text{in}}(R; R_{\text{in}})$  corresponding to the minimum of the well at  $R_{\text{in}} = 120 a_0$  with  $\sigma_0 = 0.8$  is visible as black curve in the figure (amplitude in arbitrary units) and serves as initial electronic state for the transition to the HRS. Its P-wave character relative to the ground-state atom is



reflected by the node at the potential minimum, where the gradient of the wave function is maximal. The electron density is shown in the inset and resembles a p state with the ground-state atom trapped between two maxima of the electron density.

The potential well around  $R_{\text{in}}$  supports vibrational states which are visible in figure A1 as colored curves. The vibrational ground state is labeled  $\chi_{\text{in}}(R)$  and serves as initial nuclear state.

Here, due to the smaller internuclear distance the addressable principal quantum numbers of the heavy Rydberg system are around  $\nu^{\ddagger} = 2172$ , however, the laser wave length for the optical transition  $\lambda^{\ddagger} = 2218.5$  nm is slightly larger, since the initial electronic state of the Rydberg molecule is lower in energy. The Franck–Condon overlap is  $\langle \chi_{\text{in}} | \chi_{\nu^{\ddagger}}^0 \rangle = 0.16$  and the energy spacing of the Rydberg series in this region is approximately 50 GHz. The spatial contribution to the electronic transition  $\frac{\langle \psi_{\text{in}} | \hat{\epsilon} r | \psi_{\text{in}} \rangle}{\langle S | \psi_{\text{in}} \rangle}$  is in this case two orders of magnitude smaller than for the 24f state, but still on the same order of magnitude as the Rydberg transition from the ground state to the 12p state.

The spacial contribution of the electronic dipole transition can be increased by going to larger internuclear separations, however this results in a decrease of the spin contribution. For example, in the case of a 16p Rydberg molecule, the spacial contribution doubles, while the spin contribution halves leading to the same transition strength.

## ORCID iDs

P Schmelcher <https://orcid.org/0000-0002-2637-0937>

H Ott <https://orcid.org/0000-0002-3155-2719>

H R Sadeghpour <https://orcid.org/0000-0001-5707-8675>

## References

- [1] Kirrander A, Rittenhouse S, Ascoli M, Eyler E E, Gould P L and Sadeghpour H R 2013 *Phys. Rev. A* **87** 031402(R)
- [2] Reinhold E and Ubachs W 2005 *Mol. Phys.* **103** 1329
- [3] Cornett S T, Sadeghpour H R and Cavagnero M J 1999 *Phys. Rev. Lett.* **82** 2488
- [4] Harada N and Herbst E 2008 *Astrophys. J.* **685** 272–80
- [5] Vieitez M O, Ivanov T I, Reinhold E, de Lange C A and Ubachs W 2008 *Phys. Rev. Lett.* **101** 163001
- [6] Beyer M and Merkt F 2018 *J. Chem. Phys.* **149** 031102
- [7] Ban T, Beuc R, Skenderović H and Pichler G 2004 *Europhys. Lett.* **66** 485–91
- [8] Jungen C and Raoult M 1981 *Faraday Discuss. Chem. Soc.* **71** 253
- [9] Markson S and Sadeghpour H R 2016 *J. Phys. B: At. Mol. Opt. Phys.* **49** 114006
- [10] Launoy T, Loreau J, Dochain A, Liévin J, Vaeck N and Urbain X 2019 *Astrophys. J.* **883** 85
- [11] Walter C W, Gibson N D, Matyas D J, Crocker C, Dungan K A, Matola B R and Rohlén J 2014 *Phys. Rev. Lett.* **113** 063001
- [12] Tang R, Si R, Fei Z, Fu X, Lu Y, Brage T, Liu H, Chen C and Ning C 2019 *Phys. Rev. Lett.* **123** 203002
- [13] Greene C H, Dickinson A S and Sadeghpour H R 2000 *Phys. Rev. Lett.* **85** 2458
- [14] Bendkowsky V, Butscher B, Nipper J, Shaffer J P, Löw R and Pfau T 2009 *Nature* **458** 1005
- [15] Shaffer J P, Rittenhouse S T and Sadeghpour H R 2018 *Nat. Commun.* **9** 1965
- [16] Fey C, Hummel F and Schmelcher P 2019 *Mol. Phys.* **118** e1679401
- [17] Khuskivadze A A, Chibisov M I and Fabrikant I I 2002 *Phys. Rev. A* **66** 042709
- [18] Markson S, Rittenhouse S T, Schmidt R, Shaffer J P and Sadeghpour H R 2016 *ChemPhysChem* **17** 3683

- [19] Eiles M T and Greene C H 2017 *Phys. Rev. A* **95** 042515
- [20] Anderson D A, Miller S A and Raithel G 2014 *Phys. Rev. A* **90** 062518
- [21] Saßmannshausen H, Merkt F and Deiglmayr J 2015 *Phys. Rev. Lett.* **114** 133201
- [22] Böttcher F, Gaj A, Westphal K M, Schlagmüller M, Kleinbach K S, Löw R, Liebsch T, Pfau T and Hofferberth S 2016 *Phys. Rev. A* **93** 032512
- [23] MacLennan J L, Chen Y J and Raithel G 2019 *Phys. Rev. A* **99** 033407
- [24] Engel F, Dieterle T, Hummel F, Fey C, Schmelcher P, Löw R, Pfau T and Meinert F 2019 *Phys. Rev. Lett.* **123** 073003
- [25] Deiß M, Haze S, Wolf J, Wang L, Meinert F, Fey C, Hummel F, Schmelcher P and Denschlag J H 2019 arXiv:1901.08792
- [26] Chibisov M I, Khuskivadze A A and Fabrikant I I 2002 *J. Phys. B: At. Mol. Opt. Phys.* **35** L193
- [27] Hamilton E L, Greene C H and Sadeghpour H R 2002 *J. Phys. B: At. Mol. Opt. Phys.* **35** L199
- [28] Niederprüm T, Thomas O, Eichert T, Lippe C, Pérez-Ríos J, Greene C H and Ott H 2016 *Nat. Commun.* **7** 12820
- [29] Li W, Mourachko I, Noel M W and Gallagher T F 2003 *Phys. Rev. A* **67** 052502
- [30] Han J, Jamil Y, Norum D V L, Tanner P J and Gallagher T F 2006 *Phys. Rev. A* **74** 054502
- [31] Arimondo E, Inguscio M and Violino P 1977 *Rev. Mod. Phys.* **49** 31
- [32] Mitroy J, Safranov M S and Clark C W 2010 *J. Phys. B: At. Mol. Opt. Phys.* **43** 202001
- [33] Fermi E 1934 *Il Nuovo Cimento* **11** 157
- [34] Omont A 1977 *J. Physique* **38** 1343
- [35] Fey C, Kurz M, Schmelcher P, Rittenhouse S T and Sadeghpour H R 2015 *New J. Phys.* **17** 055010
- [36] Frey P, Breyer F and Hotop H 1978 *J. Phys. B: At. Mol. Phys.* **11** L589
- [37] Fabrikant I I 1993 *J. Phys. B: At. Mol. Opt. Phys.* **26** 2533
- [38] Eckart C 1930 *Phys. Rev.* **35** 1303
- [39] Booth D, Rittenhouse S T, Yang J, Sadeghpour H R and Shaffer J P 2015 *Science* **348** 99
- [40] Park S J, Suh S W, Lee Y S and Jeung G H 2001 *J. Mol. Spectrosc.* **207** 129
- [41] Bethe H A and Salpeter E E 1957 *Quantum Mechanics of One- and Two-Electron Atoms* (Berlin: Springer)
- [42] Peper M and Deiglmayr J 2020 *J. Phys. B: At. Mol. Opt. Phys.* **53** 064001

### 3.6 Synthetic dimension-induced conical intersections in Rydberg molecules

## Synthetic Dimension-Induced Conical Intersections in Rydberg Molecules

Frederic Hummel<sup>1,\*</sup>, Matthew T. Eiles<sup>2</sup>, and Peter Schmelcher<sup>1,3</sup>

<sup>1</sup>Zentrum für Optische Quantentechnologien, Fachbereich Physik, Universität Hamburg,  
Luruper Chaussee 149, 22761 Hamburg, Germany

<sup>2</sup>Max-Planck-Institut für Physik komplexer Systeme, Nöthnitzer Straße 38, 01187 Dresden, Germany

<sup>3</sup>The Hamburg Centre for Ultrafast Imaging, Universität Hamburg, Luruper Chaussee 149, 22761 Hamburg, Germany



(Received 5 February 2021; accepted 9 June 2021; published 9 July 2021)

We observe a series of conical intersections in the potential energy curves governing both the collision between a Rydberg atom and a ground-state atom and the structure of Rydberg molecules. By employing the electronic energy of the Rydberg atom as a synthetic dimension we circumvent the von Neumann–Wigner theorem. These conical intersections can occur when the Rydberg atom’s quantum defect is similar in size to the electron–ground-state atom scattering phase shift divided by  $\pi$ , a condition satisfied in several commonly studied atomic species. The conical intersections have an observable consequence in the rate of ultracold  $l$ -changing collisions of the type  $\text{Rb}(nf) + \text{Rb}(5s) \rightarrow \text{Rb}(nl > 3) + \text{Rb}(5s)$ . In the vicinity of a conical intersection, this rate is strongly suppressed, and the Rydberg atom becomes nearly transparent to the ground-state atom.

DOI: 10.1103/PhysRevLett.127.023003

The Born-Oppenheimer approximation is a cornerstone of chemical and molecular physics. It provides us with the adiabatic separation of the fast electronic from the slow vibrational motion, resulting in adiabatic potential energy surfaces (PES) determined by the electronic structure for a given nuclear geometry [1]. When PES become degenerate at a conical intersection (CI), nonadiabatic interaction effects are important and the Born-Oppenheimer-based intuition developed in molecular physics breaks down [2–4]. CI occur frequently in larger molecules with many vibrational degrees of freedom, for example in the nucleobases [5], and play a key role in photosynthesis [6]. CI are responsible for ultrafast radiationless decay mechanisms on the femtosecond time scale [2,7,8]. A controlled environment to study CI can be provided by external optical fields [9,10] or by ultracold interacting Rydberg systems [11,12]. Diatomic molecules provide here an exception. Generally, the von Neumann–Wigner noncrossing theorem forbids the crossing of potential energy curves (PEC) in diatomic systems, which are determined by a single vibrational parameter, the internuclear coordinate  $R$  [13,14].

Excited electronic states are key players in the appearance of CI. A particular, highly excited, diatomic system, the collisional complex consisting of a Rydberg atom and a ground-state atom, has attracted significant interest since nearly the advent of quantum physics [15–19]. The interaction between these two atoms, as described by the Fermi pseudopotential, is primarily determined by the  $s$ -wave electron-atom scattering phase shift  $\delta_s$  [15,16]. The resulting Born-Oppenheimer PEC can be labeled by the principal quantum number  $n$  and angular momentum quantum number  $l$  of the Rydberg atom. These PEC can be

sufficiently attractive to support bound states, known as ultra-long-range Rydberg molecules [20–23]. At positive energies, they are responsible for the collisional dynamics between the two highly asymmetrically excited atomic partners. Just as the characteristics of a Rydberg atom are smoothly varying polynomial functions of  $n$ , so too are the typical molecular properties, for example the potential depths, dipole moments, and bond lengths.

For this reason, it is illustrative to imagine that this diatomic system evolves along a two-dimensional potential energy *surface*, where the principal quantum number  $n$  plays the role of an additional *synthetic* dimension. In many other contexts, the introduction of synthetic dimensions provides a means to control the dimensionality of a system by mimicking additional degrees of freedom. Synthetic dimensions have been realized in optical lattices [24,25], and have applications in the study of gauge fields [26], quantum simulation [27], and photonics [28].

In the present work, we utilize the synthetic dimension  $n$  to circumvent the noncrossing theorem, and in doing so, we show that CI can appear in the Rydberg–ground-state atom PES. These CI occur when the Rydberg atom is initially in a state  $|nl_0\rangle$  whose fractional quantum defect  $\mu_{l_0}$  is similar in size to  $\delta_s/\pi$ , which is typically satisfied in states with higher than  $d$ -wave angular momentum  $l_0$ . We highlight results for Rb, where  $l_0 = 3$ , since interest in such a state has recently grown due to its importance for the preparation of circular Rydberg states in the scope of quantum simulation and quantum computing based on neutral-atom platforms [29–32].

Similar to how CI in more traditional molecular systems provide fast radiationless decays between electronic states,

the synthetic CI can facilitate fast dynamics in Rydberg-ground-state atom collisions. In particular, we demonstrate that they dramatically suppress the  $l$ -changing collision rate, which is otherwise a dominant process in this collision. This provides a clear experimental observable, heralding the presence of synthetic CI in several different atomic species.

The interaction between the two atoms is given by Fermi's pseudopotential,

$$V(\mathbf{r}, \mathbf{R}) = 2\pi a(k)\delta^3(\mathbf{r} - \mathbf{R}), \quad (1)$$

where  $a(k) = -\tan \delta_s(k)/k = a(0) + \pi\alpha k/3$  is the low-energy  $s$ -wave scattering length,  $\alpha$  is the ground-state atom's polarizability, and the wave number  $k$  is determined semiclassically by  $k^2/2 - 1/R = -1/2n^2$ . Higher partial waves can be neglected because the electron energy is close to zero at the large internuclear distances considered here. Since  $V(\mathbf{r}, \mathbf{R})$  is a weak perturbation to the Coulomb potential, we calculate the PEC by diagonalizing  $V(\mathbf{r}, \mathbf{R})$  within a restricted basis. This includes only the initial state  $|nl_0\rangle$ , whose energy we take as the reference energy, and the degenerate manifold of hydrogenic  $l > l_0$  states with vanishingly small quantum defects. These are blue detuned by a shift  $\Delta$  from the initial state. The  $l < l_0$  states can be ignored since they are far detuned,  $\Delta_{l < l_0} \gg \Delta$ , and states with  $l > l_0$  have very small detunings relative to  $\Delta$ , and can be subsumed into the degenerate manifold.

Two adiabatic PEC result from this diagonalization,

$$V_{\pm}(n, R) = \frac{1}{2} \left[ q + t + \Delta \pm \sqrt{(q + t + \Delta)^2 - 4q\Delta} \right], \quad (2)$$

where

$$q(n, R) = a(k) \frac{2l_0 + 1}{2} \frac{u_{nl_0}^2(R)}{R^2}, \quad (3a)$$

$$t(n, R) = a(k) \sum_{l=l_0+1}^{n-1} \frac{2l + 1}{2} \frac{u_{nl}^2(R)}{R^2}, \quad (3b)$$

and the hydrogen atom's radial wave functions are  $u_{nl}(r)$ . We have confirmed the accuracy of the PEC quantitatively with large-scale diagonalizations involving many more Rydberg states [20,33]. Alternatively, Green's function methods [34–36] or local frame transformation techniques [37] may be employed.

The PEC are shown in Fig. 1(a) using scaled distances and energies for several principle quantum numbers  $n \in \{40, 50, 60, 70\}$ . They represent the key ingredient for the investigation of the collisional dynamics between the Rydberg atom  $|nl_0\rangle$  and a ground-state atom, which is initialized at large  $R$  with the ground-state atom propagating freely with velocity  $v$  along the asymptotically flat potential  $V_-$ . The degenerate manifold is strongly

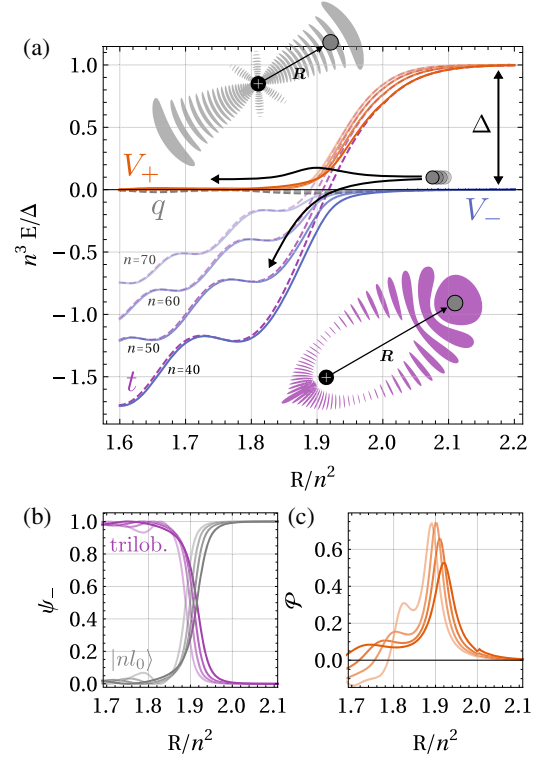


FIG. 1. (a) Illustration of the atomic collision and the corresponding adiabatic (solid, red  $V_+$ , and blue  $V_-$ ) and diabatic (dashed, purple  $t$ , and gray  $q$ ) PEC for different principle quantum numbers  $n \in \{40, 50, 60, 70\}$  (increasing  $n$  is plotted with increasing opacity). At large internuclear distances, the difference of the potentials  $\Delta$  is determined by the quantum defect of the state with angular momentum  $l_0$ . The axes are rescaled in order to shift the curves onto the same energy scale. A semiclassical ground-state atom propagating on  $V_-$  can either adiabatically follow the potential and pick up orbital angular momentum to form a trilobite state, the electronic density of which is shown at the bottom, or hop to the potential  $V_+$  and continue with an  $f$ -state electronic orbital depicted at the top. (b) The eigenvector components  $\psi_-$  corresponding to  $V_-$  and (c) the nonadiabatic coupling matrix element  $\mathcal{P}$  with varying (scaled)  $R$  for different  $n$ .

perturbed by the ground-state atom, causing an attractive potential  $V_+$  to descend. At large  $R$ , its adiabatic electronic state  $\psi_+$  is a superposition of high- $l$  states known colloquially as the *trilobite* state (see inset wave function). Level repulsion induces an avoided crossing at  $R = R_0 \approx 1.9n^2$ , and as a result  $V_-$  sharply bends away.

From this picture, we see that, if the collision is purely adiabatic, the Rydberg atom's electronic state will change from its original electronic state (see upper inset) into the trilobite state (see lower inset) as the ground-state atom drops into the attractive potential of  $V_-$ . This is illustrated in Fig. 1(b), which shows how the trilobite- and  $|nl_0\rangle$ -state components of the corresponding adiabatic state  $\psi_-$  reverse

after the crossing is traversed. This has observable consequences, as it induces an  $l$ -changing collision at a rate  $\gamma = \sigma\rho v$ , where  $\sigma$  is the collisional cross section and  $\rho$  the density of ground-state atoms [38,39]. Since the Rydberg state changes character nearly at the outer turning point of the Rydberg orbit due to the steep potential curve arising from the strong perturbation of the degenerate manifold, we take  $\sigma = \pi R_0^2$ . This purely adiabatic rate  $\gamma$  holds unless the velocity or the nonadiabatic coupling are large enough for a nonadiabatic transition to occur, in which case the ground-state atom hops across onto  $V_+$ , preserving the electronic character of the Rydberg atom which continues through diabatically. In particular, at a CI, where  $V_{\pm}$  become degenerate, the nonadiabatic couplings diverge.

We search for CI in the PES, functions of both the real adiabatic parameter  $R$  and the synthetic parameter  $n$ , by employing the closed-form summation of  $t(R)$  [23,34], and then allowing  $n$  to become a continuous variable by replacing the hydrogenic radial wave functions with Whittaker Coulomb functions valid for noninteger  $n$ . Figure 2 shows these potential surfaces over a range of  $n$ . In this region, the potentials are smoothly oscillatory functions of  $R$  and  $n$ , but CI appear near the  $n$  values  $n_1 = 79$ ,  $n_2 = 99$ , and  $n_3 = 111$ . Here, we must include the effects of nonadiabatic coupling and interactions.

In a beyond Born-Oppenheimer treatment, the nonadiabatic effects are manifested in the vibrational Schrödinger equation as derivative coupling elements of first and second degree. For the electronic two-state problem, an analytical unitary transformation  $U(n)$  exists such that the derivative terms are eliminated.  $U$  represents a

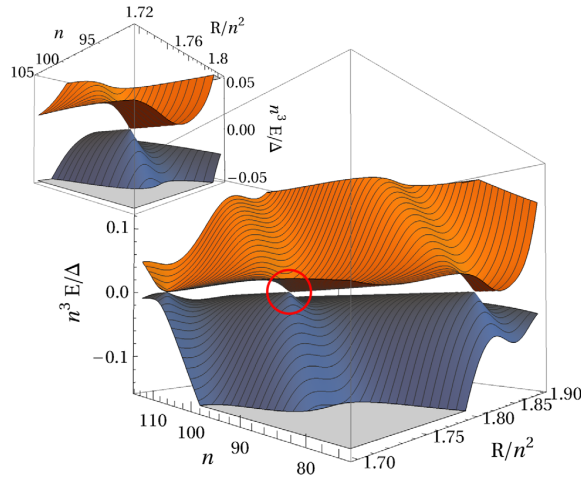


FIG. 2. The adiabatic potential energy surfaces, for which the principle quantum number  $n$  of the Rydberg atom serves as a synthetic parameter and dimension and the internuclear distance  $R$  as the conventional parameter. Conical intersections occur at  $n_1 = 79$ ,  $n_2 = 99$ , and  $n_3 = 111$ , where the potentials become degenerate. Each mesh line corresponds to an integer  $n$ . The inset shows an enlargement of the region in the vicinity of  $n_2$ .

rotation about the angle  $\varphi(n, R) = \int_R^{\infty} dR' \mathcal{P}(n, R')$ , where the nonadiabatic derivative coupling matrix element  $\mathcal{P}(n, R) = \langle \psi_+ | \nabla_R \psi_- \rangle$  quantifies the coupling between the adiabatic states.  $\nabla_R$  represents the gradient operator with respect to  $R$ . Applying this transformation results in a nondiagonal potential in the diabatic representation [2],

$$V_{\text{diabatic}}(n, R) = \begin{pmatrix} q & \sqrt{qt} \\ \sqrt{qt} & t + \Delta \end{pmatrix}. \quad (4)$$

The diabatic PEC  $q$  and  $t + \Delta$  are shown as dashed curves in Fig. 1(a). The position  $R_0$  of the avoided crossing of the adiabatic potentials is characterized by a local maximum of  $\mathcal{P}$ , which is illustrated in Fig. 1(c). It typically coincides with a crossing of the diabatic PEC, which occurs at a position  $R_0$  obtained from  $d(n, R_0) = 2\sqrt{qt}$ , where  $d(n, R) = |V_+ - V_-|$  is the energy gap between the adiabatic potentials. From the diabatic representation, the positions of CI can be obtained easily as the  $(n, R)$  values where the off-diagonal coupling vanishes and the diagonal elements become degenerate. This is possible due to the oscillatory character of the potentials, since  $q$  vanishes at a node of the  $|nl_0\rangle$  wave function. If, simultaneously,  $t = -\Delta$ , then the gap vanishes  $\lim_{R_0 \rightarrow R_i} d(n_i, R) = 0$ , and the derivative coupling diverges  $\lim_{R_0 \rightarrow R_i} \mathcal{P}(n_i, R) = \infty$ . This is characteristic for a CI [3]. Here, the Born-Oppenheimer approximation clearly breaks down. With the aid of the principle quantum number  $n$ , we can tune  $q$  and  $t$  such that a CI can be realized.

We account for the probability of a nonadiabatic transition between the adiabatic potential surfaces at the avoided crossing via the semiclassical hopping probability [40],

$$P(n, v) = \exp\left(\frac{-\pi d(n, R_0)}{4v|\mathcal{P}(n, R_0)|}\right). \quad (5)$$

The  $l$ -changing rate can now be extended to account for this nonadiabatic process,

$$\gamma(n, v) = \pi R_0^2 \rho v [1 - P(n, v)]. \quad (6)$$

At the CI,  $P(n_i, v) = 1$  and the analog of radiationless transitions in polyatomic molecular systems occurs. Here, the Rydberg atom becomes *transparent* to the colliding ground-state atom.

Figure 3 shows the rate of  $l$ -changing collisions of Rydberg  $f$  states as a function of  $n$  and across four decades of temperatures for both rubidium (a) and cesium (b) gases. The density,  $\rho = 1.95 \times 10^{12} \text{ cm}^{-3}$ , is typical for ultracold atomic clouds. The temperature determines the mean relative velocity of two atoms of the ensemble via  $v = \sqrt{6k_B T/M}$ , where  $k_B$  is the Boltzmann constant and  $M$  is the atomic mass. We focus first on the regime where no CI are found in the PES, namely  $n < 75$  in Rb

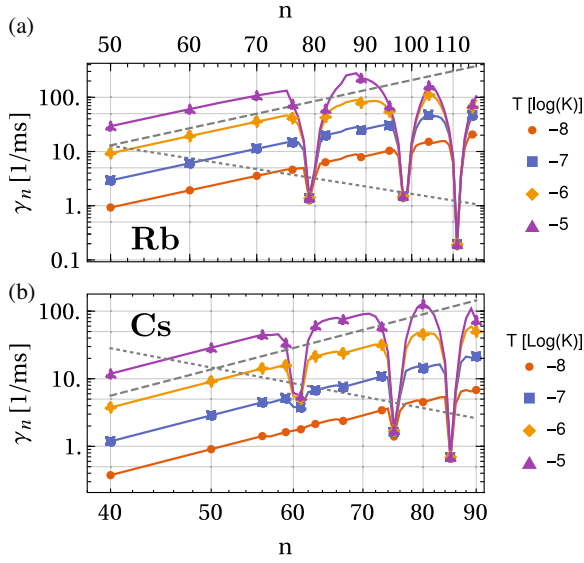


FIG. 3. The rate of  $l$ -changing collisions of Rydberg  $f$  states in (a) rubidium or (b) cesium gas, each with density  $\rho = 1.95 \times 10^{12} \text{ cm}^{-3}$  for different temperatures from 10 nK (circles) to 10  $\mu\text{K}$  (triangles). The dashed, gray line shows the asymptotic behavior of the rates, proportional to  $n^4$ , while the dotted, gray line shows the radiative decay rate. Very rapid variations in the rate as a function of  $n$  occur in rubidium (a) at  $n_1 = 79$ ,  $n_2 = 99$ , and  $n_3 = 111$ , where the rate decreases drastically and becomes independent of temperature and in cesium (b) at  $n_1 = 61$ ,  $n_2 = 75$ , and  $n_3 = 85$ .

and  $n < 40$  in Cs. Here, the splitting of the adiabatic functions scales as the difference in energy between the potential  $V_-$  and the detuning  $\Delta$ , satisfying  $d(n, R_0) \sim n^{-4}$ . Since no CI are present to induce rapid variation in the derivative coupling, it remains approximately constant as a function of  $n$ ,  $\mathcal{P}(n, R_0) \sim p$  [compare Fig. 1(c)]. For low temperatures, the hopping probability is heavily suppressed,  $P(n, v) \rightarrow 0$ , since  $(vn^4p)^{-1}$  is large. In this limit, we obtain the adiabatic rate, proportional to the geometric cross section of the Rydberg atom  $\sim n^4$ , while at high temperatures,  $(vn^4p)^{-1}$  is small. Taking the first order expression for  $P(n, v)$  in this limit, we find that the rate becomes independent of  $n$  and  $v$ . We note that in this high temperature limit, our approach fails to account for many other physical processes which contribute to  $l$  mixing and are not included in our two-level approximation, such as the effect of the ion-atom polarization potential, molecular ion formation, and  $n$ -changing collisions. More comprehensive studies applicable to this thermal limit can be found in Refs. [16,17,19,41]. At larger  $n$  values, this same behavior continues except for the notable exceptions around specific  $n$  values, where the rate drops drastically and becomes nearly independent of the temperature. These are the points of collisional transparency induced by the synthetic conical intersections, where  $l$ -changing processes are strongly

TABLE I. Table of alkaline atomic species and the occurrence of collisional transparency at the lowest few principle quantum numbers  $n_i$  depending on the quantum defect  $\mu_{l_0}$  [45–48], the zero-energy scattering length  $a(0)$  [49–52], and the atomic polarizability  $\alpha$  [53–56].

Species	$l_0$	$\mu_{l_0}$	$a(0)$	$\alpha$	$n_i$
Li	2	0.002 129	-6.7	164.2	$\sim 200$
Na	2	0.015 543	-5.9	162.7	31, 38, 44
K	3	0.010 098	-15	290.6	116, 144
Rb	3	0.016 5192	-15.2	319.2	79, 99, 111
Cs	0	4.049 425	-21.8	401	43, 54, 61, 67
Cs	3	0.033 392	-21.8	401	61, 75, 85

suppressed. Measurements of the  $l$ -changing collision rate are routinely taken, typically via field ionization schemes, and should be capable of directly probing these features. At a CI the  $l$ -changing rate we describe here becomes slow enough that other decay processes, such as  $l$ -changing due to ion-atom collisions at small  $R$  values, collisions between multiple atoms, and radiative decay will become the dominant processes [21,39,42,43]. A more complete picture of the decay of the Rydberg state must take these processes into account alongside the rate we calculate here.

The points of collisional transparency are relevant for the preparation of circular Rydberg states, where the  $f$  state provides the starting point for microwave sweeps to reach  $l = n - 1$ . Its stability over the time span required for the adiabatic passage into circular states is therefore vital [44]. Experimental schemes attempting to build applications on these high- $l$  Rydberg states, must either be performed at low densities or very low temperatures to avoid rapid decay of the  $l_0$  state into higher- $l$  components. Apart from their fundamental interest, this gives the CI-induced collisional transparencies a crucial application since they suppress this rate over a wide range of temperatures and densities.

In Table I, we present estimates for the occurrence of synthetic CI in the alkaline atomic species. In each species, a low- $l$  state with angular momentum  $l_0$  is selected such that its quantum defect  $\mu_{l_0}$  comes closest to satisfying  $\delta_s/\pi$ . Note that two such states can satisfy this condition in Cs. Depending furthermore on the zero-energy scattering length  $a(0)$  and the polarizability  $\alpha$ , we can predict the principle quantum numbers  $n_i$  at which the corresponding collisional transparency is achieved. At large  $n > 70$ , the effect of collisional transparency tends to be more pronounced in the sense that sub- $\mu\text{K}$  temperatures are affected. As the electronic density of states increases with  $n$ , it is more likely that the synthetic CI, occurring in continuous  $n$  space, occur at nearly integer values of  $n$ . At low  $n$ , this is a matter of chance. However, by selecting appropriate fine and hyperfine structure states (which are not accounted for in our analysis), one may further tune the quantum defect to achieve a stronger effect.

In conclusion, we investigate low-temperature  $l$ -changing collisions of ground-state atoms with Rydberg atoms based on the analysis of the adiabatic Born-Oppenheimer PES underlying this process. These collisions modify the lifetime of Rydberg states, and along with the associated cross sections, provide avenues to probe fundamental atomic properties [38,57–59]. Emerging from the oscillatory character of both these PES and the corresponding nonadiabatic coupling elements, we find that certain principle quantum numbers  $n_i$  exist where the  $l$ -changing rate is strongly suppressed, independently of temperature, leading to collisional transparency. This process can be explained by the existence of hidden conical intersections occurring in the vibrational coordinate  $R$  and the synthetic dimension  $n$ . This unconventional mechanism for the occurrence of CI in a diatomic setup provides a unique environment for tests of fundamental quantum processes such as vibronic couplings, radiationless decay, and geometric phases, with applications in Rydberg quantum chemistry. Furthermore, our results provide immediate opportunities for the control of lifetimes of low- $l$  Rydberg states as well as means to circumvent unintended limitations in the preparation of these states and of circular Rydberg states. The collisional transparency allows also for precision measurements of quantum defects and low-energy  $s$ -wave scattering lengths of the underlying electron-atom interaction, because the positions of conical intersections at specific  $n_i$  depend sensitively on these parameters. Although we have focused on the effect of the conical intersections on collisions between Rydberg and ground-state atoms, they will also be present in the potential energy surfaces governing Rydberg molecule–ground-state atom collisions and will play a role in the autoionization of Rydberg molecules for vibrational states prepared in potential wells affected by these CI. Their implications for molecular decay will therefore be interesting to study in future work.

The authors gratefully acknowledge valuable discussions about the applicability of our results in the scope of high- $l$ -state production with Tilman Pfau, Florian Meinert, Thomas Dieterle, and Christian Hölzl. The authors are indebted to Panos Giannakeas for valuable discussions. M. E. acknowledges partial support from the Alexander von Humboldt Stiftung. P. S. acknowledges support from the German Research Foundation (DFG) within the priority program “Giant Interactions in Rydberg Systems” [DFG SPP 1929 GiRyd project SCHM 885/30-1].

\*frederic.hummel@physnet.uni-hamburg.de

- [1] M. Born and R. Oppenheimer, *Ann. Phys. (Leipzig)* **389**, 457 (1927).
- [2] H. Köppel, W. Domcke, and L. S. Cederbaum, Multimode molecular dynamics beyond the Born-Oppenheimer approximation, in *Advances in Chemical Physics* (John Wiley & Sons, Ltd., New York, 1984), pp. 59–246.
- [3] G. A. Worth and L. S. Cederbaum, *Annu. Rev. Phys. Chem.* **55**, 127 (2004).
- [4] G. A. Worth, H.-D. Meyer, H. Köppel, L. S. Cederbaum, and I. Burghardt, *Int. Rev. Phys. Chem.* **27**, 569 (2008).
- [5] M. Barbatti, A. J. A. Aquino, J. J. Szymczak, D. Nachtigallová, P. Hobza, and H. Lischka, *Proc. Natl. Acad. Sci. U.S.A.* **107**, 21453 (2010).
- [6] L. Hammarström and S. Styring, *Phil. Trans. R. Soc. B* **363**, 1283 (2008).
- [7] C. Arnold, O. Vendrell, R. Welsch, and R. Santra, *Phys. Rev. Lett.* **120**, 123001 (2018).
- [8] N. Mabrouk, W. Zrafi, and H. Berriche, *Mol. Phys.* **118**, e1605098 (2020).
- [9] N. Moiseyev, M. Šindelka, and L. S. Cederbaum, *J. Phys. B* **41**, 221001 (2008).
- [10] M. Šindelka, N. Moiseyev, and L. S. Cederbaum, *J. Phys. B* **44**, 045603 (2011).
- [11] S. Wüster, A. Eisfeld, and J. M. Rost, *Phys. Rev. Lett.* **106**, 153002 (2011).
- [12] F. M. Gambetta, C. Zhang, M. Hennrich, I. Lesanovsky, and W. Li, *Phys. Rev. Lett.* **126**, 233404 (2021).
- [13] J. von Neumann and E. P. Wigner, *Phys. Z.* **30**, 467 (1929).
- [14] E. Teller, *J. Phys. Chem.* **41**, 109 (1937).
- [15] E. Fermi, *Nuovo Cim.* **11**, 157 (1934).
- [16] A. Omont, *J. Phys. France* **38**, 1343 (1977).
- [17] A. P. Hickman, *Phys. Rev. A* **19**, 994 (1979).
- [18] T. F. Gallagher, *Rep. Prog. Phys.* **51**, 143 (1988).
- [19] V. S. Lebedev and I. I. Fabrikant, *Phys. Rev. A* **54**, 2888 (1996).
- [20] C. H. Greene, A. S. Dickinson, and H. R. Sadeghpour, *Phys. Rev. Lett.* **85**, 2458 (2000).
- [21] V. Bendkowsky, B. Butscher, J. Nipper, J. P. Shaffer, R. Löw, and T. Pfau, *Nature (London)* **458**, 1005 (2009).
- [22] C. Fey, F. Hummel, and P. Schmelcher, *Mol. Phys.* **118**, e1679401 (2020).
- [23] M. T. Eiles, *J. Phys. B* **52**, 113001 (2019).
- [24] L. Levi, M. Rechtsman, B. Freedman, T. Schwartz, O. Manela, and M. Segev, *Science* **332**, 1541 (2011).
- [25] S. Kolkowitz, S. L. Bromley, T. Bothwell, M. L. Wall, G. E. Marti, A. P. Koller, X. Zhang, M. Rey, and J. Ye, *Nature (London)* **542**, 66 (2017).
- [26] A. Celi, P. Massignan, J. Ruseckas, N. Goldman, I. B. Spielman, G. Juzeliūnas, and M. Lewenstein, *Phys. Rev. Lett.* **112**, 043001 (2014).
- [27] O. Boada, A. Celi, J. I. Latorre, and M. Lewenstein, *Phys. Rev. Lett.* **108**, 133001 (2012).
- [28] T. Ozawa, H. M. Price, A. Amo, N. Goldman, M. Hafezi, L. Lu, M. C. Rechtsman, D. Schuster, J. Simon, O. Zilberberg, and I. Carusotto, *Rev. Mod. Phys.* **91**, 015006 (2019).
- [29] D. A. Anderson, A. Schwarzkopf, R. E. Sapiro, and G. Raithe, *Phys. Rev. A* **88**, 031401(R) (2013).
- [30] T. L. Nguyen, J. M. Raimond, C. Sayrin, R. Cortiñas, T. Cantat-Moltrecht, F. Assemat, I. Dotsenko, S. Gleyzes, S. Haroche, G. Roux, T. Jolicoeur, and M. Brune, *Phys. Rev. X* **8**, 011032 (2018).
- [31] R. G. Cortiñas, M. Favier, B. Ravon, P. Méhaignerie, Y. Machu, J. M. Raimond, C. Sayrin, and M. Brune, *Phys. Rev. Lett.* **124**, 123201 (2020).

PHYSICAL REVIEW LETTERS **127**, 023003 (2021)

- [32] T. Cantat-Moltrecht, R. Cortiñas, B. Ravon, P. Méhaignerie, S. Haroche, J. M. Raimond, M. Favier, M. Brune, and C. Sayrin, *Phys. Rev. Research* **2**, 022032(R) (2020).
- [33] E. L. Hamilton, C. H. Greene, and H. R. Sadeghpour, *J. Phys. B* **35**, L199 (2002).
- [34] M. I. Chibisov, A. A. Khuskivadze, and I. I. Fabrikant, *J. Phys. B* **35**, L193 (2002).
- [35] A. A. Khuskivadze, M. I. Chibisov, and I. I. Fabrikant, *Phys. Rev. A* **66**, 042709 (2002).
- [36] C. H. Greene, E. L. Hamilton, H. Crowell, C. Vadla, and K. Niemax, *Phys. Rev. Lett.* **97**, 233002 (2006).
- [37] P. Giannakeas, M. T. Eiles, F. Robicheaux, and J. M. Rost, *Phys. Rev. A* **102**, 033315 (2020).
- [38] T. Niederprüm, O. Thomas, T. Manthey, T. M. Weber, and H. Ott, *Phys. Rev. Lett.* **115**, 013003 (2015).
- [39] T. F. Gallagher, *Rydberg Atoms*, Cambridge Monographs on Atomic, Molecular and Chemical Physics (Cambridge University Press, Cambridge, England, 1994).
- [40] C. W. Clark, *Phys. Lett.* **70A**, 295 (1979).
- [41] I. I. Fabrikant, *J. Phys. B* **19**, 1527 (1986).
- [42] M. Schlagmüller, T. C. Liebisch, H. Nguyen, G. Lohead, F. Engel, F. Böttcher, K. M. Westphal, K. S. Kleinbach, R. Löw, S. Hofferberth, T. Pfau, J. Pérez-Ríos, and C. H. Greene, *Phys. Rev. Lett.* **116**, 053001 (2016).
- [43] F. Camargo, J. D. Whalen, R. Ding, H. R. Sadeghpour, S. Yoshida, J. Burgdörfer, F. B. Dunning, and T. C. Killian, *Phys. Rev. A* **93**, 022702 (2016).
- [44] C. Hölzl, Towards high  $n$  circular Rydberg states in ultracold atomic gases, Master's thesis, Universität Stuttgart, 2019.
- [45] C.-J. Lorenzen and K. Niemax, *Phys. Scr.* **27**, 300 (1983).
- [46] J. Han, Y. Jamil, D. V. L. Norum, P. J. Tanner, and T. F. Gallagher, *Phys. Rev. A* **74**, 054502 (2006).
- [47] P. Goy, J. M. Raimond, G. Vitrant, and S. Haroche, *Phys. Rev. A* **26**, 2733 (1982).
- [48] K.-H. Weber and C. J. Sansonetti, *Phys. Rev. A* **35**, 4650 (1987).
- [49] M. T. Eiles, *Phys. Rev. A* **98**, 042706 (2018).
- [50] E. Karule, *Phys. Lett.* **15**, 137 (1965).
- [51] F. Engel, T. Dieterle, F. Hummel, C. Fey, P. Schmelcher, R. Löw, T. Pfau, and F. Meinert, *Phys. Rev. Lett.* **123**, 073003 (2019).
- [52] H. Saßmannshausen, F. Merkt, and J. Deiglmayr, *Phys. Rev. Lett.* **114**, 133201 (2015).
- [53] A. Miffre, M. Jacquey, M. Büchner, G. Tréneç, and J. Vigué, *Eur. Phys. J. D* **38**, 353 (2006).
- [54] W. F. Holmgren, M. C. Revelle, V. P. A. Lonij, and A. D. Cronin, *Phys. Rev. A* **81**, 053607 (2010).
- [55] J. M. Amini and H. Gould, *Phys. Rev. Lett.* **91**, 153001 (2003).
- [56] J. Mitroy, M. S. Safranova, and C. W. Clark, *J. Phys. B* **43**, 202001 (2010).
- [57] M. Schlagmüller, T. C. Liebisch, F. Engel, K. S. Kleinbach, F. Böttcher, U. Hermann, K. M. Westphal, A. Gaj, R. Löw, S. Hofferberth, T. Pfau, J. Pérez-Ríos, and C. H. Greene, *Phys. Rev. X* **6**, 031020 (2016).
- [58] S. K. Kanungo, J. D. Whalen, Y. Lu, T. C. Killian, F. B. Dunning, S. Yoshida, and J. Burgdörfer, *Phys. Rev. A* **102**, 063317 (2020).
- [59] P. Geppert, M. Althön, D. Fichtner, and H. Ott, *Nat. Commun.* **12**, 3900 (2021).



### 3.7 Electric field-induced wave-packet dynamics and geometrical rearrangement of Trilobite Rydberg molecules

## Electric-field-induced wave-packet dynamics and geometrical rearrangement of trilobite Rydberg molecules

Frederic Hummel <sup>1,\*</sup>, Kevin Keiler,<sup>1</sup> and Peter Schmelcher <sup>1,2</sup>

<sup>1</sup>Zentrum für Optische Quantentechnologien, Fachbereich Physik, Universität Hamburg, Luruper Chaussee 149, 22761 Hamburg, Germany

<sup>2</sup>The Hamburg Centre for Ultrafast Imaging, Universität Hamburg, Luruper Chaussee 149, 22761 Hamburg, Germany



(Received 14 December 2020; accepted 5 February 2021; published 19 February 2021)

We investigate the quantum dynamics of ultra-long-range trilobite molecules exposed to homogeneous electric fields. A trilobite molecule consists of a Rydberg atom and a ground-state atom, which is trapped at large internuclear distances in an oscillatory potential due to scattering of the Rydberg electron off the ground-state atom. Within the Born-Oppenheimer approximation, we derive an analytic expression for the two-dimensional adiabatic electronic potential energy surface in weak electric fields valid up to 500 V/m. This is used to unravel the molecular quantum dynamics employing the multiconfigurational time-dependent Hartree method. Quenches of the electric field are performed to trigger the wave-packet dynamics including the case of field inversion. Depending on the initial wave packet, we observe radial intrawell and interwell oscillations as well as angular oscillations and rotations of the respective one-body probability densities. Opportunities to control the molecular configuration are identified, a specific example being the possibility to superimpose different molecular bond lengths by a series of periodic quenches of the electric field.

DOI: [10.1103/PhysRevA.103.022827](https://doi.org/10.1103/PhysRevA.103.022827)

### I. INTRODUCTION

Trilobite Rydberg molecules are a prototype of an exotic molecular species called ultra-long-range Rydberg molecules (ULRM). The binding mechanism of ULRM is based on the low-energy scattering of the highly excited valence electron of a Rydberg atom off a ground-state atom. These molecules differ from conventional molecules with covalent or ionic bonds by their gigantic bond lengths of several hundreds or even thousands of angstroms and correspondingly huge dipole moments of up to a few kilo debye, e.g., in the case of trilobite molecules. Qualitatively, ULRM can be divided into two classes according to the orbital angular momentum  $l$  of the Rydberg electron: nonpolar molecules for  $l \leq 3$ , when the electronic state is energetically split off the quasidegenerate hydrogenlike manifold due to a noninteger quantum defect and polar molecules with  $l > 3$  such as the trilobite, in which the Rydberg electron is in a superposition of high angular momentum states.

ULRM have first been explored theoretically in the year 2000 [1] and discovered experimentally in 2008 [2]. They have been realized experimentally in cold or ultra-cold ensembles of the atomic species rubidium [3–8], cesium [9,10], strontium [11,12], and even in hetero-nuclear gases [13,14]. Their binding energies are on the order of a few gigahertz (GHz) in the case of polar molecules and of a few megahertz (MHz) for nonpolar molecules. Several extensions of the theoretical modeling of ULRM alongside with the increasing resolution of the experiments have been developed to accommodate for scattering of higher partial

waves [15,16], electronic fine and hyperfine structure [17], and spin-orbit coupling [18–21]. This led to applications of ULRM for the characterization of low-energy electron-atom collisions [22–26] and for probing spatial correlations in the underlying atomic gases [27–29]. Their molecular properties such as dipole moments or alignment can be controlled via weak external electric and magnetic fields [30–36]. Recently, ULRM have been proposed as candidates for the production of ultracold negative ions [37,38] and other classes of exotic molecules via ion-pair dressing [39] and Rydberg dressing [40].

So far, all studies of ULRM both theoretically and experimentally have been focusing on the electronic and vibrational structure. In this work, we explore the quantum dynamics and wave-packet evolution of trilobite molecules exposed to a weak electric field. The presence of the field breaks the spherical symmetry of the molecule which leads effectively to a two-dimensional adiabatic potential energy surface. For the nuclear quantum dynamics, we employ the multiconfigurational time-dependent Hartree (MCTDH) method [41–44], an *ab initio* wave-packet propagation method that combines the benefits of numerical precision and low computational cost by variationally optimizing both basis functions and coefficients at each time step.

To trigger the dynamics, we focus on different quenches of the electric field. In our first scenario, the ULRM is initialized in an eigenstate of the field-free configuration with an isotropic angular distribution. Following a sudden switch on of the field, we observe a correlated wave-packet dynamics classified as intrawell oscillations on different timescales. Secondly, the ULRM is initialized in an eigenstate for a specific field strength  $F_0$  such that the angular density is localized and the field is quenched to a different field strength  $F$  with

\*frederic.hummel@physnet.uni-hamburg.de

opposite direction. For strong fields, additional interwell oscillations occur and the molecule exists in a superposition of different geometries. Finally, we explore the case of a periodic sequence of quenches. This allows us to prepare the molecule in equally mixed radial eigenstates with a distinct radial localization in different potential wells deviating by hundreds of angstroms.

Our work is structured as follows. In Sec. II, we provide the underlying methodology covering the electronic structure, the field impact, and the nuclear dynamics. Our numerical results are presented in Sec. III addressing the cases of single quenches in Secs. III B and III C and periodic sequences of quenches in Sec. III D. Section IV contains the conclusions and a brief outlook.

## II. METHODOLOGY

### A. Electronic structure

Let us consider two  $^{87}\text{Rb}$  atoms, one of which is in a Rydberg state and the second one is in its ground state. The ionic core of the Rydberg atom is located at the coordinate origin and the excited electron at position  $\mathbf{r}$ , while the position of the ground-state atom is  $\mathbf{R}$ . According to the Born-Oppenheimer approximation, the adiabatic electronic Hamiltonian is given by  $H_e = H_c + V$ , where  $H_c$  describes the Rydberg electron in the potential of the ionic core and  $V$  models the interaction between the Rydberg electron and the ground-state atom. The low angular momentum states  $l < 3$  are energetically detuned from a degenerate manifold of high angular momentum states. The latter are well described by hydrogenic wave functions  $\phi_{nlm}(\mathbf{r})$  with energies  $-1/(2n^2)$  (in atomic units), where  $l \geq 3$  and  $n$  and  $m$  are the principle and magnetic quantum numbers, respectively.

The interaction of the Rydberg electron with the ground-state atom is modeled by a scattering pseudo potential [45]

$$V = 2\pi a(k)\delta(\mathbf{r} - \mathbf{R}), \quad (1)$$

where  $a(k)$  is the energy-dependent scattering length obtained via modified effective range theory [46,47]  $a(k) = a(0) + \pi\alpha k/3$ , with the electron's wave number  $k$ , polarizability  $\alpha = 319.2$  [48], and zero-energy scattering length  $a(0) = -16.1$  [49]. The wave number is determined in a semiclassical approximation via  $k^2/2 - 1/R = -1/(2n^2)$ .

This simplistic model Hamiltonian captures the essential features of trilobite Rydberg molecules [1,2] and is sufficient for the purpose of the present work: A quantum dynamical study of ULRM. Quantitative corrections originate from  $p$ -wave scattering [15,16], fine structure of the Rydberg atom and hyperfine structure of the ground-state atom [17], as well as spin-spin and spin-orbit interactions [19,20]. The Hamiltonian  $H_e$  can be solved analytically by degenerate perturbation theory [1]. Alternative approaches to the electronic structure rely on Green's function methods [18,50,51] or local frame transformation [52]. The result is the (unnormalized) trilobite state

$$|\psi(\mathbf{r}, \mathbf{R})\rangle^2 = \sum_{lm} \phi_{nlm}^*(\mathbf{R})\phi_{nlm}(\mathbf{r}), \quad (2)$$

and the corresponding trilobite potential

$$\epsilon_0(R) = 2\pi a(k(R))|\psi(\mathbf{R}, \mathbf{R})\rangle^2, \quad (3)$$

which depends only on the internuclear distance  $R$  and is discussed in Sec. II A and shown in Fig. 1(b).

### B. Impact of an electric field

We consider an electric field parallel to the  $z$  axis of our coordinate system. This leads to an additional term in the Hamiltonian, which can be evaluated in perturbation theory to

$$\langle \psi | \mathbf{F} \mathbf{r} | \psi \rangle = F d(R) \cos \theta, \quad (4)$$

where  $F$  is the electric field strength,  $\theta$  is the relative angle between the electric field and the internuclear axis, and  $d(R)$  is the dipole moment function of the trilobite state as seen in Figs. 1(a) and 1(b), respectively. This approximation is valid as long as the interaction of the Rydberg electron with the ground-state atom dominates the electric field interaction. The latter holds, if the Stark splitting of the degenerate hydrogenic manifold of high angular momentum states, which scales as  $F n^2$ , remains small compared to the potential depth of the trilobite's adiabatic electronic potential energy surface, which scales as  $n^{-3}$ . This means that the critical field strength decreases rapidly as  $n^{-5}$ . However, for  $n = 30$ , we have ensured that the perturbative results are in excellent agreement with the results of an exact diagonalization of the complete electronic Hamiltonian in a finite basis set up to field strength of  $F = 500$  V/m. The deviations due to the nonperturbative contribution to the potential are less than 1% for the internuclear distances covered in the dynamics.

In total, we obtain a two-dimensional potential energy surface,

$$\epsilon(R, \theta) = \epsilon_0(R) + F d(R) \cos \theta, \quad (5)$$

which depends on the internuclear separation  $R$  of the ionic core of the Rydberg atom and the ground-state atom and the relative angle  $\theta$  between the internuclear axis and the electric field. The sign of  $F$  determines the field direction. This potential is discussed in Sec. II A and shown in Fig. 1(c).

### C. Nuclear dynamics

To analyze the nuclear dynamics, we have to solve the corresponding time-dependent Schrödinger equation:

$$i \frac{\partial}{\partial t} \chi(R, \theta, t) = H_n \chi(R, \theta, t), \quad (6)$$

$$H_n = -\frac{1}{2\mu} (\Delta_R + \Delta_\theta) + \epsilon(R, \theta), \quad (7)$$

$$\Delta_R = \frac{\partial^2}{\partial R^2} + \frac{2}{R} \frac{\partial}{\partial R}, \quad (8)$$

$$\Delta_\theta = \frac{1}{R^2} \left( \frac{\partial^2}{\partial \theta^2} + \cot \theta \frac{\partial}{\partial \theta} \right), \quad (9)$$

where  $\mu = m/2$  and  $m$  is the atomic mass of  $^{87}\text{Rb}$ . Due to the cylindrical symmetry of the system, the polar angle  $\phi$

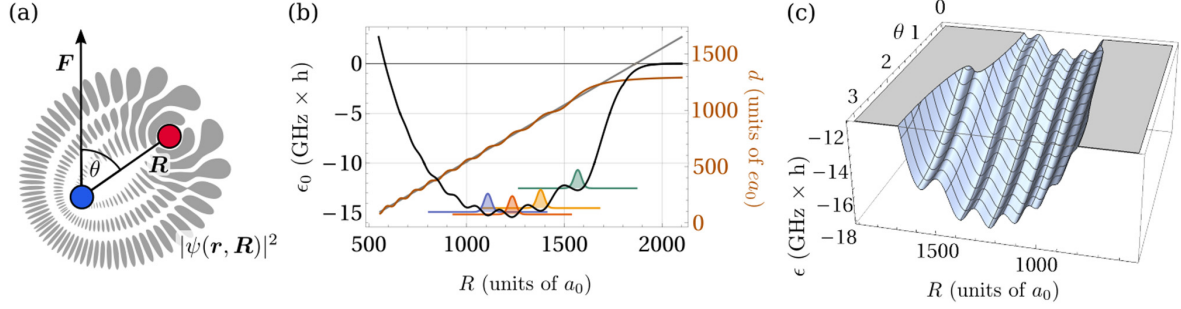


FIG. 1. (a) Illustration of a trilobite molecule in an electric field. The Rydberg electronic density (gray) ties the ionic core (blue) and the ground-state atom (red) together along  $\mathbf{R}$ .  $\theta$  is the angle relative to the electric field axis  $\mathbf{F}$ . (b) The field-free adiabatic potential  $\epsilon_0(R)$  (black) along with the dipole moment  $d(R)$  (brown), a classical dipole  $r - n^2/2$  for comparison (gray), and selected vibrational levels (colored). (c) The two-dimensional adiabatic potential  $\epsilon(R, \theta)$  for the field strength  $F = 200$  V/m.

is a cyclic coordinate and the corresponding magnetic quantum number  $M$  is a conserved quantity. Here, we restrict ourselves to the case  $M = 0$ . To solve Eq. (6), we employ the multiconfigurational time-dependent Hartree (MCTDH) approach [41–44]. In the following, we briefly describe the underlying method. More detailed descriptions are provided for example in references [42,44].

MCTDH is an *ab initio* tool for propagating wave packets in high dimensional spaces. Within this approach the time-dependent nuclear wave function  $\chi(R, \theta, t)$  of our trilobite molecule in an electric field is expressed as

$$\chi(R, \theta, t) = \sum_{i_1=1}^{n_1} \sum_{i_2=1}^{n_2} \tilde{c}_{i_1, i_2}(t) \tilde{\varphi}_{i_1}^{(1)}(R, t) \tilde{\varphi}_{i_2}^{(2)}(\theta, t), \quad (10)$$

where  $\tilde{c}_{i_1, i_2}(t)$  is a time-dependent coefficient,  $\tilde{\varphi}_{i_d}^{(d)}(q_d, t)$  is the  $i_d$ th time-dependent single-particle function (SPF) of the  $d$ th degree of freedom  $q_d \in \{R, \theta\}$ , and  $n_d$  is the number of single particle functions employed for the  $d$ th degree of freedom. For the case of two degrees of freedom, by employing the Schmidt decomposition of the two orthonormal basis sets represented by the SPFs, we can choose  $n_1 = n_2 \equiv N$ . The square matrix of coefficients  $\tilde{C}(t)$  can now be diagonalized and the SPFs are transformed accordingly such that we obtain

$$\chi(R, \theta, t) = \sum_i^N c_i(t) \varphi_i^{(1)}(R, t) \varphi_i^{(2)}(\theta, t). \quad (11)$$

The key idea of the MCTDH method is to keep the number of necessary SPFs small by employing variationally optimized coefficients  $c_i(t)$  and basis functions  $\varphi_i^{(d)}(q_d, t)$  obtained from the Dirac-Frenckel variational principle  $\langle \delta \chi | i \partial_t - H_n | \chi \rangle = 0$  [53,54] and requiring orthonormality of the SPFs  $\langle \varphi_i | \varphi_j \rangle = \delta_{ij}$  and  $\langle \varphi_i | \dot{\varphi}_j \rangle = 0$ . This ansatz allows a sizable reduction of the computational cost compared to e.g. a corresponding approach where only the coefficients are time-dependent.

The SPFs are normalized as

$$\int dR |\varphi_i^{(1)}(R, t)|^2 = 1, \quad (12)$$

$$\int d\theta \sin \theta |\varphi_i^{(2)}(\theta, t)|^2 = 1 \quad (13)$$

and represented on a grid by a discrete variable representation (DVR) [55]. In our case, the natural choices are the sine DVR for the radial degree of freedom, where we use 712 grid points, and the Legendre DVR for the angular degree of freedom, where we use 601 grid points.

In this study, we employ two different types of initial states for the wave-packet propagation. Firstly, we consider field-free molecular configurations. In this case, the degrees of freedom  $R$  and  $\theta$  decouple, since the electronic potential does not depend on the angle  $\theta$ . MCTDH provides a build-in function to obtain the field-free vibrational eigenstates  $\xi_{i_d}^{(d)}(q_d)$  of the one-body Hamiltonians

$$H_R = -\frac{1}{2\mu} \Delta_R + \epsilon_0(R), \quad (14)$$

$$H_\theta = -\frac{1}{2\mu} \Delta_\theta, \quad (15)$$

using the Lanczos algorithm, for  $\Delta_R$  and  $\Delta_\theta$  as defined in Eqs. (8) and (9), respectively. The solutions of Eq. (15) are the Legendre polynomials. Secondly, we consider the vibrational ground state in nonzero electric fields. To this end, we employ the relaxation method of the MCTDH method that uses imaginary-time evolution of the Hamiltonian  $H_n$ .

The number of SPFs necessary in order to retrieve converged results of the propagation depends strongly on the field strength under consideration, the chosen initial state, and the quench protocol. We consider a calculation to be converged in this context, if the occupation of the  $N$ th SPF remains sufficiently close to zero, i.e., below 0.1%, and the occupations  $c_i$  decrease exponentially. For propagation in fields up to  $F = 50$  V/m, we obtain converged results for  $N = 8$ , for fields up to  $F = 400$  V/m, we employ  $N = 32$ .

### III. RESULTS AND DISCUSSION

#### A. Adiabatic potential energy surfaces

Before we investigate the nuclear dynamics of the trilobite molecule in an electric field, let us briefly review the main properties of the underlying adiabatic electronic potential energy surface. In the field-free case, the multi-well structure of the trilobite potential  $\epsilon_0(R)$  [Eq. (3)] allows for localized

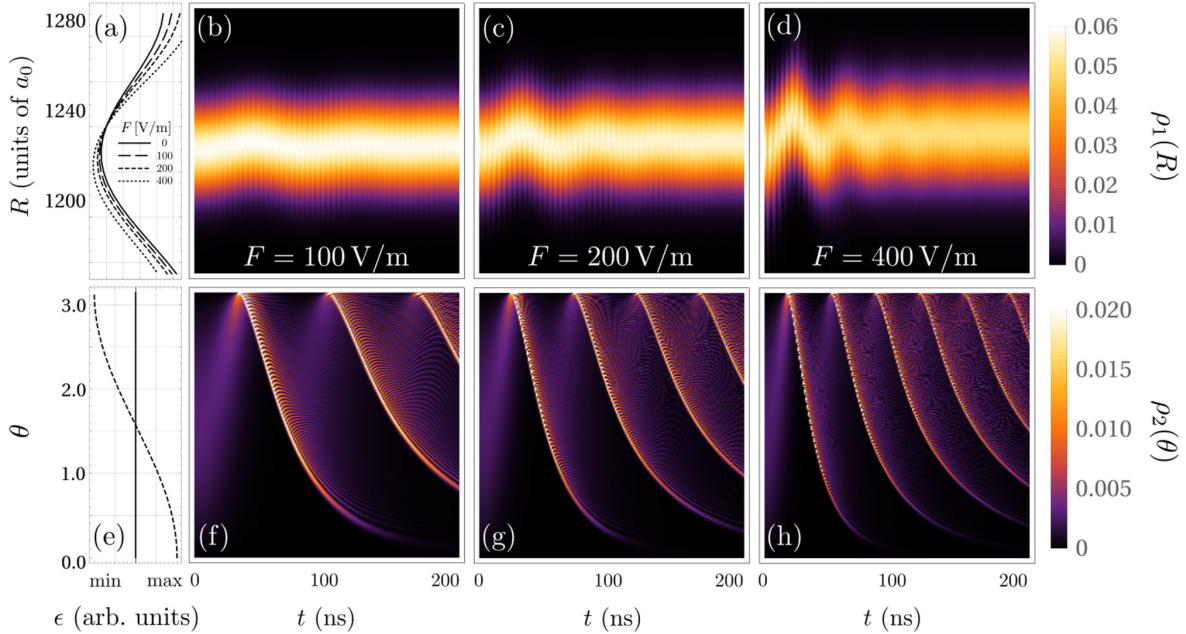


FIG. 2. Molecular wave-packet dynamics after a sudden quench of the electric field, initialized from the isotropic, field-free ground state. (a) Dynamically relevant section of the radial potential before (solid) and after the quench to different field strengths  $F$ . [(b)–(d)] Temporal evolution of the radial density  $\rho_1(R)$  corresponding to the fields. (e) The angular potential before (solid) and after (dashed) the quench. [(f)–(h)] Temporal evolution of the corresponding angular density  $\rho_2(\theta)$ . Two timescales of radial oscillations are apparent, the slower of which is correlated to the angular oscillations and depends on the field strength  $F$ .

vibrational states at the distinct radial positions of the potential wells. For the example case of  $n = 30$ , five such wells are of relevance as can be seen in Fig. 1(b). The four outermost wells host a Gaussian-shaped state (shown in colors in the same figure), while the state dominantly localizing in the inner well around  $R = 1000 a_0$  [not shown in Fig. 1(b)] possesses a nonzero probability amplitude in the outer wells. Additionally, the three potential wells between  $1100 a_0 < R < 1400 a_0$  each host an excited localized state with a single node. Other vibrational states are typically delocalized over two or more wells. Counting from the outermost well at large internuclear distances, the third well hosts the global potential minimum and the vibrational ground state  $\xi_0^{(1)}$  (red), where the upper index refers to the radial degree of freedom. The first excited state  $\xi_1^{(1)}$  (blue) localizes in the neighboring well at smaller internuclear distance, while the second excited state  $\xi_2^{(1)}$  exhibits a single node and localizes in the same well as the ground state.

The dipole moment function of the trilobite molecule  $d(R)$  increases with increasing  $R$ . This can be understood by the fact that the potential energy of the molecule is minimized, when the Rydberg electron localizes density at the position of the perturbing ground-state atom. Thus the distance of the ground-state atom to the ionic core of the Rydberg atom determines the separation of the positive charge of the ionic core and the negative charge of the electron. For large internuclear distances  $R > 2n^2 = 1800 a_0$ , we approach the dissociation limit and the dipole moment saturates which is shown in Fig. 1(b) in brown.

Due to the large dipole moment of the trilobite molecule, the relative depth of the potential wells can be tuned by rather weak electric field strengths [31]. In an arbitrary nonzero field, the equilibrium configuration is  $\theta = \pi$  [compare Fig. 1(c)]. At a field strength of  $F \approx 325$  V/m, the second outermost potential well becomes as low in energy as the third one. Therefore, for larger fields, the second outermost well hosts the global potential minimum in the configuration  $\theta = \pi$ , such that the vibrational ground state is shifted to the adjacent well. Oppositely, for the configuration  $\theta = 0$ , the inner wells increase in depth relative to the outer wells. At a field strength stronger than  $F \approx 110$  V/m, the fourth outermost well becomes lower in energy as the third. This highlights the relevance of the angular dynamics for the overall radial configuration of the molecule: Rotation of a molecule in an electric field may induce oscillations between different radial configurations.

### B. Quench dynamics for an isotropic initial state

In a first series of simulations, we prepare the molecule in the isotropic, field-free ground state and switch on the electric field at  $t = 0$ , i.e., the potential is quenched from  $\epsilon_0(R)$  [Eq. (3)] to  $\epsilon(R, \theta)$  [Eq. (5)]. Figure 2 shows both the radial (b)–(d) and the angular (f)–(h) dynamics of the molecule, while (a) and (e) show the dynamically relevant sections of the radial and angular potential, respectively, as a guide for the eye. Column-wise, the figure shows the dynamics for different field strength ranging from  $F = 100$ – $400$  V/m, each for an

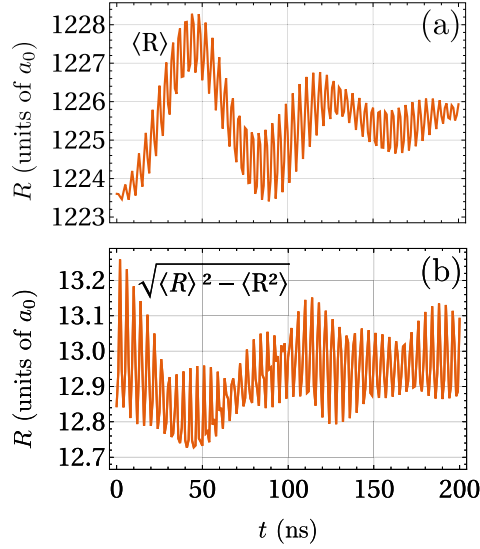


FIG. 3. Mean value (a) and variance (b) of the radial one-body density after a quench of the electric field to  $F = 100$  V/m initialized from the isotropic, field-free ground state. This corresponds to the density shown in Fig. 2(b) and highlights the presence of two dipole-oscillation modes accompanied by breathing oscillations.

evolution time of 200 ns. The radial one-body probability density (OBD)

$$\rho_1(R, t) = \sum_i |c_i(t)\varphi_i^{(1)}(R, t)|^2 \quad (16)$$

oscillates inside the initially populated potential well. Hence, we classify the dynamics as *intrawell* oscillations. Furthermore, the radial OBD reveals two distinct timescales for radial dynamics: A high-frequency oscillation with a period of few ns and a slow oscillation with a period of 30–100 ns depending on the field strength.

This is highlighted in Fig. 3, where the mean value (a) and the variance (b) of the radial OBD is shown in the case of  $F = 100$  V/m [compare Fig. 2(b)]. Shortly after the quench, the high-frequency oscillation is dominated by breathing (oscillation of the variance), however, after a few nano seconds, this is accompanied by dipole-type oscillations (oscillation of the mean). The period of a few ns is independent of the field strength, however, the corresponding amplitude slightly increases for stronger fields [not shown in Fig. 3, compare Figs. 2(b)–2(d)]. This can be attributed to a small field-dependent displacement of the potential well, which is shown in Fig. 2(a). In this figure, the absolute energetic position of the wells at different field strengths is neglected and only the relative well depth and radial position is shown.

The slow oscillation with a period of 30–100 ns is dominantly of dipole character. Its period corresponds to the period of the angular dynamics [compare Figs. 2(f)–2(h)] From the isotropic initial state, the angular OBD

$$\rho_2(\theta, t) = \sum_i \sin \theta |c_i(t)\varphi_i^{(2)}(\theta, t)|^2 \quad (17)$$

maximizes close to the equilibrium position obtaining a very steep slope around  $\theta = \pi$ . Afterwards, an oscillatory behavior along  $\theta$  emerges with a period that decreases for increasing field strength. This dynamics can be compared to a classical pendulum, where the initial displacement does not influence the period of the oscillation. Therefore, the isotropic initial state  $\xi_0^{(2)}$  can be understood as a superposition of all possible displacements which converge at the equilibrium position  $\theta = \pi$  after the same evolution time. This picture, however, only holds for the first oscillation [ $t < 100$  ns in Fig. 2(f)]. Afterwards, we find that part of the wave packet performs a large amplitude oscillation, while significant parts of it already maximize again around the equilibrium position [compare, for example, Fig. 2(f) around  $t = 100$  ns]. The oscillation period scales as  $1/\sqrt{F}$  corresponding to the classical scaling of a dipole in an external electric field. The radial OBD oscillates with the same period and the radial displacement is maximal when the angular wave packet localizes at the equilibrium position. Here, the wave packet's velocity and the corresponding centrifugal force are largest. Consequently, the amplitude of the oscillation increases for larger fields and is therefore most prominent in Fig. 2(d). For long evolution times, the oscillations are damped corresponding to the broadening distribution of the angular OBD.

### C. Quench dynamics for a localized initial state

Opposite to the quench discussed in the previous section, here, we investigate the molecular dynamics initialized from the vibrational ground state in the presence of an electric field  $F_0 = -400$  V/m. The quench consists of an inversion of the electric field direction. Our particular choice has two effects: Firstly, switching the sign of the electric field direction shifts the equilibrium position from  $\theta = 0$  (pre-quench) to  $\theta = \pi$  (post-quench) and, secondly, choosing a large pre-quench field strength shifts the vibrational ground state to the adjacent outer potential well as described in Sec. III A.

Figure 4 is structured similarly to Fig. 2 and shows the dynamically relevant sections of the radial (a) and angular (e) potentials as well as the temporal evolution of the radial [(b)–(d)] and angular OBD [(f)–(h)] for field strengths from  $F = 50$  to 200 V/m. We find that for this quench protocol, the radial intrawell oscillations are more prominent and of dipole character. Again, there are two distinct timescales: a high-frequency oscillation with a period of few ns and a slow oscillation with a field-dependent period. The period of the high-frequency oscillation does not depend on the field strength, however, its amplitude slightly increases with increasing field strength. In a weak field of  $F = 50$  V/m, the angular OBD (f) disperses from its initial position around  $\theta = 0$  and passes through the new equilibrium position at  $\theta = \pi$  after approximately  $t = 120$  ns. At that time, an interference pattern is visible, which we attribute to the molecule's fast radial oscillations, which in a classical picture leads to different rotational constants and consequently slightly differing arrival times at  $\theta = \pi$ . Afterwards, the wave packet travels back to its initial position, where it arrives at approximately  $t = 250$  ns (not shown in the figure). This behavior can be interpreted as a molecular rotation in contrast to the oscillation discussed in the previous section, where not the entire range of  $\theta$  is

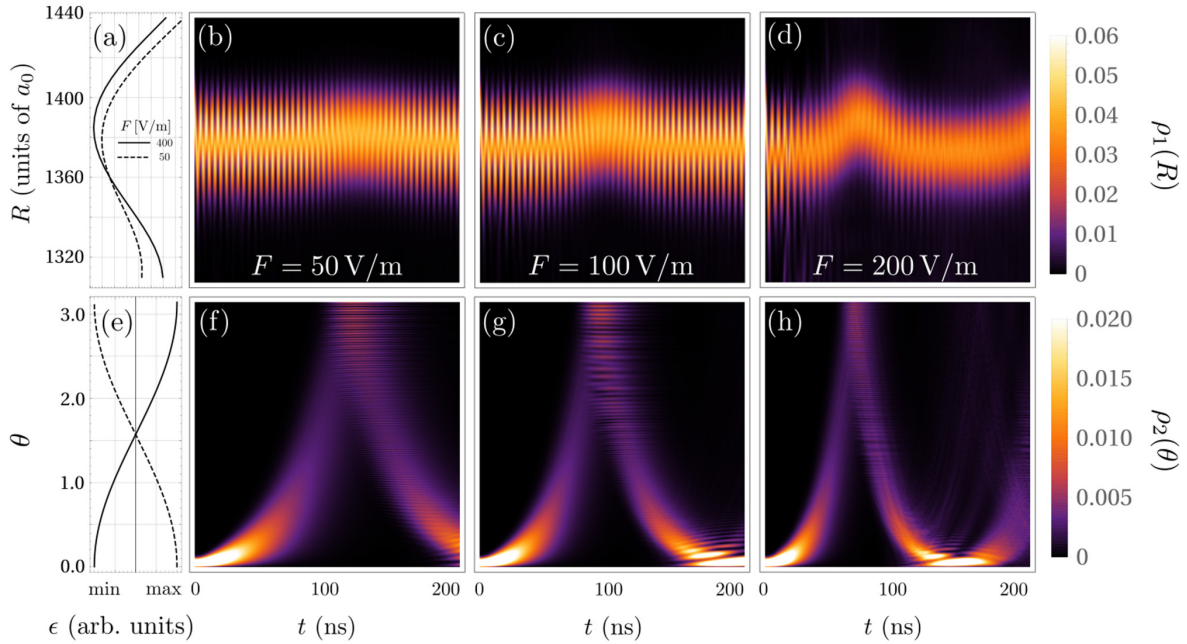


FIG. 4. Molecular wave-packet dynamics after a sudden inversion of the electric field direction initialized from the localized, vibrational ground state at  $F_0 = -400$  V/m. (a) Dynamically relevant section of the radial potential before (solid) and after the quench (dashed) in the case of  $F = 50$  V/m. [(b)–(d)] Temporal evolution of the radial radial density  $\rho_1(R)$  for different field strengths  $F$ . (e) The angular potential before (solid) and after (dashed) the quench. [(f)–(h)] Temporal evolution of the corresponding angular density  $\rho_2(\theta)$ . The angular dynamics correspond to a rotation.

covered. The rotation period decreases with increasing field. When the angular OBD has performed one half of its rotation, we find a displacement of the radial OBD to larger internuclear distances. This corresponds to the dynamics described in the previous section and can be attributed to the centrifugal force induced by the rotation, which becomes largest for the highest speed of the wave packet occurring at  $\theta = \pi$ .

The overall structure of the molecular dynamics changes drastically in a stronger field. Figure 5 shows the radial (b) and angular (c) OBD in a field of  $F = 400$  V/m along with the dynamically relevant sections of the radial (a) and angular (d) potentials before (solid) and after (dashed) the quench. Due to the symmetry  $F = -F_0$ , in (a), the radial potentials correspond additionally to different configurations  $\theta = \pi$  (dashed)

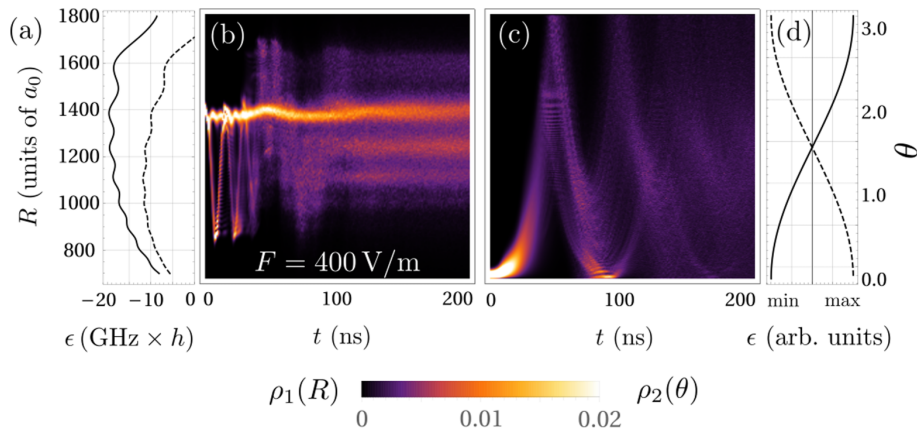


FIG. 5. Molecular wave-packet dynamics after a sudden inversion of the electric field direction initialized from the localized, vibrational ground state at  $F_0 = -400$  V/m. (a) The dynamically relevant cuts of the radial potential at  $\theta = 0$  before (solid) and after (dashed) the quench (or vice versa at  $\theta = \pi$ ). (b) Temporal evolution of the radial and (c) angular densities. (d) The angular potential before (solid) and after (dashed) the quench. For this field strength, radial, large-amplitude, interwell oscillations occur and correspondingly, the angular rotation blurs out after approximately half its period.

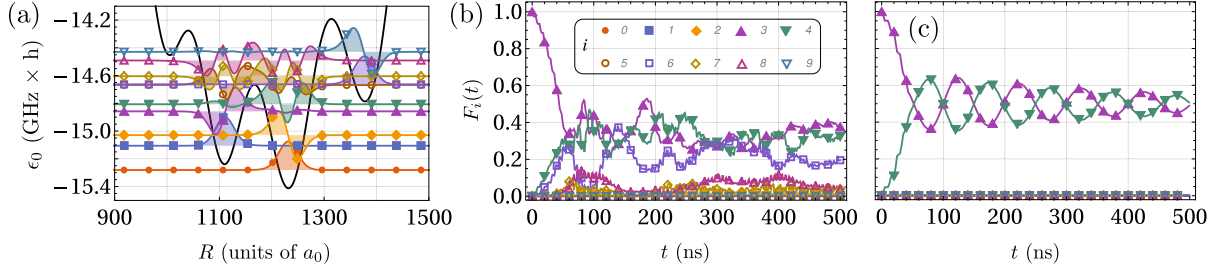


FIG. 6. Analysis of the radial components of the initial wave function. (a) The field-free trilobite potential (solid) with its vibrational eigenstates (symbol and color). [(b) and (c)] Fidelities  $F_i$  of the radial components with these eigenstates (same symbol and color) for a waiting time between quenches of (b)  $T = 3$  and (c) 5 ns. The waiting time strongly influences the number of contributing states. In (c), the quenches are discontinued after  $t = 50$  ns and coherent oscillations follow.

and  $\theta = 0$  (solid) after the quench (or inversely before the quench). We observe oscillations across many potential wells which we classify as *interwell* oscillations. At short evolution times, the angular OBD exhibits the same behavior as shown in Figs. 4(e)–4(g), where the angular wave packet rotates along  $\theta$ . However, after half a rotation at approximately  $t = 50$  ns, the wave packet is blurred out and after approximately  $t = 150$  ns, an almost equal superposition of angles is reached. This can be attributed to the vastly varying arclengths associated to radially oscillating wave packet such that a coherent rotation is not possible. Correspondingly, the radial interwell dynamics also effectively blurs out after the angular wave packet has performed half a rotation. The initial radial wave packet is localized at approximately  $R = 1400 a_0$ , which corresponds to the outer potential well. In the first 50 ns, it performs three radial, large-amplitude oscillations covering a range of  $600 a_0$ , before the oscillation blurs out. This corresponds to the strong tilt that the potential experiences after changing the direction of the electric field. After an evolution time of  $t = 100$  ns, the radial OBD is widely spread between  $1000 a_0 < R < 1600 a_0$ .

#### D. Periodic quenches

In the second series of simulations, we switch the field on and off periodically. In other words, we apply a sequence of quenches back and forth between the potentials  $\epsilon_0(R)$  and  $\epsilon(R, \theta)$ . Here, the waiting time  $T$  between quenches plays a crucial role. Exemplarily, we consider a radially excited initial state from the isotropic, field-free configuration to initialize the dynamics. Specifically, we consider the radial eigenstate  $\xi_3^{(1)}$  that localizes in an inner well of the trilobite and exhibits a single radial node. The field is switched periodically between  $F = 0$  and 50 V/m.

Figure 6 shows a state analysis for the waiting times  $T = 3$  and 5 ns. To this end, we focus on the radial components of the nuclear wave function, i.e., the radial OBD  $\rho_1(R, t)$ . Figure 6(a) shows a magnification of the relevant wells of the field-free trilobite potential  $\epsilon_0(R)$  (black, solid) along with the corresponding eigenstates  $\xi_i^{(1)}$  (colored and indicated by a symbol). For the state analysis, we consider the probability of finding the system in the eigenstates  $\xi_i^{(1)}$  irrespective of the angle  $\theta$ . This is termed the fidelity  $F_i(t) = \sum_j |\langle \xi_i^{(1)} | \varphi_j^{(2)} \rangle|^2$ . Figures 6(b) and 6(c) show the fidelities with matching

symbols and colors according to (a). We find that the number of states participating in the overall dynamics is very sensitive to the waiting time between quenches  $T$ . In the case (b), where  $T = 3$  ns, many states, also highly excited ones, contribute. This corresponds to a delocalization of the wave packet across several potential wells, e.g.,  $\xi_6^{(1)}$  shown in Fig. 6 with a purple square participates in the dynamics and is localized in the outer well, which is not initially populated. For  $T = 5$  ns (c), only two states dominate the evolution: the initial state  $\xi_3^{(1)}$  and the energetically adjacent state  $\xi_4^{(1)}$  that is localized to the adjacent well and exhibits two radial nodes. After propagation until  $t = 50$  ns, equal population of the two states  $\xi_3^{(1)}$  and  $\xi_4^{(1)}$  is achieved, which means that radially, the molecule exists in a superposition of states that are localized to distinct potential wells. At this point in time, we discontinue the quenches and observe the field-free evolution: the molecule coherently oscillates back and forth between the two states [see Fig. 6(c)].

#### IV. CONCLUSION

We unravel the dynamical behavior of trilobite Rydberg molecules exposed to a homogeneous electric field. The analysis of the electronic structure reveals that the multi-well potential landscape is tilted by the electric field depending on the angle  $\theta$  between the external field and the internuclear axis. For propagation protocols, in which the molecule is initially prepared in a field-free configuration and dynamically evolves in the presence of the field, the quenching of the field leads to intrawell oscillations of the radial density and oscillations around the equilibrium angle  $\theta = \pi$  of the angular density. When the molecule is initially prepared as the ground state in the presence of the field, i.e., localized in  $\theta$ , and the field is quenched to the opposite direction, the molecule starts to rotate with a field-dependent frequency. The radial intrawell oscillations are accompanied by large-amplitude interwell oscillations in strong fields  $F > 325$  V/m, when the radial position of the ground state has shifted to the adjacent outward potential well. Furthermore, we explore the possibility to prepare the molecule in a superposition of different radial configurations localizing in distinct potential wells by a series of periodic quenches with varying frequency.

We expect our results to be readily testable in state-of-art experiments, which have observed vibrational eigenstates of trilobite molecules after photoassociation from ultracold

atomic gases and subsequent ionization. The internuclear separation is experimentally accessible via measurement of the permanent electric dipole moment. After photoassociation of the molecules, the dynamics can be triggered by a fast switch of the external electric field and the radial separation can be probed time dependently to reconstruct the wave-packet propagation. The angular structure can be resolved, employing the recently developed quantum gas microscopes [56,57].

A natural extension of this work would be to allow for continuous changes of the electric field enabling state engineering by optimal control. Molecular dynamics in a magnetic field is equally of interest, a major drawback in practice being the larger switching times. However, combined electric and magnetic fields might allow for superpositions of different angular configurations. This study focuses on molecular dynamics on a single PES. Within our employed method, it is straightforward to extend the setup to a number of coupled PES and investigate dynamics beyond the Born-Oppenheimer approximation. A prime example would be the coupled PES

of the trilobite and butterfly molecules. In our model, we neglect  $p$ -wave interactions, which introduces only minor modifications to the overall structure of the trilobite. However, the additionally arising butterfly PES provides a decay mechanism of the trilobite molecule for associative ionization, which can additionally be tuned by a weak external field. This establishes an interesting avenue to study chemical reactions of ultra-long-range Rydberg molecules in unprecedented detail.

#### ACKNOWLEDGMENTS

FH thanks Matthew Eiles for fruitful discussions, especially his input on the electronic structure. KK gratefully acknowledges a scholarship of the Studienstiftung des deutschen Volkes. PS acknowledges support from the Deutsche Forschungsgemeinschaft (DFG) within the priority program “Giant Interactions in Rydberg Systems” [DFG SPP 1929 GiRyd project SCHM 885/30-1].

- 
- [1] C. H. Greene, A. S. Dickinson, and H. R. Sadeghpour, *Phys. Rev. Lett.* **85**, 2458 (2000).
- [2] V. Bendkowsky, B. Butscher, J. Nipper, J. P. Shaffer, R. Löw, and T. Pfau, *Nature (London)* **458**, 1005 (2009).
- [3] V. Bendkowsky, B. Butscher, J. Nipper, J. B. Balewski, J. P. Shaffer, R. Löw, T. Pfau, W. Li, J. Stanojevic, T. Pohl, and J. M. Rost, *Phys. Rev. Lett.* **105**, 163201 (2010).
- [4] B. Butscher, J. Nipper, J. B. Balewski, L. Kukota, V. Bendkowsky, R. Löw, and T. Pfau, *Nat. Phys.* **6**, 970 (2010).
- [5] B. Butscher, V. Bendkowsky, J. Nipper, J. B. Balewski, L. Kukota, R. Löw, T. Pfau, W. Li, T. Pohl, and J. M. Rost, *J. Phys. B: At. Mol. Opt. Phys.* **44**, 184004 (2011).
- [6] W. Li, T. Pohl, J. M. Rost, S. T. Rittenhouse, H. R. Sadeghpour, J. Nipper, B. Butscher, J. B. Balewski, V. Bendkowsky, R. Löw, and T. Pfau, *Science* **334**, 1110 (2011).
- [7] M. A. Bellos, R. Carollo, F. Banerjee, E. E. Eyler, P. L. Gould, and W. C. Stwalley, *Phys. Rev. Lett.* **111**, 053001 (2013).
- [8] K. S. Kleinbach, F. Meinert, F. Engel, W. J. Kwon, R. Löw, T. Pfau, and G. Raithel, *Phys. Rev. Lett.* **118**, 223001 (2017).
- [9] J. Tallant, S. T. Rittenhouse, D. Booth, H. R. Sadeghpour, and J. P. Shaffer, *Phys. Rev. Lett.* **109**, 173202 (2012).
- [10] D. Booth, S. T. Rittenhouse, J. Yang, H. R. Sadeghpour, and J. P. Shaffer, *Science* **348**, 99 (2015).
- [11] B. J. DeSalvo, J. A. Aman, F. B. Dunning, T. C. Killian, H. R. Sadeghpour, S. Yoshida, and J. Burgdörfer, *Phys. Rev. A* **92**, 031403(R) (2015).
- [12] F. Camargo, J. D. Whalen, R. Ding, H. R. Sadeghpour, S. Yoshida, J. Burgdörfer, F. B. Dunning, and T. C. Killian, *Phys. Rev. A* **93**, 022702 (2016).
- [13] J. D. Whalen, S. K. Kanungo, Y. Lu, S. Yoshida, J. Burgdörfer, F. B. Dunning, and T. C. Killian, *Phys. Rev. A* **101**, 060701(R) (2020).
- [14] M. Peper and J. Deiglmayr, *Phys. Rev. Lett.* **126**, 013001 (2021).
- [15] E. L. Hamilton, C. H. Greene, and H. R. Sadeghpour, *J. Phys. B: At. Mol. Opt. Phys.* **35**, L199 (2002).
- [16] M. I. Chibisov, A. A. Khuskivadze, and I. I. Fabrikant, *J. Phys. B: At. Mol. Opt. Phys.* **35**, L193 (2002).
- [17] D. A. Anderson, S. A. Miller, and G. Raithel, *Phys. Rev. A* **90**, 062518 (2014).
- [18] A. A. Khuskivadze, M. I. Chibisov, and I. I. Fabrikant, *Phys. Rev. A* **66**, 042709 (2002).
- [19] S. Markson, S. T. Rittenhouse, R. Schmidt, J. P. Shaffer, and H. R. Sadeghpour, *Chem. Phys. Chem.* **17**, 3683 (2016).
- [20] M. T. Eiles and C. H. Greene, *Phys. Rev. A* **95**, 042515 (2017).
- [21] M. Deiß, S. Haze, J. Wolf, L. Wang, F. Meinert, C. Fey, F. Hummel, P. Schmelcher, and J. Hecker Denschlag, *Phys. Rev. Res.* **2**, 013047 (2020).
- [22] D. A. Anderson, S. A. Miller, and G. Raithel, *Phys. Rev. Lett.* **112**, 163201 (2014).
- [23] H. Sassmannshausen, F. Merkt, and J. Deiglmayr, *Phys. Rev. Lett.* **114**, 133201 (2015).
- [24] F. Böttcher, A. Gaj, K. M. Westphal, M. Schlagmüller, K. S. Kleinbach, R. Löw, T. C. Liebisch, T. Pfau, and S. Hofferberth, *Phys. Rev. A* **93**, 032512 (2016).
- [25] J. L. MacLennan, Y. J. Chen, and G. Raithel, *Phys. Rev. A* **99**, 033407 (2019).
- [26] F. Engel, T. Dieterle, F. Hummel, C. Fey, P. Schmelcher, R. Löw, T. Pfau, and F. Meinert, *Phys. Rev. Lett.* **123**, 073003 (2019).
- [27] T. Manthey, T. Niederprüm, O. Thomas, and H. Ott, *New J. Phys.* **17**, 103024 (2015).
- [28] J. D. Whalen, S. K. Kanungo, R. Ding, M. Wagner, R. Schmidt, H. R. Sadeghpour, S. Yoshida, J. Burgdörfer, F. B. Dunning, and T. C. Killian, *Phys. Rev. A* **100**, 011402(R) (2019).
- [29] J. D. Whalen, R. Ding, S. K. Kanungo, T. C. Killian, S. Yoshida, J. Burgdörfer, and F. B. Dunning, *Mol. Phys.* **117**, 3088 (2019).
- [30] I. Lesanovsky, P. Schmelcher, and H. R. Sadeghpour, *J. Phys. B: At. Mol. Opt. Phys.* **39**, L69 (2006).
- [31] M. Kurz and P. Schmelcher, *Phys. Rev. A* **88**, 022501 (2013).
- [32] A. T. Krupp, A. Gaj, J. B. Balewski, P. Ilzhöfer, S. Hofferberth, R. Löw, T. Pfau, M. Kurz, and P. Schmelcher, *Phys. Rev. Lett.* **112**, 143008 (2014).
- [33] A. Gaj, A. T. Krupp, P. Ilzhöfer, R. Löw, S. Hofferberth, and T. Pfau, *Phys. Rev. Lett.* **115**, 023001 (2015).

- [34] T. Niederprüm, O. Thomas, T. Eichert, C. Lippe, J. Pérez-Ríos, C. H. Greene, and H. Ott, *Nat. Commun.* **7**, 12820 (2016).
- [35] F. Hummel, C. Fey, and P. Schmelcher, *Phys. Rev. A* **97**, 043422 (2018).
- [36] F. Hummel, C. Fey, and P. Schmelcher, *Phys. Rev. A* **99**, 023401 (2019).
- [37] F. Hummel, P. Schmelcher, H. Ott, and H. R. Sadeghpour, *New J. Phys.* **22**, 063060 (2020).
- [38] M. Peper and J. Deiglmayr, *J. Phys. B: At. Mol. Opt. Phys.* **53**, 064001 (2020).
- [39] P. Giannakeas, M. T. Eiles, F. Robicheaux, and J. M. Rost, *Phys. Rev. Lett.* **125**, 123401 (2020).
- [40] J. Wang and R. Côté, *Phys. Rev. Res.* **2**, 023019 (2020).
- [41] H.-D. Meyer, U. Manthe, and L. Cederbaum, *Chem. Phys. Lett.* **165**, 73 (1990).
- [42] M. Beck, A. Jäckle, G. Worth, and H.-D. Meyer, *Phys. Rep.* **324**, 1 (2000).
- [43] H.-D. Meyer and G. Worth, *Theor. Chem. Acc.* **109**, 251 (2003).
- [44] H.-D. Meyer, *Wiley Interdiscip. Rev.: Comp. Mol. Sci.* **2**, 351 (2012).
- [45] E. Fermi, *Il Nuovo Cimento* **11**, 157 (1934).
- [46] L. Spruch, T. F. O'Malley, and L. Rosenberg, *Phys. Rev. Lett.* **5**, 375 (1960).
- [47] T. F. O'Malley, L. Spruch, and L. Rosenberg, *J. Math. Phys.* **2**, 491 (1961).
- [48] E. Arimondo, M. Inguscio, and P. Violino, *Rev. Mod. Phys.* **49**, 31 (1977).
- [49] C. Bahrim, U. Thumm, and I. I. Fabrikant, *J. Phys. B: At. Mol. Opt. Phys.* **34**, L195 (2001).
- [50] C. Fey, M. Kurz, P. Schmelcher, S. T. Rittenhouse, and H. R. Sadeghpour, *New J. Phys.* **17**, 055010 (2015).
- [51] M. Tarana and R. Curik, *Phys. Rev. A* **93**, 012515 (2016).
- [52] P. Giannakeas, M. T. Eiles, F. Robicheaux, and J. M. Rost, *Phys. Rev. A* **102**, 033315 (2020).
- [53] P. A. M. Dirac, *Math. Proc. Cambridge Phil. Soc.* **26**, 376 (1930).
- [54] I. A. Frenkel, *Wave Mechanics* (Oxford University Press, Oxford, 1934).
- [55] D. O. Harris, G. G. Engerholm, and W. D. Gwinn, *J. Chem. Phys.* **43**, 1515 (1965).
- [56] C. Veit, N. Zuber, O. A. Herrera-Sancho, V. S. V. Anasuri, T. Schmid, F. Meinert, R. Löw, and T. Pfau, [arXiv:2008.08512](https://arxiv.org/abs/2008.08512).
- [57] P. Geppert, M. Althön, D. Fichtner, and H. Ott, [arXiv:2012.11485](https://arxiv.org/abs/2012.11485).

### 3.8 Building principle of triatomic Trilobite Rydberg molecules

## Building principle of triatomic trilobite Rydberg molecules

Christian Fey,<sup>1</sup> Frederic Hummel,<sup>1</sup> and Peter Schmelcher<sup>1,2</sup>

<sup>1</sup>Zentrum für Optische Quantentechnologien, Universität Hamburg, 22761 Hamburg, Germany

<sup>2</sup>The Hamburg Centre for Ultrafast Imaging, Universität Hamburg, Luruper Chaussee 149, 22761 Hamburg, Germany



(Received 20 December 2018; published 19 February 2019)

We investigate triatomic molecules that consist of two ground-state atoms and a highly excited Rydberg atom, bound at large internuclear distances of thousands of angstroms. In the molecular state the Rydberg electron is in a superposition of high angular momentum states whose probability densities resemble the form of trilobite fossils. The associated potential-energy landscape has an oscillatory shape and supports a rich variety of stable geometries with different bond angles and bond lengths. Based on an electronic structure investigation we analyze the molecular geometry systematically and develop a simple building principle that predicts the triatomic equilibrium configurations. As a representative example we focus on <sup>87</sup>Rb trimers correlated to the  $n = 30$  Rydberg state. Using an exact diagonalization scheme we determine and characterize localized vibrational states in these potential minima with energy spacings on the order of  $100 \text{ MHz} \times h$ .

DOI: [10.1103/PhysRevA.99.022506](https://doi.org/10.1103/PhysRevA.99.022506)

### I. INTRODUCTION

Ultralong-range Rydberg molecules (ULRM) are a manifestation of a novel type of chemical bond, where a ground-state atom is captured in the electronic cloud of a highly excited Rydberg atom [1]. In contrast to conventional diatomic molecules, ULRM possess an oscillatory potential-energy surface and huge bond lengths ranging typically from a few hundreds to thousands of Bohr radii  $a_0$ . Based on the angular momentum  $l$  of the Rydberg electron, two classes of ULRM can be distinguished: weakly bound nonpolar ULRM that correlate to quantum-defect-split Rydberg states with low angular momentum  $l < 3$ , as well as more deeply bound polar ULRM in which the Rydberg electron is in a superposition of hydrogenlike high- $l$  states and may possess large electric dipole moments on the order of hundreds to thousands of Debye. In allusion to the shape of their electronic probability density, polar ULRM are further subdivided into “trilobite” molecules with dominant  $s$ -wave interaction [1], as well as “butterfly” molecules [2,3] with dominant  $p$ -wave interactions. All of these species have been confirmed experimentally [4–8] via one- or two-photon association in ultracold samples of either Rb, Cs, or Sr. Experimental and theoretical research on ULRM demonstrated novel possibilities to tailor molecular properties via weak fields [7,9–13] and to control atom-atom interactions [14,15]. Furthermore, ULRM provide unprecedented access to the physics of electron-atom scattering [16–20] and ion-atom interactions [21–23].

Having control over the density of the atomic sample and the Rydberg excitation  $n$ , experiments are able to create and probe not only diatomic ULRM but also polyatomic ULRM. These are bound states between one Rydberg atom and several ground-state atoms. Although originally predicted for polar high- $l$  ULRM [24], experimental research focused so far exclusively on nonpolar types, that are more easily accessible via one- or two-photon transitions. Experiments with  $s$ -state ULRM confirmed the existence of few-body states (trimers,

tetramers, pentamers), as well as polaronic many-body states, both in excellent agreement with corresponding theoretical models [11,25–28].

From a theoretical as well as from an experimental point of view, the isotropy of the electronic wave function in polyatomic  $s$ -state ULRM has certain advantages. It simplifies the theoretical models [26,28] and grants high excitation efficiencies in the experiments, due to comparatively large Franck-Condon factors. An obvious drawback of this isotropy is, however, that there is only weak control over the molecular geometry, especially the angular geometry. This is different for polyatomic  $p$ - and  $d$ -state ULRM [29,30], which exist in linear and bent geometries. The Hilbert space of energetically available electronic states is here larger, and provides more possibilities for the Rydberg electron to optimize its wave function. Consequently, for polyatomic trilobite ULRM, with their large manifold of energetically degenerate hydrogenic states, even more complex geometries with deeper potential wells are expected. Previous studies predicted exotic properties of these molecules, such as their capability to form Borromeanlike states [31] or the appearance of quantum scars [32]. Furthermore, the large electric dipole moments allow one to tune their geometry via weak electric fields [33]. However, all of these theoretical works focused so far only on constrained geometries, such as linear, planar, or cubic configurations, or on polyatomic trilobite states in random configurations [32]. Consequently, a thorough understanding of the molecular geometry of even the simplest polyatomic trilobite ULRM, the trilobite trimer, is missing. In our work we aim at closing this gap. We analyze the full three-dimensional potential-energy landscape of trilobite trimers by means of an investigation of their electronic structure and derive a simple building principle that explains the resulting equilibrium positions. Subsequently we employ an exact diagonalization scheme to predict energies and wave functions of bound vibrational states, which are relevant for spectroscopic measurements.

This work is organized as follows. In Sec. II we present the electronic Hamiltonian of the molecular system and derive the corresponding potential-energy surfaces (PES). Furthermore, we identify equilibrium positions and explain their geometrical arrangement. In Sec. III we provide the theoretical framework for the description of vibrational states in these PES. Subsequently, we present energies and probability densities of vibrational states and discuss their properties. Section IV contains our conclusions.

## II. ENERGY LANDSCAPE

General polyatomic ULRM consist of an ionic core (here at the coordinate origin), a Rydberg electron at position  $\mathbf{r}$ , and  $N$  neutral ground-state atoms at positions  $\mathbf{R}_i$  where  $i = 1, \dots, N$ . A sketch of the setup for  $N = 2$  is presented in Fig. 1(a). In the Born-Oppenheimer approximation the adiabatic electronic Hamiltonian is given by  $H = H_0 + V$ , where  $H_0$  describes the Rydberg electron in its ionic core potential while  $V$  is the interaction between the Rydberg electron and the ground-state atoms. In dependence of the electronic angular momentum  $l$ , the eigenstates of  $H_0$  can be divided into low- $l$  and high- $l$  states. Due to their centrifugal barrier, high- $l$  states (typically  $l \geq 3$ ) are shielded from the ionic core. To a good approximation they are given by hydrogen wave functions  $\varphi_{nlm}(\mathbf{r})$  with energies  $-1/(2n^2)$  (in atomic units) where  $n$  and  $m$  are the principal and the magnetic quantum number, respectively. However, due to the presence of the ground-state atoms (perturbers) inside the Rydberg orbit, the hydrogenic states become coupled. We focus on  $^{87}\text{Rb}$  ULRM where this coupling is small compared to the energy splitting between high- $l$  ( $l \geq 3$ ) and low- $l$  ( $l < 3$ ) states, such that a perturbative approach is appropriate [1]. Working in atomic units, we model this interaction with the perturber via a contact potential [1,34,35]

$$V = \sum_{j=1}^N 2\pi a[k(R_j)]\delta(\mathbf{r} - \mathbf{R}_j). \quad (1)$$

The energy dependence of the scattering length is obtained via modified effective range theory [36,37]  $a(k) = a(0) + (\pi/3)\alpha k$  with the electron wave number  $k$ , the Rb(5s) polarizability  $\alpha = 319.2$ , and the zero-energy scattering length  $a(0) = -16.1$  for  $e\text{-Rb}(5s)$  triplet scattering ( $^3S$ ) [38]. In a semiclassical approximation the wave number is determined via  $k^2/2 - 1/R = -1/(2n_0^2)$ , where  $n_0$  is the principal quantum number of interest. Despite its simplicity, the Hamiltonian  $H$  captures the essential features of trilobite ULRM. Quantitative corrections originate from the  $^{87}\text{Rb}$  fine and hyperfine structure, additional  $p$ -wave interactions, as well as spin-spin and spin-orbit couplings [2,3,16,39–42]. Furthermore, there exist nonperturbative methods relying on Greens's function methods [3,25,43,44].

For dimers ( $N = 1$ ,  $\mathbf{R}_1 = \mathbf{R}$ ) the contact interaction gives rise to an electronic eigenstate that strongly localizes on the perturber and resembles the shape of a trilobite fossil; see Fig. 1(a) for two examples. Performing first-order perturbation theory in the Hilbert space of quasidegenerate hydrogenic states with  $n = n_0$  and  $l \geq 3$ , its wave function can be

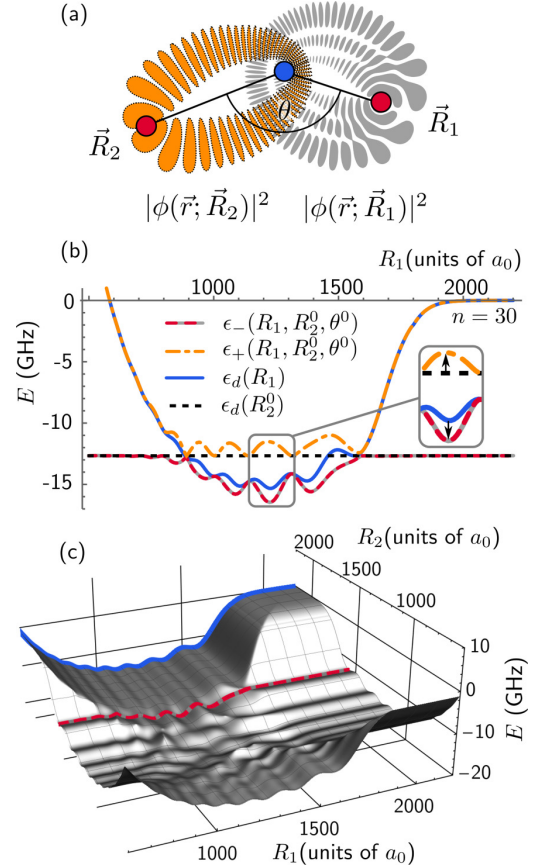


FIG. 1. (a) Trilobite trimer consisting of two ground-state atoms (red) at positions  $\mathbf{R}_{1/2}$  relative to the ionic core (blue). The Rydberg electron (here  $n = 30$ ) is in a superposition of the two trilobite states  $\phi(\mathbf{r}; \mathbf{R}_{1/2})$  (orange vs gray density). (b) Cuts of the two trimer PES  $\epsilon_{\pm}(R_1, R_2^0, \theta^0)$  for fixed  $R_2 = R_2^0 = 1563a_0$  and  $\theta = \theta^0 = 0.12\pi$ . The energy of the hydrogenic states with  $n = 30$  is set to zero. These potentials are compared to the diatomic PES  $\epsilon_d(R_1)$  and  $\epsilon_d(R_2^0)$ . A magnification of the deviations is presented in the inset. (c) 2D cut of the lower PES  $\epsilon_-(R_1, R_2, \theta^0)$  where only  $\theta^0 = 0.12\pi$  is fixed. The colored lines mark cuts  $\epsilon_-(R_1, R_2^0, \theta^0)$  (red-gray dashed) and  $\epsilon_d(R_1)$  (solid blue) that are also visible in (b).

expressed as  $\Psi(\mathbf{r}; \mathbf{R}) = \mathcal{N}\phi(\mathbf{r}; \mathbf{R})$  with the trilobite orbital

$$\phi(\mathbf{r}; \mathbf{R}) = \sum_{l=3}^{n_0-1} \sum_{m=-l}^l \varphi_{n_0lm}^*(\mathbf{R})\varphi_{n_0lm}(\mathbf{r}) \quad (2)$$

and the normalization constant  $\mathcal{N} = \phi(\mathbf{R}; \mathbf{R})^{-1/2}$  [24]. It is the superposition of all hydrogen states that minimizes its energy by maximizing its density on the perturber. This density is azimuthally symmetric around the internuclear axis  $\mathbf{R}$ . In particular, if  $\mathbf{R}$  points along the  $z$  axis, only terms with  $m = 0$  contribute. The associated energy shift (first order) is given by

$$\epsilon_d(R) = 2\pi a[k(R)]\phi(\mathbf{R}; \mathbf{R}). \quad (3)$$

This is the potential-energy surface (PES) of the molecule. It is straightforward to show that the PES depends only on  $R = |\mathbf{R}|$ . An example for  $n_0 = 30$  (solid blue line) is presented

in Fig. 1(b). The deepest minima support a series of localized vibrational states [1].

The electronic structure becomes altered when a second perturber is present ( $N = 2$ ). To obtain the electronic trimer states efficiently, we separate the Hilbert space with  $n = n_0$  and  $l \geq 3$  into the subspace spanned by the two dimer solutions  $\phi(\mathbf{r}; \mathbf{R}_j)$  with  $j = 1, 2$  and the remaining complement, that may be obtained via Gram-Schmidt orthogonalization. One can show that all states in the complement have nodes at  $\mathbf{R}_1$  and  $\mathbf{R}_2$  and thus do not probe the ground-state atoms [31]. A proof is provided in the Appendix. Consequently, within first-order perturbation theory, we can express the trimer state as a linear combination of the two dimer solutions [24,29,31,40]

$$\psi(\mathbf{r}; \mathbf{R}_1, \mathbf{R}_2) = \sum_{j=1}^2 c_j \phi(\mathbf{r}; \mathbf{R}_j), \quad (4)$$

with coefficients  $c_j$  that depend on  $\mathbf{R}_1$  and  $\mathbf{R}_2$ . This situation is visualized in Fig. 1(a) schematically, where we take into account that the shape of the trilobite state  $\phi(\mathbf{r}; \mathbf{R}_j)$  depends explicitly on the nuclear coordinate  $\mathbf{R}_j$ . Eigenstates of this two-level system are determined by solving the corresponding generalized eigenvalue problem for  $H$ . The two resulting PES

$$\epsilon_{\pm}(\mathbf{R}_1, \mathbf{R}_2) = \frac{\epsilon_d(R_1) + \epsilon_d(R_2)}{2} \pm \frac{1}{2} \sqrt{[\epsilon_d(R_1) - \epsilon_d(R_2)]^2 + 4c(\mathbf{R}_1, \mathbf{R}_2)} \quad (5)$$

can be expressed in terms of the diatomic potentials (3) and a term

$$c(\mathbf{R}_1, \mathbf{R}_2) = 4\pi^2 a [k(R_1)] a [k(R_2)] |\phi(\mathbf{R}_2; \mathbf{R}_1)|^2. \quad (6)$$

The latter contains the trilobite orbital (2) as a function of the two nuclear coordinates. It depends, in addition to  $R_1 = |\mathbf{R}_1|$  and  $R_2 = |\mathbf{R}_2|$ , also on the relative angle  $\theta = \arccos[(\mathbf{R}_1 \cdot \mathbf{R}_2)/(R_1 R_2)]$  and adds thus an anisotropy to the PES. Furthermore, it satisfies  $c(\mathbf{R}_1, \mathbf{R}_2) = c(\mathbf{R}_2, \mathbf{R}_1)$ .

Exemplary cuts of the PES  $\epsilon_{\pm}(R_1, R_2^0, \theta^0)$  are presented in Fig. 1(b) for fixed  $R_2 = R_2^0 = 1563a_0$  and  $\theta = \theta^0 = 0.12\pi$  but variable  $R_1$  (dashed gray-red and dashed-dotted yellow line). These potentials are compared to the corresponding diatomic PES  $\epsilon_d(R_1)$  and  $\epsilon_d(R_2^0)$  (solid blue and dashed black line), i.e., the PES when the presence of the second ground-state atom is ignored. While the trimer PES coincide with the dimer PES for very large and very small separations  $R_1$ , there is an intermediate regime, here  $900a_0 < R_1 < 1600a_0$ , where one finds substantial deviations. These deviations result solely from the term  $c(\mathbf{R}_1, \mathbf{R}_2)$ , which, based on the structure of (5), can be interpreted as an effective coupling of the two dimer states  $\phi(\mathbf{r}; \mathbf{R}_1)$  and  $\phi(\mathbf{r}; \mathbf{R}_2)$ . For example, whenever one has  $c(\mathbf{R}_1, \mathbf{R}_2) = 0$ , there is no coupling and the two PES  $\epsilon_{\pm}(R_1, R_2^0, \theta^0)$  coincide with the diatomic PES. In this limit one has

$$\begin{aligned} \epsilon_+(R_1, R_2, \theta) &= \max[\epsilon_d(R_1), \epsilon_d(R_2)], \\ \epsilon_-(R_1, R_2, \theta) &= \min[\epsilon_d(R_1), \epsilon_d(R_2)]. \end{aligned} \quad (7)$$

In contrast, a nonvanishing coupling  $c(\mathbf{R}_1, \mathbf{R}_2)$  introduces a level repulsion between the two diatomic PES. This is

represented by the black arrows in the inset in Fig. 1(b). Importantly, in the lower PES  $\epsilon_-(R_1, R_2, \theta)$  this effect leads to an energy drop below the dimer PES and can therefore stabilize trimer states. This effect is also visible in the higher-dimensional cut of the PES  $\epsilon_-(R_1, R_2, \theta^0)$  in Fig. 1(c). Level repulsion takes place in the region where  $R_1 < 1600a_0$  and  $R_2 < 1600a_0$ , where it induces a rich oscillatory pattern with many radial minima that are energetically well below the dimer PES (solid blue line). To provide some visual orientation, the dashed red line marks the curve  $\epsilon_-(R_1, R_2^0, \theta^0)$  and links Fig. 1(b) to Fig. 1(c).

The exemplary cuts of the PES in Figs. 1(b) and 1(c) demonstrate that the coupling  $c(\mathbf{R}_1, \mathbf{R}_2)$  has a crucial impact on the PES. In the following we study as to what extent this mechanism affects the equilibrium configuration of the trimer (stable in  $R_1, R_2$ , and  $\theta$ ). To this aim we evaluate  $\epsilon_-(R_1, R_2, \theta)$  on a cubic grid and detect all local minima. Surprisingly, this yields a large set of the order of one thousand equilibrium positions. We analyze these positions in two steps. First, we classify the equilibria with respect to the coordinate  $R_1$ . Subsequently, in a second step, we focus on the structure with respect to the remaining coordinates  $R_2$  and  $\theta$ .

The histogram in Fig. 2(a) presents the abundance of minima in dependence of the coordinate  $R_1$ . Due to the indistinguishability of the two ground-state atoms, the histogram does not change if one replaces  $R_1$  by  $R_2$ . As can be seen, the minima are not distributed homogeneously along the  $R_1$  axis but cluster around certain separations  $R_c \in \{650, 725, 802, 886, 1001, 1105, 1228, 1374, 1563\}a_0$  marked by vertical dashed lines in Fig. 2(b). Comparing these values to the shape of the dimer PES in Fig. 2(b), we find that the positions of the strongest peaks in the histogram coincide with the equilibrium positions of the dimer PES. Moreover, all peak positions can be identified with the critical radii found in [45] at which the trilobite state  $\phi(\mathbf{r}; \mathbf{R})$  satisfies semiclassical Einstein-Brillouin-Keller quantization conditions. The elliptically shaped densities of these states can be characterized by two integers  $(n_1, n_2)$  counting the nodes along different elliptical directions. Exemplary probability densities for (0,29) and (2,27) are depicted in Fig. 2. We interpret these results in the following way. The radial structure of trimer PES is governed dominantly by the dimer PES. For instance, the cut  $\epsilon_-(R_1, R_2^0, \theta^0)$  in Fig. 1(b) (dashed gray-red line) is on a large scale well approximated by (7) (solid blue and dashed black line). However, the coupling  $c(\mathbf{R}_1, \mathbf{R}_2)$  induces oscillatory deviations and leads to a substructure which is not captured by (7). Due to these deviations the peaks in the histogram are not sharp but possess a certain width. Furthermore, when Einstein-Brillouin-Keller quantization conditions are fulfilled, these deviations are sufficiently strong to induce minima at radii which are not stable in the diatomic system, e.g., at  $R_1 = 800a_0$ . The formation of ultralong-range Rydberg trimers with repulsive two-body interaction studied in [31] is a special example for this effect.

Having analyzed the clustering with respect to the  $R_1$  coordinate we focus, in a second step, on the configuration of the remaining coordinates  $R_2$  and  $\theta$ . To this aim we select subsets of minima sharing the same  $R_1 \approx R_c$ , i.e., belonging to the same cluster. As an example, Fig. 2(c) depicts the minima of

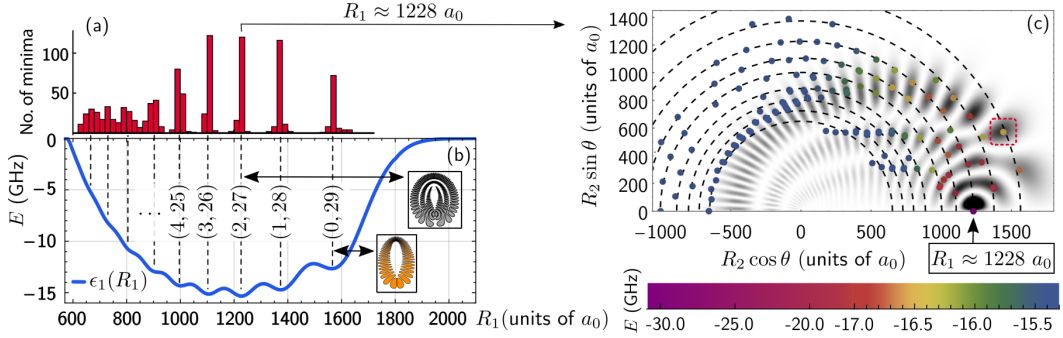


FIG. 2. Analysis of the positions of minima  $(R_1, R_2, \theta)$  in the trilobite trimer PES  $\epsilon_-(R_1, R_2, \theta)$  given in (5). (a) The histogram depicts the number of minima as a function of their coordinate  $R_1$ . (b) Peak positions  $R_c$  in the histogram (dashed lines) occur at radii  $R_1$  where the trilobite wave function  $\phi(\mathbf{r}; \mathbf{R}_1)$  is dominated by orbitals having integer number of nodes  $(n_1, n_2)$  along two different elliptical directions [45]. The insets present exemplary probability densities for (0,29) and (2,27). Minima in the diatomic PES  $\epsilon_d(R_1)$  (blue line) coincide with these radii  $R_c$ . (c) Each dot represents the coordinates  $R_2$  and  $\theta$  of a minimum in the subset with  $R_1 \approx 1228a_0$ . The color encodes the potential well depths. The additional gray shading represents the electronic density of the trilobite dimer  $|\phi(\mathbf{R}_2; \mathbf{R}_1)|^2$  associated to the subset with  $R_1 = 1228a_0$  and characterized by (2,27). Deep minima occur at positions where circles of radius  $R_c$  (dashed lines) intersect the peaks of the trilobite density, e.g., at the position marked by the dashed red square. Bound vibrational states in this minimum are presented in Fig. 3 as an example case.

the cluster with  $R_1 \approx 1228a_0$ . Every dot represents the coordinates of a minimum, i.e.,  $R_2$  and  $\theta$ , in the plane perpendicular to  $\mathbf{R}_1$ . The dot color encodes the well depth ranging from  $-30$  GHz to  $-15$  GHz. In addition to the minima we present the trilobite density from (6)  $|\phi(\mathbf{R}_2; \mathbf{R}_1)|^2$  (shaded gray) as well as the regions where  $|R_2|$  coincides with cluster radii  $R_c$  (dashed circles). Minima are expected to support stable trimer states only if their depth is significantly lower than the depth of the dimer PES  $\epsilon_d(1228a_0) \approx -15$  GHz. As can be seen in Fig. 2(c), sufficiently deep minima (with color coding different from blue) occur always close to positions where the dashed circles intersect with strong peaks in the trilobite density. An example for such an intersection is marked by the dashed red square. This geometrical arrangement of the minima is a consequence of the coupling in (6). While radial coordinates of the minima are mostly determined by the properties of the diatomic system via Eq. (7), the angular structure is dominated by the coupling (6) proportional to the trilobite density. This can be formulated as a simple bottom-up building principle: based on an existing stable trilobite dimer, a stable trilobite trimer can be constructed by placing an additional ground-state atom in a peak of the diatomic trilobite density (shaded gray density in Fig. 2). Since the trilobite density possesses many peaks at different positions, this binding mechanism gives rise to a plethora of equilibrium geometries. The crucial role of diatomic trilobite orbitals as building blocks for polyatomic ULRM has also been pointed out in [24,31,32,40]. These studies focused, however, on constrained geometries or random configurations of the molecules and did not capture its angular equilibrium structure. These angular structures result from the mixing of Rydberg wave functions with different quantum numbers  $l$  and  $m$  as described in (4). Bent equilibrium geometries are therefore absent in polyatomic  $s$ -state ULRM with almost isotropic PES but can occur also in  $p$ - and  $d$ -state trimers [11,25,26,29,30].

### III. VIBRATIONAL STATES

In the following we focus on one of the trimer equilibrium positions in more detail and predict the supported vibrational states. This is the minimum marked by the dashed red line in Fig. 2(c) with coordinates  $(R_1^0, R_2^0, \theta^0) = (1228a_0, 1563a_0, 0.12\pi)$ . This analysis serves as an example case to illustrate properties of bound states that occur also in other minima of the PES.

After separating the center-of-mass motion, the Hamiltonian for the relative nuclear motion can be written as  $H^{\text{rel}} = H^{\text{vib}} + H^{\text{rovib}}$ , where  $H^{\text{vib}}$  describes pure vibrational dynamics (depending only on  $R_1, R_2, \theta$ ) and  $H^{\text{rovib}}$  describes rotational as well as rovibrational dynamics. The vibrational part reads [29,46,47]

$$\begin{aligned}
 H^{\text{vib}} = & \frac{1}{m} \left[ -\frac{\partial^2}{\partial R_1^2} - \frac{\partial^2}{\partial R_2^2} - \cos\theta \frac{\partial}{\partial R_1} \frac{\partial}{\partial R_2} \right] \\
 & - \frac{1}{m} \left( \frac{1}{R_1^2} + \frac{1}{R_2^2} - \frac{\cos\theta}{R_1 R_2} \right) \left( \frac{\partial^2}{\partial \theta^2} + \cot\theta \frac{\partial}{\partial \theta} \right) \\
 & - \frac{1}{m} \left( \frac{1}{R_1 R_2} - \frac{1}{R_2} \frac{\partial}{\partial R_1} - \frac{1}{R_1} \frac{\partial}{\partial R_2} \right) \left( \cos\theta + \sin\theta \frac{\partial}{\partial \theta} \right) \\
 & + \epsilon_-(R_1, R_2, \theta). \tag{8}
 \end{aligned}$$

This Hamiltonian acts on wave functions  $\chi(R_1, R_2, \theta)$  being normalized as  $\int dR_1 dR_2 d\theta \sin\theta |\chi(R_1, R_2, \theta)|^2 = 1$ . The total angular momentum  $J$  of the nuclei is conserved and we focus on  $J = 0$ , for which case the rovibrational part of the Hamiltonian vanishes. For  $^{87}\text{Rb}$  we use  $m = 1.58 \times 10^5$  a.u. and consider only bosonic states which satisfy, according to spin statistics,  $\chi(R_1, R_2, \theta) = \chi(R_2, R_1, \theta)$ .

Eigenstates of (8) are obtained numerically in position space representation on a three-dimensional cubic grid. For the  $R_1$  and  $R_2$  direction we use equidistant grid points and build the derivative operators via finite difference expressions.

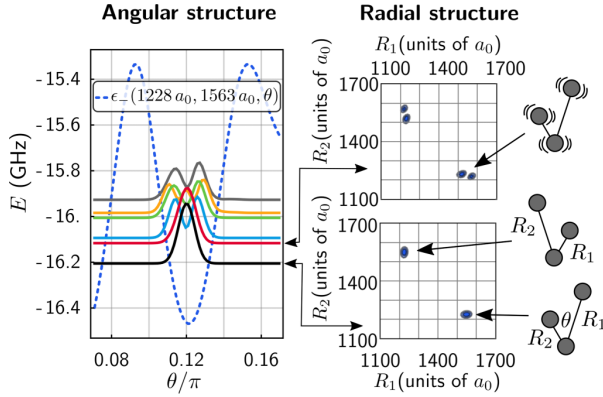


FIG. 3. Bound vibrational states localized in the minimum  $(R_1^0, R_2^0, \theta^0) = (1228a_0, 1563a_0, 0.12\pi)$ , that is marked by the dashed red line in Fig. 2. (Left) Angular cuts through the potential minimum (dashed blue lines) and reduced angular densities of vibrational states (solid lines). The offset is adjusted to their binding energy. (Right) Contour plots in the  $R_1$ - $R_2$  plane of reduced radial densities for the two lowest states. Pictorial representation of the molecular geometry are used to interpret these densities.

For the  $\theta$  degree of freedom we employ a discrete variable representation (DVR) approach [48]. In a first step Legendre polynomials  $P_l(\cos \theta)$  are used as basis functions to construct all kinetic-energy operators related to  $\theta$  as well as the operator  $\cos(\theta)$ . In a second step these operators are transformed into a new basis of eigenstates of  $\cos(\theta)$ , which can be viewed as a discrete approximation of position states  $|\theta\rangle$ . This approach is nonvariational but has the advantage that the operator of the PES  $\epsilon_-(R_1, R_2, \theta)$  is diagonal, i.e., there is no need to evaluate overlap integrals. We achieve good convergence by using typically a set of 80 grid points in each dimension.

Figure 3 presents reduced densities of the six energetically lowest vibrational states  $\chi(R_1, R_2, \theta)$  that localize in the potential well at  $(R_1^0, R_2^0, \theta^0) = (1228a_0, 1563a_0, 0.12\pi)$ . Out of all resulting eigenstates, the states shown in Fig. 3 were obtained by selecting those having the largest integrated probability density in the potential well considered. The angular densities  $[\int dR_1 dR_2 |\chi(R_1, R_2, \theta)|^2]$  of these states are depicted in Fig. 3 (left) together with an angular cut of the PES through the minimum  $\epsilon_-(1228a_0, 1563a_0, \theta)$ . All depicted densities are very localized around the minimum  $\theta^0$ . The ground state has an energy of  $-16.2$  GHz and a Gaussian-shaped angular density. The corresponding radial density  $[\int d\theta |\chi(R_1, R_2, \theta)|^2 \sin \theta]$  is presented in Fig. 3 (right) and exhibits two peaks. One near  $(R_1, R_2) = (R_1^0, R_2^0)$  and the other near  $(R_1, R_2) = (R_2^0, R_1^0)$ . This double-peak structure is a consequence of the bosonic symmetry and implies that the molecule is in a superposition of the two “check-mark” geometries, that are shown as cartoons in Fig. 3. The next higher vibrational state appears approximately 100 MHz above the ground state. While its angular density resembles the density of the ground state, its radial density possesses additional nodes that indicate an excited stretching mode vibration; see pictorial representation in Fig. 3. Even higher excited states exhibit combined bending and stretching excitations.

Altogether, the resulting vibrational states demonstrate that the bent equilibrium geometries of trilobite trimers are stable enough to support a number of vibrational states and that their vibrational spacing is large enough to be resolved in current experimental setups [8].

#### IV. CONCLUSIONS

We presented the rich molecular structure of trilobite trimers and derived a simple building principle that explains their geometry. Starting from a stable diatomic trilobite, a robust trimer can be formed when the second ground-state atom is placed in a density maximum of the diatomic trilobite wave function. For  $^{87}\text{Rb}$  trimers correlated to  $n = 30$ , we demonstrated that the resulting potential minima are deep enough to support a series of localized vibrational states with energy spacings on the order of 100 MHz. The plethora of equilibrium geometries opens fascinating possibilities to control the arrangement of triatomic molecules but poses also a new challenge to experiments: states in different molecular geometries can have comparable vibrational energies and can therefore hardly be distinguished spectroscopically. Future studies might therefore investigate as to which extent external fields or optical lattices could serve as additional selection mechanisms. Furthermore, it might be interesting to generalize the derived building principle of trilobite trimers to tetramers or even larger clusters.

#### ACKNOWLEDGMENTS

F.H. and P.S. acknowledge support from the German Research Foundation within the priority program “Giant Interactions in Rydberg Systems” (DFG SPP 1929 GiRyd). C.F. gratefully acknowledges a scholarship by the Studienstiftung des deutschen Volkes. We thank M. T. Eiles for fruitful discussions.

#### APPENDIX: TRILOBITE ORBITALS

To derive and to interpret the PES of the triatomic molecule (5) we employed a two-dimensional basis that consists of the trilobite orbitals  $\phi(\mathbf{r}; \mathbf{R}_1)$  and  $\phi(\mathbf{r}; \mathbf{R}_2)$ ; see (4). One can show that this approach is exact in the sense that it yields the same PES (5) and the same electronic states as the diagonalization of the interaction  $V$  in the larger basis set of hydrogenic states  $\varphi_{n_0 l m}(\mathbf{r})$  with fixed  $n_0$ ,  $3 \leq l \leq n_0 - 1$ , and  $|m| \leq l$ . We prove this by demonstrating that the interaction matrix  $V$  in (1) can be written as

$$V = \sum_{j=1}^N 2\pi a[k(R_j)] |\phi_j\rangle \langle \phi_j|, \quad (\text{A1})$$

where  $|\phi_j\rangle$  denotes the unnormalized trilobite state with wave function  $\langle \mathbf{r} | \phi_j \rangle = \phi(\mathbf{r}; \mathbf{R}_j)$  as defined in (2). The number of ground-state atoms  $N$  is in our case  $N = 2$ . From (A1) it becomes evident that all basis states which are perpendicular to the trilobite orbitals  $\phi(\mathbf{r}; \mathbf{R}_1)$  and  $\phi(\mathbf{r}; \mathbf{R}_2)$  will not interact with the ground-state atoms and will, therefore, not contribute to the trimer PES, nor to its molecular states.

To prove (A1) we introduce the multi-index  $\alpha = (n_0, l, m)$  that labels all basis states compactly as  $\varphi_\alpha(\mathbf{r})$ . The matrix

elements of the delta potential of the  $j$ th perturber read in this basis

$$\langle \varphi_\alpha | \delta(\mathbf{r} - \mathbf{R}_j) | \varphi_{\alpha'} \rangle = \varphi_\alpha^*(\mathbf{R}_j) \varphi_{\alpha'}(\mathbf{R}_j). \quad (\text{A2})$$

A particular property of this matrix is that all rows are linear dependent, e.g., the first row

$$\varphi_1^*(\mathbf{R}_j) [\varphi_1(\mathbf{R}_j), \varphi_2(\mathbf{R}_j), \varphi_3(\mathbf{R}_j), \dots] \quad (\text{A3})$$

is proportional to the second row

$$\varphi_2^*(\mathbf{R}_j) [\varphi_1(\mathbf{R}_j), \varphi_2(\mathbf{R}_j), \varphi_3(\mathbf{R}_j), \dots], \quad (\text{A4})$$

etc. Consequently, the rank of the matrix representation (A2) is maximally one and there is, hence, maximally one eigenstate of this matrix with a nonzero eigenvalue. This is the trilobite state (2)

$$|\phi_j\rangle = \sum_\alpha \varphi_\alpha^*(\mathbf{R}_j) |\varphi_\alpha\rangle \quad (\text{A5})$$

with eigenvalue  $\sum_\alpha |\varphi_\alpha(\mathbf{R}_j)|^2 = \langle \phi_j | \phi_j \rangle$ . For this reason one can replace the delta potential (in the here considered basis set) by

$$\delta(\mathbf{r} - \mathbf{R}_j) = |\phi_j\rangle \langle \phi_j|, \quad (\text{A6})$$

which proves (A1).

- 
- [1] C. H. Greene, A. S. Dickinson, and H. R. Sadeghpour, *Phys. Rev. Lett.* **85**, 2458 (2000).
- [2] E. L. Hamilton, C. H. Greene, and H. R. Sadeghpour, *J. Phys. B: At. Mol. Opt. Phys.* **35**, L199 (2002).
- [3] A. A. Khuskivadze, M. I. Chibisov, and I. I. Fabrikant, *Phys. Rev. A* **66**, 042709 (2002).
- [4] J. Tallant, S. T. Rittenhouse, D. Booth, H. R. Sadeghpour, and J. P. Shaffer, *Phys. Rev. Lett.* **109**, 173202 (2012).
- [5] B. J. DeSalvo, J. A. Aman, F. B. Dunning, T. C. Killian, H. R. Sadeghpour, S. Yoshida, and J. Burgdörfer, *Phys. Rev. A* **92**, 031403 (2015).
- [6] D. Booth, S. T. Rittenhouse, J. Yang, H. R. Sadeghpour, and J. P. Shaffer, *Science* **348**, 99 (2015).
- [7] T. Niederprüm, O. Thomas, T. Eichert, C. Lippe, J. Pérez-Ríos, C. H. Greene, and H. Ott, *Nat. Commun.* **7**, 12820 (2016).
- [8] K. S. Kleinbach, F. Meinert, F. Engel, W. J. Kwon, R. Löw, T. Pfau, and G. Raithel, *Phys. Rev. Lett.* **118**, 223001 (2017).
- [9] A. T. Krupp, A. Gaj, J. B. Balewski, P. Ilzhöfer, S. Hofferberth, R. Löw, T. Pfau, M. Kurz, and P. Schmelcher, *Phys. Rev. Lett.* **112**, 143008 (2014).
- [10] I. Lesanovsky, P. Schmelcher, and H. R. Sadeghpour, *J. Phys. B: At. Mol. Opt. Phys.* **39**, L69 (2006).
- [11] A. Gaj, A. T. Krupp, J. B. Balewski, R. Löw, S. Hofferberth, and T. Pfau, *Nat. Commun.* **5**, 4546 (2014).
- [12] M. Kurz and P. Schmelcher, *Phys. Rev. A* **88**, 022501 (2013).
- [13] M. Kurz and P. Schmelcher, *J. Phys. B: At. Mol. Opt. Phys.* **47**, 165101 (2014).
- [14] N. Sándor, R. González-Férez, P. S. Julienne, and G. Pupillo, *Phys. Rev. A* **96**, 032719 (2017).
- [15] O. Thomas, C. Lippe, T. Eichert, and H. Ott, *Nat. Commun.* **9**, 2238 (2018).
- [16] D. A. Anderson, S. A. Miller, and G. Raithel, *Phys. Rev. Lett.* **112**, 163201 (2014).
- [17] H. Saßmannshausen, F. Merkt, and J. Deiglmayr, *Phys. Rev. Lett.* **114**, 133201 (2015).
- [18] F. Böttcher, A. Gaj, K. M. Westphal, M. Schlagmüller, K. S. Kleinbach, R. Löw, T. C. Liebisch, T. Pfau, and S. Hofferberth, *Phys. Rev. A* **93**, 032512 (2016).
- [19] M. Schlagmüller, T. C. Liebisch, H. Nguyen, G. Lochead, F. Engel, F. Böttcher, K. M. Westphal, K. S. Kleinbach, R. Löw, S. Hofferberth, T. Pfau, J. Pérez-Ríos, and C. H. Greene, *Phys. Rev. Lett.* **116**, 053001 (2016).
- [20] J. L. MacLennan, Y.-J. Chen, and G. Raithel, [arXiv:1808.05136](https://arxiv.org/abs/1808.05136) [*Phys. Rev. A* (to be published)].
- [21] K. S. Kleinbach, F. Engel, T. Dieterle, R. Löw, T. Pfau, and F. Meinert, *Phys. Rev. Lett.* **120**, 193401 (2018).
- [22] T. Schmid, C. Veit, N. Zuber, R. Löw, T. Pfau, M. Tarana, and M. Tomza, *Phys. Rev. Lett.* **120**, 153401 (2018).
- [23] F. Engel, T. Dieterle, T. Schmid, C. Tomschitz, C. Veit, N. Zuber, R. Löw, T. Pfau, and F. Meinert, *Phys. Rev. Lett.* **121**, 193401 (2018).
- [24] I. C. H. Liu and J. M. Rost, *Eur. Phys. J. D* **40**, 65 (2006).
- [25] V. Bendkowsky, B. Butscher, J. Nipper, J. B. Balewski, J. P. Shaffer, R. Löw, T. Pfau, W. Li, J. Stanojevic, T. Pohl, and J. M. Rost, *Phys. Rev. Lett.* **105**, 163201 (2010).
- [26] R. Schmidt, H. R. Sadeghpour, and E. Demler, *Phys. Rev. Lett.* **116**, 105302 (2016).
- [27] F. Camargo, R. Schmidt, J. D. Whalen, R. Ding, G. Woehl, S. Yoshida, J. Burgdörfer, F. B. Dunning, H. R. Sadeghpour, E. Demler, and T. C. Killian, *Phys. Rev. Lett.* **120**, 083401 (2018).
- [28] R. Schmidt, J. D. Whalen, R. Ding, F. Camargo, G. Woehl, S. Yoshida, J. Burgdörfer, F. B. Dunning, E. Demler, H. R. Sadeghpour, and T. C. Killian, *Phys. Rev. A* **97**, 022707 (2018).
- [29] C. Fey, M. Kurz, and P. Schmelcher, *Phys. Rev. A* **94**, 012516 (2016).
- [30] C. Fey, J. Yang, S. T. Rittenhouse, F. Munkes, P. Schmelcher, H. R. Sadeghpour, and J. P. Shaffer, [arXiv:1803.09781](https://arxiv.org/abs/1803.09781) [*Phys. Rev. Lett.* (to be published)].
- [31] I. C. H. Liu, J. Stanojevic, and J. M. Rost, *Phys. Rev. Lett.* **102**, 173001 (2009).
- [32] P. J. J. Luukko and J.-M. Rost, *Phys. Rev. Lett.* **119**, 203001 (2017).
- [33] J. A. Fernández, P. Schmelcher, and R. González-Férez, *J. Phys. B: At. Mol. Opt. Phys.* **49**, 124002 (2016).
- [34] E. Fermi, *Nuovo Cimento* (1924–1942) **11**, 157 (1934).
- [35] A. Omont, *J. Phys. (Paris)* **38**, 1343 (1977).
- [36] L. Spruch, T. F. O'Malley, and L. Rosenberg, *Phys. Rev. Lett.* **5**, 375 (1960).
- [37] T. F. O'Malley, L. Spruch, and L. Rosenberg, *J. Math. Phys.* **2**, 491 (1961).
- [38] C. Bahrim, U. Thumm, and I. I. Fabrikant, *J. Phys. B: At. Mol. Opt. Phys.* **34**, L195 (2001).

- [39] M. T. Eiles and C. H. Greene, *Phys. Rev. A* **95**, 042515 (2017).
- [40] M. T. Eiles, J. Pérez-Ríos, F. Robicheaux, and C. H. Greene, *J. Phys. B: At. Mol. Opt. Phys.* **49**, 114005 (2016).
- [41] F. Hummel, C. Fey, and P. Schmelcher, *Phys. Rev. A* **97**, 043422 (2018).
- [42] F. Hummel, C. Fey, and P. Schmelcher, *Phys. Rev. A* **99**, 023401 (2019).
- [43] C. Fey, M. Kurz, P. Schmelcher, S. T. Rittenhouse, and H. R. Sadeghpour, *New J. Phys.* **17**, 055010 (2015).
- [44] M. Tarana and R. Čurík, *Phys. Rev. A* **93**, 012515 (2016).
- [45] B. E. Granger, E. L. Hamilton, and C. H. Greene, *Phys. Rev. A* **64**, 042508 (2001).
- [46] N. Handy and S. Carter, *Mol. Phys.* **47**, 1445 (1982).
- [47] N. Handy, *Mol. Phys.* **61**, 207 (1987).
- [48] M. Beck and H.-D. Meyer, *Phys. Rep.* **324**, 1 (2000).

### 3.9 Triatomic Butterfly molecules

# Triatomic butterfly molecules

Matthew T Eiles<sup>1</sup>, Christian Fey<sup>2</sup>, Frederic Hummel<sup>3</sup> and Peter Schmelcher<sup>3,4</sup>

<sup>1</sup>Max-Planck-Institut für Physik komplexer Systeme, Nöthnitzer Str. 38, D-01187 Dresden, Germany

<sup>2</sup>Max-Planck-Institute of Quantum Optics, Hans-Kopfermann-Strasse. 1, D-85748 Garching, Germany

<sup>3</sup>Zentrum für Optische Quantentechnologien, Fachbereich Physik, Universität Hamburg, Luruper Chaussee 149, D-22761 Hamburg, Germany

<sup>4</sup>The Hamburg Centre for Ultrafast Imaging, Universität Hamburg, Luruper Chaussee 149, D-22761 Hamburg, Germany

E-mail: [meiles@mpg.pks.de](mailto:meiles@mpg.pks.de)

Received 5 September 2019, revised 25 October 2019

Accepted for publication 5 February 2020

Published 16 March 2020



CrossMark

## Abstract

We detail the rich electronic and vibrational structure of triatomic ‘butterfly’ molecules, ultra-long-range Rydberg molecules bound by resonant  $p$ -wave scattering. We divide these molecules into two sub-classes depending on their parity under reflection of the electronic wave function through the molecular plane. The trimers with odd reflection parity have smoothly varying, non-oscillatory potential energy surfaces except near the collinear configuration. Here, the vibrational wave function is confined tightly in the symmetric-stretch and bending modes, but only loosely in the asymmetric stretch mode. The trimers with even reflection parity exhibit far richer potential surfaces with abundant minima, but only a few of these are deep enough to localize the vibrational states. These minima are correlated with the electronic wave functions of the butterfly dimer, contributing to a building principle for trimers.

Keywords: external fields, ultralong-range molecules, rydberg states

(Some figures may appear in colour only in the online journal)

## 1. Introduction

With very few exceptions, atomic negative ions—weakly bound systems composed of an electron ( $e^-$ ) and a neutral atom ( $B$ )—possess only a single bound state [1, 2]. In the alkali atoms this is the  $^1S$  state, bound by about 500 meV. For several years the existence of an excited  $^3P$  state in cesium was under debate until photodetachment experiments eventually revealed that it is in fact an unbound shape resonance [3–9]. Indeed, all alkali species possess a  $p$ -wave shape resonance just a few meV above threshold [1, 2, 10].

Despite the transient nature of these resonances, they are responsible for the formation of a class of ultra-long-range Rydberg molecules known as ‘butterflies.’ A butterfly molecule consists of a Rydberg atom ( $B^+ + e^-$ ) bound to a neutral ground state atom ( $B$ ) via the  $e^- + B$   $p$ -wave scattering interaction, which leads at resonance to a short-lived ion-pair state [11–13]. Superimposed onto this ion-pair potential is the oscillatory structure of the Rydberg wave function, and vibrational states form in the resulting potential wells. Butterfly molecules have been observed in rubidium and, due to

their large dipole moments, exhibit pendular behavior in weak external fields [14, 15].

In this article, we show that this  $p$ -wave binding mechanism can bind a second ground-state atom to the Rydberg atom, forming a triatomic butterfly molecule. Other ultra-long-range triatomic Rydberg molecules formed by the  $s$ -wave scattering interaction have been studied previously theoretically and experimentally [16–23], but a study of the butterfly trimer’s full electronic and vibrational structure has not yet been attempted. We determine this structure by computing, analyzing, and interpreting the underlying three-dimensional potential energy surfaces based on the Born–Oppenheimer approximation and the resulting nuclear eigenstates. The latter are obtained using a combined discrete variable and finite difference approach. This effort is simplified by the fact that the potential surfaces decouple into two groups distinguished by their electronic parity under reflection through the molecular plane. We refer to these two classes as *odd* and *even* butterfly trimers. The equilibrium geometries supporting trimer states vary greatly between these two classes: the odd butterflies have only a few minima

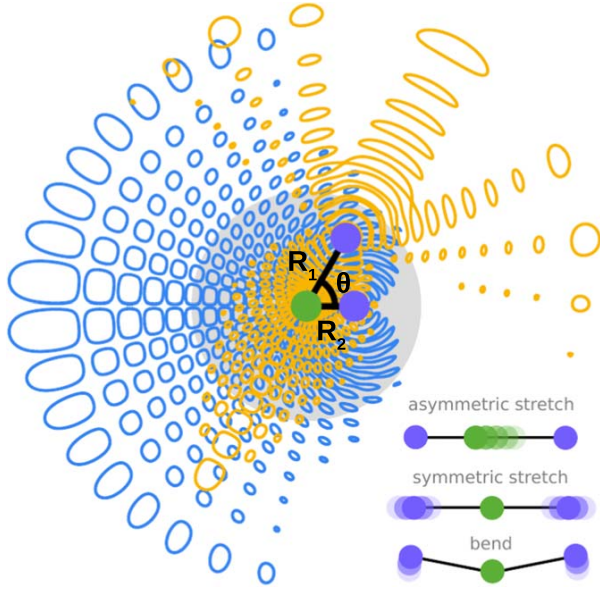


**Figure 1.** A schematic of the  $n = 30$  butterfly trimer. The two ground-state atoms are marked in purple, and the Rydberg atom is shown in green. The approximate range of bond lengths considered in this butterfly regime lie within the shaded region. The electronic densities of the  $\theta_2$ -butterfly and the  $R_1$ -butterfly are depicted in blue and yellow contours, respectively, where each contour specifies when the wave function amplitude evaluated in the molecular plane equals  $1 \times 10^{-4.8}$ . The two bond lengths and bending angle are labeled. On the lower right the three types of nuclear motion exhibited by the trimer are depicted.

in a constrained range of possible molecular geometries close to the collinear arrangement, whereas the even butterflies possess a plethora of equilibrium configurations with a rich diversity in the electronic character. The geometries at which these minima occur can be analyzed and understood from features in the electronic wave functions of the diatomic butterfly molecule.

In section 2 we discuss our approach to the electronic structure of the trimers and, specifically, their Born–Oppenheimer adiabatic potential energy surfaces. Sections 3 and 4 are dedicated to a discussion of the equilibrium configurations and geometries and the development of a building principles for the even trimers, respectively. Section 5 analyzes the vibrational dynamics of our butterfly trimers. Finally, section 6 contains our brief conclusions and an outlook.

## 2. Computational approach to the electronic structure and Born–Oppenheimer potential energy surfaces

The eigenenergies of the electronic Hamiltonian for fixed nuclei represent the Born–Oppenheimer potential energy surfaces. For our trimers, they depend on the two bond lengths,  $R_1$  and  $R_2$ , and a single bending angle,  $\theta$ . This geometry is illustrated in figure 1. The trimer can exhibit three vibrational modes: a symmetric stretch, in which  $R_1 = R_2$ ; an

asymmetric stretch, in which  $R_1$  grows while  $R_2$  shrinks (or vice versa); and a bending mode in which  $\theta$  oscillates.

The interaction of the electron with a ground-state atom is given by the Fermi pseudopotential, generalized by Omont to arbitrary partial waves [24, 25]. Including contributions from  $s$ - and  $p$ -scattering partial waves only, we obtain the Hamiltonian

$$H(\vec{r}; R_1, R_2, \theta) = -\sum_{nlm} \frac{|nlm\rangle\langle nlm|}{2(n-\mu_l)^2} + 2\pi\sum_{i=1}^2\sum_{\xi=1}^4 a_i^{(\xi)} |i\xi\rangle\langle i\xi|. \quad (1)$$

The first line describes the Rydberg atom using its known eigenfunctions  $\phi_{nlm}(\vec{r}) = \frac{u_{nl}(r)}{r} Y_{lm}(\theta, \varphi) = \langle \vec{r} | nlm \rangle$  and eigenenergies  $-\frac{1}{2(n-\mu_l)^2}$ , where  $n$  is the principal quantum number and  $l$  and  $m$  are the orbital and magnetic quantum numbers. For a given  $n$  only a few states with  $l \leq l_{\min}$  have non-vanishing quantum defects  $\mu_l$  which shift them out of the degenerate manifold of high- $l$  states. The second line of equation (1) describes the electron–atom interactions using the Fermi–Omont pseudopotential operator,  $\hat{V}^{(i\xi)} = |i\xi\rangle\langle i\xi|$ , which has the following matrix representation in the Rydberg basis

$$\hat{V}_{n'l'm',nlm}^{(i\xi)} = \tilde{\partial}_\xi[\phi_{n'l'm'}(\vec{r})]^* \tilde{\partial}_\xi[\phi_{nlm}(\vec{r})] |_{\vec{r}=\vec{R}_i}. \quad (2)$$

This employs a shorthand for the derivative operators used in the pseudopotentials:  $\tilde{\partial}_{\xi=1} = 1$ ,  $\tilde{\partial}_{\xi=2} = \partial_r$ ,  $\tilde{\partial}_{\xi=3} = \frac{1}{r}\partial_\theta$ , and  $\tilde{\partial}_{\xi=4} = \frac{1}{r\sin\theta}\partial_\varphi$ . The three  $\xi > 1$  terms correspond to the three components of the gradient in the  $p$ -wave operator. The scattering volumes are  $a_i^{(\xi=1)} = a_s[k(R_i)]$  and  $a_i^{(\xi>1)} = 3a_p^3[k(R_i)]$ . Equation (1) neglects all spin degrees of freedom, and assumes the scattering occurs only in the triplet channel [26–29].

A convenient approach to diagonalize equation (1) has been developed which does not require the complete Rydberg basis. For a given  $i$ ,  $\xi$ ,  $n$ , and for  $l > l_{\min}$ , the matrix defined in equation (2) has a single non-trivial eigenstate. It follows that there are four ‘dimer orbitals’ in total for each atom,  $i = 1, 2$ : one ‘trilobite’ for  $\xi = 1$ , an ‘ $R_i$ -butterfly’ for  $\xi = 2$ , a ‘ $\theta_i$ -butterfly’ for  $\xi = 3$ , and a ‘ $\varphi_i$ -butterfly’ for  $\xi = 4$ . Figure 1 shows two of these dimer orbitals, the  $R_1$ -butterfly (orange) and  $\theta_2$ -butterfly (blue). The nodal structures of the butterfly dimer orbitals are arranged such that, at the position of the ground state atom, the wave function changes most rapidly parallel to ( $R$ -butterfly) or perpendicular to ( $\theta$ - and  $\varphi$ -butterflies, in mutually orthogonal directions) the internuclear axis. The  $R$ -butterfly orbital therefore concentrates electron probability around the internuclear axis, while in the  $\theta$ - and  $\varphi$ -butterflies the electronic density fans out over a larger area. The electronic energies of the  $\theta$ -butterfly and  $\varphi$ -butterfly dimer orbitals are degenerate. In general, the dimer orbitals are not orthogonal: a  $\xi = \alpha$  orbital for the atom located at  $\vec{R}_p$  has an overlap with the  $\xi = \beta$  orbital at position  $\vec{R}_q$  equal to [16, 17, 19, 23]

$$\Upsilon_{pq}^{\alpha\beta} = \sum_{l>l_{\min}}^{n-1} \sum_{m=-l}^{m=l} \tilde{\partial}_\alpha[\phi_{nlm}(\vec{R}_p)]^* \tilde{\partial}_\beta\phi_{nlm}(\vec{R}_q). \quad (3)$$

Several of these overlap elements vanish at specific geometries. As detailed in [19, 30], the projection of the orbital angular momentum of the  $\xi = 2$  orbital onto the internuclear axis is zero, while it is unity for the  $\xi = 3$  and  $\xi = 4$  orbitals. Therefore, the matrix elements  $\Upsilon_{ii}^{23}$  and  $\Upsilon_{ii}^{24}$  vanish. Furthermore, the  $\xi = 4$  orbital has odd parity under reflection through the molecular plane, i.e.  $\varphi \rightarrow -\varphi$ , while the  $\xi = 2$  orbital is independent of this angle and the  $\xi = 3$  orbital is an even function of  $\varphi$ . Thus, both  $\xi = 2, 3$  orbitals have even parity under this same operation. This implies that these orbitals decouple completely from  $\xi = 4$ , i.e.  $\Upsilon_{ii'}^{4\beta} = 0$  for  $\beta = 2, 3$ . For this reason, in this paper we distinguish between the *even* trimers, which are linear combinations of the  $R_1, R_2, \theta_1$ , and  $\theta_2$  dimer orbitals, and the *odd* trimers, linear combinations of the two  $\varphi_1$  and  $\varphi_2$  dimer orbitals.

Due to the effects of the  $p$ -wave resonance, the trilobite states are energetically decoupled from the butterfly states and from other  $n$  manifolds, and to a good approximation can be studied independently. References [17, 23] have already investigated the trilobite trimer, i.e. the states defined by the Hamiltonian in the  $2 \times 2$  trilobite subspace:

$$\tilde{H}_t = \begin{pmatrix} a_1^{(1)}[k(R_1)]\Upsilon_{11}^{11} & a_1^{(1)}[k(R_1)]\Upsilon_{12}^{11} \\ a_1^{(1)}[k(R_2)]\Upsilon_{21}^{11} & a_1^{(1)}[k(R_2)]\Upsilon_{22}^{11} \end{pmatrix}, \quad (4)$$

where the overall Rydberg energy  $-\frac{1}{2n^2}$  has been set to zero. This separation of trilobite and butterfly states implies that the butterfly states of a single  $n$  manifold are governed by the Hamiltonian  $\tilde{H}_b$ :

$$\begin{pmatrix} a_1^{(2)}\Upsilon_{11}^{22} & a_1^{(2)}\Upsilon_{21}^{22} & 0 & a_1^{(2)}\Upsilon_{21}^{32} & 0 & 0 \\ a_2^{(2)}\Upsilon_{12}^{22} & a_2^{(2)}\Upsilon_{22}^{22} & a_2^{(2)}\Upsilon_{12}^{32} & 0 & 0 & 0 \\ 0 & a_1^{(3)}\Upsilon_{21}^{23} & a_1^{(3)}\Upsilon_{11}^{33} & a_1^{(3)}\Upsilon_{21}^{33} & 0 & 0 \\ a_2^{(3)}\Upsilon_{12}^{23} & 0 & a_2^{(3)}\Upsilon_{12}^{33} & a_2^{(3)}\Upsilon_{22}^{33} & 0 & 0 \\ 0 & 0 & 0 & 0 & a_1^{(4)}\Upsilon_{11}^{44} & a_1^{(4)}\Upsilon_{21}^{44} \\ 0 & 0 & 0 & 0 & a_2^{(4)}\Upsilon_{12}^{44} & a_2^{(4)}\Upsilon_{22}^{44} \end{pmatrix}. \quad (5)$$

Note that in equations (4) and (5) the Hamiltonian marked by a tilde is modified from the original Hamiltonian  $H$  since it includes the effect of the non-orthogonal basis:

$$\frac{\Upsilon^{-1}H\psi}{\tilde{H}} = E \underbrace{\Upsilon^{-1}\Upsilon}_{\mathbf{1}}\psi. \quad (6)$$

The studies of trilobite trimers in [16, 23] found that the eigenvalues of equation (4) are nearly identical to those computed using the full Rydberg basis, consisting of states with finite quantum defects and multiple Rydberg manifolds. This is because the coupling between the trilobite and these other states is negligible. However, this same treatment fails catastrophically for studies of butterfly states as it is impossible to obtain even qualitatively accurate predictions within perturbation theory. The  $p$ -wave shape resonance causes the scattering volume to diverge, and the butterfly potential surfaces are only constrained to finite values via coupling to additional Rydberg manifolds. Additionally, the butterfly potential surface plunges through and couples to all quantum

defect states before being repelled from the lower Rydberg manifold [11]. This coupling is quantitatively important.

These problems are addressed by including trilobite and butterfly dimer orbitals for several  $n$  manifolds ( $\mathcal{M}$  is the number of manifolds) as well as the atomic basis states which have non-zero quantum defects in a hybrid basis [19, 30]. The potential energy surfaces obtained with this method are identical to those computed via the full diagonalization using the Rydberg basis implied in equation (1), but have the advantage of a much more compact matrix representation. The Hamiltonian for a  $N$ -perturber molecule in this basis is written

$$\tilde{H} = \begin{pmatrix} O_{PP'} & 0 \\ 0 & 1_{QQ'} \end{pmatrix}^{-1} \begin{pmatrix} H_{PP'} & H_{PQ'} \\ H_{QP'} & H_{QQ'} \end{pmatrix}, \quad (7)$$

where the sub-block  $H_{PP'}$  of dimension  $4\mathcal{M}N$ , the quantum defect sub-block  $H_{QQ'}$  of dimension  $\mathcal{M}(l_{\min} + 1)^2$ , and the overlap matrix  $O_{PP'}$  have matrix elements

$$H_{PP'} = -\frac{1}{2n^2} \Upsilon_{pq,n}^{\alpha\beta} \delta_{nn'} + 2\pi \sum_{i=1}^N \sum_{\xi=1}^4 a_i^{(\xi)} \Upsilon_{pi,n}^{\alpha\xi} \Upsilon_{iq,n'}^{\xi\beta}, \quad (8)$$

$$H_{QQ'} = -\frac{\delta_{nn'} \delta_{ll'}}{2(n - \mu_l)^2} + 2\pi \sum_{i=1}^N \sum_{\xi=1}^4 a_i^{(\xi)} \phi_{nlm}^{\xi}(R_i) \phi_{n'l'm'}^{\xi}(R_i) \quad (9)$$

$$O_{PP'} = \Upsilon_{pq,n}^{\alpha\beta} \delta_{nn'}. \quad (10)$$

Additionally, there are coupling terms between dimer orbitals and the low  $-l$  quantum defect states

$$H_{PQ'} = 2\pi \sum_{i=1}^N \sum_{\xi=1}^4 a_i^{(\xi)} \Upsilon_{pi,n}^{\alpha\xi} \phi_{n'l'm'}^{\xi}(R_i). \quad (11)$$

In our present calculations we use the  $n = 29, 30$ , and  $31$  Rydberg manifolds and include quantum defects for  $s, p$ , and  $d$  waves ( $l_{\min} = 2$ ). These parameters give adequately converged potential energy surfaces for reasonable qualitative results. Using a zero-range pseudopotential entails the assumption of several approximations which can become poor at small internuclear distances. However, recent experiments in this regime [14, 31] along with comparisons with more accurate theoretical approaches [11, 13, 32] have shown that, for  $R > 100a_0$ , the pseudopotential remains quite accurate, especially considering our neglect of spin-dependent interactions which is a much larger source of error. We emphasize that our goal is to provide quantitatively accurate results within our stated approximations and use these to build up a qualitatively rigorous analysis of the structure of these molecules.

### 3. Analysis of adiabatic potential energy surfaces

For the paradigmatic Rydberg state studied here,  $n = 30$ , the allowed range of internuclear distances for the butterfly states is  $R_i \in (100, 600)$ . This range is determined by the energy dependence of the  $p$ -wave scattering volume, which in turn depends on  $R$  through the semiclassical kinetic energy of the electron,  $k(R)^2 = 2R^{-1} - n^{-2}$ . The bond length  $R_{\text{res}}$  associated with the shape resonance is therefore determined by the

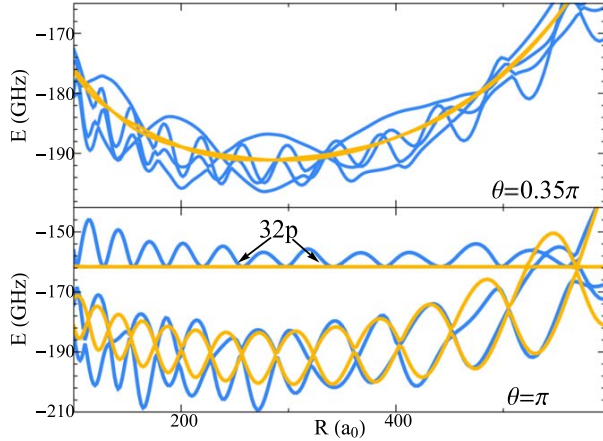


**Figure 2.** Breathing mode slices of the  $\text{Rb}_3$  potential surface for different bending angles  $\theta$ . Note the different energy axes in the two panels. The orange and blue curves have odd and even parity, respectively. The energies are relative to the hydrogenic  $n = 30$  energy. The potential energy surface associated with the  $32p$  state cuts through the lower panel.

equation  $2R_{\text{res}}^{-1} - n^{-2} = 2E_{\text{res}}$ . For  $n = 30$ ,  $R_{\text{res}} \approx 600 a_0$ . It varies slowly as a function of  $n$ . The typical bond lengths of these molecules therefore do not scale proportional to  $n^2$  as in the trilobite molecules. Just as  $E_{\text{res}}$  varies among atomic species, so do these typical bond lengths [10].

The three-dimensional potential surfaces are challenging to visually investigate. Therefore, to get an impression of their behavior, we first exhibit in figure 2 the breathing mode potential curves (symmetric stretch vibration): these are cut through the surface with varying  $R = R_1 = R_2$  and fixed  $\theta$ . The two odd trimer potential curves (orange) oscillate dramatically in the collinear configuration, but at  $\theta = 0.35\pi$  they are very smooth and almost degenerate with each other and with the diatomic potential energy curve for the  $\xi = 4$  state (see figure 6). The four even trimer curves, on the other hand, oscillate for all values of  $\theta$ . When  $\theta = \pi$ , two of the potential curves become degenerate with the odd-trimer curves. For  $\theta \neq \pi$ , the even trimer curves separate into two sets having relatively fast and slow oscillation frequencies, respectively. The quickly (slowly) varying curves are predominantly mixtures of  $R_1$  and  $R_2$  ( $\theta_1$  and  $\theta_2$ ) dimer orbitals, as the coupling  $\Upsilon_{12}^{23}$  is typically small.

To gain further insight, we must move beyond the impediment of these low-dimensional potential cuts. Figure 3 presents the energetically deepest potential energy surface of the odd trimer state as a contour plot in the three nuclear coordinates. The deepest energy contours are only found near the collinear geometry ( $\theta = \pi$ ), where cylindrically shaped wells around deep minima can be found. As  $\theta$  decreases from  $\pi$ , the potential surface quickly becomes independent of  $\theta$ , and hence the constant energy contours become quite flat. Figure 4 shows the full potential energy surface  $V(R_1, R_2, \theta)$  for the same two fixed angles  $\theta = \pi, 0.35\pi$  as in figure 2. This shows in more detail the deep potential wells in the

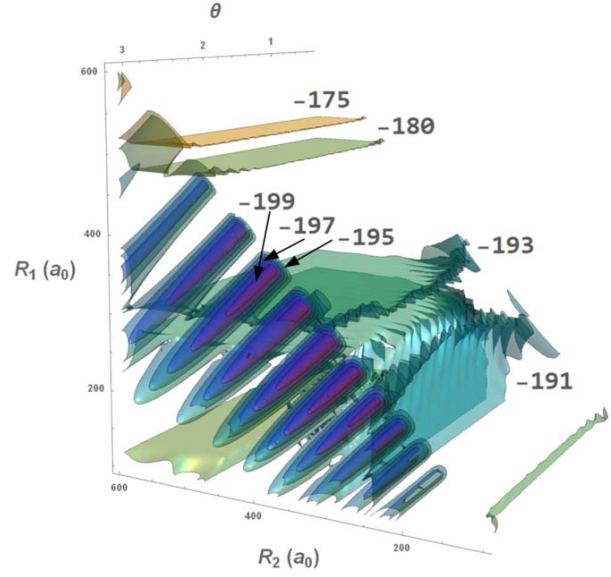


**Figure 3.** Contours of the complete potential energy surface for the odd trimer state. Each contour, specified by a different color, represents a surface of constant energy whose value is given in GHz in each label. The deepest contours are only found near the  $\theta = \pi$  plane, and the higher energy contours are insensitive to changes in  $\theta$ . Since the potentials are symmetric with respect to reflection across the  $R_1 = R_2$  line, the contours are not shown for  $R_1 > R_2$  for clarity.

collinear geometry and the nearly featureless surfaces at other arrangements.

These properties of the potential surfaces can be understood by analyzing the qualitative structure of the Hamiltonian more closely, focusing on the  $\xi = 4$  sub-block of equation (5). In this subspace the two odd trimer potential surfaces are

$$\varepsilon_{\pm}(\vec{R}_1, \vec{R}_2) = \frac{\varepsilon_d(R_1) + \varepsilon_d(R_2)}{2} \pm \frac{1}{2} \sqrt{[\varepsilon_d(R_1) - \varepsilon_d(R_2)]^2 + 4c(\vec{R}_1, \vec{R}_2)}, \quad (12)$$

where the cross term is

$$c(\vec{R}_1, \vec{R}_2) = 4a_1^{(4)}a_2^{(4)} \left| \sum_{l>l_{\min}}^{n-1} D_{l1}(R_1, 0)D_{l1}(R_2, \theta) \right|^2; \quad D_{lm}(R, \theta) = m \frac{u_{nl}(R)}{R^2} \frac{Y_{lm}(\theta, 0)}{\sin \theta}, \quad (13)$$

and the dimer potential is

$$\varepsilon_d(R) = a_1^{(4)} \sum_{l>l_{\min}}^{n-1} \left| \frac{u_{nl}(R)}{R^2} \right|^2 \frac{(2l+1)(l+1)l}{8\pi}. \quad (14)$$

When  $c(\vec{R}_1, \vec{R}_2)$  vanishes, the trimer potentials reduce to independent dimer potentials,  $\varepsilon_+(\vec{R}_1, \vec{R}_2) = \max[\varepsilon_d(R_1), \varepsilon_d(R_2)]$ ,  $\varepsilon_-(\vec{R}_1, \vec{R}_2) = \min[\varepsilon_d(R_1), \varepsilon_d(R_2)]$ , which are smooth and have a single global minimum. The cross-term induces mixing and creates additional wells in the potentials; however, it depends very sharply on  $\theta$ ,  $c(\vec{R}_1, \vec{R}_2) \sim \frac{1}{\sin^4 \theta}$ . This explains the appearance of interesting triatomic features only near the collinear geometry where  $\theta = \pi$ . We exclude angles near  $\theta = 0$

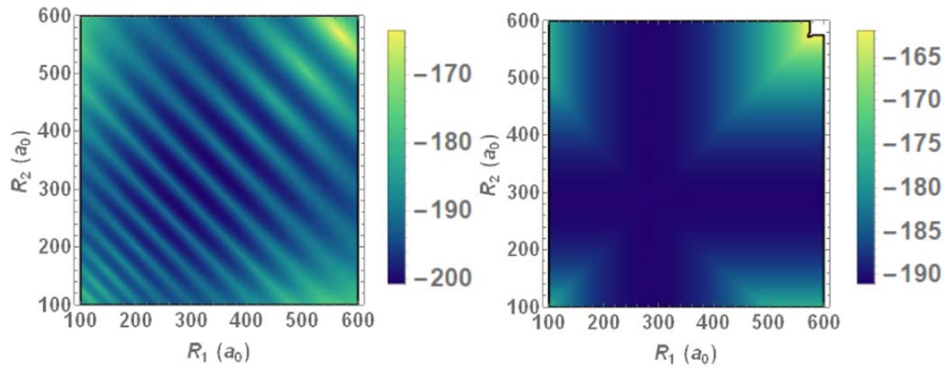


**Figure 4.** Odd parity potential surfaces at  $\theta = \pi$  and  $\theta = 0.35\pi$  (left and right, respectively). The units of potential energy are in GHz.

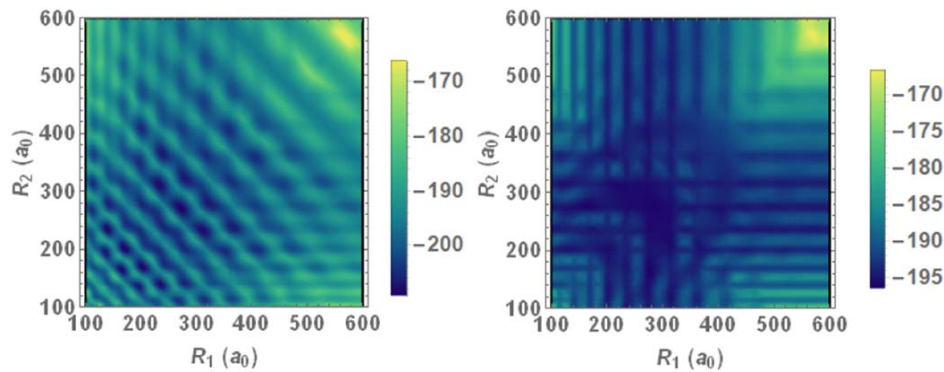


**Figure 5.** Even trimer potential surfaces at  $\theta = \pi$  and  $\theta = 0.35\pi$  (left and right, respectively). The units of potential energy are in GHz.

from our analysis as we have not included atom-atom interactions which would become highly relevant at these geometries.

In contrast to the simplicity of the odd trimer potential surfaces, the even trimer potential surfaces are highly complex, varying much more rapidly as a function of all coordinates, but particularly as a function of  $\theta$ . For this reason a contour plot visualization is unintelligible, and we only show radial potential cuts in figure 5 at the same two angles as before. These have minima at a plethora of stable molecular geometries. By comparing the two panels in figure 5 we find that the potential wells in which these minima form are much more isolated from one another in the collinear geometry, and hence more suitable for localizing nuclear wave functions.

These analyses of the potential energy surfaces showed that for both types of trimers the collinear geometry is preferred. We now turn to the question of which bond lengths are optimal. After finding minima in the complete potential surface, we bin them as a function of  $R_1$  and energy and show them alongside the dimer potential curves in figure 6. The even trimer minima are clustered around and typically just slightly deeper in energy than the dimer minima, but a sizable number of trimer minima are found as far as 20 GHz deeper in energy. From this one can conclude that, although there are exceptions, many trimer minima are found when one bond length is equal to a stable dimer bond length. In the following

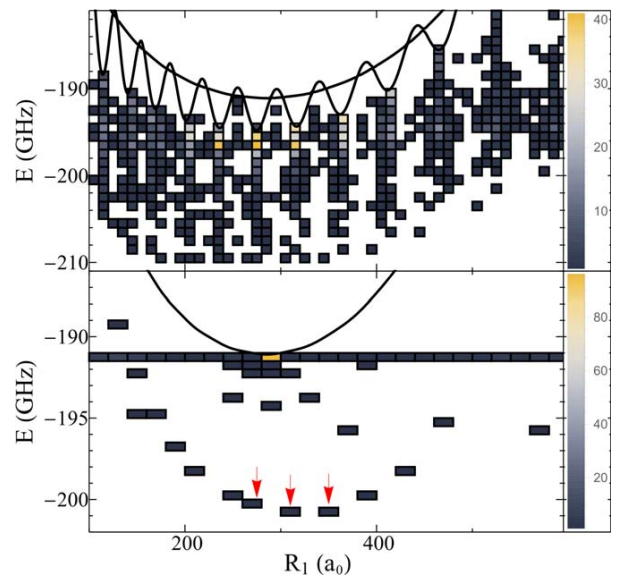


**Figure 6.** Analysis of the energies and positions of trimer minima. Top: even-trimer; bottom: odd-trimer. The color code indicates the number of minima per bin at energy  $E$  and position  $R_1$ . The dimer potential energy curves are shown in black. States considered in section 5 are highlighted with red arrows.

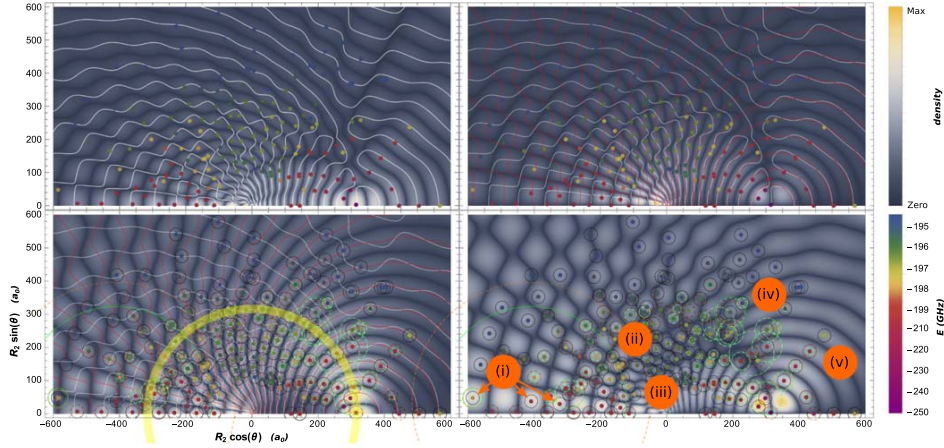


**Figure 7.** A study of the even-trimer with one bond length fixed at  $R_1 = 316 a_0$ . The background density plot in each panel is different, corresponding to  $|\Upsilon_{12}^{22}|$  in the top left,  $|\Upsilon_{12}^{23}|$  in the top right;  $|\Upsilon_{12}^{33}|$  in the bottom left, and  $|\Upsilon_{12}^{32}|$  in the bottom right. Positions of the potential energy minima are shown as colored dots in all four panels. The contour lines plotted correspond to  $\Upsilon_{12}^{31} = 0$  (red) and  $\Upsilon_{12}^{21} = 0$  (white), and are not shown in some panels for clarity. The yellow circle in the bottom left panel indicates  $R_2 = R_1$ . The other circles in the bottom panels provide information about the electronic state: their radii indicate the amplitude of each dimer orbital, normalized to the  $R_1$ -butterfly orbital (black). The  $R_2$ -butterfly is orange; the  $\theta_2$ -butterfly is white, and the  $\theta_1$ -butterfly is green. Regions of interest expounded upon in the text are labeled in orange in the bottom right panel.

section we will analyze the specific case  $R_1 = 316 a_0$  to study the dependence of the minima depths on  $R_2$  and  $\theta$ , and thus characterize a subset of the stable geometries.

In contrast, the histogram of odd-trimer minima is strongly peaked at the trivial global minimum,  $R_0 \approx 286 a_0$ , of the dimer potential. At a given  $R_1 \neq R_0$  the minimum is most likely found at  $R_2 = R_0$  unless the coupling term is very large, which explains the flat band of energies at the dimer minimum, around  $-191$  GHz. At the collinear geometry the coupling becomes large, leading to a few non-trivial deep minima in the semicircle band. The global minimum shifts to  $R_1 \approx 316$ . We will investigate the vibrational states associated with the marked bond lengths in section 5.

#### 4. Building principles for the even trimer

For the pure trilobite sector of the Rydberg trimer Hamiltonian (equation (4)), it is clear that potential minima are only found at molecular geometries which maximize the matrix element  $\Upsilon_{12}^{11}$ . By definition, this implies that the trilobite trimer minima can be found when one perturber sits in a local maximum of the electronic wave function of a stable trilobite dimer. In the butterfly sector (equation (5)) the vectorial nature of the  $p$ -wave operator complicates this situation. There are now four possible coupling elements to maximize:  $\Upsilon_{12}^{22}$  and  $\Upsilon_{12}^{32}$ , which correspond to the derivative  $\frac{\partial}{\partial R}$  of the  $R$ -butterfly and the  $\theta$ -butterfly, and  $\Upsilon_{12}^{33}$  and  $\Upsilon_{12}^{23}$ , the derivative  $\frac{\partial}{\partial \theta}$  of the same respective orbitals. One can find minima in the butterfly trimer potential surfaces when the second atom is placed at a point of locally steepest gradient of the wave function of a stable dimer of either the  $R$ -butterfly or  $\theta$ -butterfly type.

To study this more complex building principle we show in the four panels of figure 7 density plots of these four derivative terms, respectively. We overlay the potential energy minima (colored dots) associated with  $R_1 = 316 a_0$  so that we can correlate the values of  $R_2$  and  $\theta$  at these minima geometries with features in the wave function gradients. The extremely deep minima ( $< -210$  GHz) are found when  $\vec{R}_1 \approx \vec{R}_2$ , and we ignore them, as they are expected to be highly modified by the neutral-neutral interatomic interactions that we have neglected. The gradient maxima often coincide with the nodes of either of the two relevant butterfly wave functions, which we depict using white ( $\xi = 2$ ,  $R$ -butterfly) and red ( $\xi = 3$ ,  $\theta$ -butterfly) contours.

Potential with the building principle sketched above, all of the potential minima occur at a nuclear configuration which maximizes at least one gradient. Two concrete examples are the yellow dot at the point (480, 210), which lies at a maximum of all four gradients, and the red dot at (-400, 50), which lies at a maximum of only the two cross-gradients displayed in the right panels. When certain coupling terms dominate at different nuclear configurations, this leads to a rich diversity of possible electronic states described by the linear combination of butterfly orbitals  $\Psi(\vec{r}) = \sum_{i=1}^2 \sum_{\xi=2}^3 c_i^{(\xi)} \Upsilon_{ir}^{\xi 1}$ . In the bottom panels of figure 7 we depict this electronic eigenstate for each minimum configuration using four circles whose radii are proportional to the four mixing coefficients  $c_i^{(\xi)}$ . The orange circles have radius  $|c_2^{(2)}|$ , the white circles  $|c_2^{(3)}|$ , the green circles  $|c_1^{(3)}|$ ; these radii are normalized to the  $R_1$ -butterfly amplitude  $|c_1^{(2)}|$  (black), which is why some circles (notably in the bottom right panel) can become uncharacteristically large. Along the contour  $R_1 = R_2$ , highlighted in yellow in the bottom left panel, the electronic state is typically an equal mixture of  $R_1$ - and  $R_2$ -butterflies which resembles the trilobite trimer studied in previous works [16, 19, 23]. Deep within this circle and far outside of it, the

electronic states tend to be dominated by the  $R_1$ -butterfly component. Most of the remaining states are predominantly mixtures of either the two  $R_1$ -,  $R_2$ -butterflies or the two  $\theta_1$ -,  $\theta_2$ -butterflies.

By studying these four panels, one can identify several generic patterns such as these, as well as a few notable exceptions. We have identified five interesting regions of the phase space as labeled in orange:

- (i) The states indicated by the arrows at this marker are unique in that they are mixtures of  $\xi = 2$  and  $\xi = 3$  orbitals. To the immediate left and right of the marker lie states dominated by  $\theta_1$ - and  $R_2$ - butterflies (green and orange, respectively). Further to the right is the opposite case, an equal mixture of  $R_1$ - and  $\theta_2$ - butterflies (black and white, respectively) with vanishing  $R_2$  and  $\theta_1$  components. These potential minima are located at the nodes of the  $\Upsilon_{12}^{22}$  and  $\Upsilon_{12}^{33}$  derivative surfaces (see left panels), but at the maxima of the  $\Upsilon_{12}^{23}$  and  $\Upsilon_{12}^{32}$  surfaces (right panels); these trimer states are therefore only possible due to the coupling between different types of butterfly states. A trimer of this type can have unusual electronic properties as a result of this coupling, since the  $\xi = 2$  and  $\xi = 3$  dipole moments have very different magnitudes and even different signs [13, 27].
- (ii) Immediately above this marker are two states with nearly equal contributions from all four dimer orbitals; along with a similar state at  $(x, y) \approx (-380, 60)$ , these seem to be the only states with this composition for  $R_1 = 316 a_0$ .
- (iii) Along the  $\theta = \pi$  line along the bottom of each panel, the electronic states change from primarily dimer-like at small  $R_2$  to very trimer-like as  $R_2$  increases. By dimer-like we mean that the eigenstate is dominated by the butterfly orbital of a single ground state atom, whereas trimer-like refers to a state which has significant contributions from butterfly states for each orbital, for example an even mixture of  $R_1$ - and  $R_2$ - butterflies. These potential minima are the deepest found in this geometry and are better isolated from nearby minima than most of the other configurations, allowing for tight localization of vibrational states. In the next section, we find that nearly all of the deep vibrational states found have this type of molecular geometry.
- (iv) In this cluster, the states have large  $\theta_1$ - and  $\theta_2$ - butterfly mixing (green and white circles), in nearly equal amounts. Further to the left, closer to the (ii) marker, the opposite is mostly true (black and orange circles).
- (v) Along this ray, the mixing between all orbitals is high and the minima are deep and well-isolated from other minima out to quite large distances: one of the few vibrational states found at  $\theta \neq 0, \pi$  in the following section is positioned in this ray.

Our goal in this phenomenological description of the electronic and nuclear state-space is not to systematically describe or classify all of the trimer states, but simply to reveal some of the rich diversity of possible electronic configurations.

## 5. Nuclear wave functions and vibrational spectra

Having discussed the electronic structure and the arrangement of minima in the potential energy landscape, we can now present the properties of supported vibrational states. We obtain vibrational wave functions  $\chi(R_1, R_2, \theta)$  numerically as eigenstates of the vibrational Hamiltonian

$$\begin{aligned}
 H^{\text{vib}} = & \frac{1}{m} \left[ -\frac{\partial^2}{\partial R_1^2} - \frac{\partial^2}{\partial R_2^2} - \cos \theta \frac{\partial}{\partial R_1} \frac{\partial}{\partial R_2} \right] \\
 & - \frac{1}{m} \left( \frac{1}{R_1^2} + \frac{1}{R_2^2} - \frac{\cos \theta}{R_1 R_2} \right) \left( \frac{\partial^2}{\partial \theta^2} + \cot \theta \frac{\partial}{\partial \theta} \right) \\
 & - \frac{1}{m} \left( \frac{1}{R_1 R_2} - \frac{1}{R_2} \frac{\partial}{\partial R_1} - \frac{1}{R_1} \frac{\partial}{\partial R_2} \right) \left( \cos \theta + \sin \theta \frac{\partial}{\partial \theta} \right) \\
 & + \epsilon(R_1, R_2, \theta),
 \end{aligned} \tag{15}$$

where  $m$  is the mass of  $^{87}\text{Rb}$ . This Hamiltonian describes the pure vibrational dynamics of the trimer (depending only on  $R_1, R_2, \theta$ ) and can be obtained from the full nuclear Hamiltonian by separating the center-of-mass motion and projecting onto the subspace of conserved relative angular momentum  $L = 0$  [20, 23, 33, 34]. The wave functions are normalized as  $\int dR_1 dR_2 d\theta \sin \theta |\chi(R_1, R_2, \theta)|^2 = 1$ . In our numerical approach we construct the Hamiltonian on a three-dimensional grid in position space using a finite difference representation for the radial degrees of freedom,  $R_1$  and  $R_2$ , and a discrete variable representation for the  $\theta$  direction [35]. According to the spin statistics of  $^{87}\text{Rb}$ , we consider only bosonic states with  $\chi(R_1, R_2, \theta) = \chi(R_2, R_1, \theta)$ .

Fig. 8(a)–(e) presents energies and reduced probability densities of the energetically lowest vibrational states of the odd butterfly. The reduced densities are obtained by averaging the density  $|\chi(R_1, R_2, \theta)|^2$  over one or two degrees of freedom, respectively, and contain information about the likelihood to find the trimer in a certain geometry. For instance, we can infer from the radial densities (orange) that the ground-state (a) has a bond length of  $R_1 = R_2 = 316 a_0$ . This state is 30 MHz detuned from the next excited state (b) with a bond length of  $R_1 = R_2 = 340 a_0$ . Both states are spatially well separated and strongly confined to a collinear geometry as indicated by the angular density (blue). The following states (c) and (d) correspond to excitations of asymmetric stretching modes of the states (b) and (a), respectively. The bosonic spin statistics are reflected here by the absence of states with odd numbers of nodes along the asymmetric stretch mode. State (e) populates yet another equilibrium geometry with a bond length of  $R_1 = R_2 = 270 a_0$ . A selection of even higher lying states is shown in figures 8(f)–(j). Some of them exhibit excitations of symmetric stretching modes (f), (h), highly excited asymmetric stretching modes (g), as well as bending modes (i), (j). To an excellent approximation states belonging to the same bond length are well described by an harmonic ladder with spacings of approximately 400 MHz for the asymmetric stretching, 1.2 GHz for the symmetric stretching, and

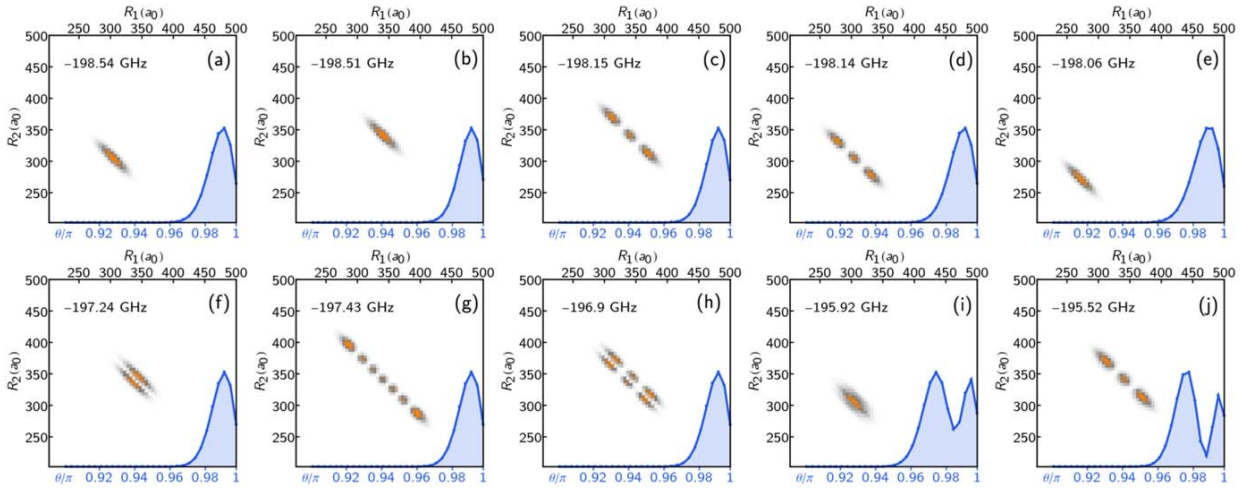


**Figure 8.** Vibrational states of the odd trimer. Reduced radial probability densities,  $\int |\chi(r_1, r_2, \theta)|^2 \sin(\theta) d\theta$ , are presented for different states together with their reduced angular densities,  $\int |\chi(r_1, r_2, \theta)|^2 \sin(\theta) dr_1 dr_2$ , (orange and blue, respectively) and are labeled by their vibrational energies. (a)–(e) are the five energetically lowest states in the specified coordinate range while (f)–(j) are a selection of excited states that illustrate excitations of additional bending and stretching modes. (f) and (h) show symmetric stretch excitations of the configurations of (b) and (c), respectively, while (g) is a highly excited asymmetric stretch state of (b). (i) and (j) have the same stretching excitation as (a) and (c), but an additional bending excitation.

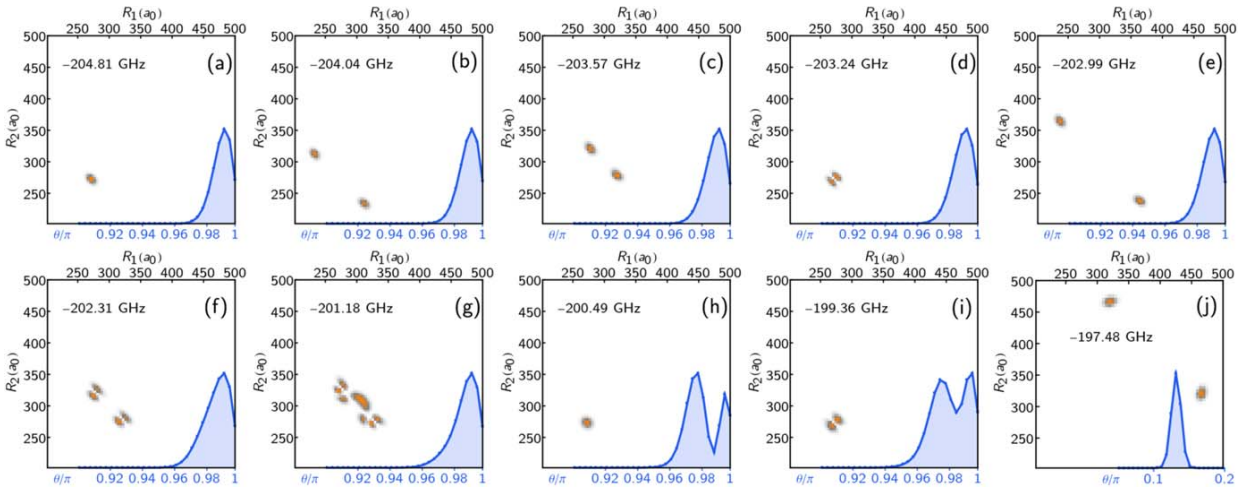


**Figure 9.** Vibrational states of the even trimer showing similar quantities as in figure 8. (a)–(e) are the five energetically lowest states in the specified coordinate range while (f)–(j) are selected excited states that illustrate effects of delocalization (g) as well as excitations of additional bending (h), (i) and stretching (f), (i) modes, as well as a non-collinear configuration (j).

2.5 GHz for the bending modes. Importantly, the order of these spacings differs from triatomic low- $l$  Rydberg molecules, where the energy spacing of bending motion is typically much smaller than stretching motion [20]. It also differs from the trilobite trimer, as shown by an example in reference [23] where the spacing of bending and stretching modes is almost equal.

Reduced probability densities of the even butterfly trimer are shown in figure 9. Again we present the energetically lowest states (a)–(f) as well as a selection of excited states. Due to the different potential energy surface, the vibrational states of the even trimer differ accordingly in some of their properties from the odd trimer states. First, there are not only symmetric states where both ground-state atoms share the

same bond length (as in panel (a)) but also states where one ground-state atom is always closer to the Rydberg core than the other one, see e.g. (b), (c) and (e). However, due to the bosonic character of the ground-state atoms all densities are symmetric under reflection with respect to the  $R_1 = R_2$  diagonal. When these states become excited they can couple to states belonging to different equilibrium configurations to form more complex superpositions, e.g. (g). A second difference is the possibility to form well-localized states in non-collinear arrangements (j). Despite their much more complex underlying electronic structure, vibrational states of the even butterfly trimers are in this respect very similar to trilobite trimers [23].

## 6. Conclusions

We have extended the analysis of triatomic ultra-long-range Rydberg molecules begun in [20, 23], which focused on low- $l$  states and trilobite states, to the butterfly states. These trimers come in two varieties which behave very differently. The odd trimers are only stable in the collinear geometry, have very few equilibrium geometries with equal bond length  $R_1 = R_2$ , and due to the simple structure of the potential surface at  $\theta = \pi$  have nearly independent asymmetric stretch, symmetric stretch, and bending modes. In contrast, the even trimers exhibit complex and vibrant potential surfaces with a rich pattern of potential wells; many of these, however, are insufficiently isolated from other wells to localize vibrational states. As in the odd trimers, many—but not all—of the even trimers have a collinear geometry, but many have equilibrium positions at  $R_1 \neq R_2$  and have a more complex excitation spectrum.

Although we have not mentioned in detail the large dipole moments of the dimer orbitals, many of the equilibrium configurations of the even trimer will have non-zero dipole moments stemming from either the asymmetry in bond lengths or the mixing of  $R$ - and  $\theta$ - dimer orbitals. These trimers therefore possess interesting field control possibilities [36]. In the present study we neglected the complex spin structure of these molecules. Including these effects in a polyatomic context is challenging, but will be necessary for quantitative predictions [22]. The mixing of symmetric and asymmetric stretch modes hinted by figure 9(g) implies that the dynamical behavior of vibrational wave packets across these oscillatory potential surfaces will likely be very rich and offer interesting avenues to explore non-adiabatic physics.

## Acknowledgments

MTE acknowledges support from the Max-Planck Gesellschaft via the MPI-PKS visitors program and from an Alexander von Humboldt Stiftung postdoctoral fellowship. FH and PS acknowledge support from the Deutsche Forschungsgemeinschaft within the priority program ‘Giant interactions in Rydberg systems’ [DFG SPP 1929 GiRyd project SCHM 885/30-1].

## ORCID iDs

Matthew T Eiles  <https://orcid.org/0000-0002-0569-7551>

Peter Schmelcher  <https://orcid.org/0000-0002-2637-0937>

## References

- [1] Andersen T 2004 *Phys. Rep.* **394** 157
- [2] Buckman S J and Clark C W 1994 *Rev. Mod. Phys.* **66** 539
- [3] Greene C H 1990 *Phys. Rev. A* **42** 1405
- [4] Thumm U and Norcross D W 1991 *Phys. Rev. Lett.* **67** 3495
- [5] Thumm U and Norcross D W 1992 *Phys. Rev. A* **45** 6349
- [6] Scheer M, Thølgersen J, Bilodeau R C, Brodie C A, Haugen H K, Andersen H H, Kristensen P and Andersen T 1998 *Phys. Rev. Lett.* **80** 684
- [7] Bahrim C and Thumm U 2000 *Phys. Rev. A* **61** 022722
- [8] Bahrim C, Thumm U and Fabrikant I I 2001 *Phys. Rev. A* **63** 042710
- [9] Bahrim C, Thumm U, Khuskivadze A A and Fabrikant I I 2002 *Phys. Rev. A* **66** 052712
- [10] Eiles M T 2018 *Phys. Rev. A* **98** 042706
- [11] Hamilton E L, Greene C H and Sadehpour H R 2002 *J. Phys. B: At. Mol. Opt. Phys.* **35** L199
- [12] Chibisov M I, Khuskivadze A A and Fabrikant I I 2002 *J. Phys. B: At. Mol. Opt. Phys.* **35** L193
- [13] Khuskivadze A A, Chibisov M I and Fabrikant I I 2002 *Phys. Rev. A* **66** 042709
- [14] Niederprüm T, Thomas O, Eichert T, Lippe C, Pérez-Ríos J, Greene C H and Ott H 2016 *Nat. Commun.* **7** 12820
- [15] Eiles M T, Lee H, Pérez-Ríos J and Greene C H 2017 *Phys. Rev. A* **95** 052708
- [16] Liu I C H and Rost J M 2006 *Eur. Phys. J. D* **40** 65
- [17] Liu I C H, Stanojevic J and Rost J M 2009 *Phys. Rev. Lett.* **102** 173001
- [18] Bendkowsky V *et al* 2010 *Phys. Rev. Lett.* **105** 163201
- [19] Eiles M, Pérez-Ríos J, Robicheaux F and Greene C H 2016 *J. Phys. B: At. Mol. Opt. Phys.* **49** 114005
- [20] Fey C, Kurz M and Schmelcher P 2016 *Phys. Rev. A* **94** 012516
- [21] Pérez-Ríos J, Eiles M T and Greene C H 2016 *J. Phys. B: At. Mol. Opt. Phys.* **49** 14LT01
- [22] Fey C, Yang J, Rittenhouse S T, Munkes F, Baluktisian M, Schmelcher P, Sadehpour H R and Shaffer J P 2019 *Phys. Rev. Lett.* **122** 103001
- [23] Fey C, Hummel F and Schmelcher P 2019 *Phys. Rev. A* **99** 022506
- [24] Fermi E 1934 *Il Nuovo Cimento* **11** 157
- [25] Omont A 1977 *J. Phys.* **38** 1343
- [26] Anderson D, Miller S A and Raithe G 2014 *Phys. Rev. A* **90** 062518
- [27] Eiles M T and Greene C H 2017 *Phys. Rev. A* **95** 042515
- [28] Hummel F, Fey C and Schmelcher P 2018 *Phys. Rev. A* **97** 043422
- [29] Hummel F, Fey C and Schmelcher P 2019 *Phys. Rev. A* **99** 023401
- [30] Eiles M T 2019 *J. Phys. B: At. Mol. Opt. Phys.* **52** 113001
- [31] Deiß M, Haze S, Wolf J, Wang L, Meinert F, Fey C, Hummel F, Schmelcher P and Hecker Denschlag J 2020 *Physical Review Research* **2** 013047
- [32] Tarana M and Čurík R 2016 *Phys. Rev. A* **93** 012515
- [33] Carter S and Handy N C 1982 *Mol. Phys.* **47** 1445
- [34] Handy N C 1987 *Mol. Phys.* **61** 207
- [35] Beck M and Meyer H D 2000 *Phys. Rep.* **324** 1
- [36] Kurz M and Schmelcher P 2013 *Phys. Rev. A* **88** 022501

### 3.10 Ultralong-range Rydberg molecules

## Ultralong-range Rydberg molecules

Christian Fey<sup>a,b</sup>, Frederic Hummel<sup>a</sup> and Peter Schmelcher<sup>a,c</sup>

<sup>a</sup>Fachbereich Physik, Zentrum für Optische Quantentechnologien, Universität Hamburg, Hamburg, Germany; <sup>b</sup>Max-Planck-Institute of Quantum Optics, Garching, Germany; <sup>c</sup>The Hamburg Centre for Ultrafast Imaging, Universität Hamburg, Hamburg, Germany

### ABSTRACT

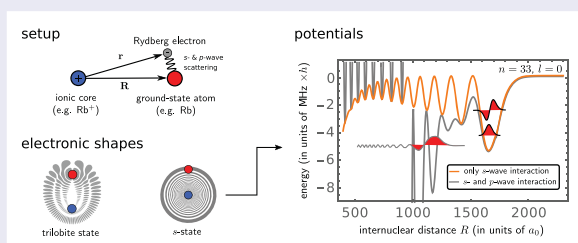
We review ultralong-range Rydberg molecules (ULRMs), which are bound states between a Rydberg atom and one or more ground-state atoms with bond lengths on the order of thousands of Bohr radii. The binding originates from multiple electron-atom scattering and leads to exotic oscillatory potential energy surfaces that reflect the probability density of the Rydberg electron. This unconventional binding mechanism opens fascinating possibilities to tune molecular properties via weak external fields, to study spin-resolved low-energy electron-atom scattering as well as to control and to probe interatomic forces in few- and many-body systems. Here, we provide an overview on recent theoretical and experimental progress in the field with an emphasis on polyatomic ULRMs, field control and spin interactions.

### ARTICLE HISTORY

Received 5 August 2019  
Accepted 4 October 2019

### KEYWORDS

Rydberg atoms; ultracold gases; atomic and molecular collision processes; electron scattering



## 1. Introduction

Ultralong-range Rydberg molecules (ULRMs) represent an exotic molecular species formed by a Rydberg atom and one or more ground-state atoms. The exaggerated properties of the Rydberg atom equip ULRMs with huge bond lengths on the order of thousands of Angstroms and exceptionally large dipole moments up to the kilo-Debye regime, while their binding energies are relatively weak and on the order of hundreds of neV. The origin of their bond lies in low-energy scattering between the Rydberg electron and the ground-state atom, which is substantially different from covalent or ionic bonding mechanisms. As a consequence, ULRMs exhibit oscillatory Born–Oppenheimer potential energy curves (PECs) that reflect the density of the Rydberg wave function.

Since their theoretical prediction in 2000 by Greene *et al.* [1] and their experimental discovery in 2009 [2], many fascinating properties and applications have been revealed. The main research directions include: (1)

control of molecular properties such as dipole moments or alignment via weak external electric and magnetic fields [3–9], (2) study of polyatomic ULRMs, where a Rydberg atom binds not only one but several ground-state atoms [10–18] and forms polaron states in the many-body limit [19–22], (3) probing of spatial correlations in ultracold atomic gases [23–25], and (4) characterisation of low-energy electron-atom collisions [26–30]. In this review we provide a brief introduction of the molecular binding mechanism and present key findings of the different research directions in the context of experimental observations and theoretical models with a focus on molecular aspects. For alternative reviews on ULRMs, see [31,32], the tutorial [33] as well as reviews addressing particular subtopics of ULRMs [34–37]. After a short discussion of the historical precursors of ULRMs in the early twentieth century in Section I, we present basic molecular properties of ULRMs in Section II. Thereafter, we focus on polyatomic ULRMs in Section

III, field control in Section IV and spin interactions in Section V. We end the review with our conclusions in Section VI that contain open questions as well as future perspectives.

## 2. Historical context

In the 1930s, E. Amaldi and E. Segré investigated spectra of highly excited alkali atoms in the presence of perturbing noble gas atoms [38,39] in Rome. Similar experiments were conducted simultaneously by C. Füchtbauer and coworkers in Rostock [40,41]. While it was expected that the polarisable medium would cause a red shift of the atomic resonances, the experiments revealed that both red and blue shifts are possible depending on the atomic buffer gas species and its density. E. Fermi successfully explained this effect by describing the interactions between the Rydberg electron and the buffer gas atom, as a low-energy scattering process [42,43]. According to this model the frequency shift is proportional to the buffer gas concentration and the zero-energy *S*-wave scattering length of the electron-atom system. This scattering length can be negative or positive and explains, hence, the occurrence of blue shifts. The theory of Fermi was not only in very good agreement with the observations but also allowed experimentalists to extract scattering lengths from measured line shifts [41,43]. Since then the Fermi pseudopotential has been an important ingredient for studies of collisional processes of Rydberg atoms in gaseous environments [43–45] with applications such as the reconstruction of interatomic potentials or the analysis of the composition of interstellar atmospheres [44,46].

With the advent of novel techniques to cool and to trap atoms [47] at the end of the twentieth century it became possible to reach ultracold temperatures below  $0.5 \mu\text{K}$  for ensembles of thousands, if not millions, of atoms and to realise Bose–Einstein condensates [48]. In the context of these developments C. H. Greene, A. S. Dickinson and H. R. Sadeghpour revealed an unexpected consequence of the Fermi pseudopotential theory when applied to ultracold atomic gases. They realised that the oscillatory probability density of the Rydberg electron can act effectively as a trap on surrounding ground-state atoms and binds atoms to the density maxima. Due to the size of the Rydberg orbit these molecules possess huge bond length, on the order of thousands of Bohr radii  $a_0$  and are for this reason called ultralong-range Rydberg molecules. Importantly, ULRMs need to be distinguished from traditional Rydberg molecules [46] that possess highly excited electronic states but only small bond lengths.

## 3. Basic molecular properties

### 3.1. Overview

The basic properties of diatomic ULRMs are illustrated in Figure 1(a–d). As shown in Figure 1(a), ULRMs consist of a ground-state atom and a Rydberg atom. The latter possesses an ionic core and an excited valence electron that interacts with the ground-state atom, which is sometimes also called ‘perturber’. Exemplary Born–Oppenheimer PECs for the case of a  $^{87}\text{Rb}$  ULRM close to the  $n = 30$  Rydberg state are presented in Figure 1(b). At large internuclear separations, where interactions between the atoms are negligible, here for  $R > 1900$  Bohr radii  $a_0$ , the PEC are nearly flat and correspond to energy levels of the isolated Rydberg atom with principal quantum number  $n$  and angular momentum  $l$ . These energies can be expressed by the Rydberg formula  $E_{nl} = -1/(2(n - \delta_l)^2)$  with an  $l$ -dependent quantum defect  $\delta_l$  that describes deviations from the hydrogen spectrum due to core penetration. In this context one distinguishes low- $l$  states with substantial quantum defects from high- $l$  hydrogen-like states, which are shielded from the ionic core by a sufficiently large centrifugal barrier and have almost vanishing quantum defects. For instance the Rydberg spectrum of  $^{87}\text{Rb}$  is well approximated [49] by  $\delta_0 = 3.13$ ,  $\delta_1 = 2.65$ ,  $\delta_2 = 1.35$ , and  $\delta_{l \geq 3} = 0$ , which leads to the ordering of energy levels depicted in Figure 1(b).

When the ground-state atom overlaps with the electron cloud of the Rydberg atom, the energies of the Rydberg electron become perturbed. This is visible in the PECs in Figure 1(b) for internuclear separations  $R < 1900 a_0$ , where electron-atom interaction is modelled via *S*-wave scattering (orange) or via *S*- and *P*-wave scattering (gray). For pure *S*-wave interactions one distinguishes two types of ULRM originally predicted in [1]: trilobite molecules and low- $l$  ULRMs. The former are correlated to the hydrogenic manifold and possess typically several  $\text{GHz} \times h$  deep PEC, see Figure 1(c). Their name refers to the shape of their electronic density (gray contour plot) which resembles a trilobite fossil. Illustratively speaking, the trilobite function is the superposition of all hydrogenic states which maximises its density on the ground-state atom. Due to this property, trilobite ULRMs are polar molecules that possess huge permanent dipole moments on the order of kilo-Debye. The second type, low- $l$  ULRMs, are associated to the corresponding low- $l$  Rydberg levels. They possess approximately thousand times shallower PEC with vibrational energy spacing on the order of  $10 \text{ MHz} \times h$ . As an example the PEC of *s*-state ULRMs are presented in Figure 1(d). The corresponding electronic state is to a good approximation isotropic (gray contour plot) but can possess small permanent dipole moments on the

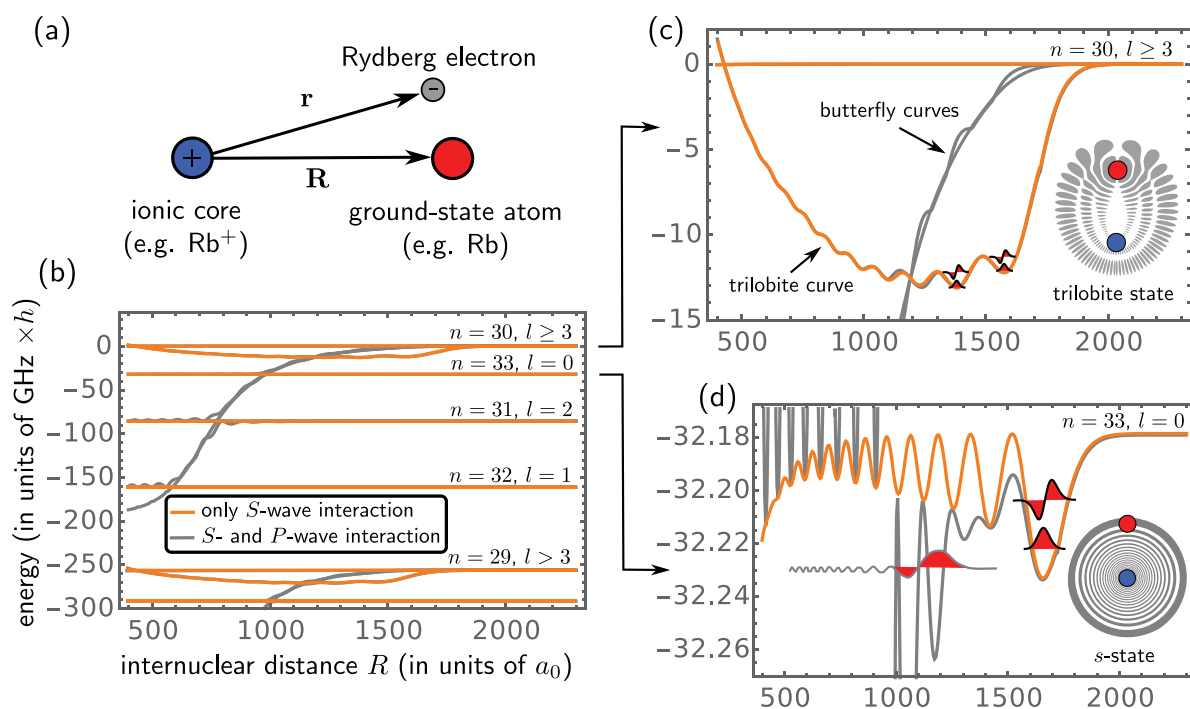


**Figure 1.** (a) Schematic illustration of an ultralong-range Rydberg molecule that consists of a Rydberg atom (ionic core and valence electron) and a ground-state atom. (b) The Born–Oppenheimer PEC for two  $^{87}\text{Rb}$  atoms illustrate the impact of the ground-state atom on the electronic Rydberg levels with quantum numbers  $n$  and  $l$  as a function of the internuclear distance  $R$ . The underlying interaction between the electron and the ground-state atom is modelled via  $S$ -wave interactions (orange curves) or  $S$ - and  $P$ -wave interactions (gray curves). The zero energy is set to the energy of the hydrogen-like  $n = 30$  manifold. (c) and (d) are magnifications of the regions close to the atomic asymptote of  $n = 30, l \geq 3$  and  $n = 33, l = 1$ , respectively. Minima of the PEC support several bound vibrational states (indicated by black curves with red filling) as well as resonances bound by quantum reflection (gray curve with red filling). Gray contour plots illustrate the typical electronic density of the molecular states.

order of one Debye upon admixture of trilobite character [50]. Accordingly, the denotation  $l$ -state ULRM does not imply that the Rydberg electron is in a pure  $l$  state but only that the molecule correlates asymptotically to the atomic  $l$ -state Rydberg line. The PEC of both types of ULRMs support several quantised vibrational states (indicated by red filled wave functions). In spite of the comparably slow electronic motion of the highly excited Rydberg electron, the Born–Oppenheimer approximation remains typically valid, since the energy spacing of adjacent Rydberg levels is usually orders of magnitude larger than the vibrational energy spacing of the nuclei.

The inclusion of additional  $P$ -wave interactions has two main impacts. Firstly, it gives rise to yet another type of polar ULRM, which are called butterfly molecules [51,52]. Again, the name refers to the shape of the electron density. Remarkably, their dipole moments are slightly larger than those of trilobite molecules, while their bond lengths are much shorter, e.g.  $R < 500 a_0$  for  $n = 30$  [51]. The second consequence of  $P$ -wave interactions are modifications of the PECs of trilobite molecules and  $s$ -state ULRMs. Due to an underlying  $P$ -wave shape resonance, which is a general feature of

electron interaction with alkaline atoms [53–55], the associated butterfly PECs cross all other Rydberg levels, see Figure 1(b,c). For the trilobite molecule this crossing is rather sharp and the shape of the trilobite PEC remains almost preserved, whereas for  $s$ -state ULRMs there are substantial modifications at inner radii. In particular the shape resonance induces a steep potential drop, visible at  $R \approx 1000 a_0$  in Figure 1(d) that acts on vibrational states effectively as a boundary and leads to the formation of vibrational resonances, see exemplary gray wave function in Figure 1(d). Illustratively speaking, these resonances are bound by internal quantum reflection at the potential drop [12].

### 3.2. Experimental observations

All of the three types of ULRMs have been realised experimentally [2,7,56]. The first to be observed were  $s$ -state ULRMs with principal quantum numbers ranging from  $n = 34$  to  $n = 40$  [2]. Starting from an ultracold sample of trapped  $^{87}\text{Rb}$  ground-state atoms, the molecules were created using a two-photon photoassociation scheme and, subsequently, detected via field ionisation.

Measured molecular lifetimes were on the order of tens of  $\mu\text{s}$  and significantly lower than the corresponding atomic lifetimes [2,57]. Subsequent studies in samples with variable atomic densities revealed that this reduction can be attributed to two decay mechanisms: firstly, molecule-atom collisions, with a collision rate that is proportional to the atomic density and, secondly, leakage of quantum states toward smaller internuclear separations caused by the crossing between the  $s$ -state PEC and the butterfly PEC [58].

Dipole moments have been quantified by performing Stark spectroscopy in weak electric fields. The observed linear Stark shifts demonstrate that  $s$ -state ULRMs can possess permanent dipole moments on the order of 1 Debye [50]. The polarisation of the electronic wave function is caused by a small admixture of trilobite character to the otherwise isotropic  $s$ -state. Arguments based on exchange and parity symmetry forbid the existence of such permanent dipole moments for homonuclear molecules and imply a quadratic Stark shift. However, for the case of ULRMs the energy splitting of the electronic  $^3\Sigma_g$  and  $^3\Sigma_u$  orbitals is negligible and the rotational splitting is very small, typically on the order of  $10 \text{ KHz} \times h$ . Compared to the experimentally relevant field strengths on the order of a few V/cm, molecular states of different parity are, therefore, energetically degenerate and exhibit linear Stark shifts [50,59].

Following these first experiments with Rb  $s$ -state ULRMs, further ULRMs with different atomic species ( $^{133}\text{Cs}$  and  $^{84}\text{Sr}$ ) as well as in different electronic states ( $p$  and  $d$  states) have been realised [5,23,26,60–62]. These different atomic species and electronic states offer some degree of control of the molecular properties. For instance there is no  $P$ -wave shape resonance in Sr ULRMs and the molecular lifetimes are not limited by the above-mentioned leakage mechanism and can become comparable to those of their parent Rydberg atoms. Another example is the particularity of Cs atoms that the Rydberg  $s$ -state lies energetically very close to an adjacent hydrogenic manifold, due to an almost integer quantum defect of  $\delta_0 = 4.05$ . As a consequence, there is a crossing between the PECs of the trilobite and the  $s$  state in Cs ULRMs. Although trilobite states are high angular momentum states and conventionally not accessible by one- or two-photon transitions due to angular momentum conservation, they possess in Cs an increased admixture of  $s$ -state character due to this crossing. This insight led to the excitation of trilobite ULRMs with huge dipole moments on the order of 2 kiloDebye [56]. In a similar spirit butterfly molecules in Rb with dipole moments on the order of 500 Debye have been excited close to a crossing with the  $25p$ -state PEC [7]. Furthermore electric fields were used to align the butterfly molecules and

deduce their bond lengths from the observed rovibrational splittings.

### 3.3. Theoretical description

A simple yet very accurate effective Hamiltonian for the Rydberg electron is given by

$$H = H_0(\vec{r}) + V_{ca}(\vec{R}) + V_{ea}(|\vec{r} - \vec{R}|), \quad (1)$$

with the internuclear axis  $\vec{R}$  and the electron position  $\vec{r}$ , see Figure 1(a).  $H_0$  describes the isolated Rydberg atom, i.e. the kinetic and potential energy of the Rydberg electron in the field of the ionic core. Working in atomic units (a.u.), its eigenstates have energies given by the Rydberg formula  $E_{nl} = -1/(2(n - \delta_l)^2)$  and wave functions  $\varphi_{nlm}(\vec{r})$ , where  $n$ ,  $l$ , and  $m$  are the principal quantum number, the angular momentum, and the magnetic quantum number, respectively. Using quantum defect theory the wave functions can be expressed in terms of appropriate superpositions of regular and irregular Coulomb wave functions that are related to Whittaker functions [33]. Alternatively, one obtains  $\varphi_{nlm}(\vec{r})$  by employing suitable model potentials for the electron-ion interaction and by solving the resulting radial Schrödinger equation numerically [63].

The long-range interaction between the ionic core and the polarisable ground-state atom is given by  $V_{ca}(R) = -\frac{\alpha}{2R^4}$ , with the polarisability  $\alpha$ . For instance the polarisability of the  $^{87}\text{Rb}(5s)$  ground-state is  $\alpha = 319$  a.u. [64]. Finally,  $V_{ea}(|\vec{r} - \vec{R}|)$  is the interaction between the Rydberg electron and the ground-state atom. Following Fermi's idea this interaction can be expressed as a zero-range pseudopotential [1,42,51,65]

$$V_{ea}(|\vec{r} - \vec{R}|) = 2\pi a_S[k(R)]\delta(\vec{R} - \vec{r}) + 6\pi a_P[k(R)]\overleftarrow{\nabla}_{\vec{r}} \cdot \delta(\vec{R} - \vec{r})\overrightarrow{\nabla}_{\vec{r}}, \quad (2)$$

where the arrows indicate that the gradient operators  $\overleftarrow{\nabla}$  and  $\overrightarrow{\nabla}$  act only on wave functions on the left- and right-hand side, respectively, see (3). The first term describes  $S$ -wave interactions while the second term includes additional  $P$ -wave interactions. The strength of these interactions depends on the low-energy scattering length and volume  $a_S[k]$  and  $a_P[k]$ , which are linked to the phase shifts  $\delta_S(k)$  and  $\delta_P(k)$  of a free electron with wave number  $k$  that scatters off the ground-state atom via  $a_S[k] = -\tan(\delta_S)/k$  and  $a_P[k] = -\tan(\delta_P)/k^3$ . In a semiclassical approximation the wave number  $k$  at the position of the atom is determined by  $k^2/2 - 1/R = E_{nl}$ , where  $E_{nl}$  is the energy of the Rydberg level close to the molecular PEC. The phase shifts  $\delta_S(k)$  and  $\delta_P(k)$  are required as an input for the interaction potential and are typically

extracted from computational solutions of two-active electron models [54,55,66,67] in combination with analytical low-energy expansions based on modified effective range theory [68–70]. The pseudopotential formalism is quite general and applies also to ULRMs consisting of complex multichannel Rydberg atoms such as Ca or Si [71].

Born–Oppenheimer PEC as depicted in Figure 1 can be obtained by diagonalising the Hamiltonian  $H_0$  in a finite set of basis states  $\varphi_{nlm}(\vec{r})$  that cover a certain spectral window of interest or by using alternative Green’s function methods [12,30,51,67,72] which can, additionally, be combined with R-matrix methods to take into account the finite range for the electron-atom interaction [73]. An advantage of Green’s function methods is their numerical reliability, since they are not subject to convergence issues which do currently limit the accuracy of the diagonalisation approach [72,74]. However, state-of-the-art Green’s function approaches [12,30,67,73] neglect essential interactions such as the fine structure of the Rydberg atom, the hyperfine structure of the ground-state atom as well as couplings to external fields, which are indispensable for a correct interpretation of high-resolution spectra of ULRMs. So far only diagonalisation approaches are able to capture all those effects [74].

To obtain basic molecular features it is sufficient to perform first-order (degenerate) perturbation theory. For instance the PEC close to the Rb( $ns$ ) state is well captured by

$$E(R) = E_{ns} - \frac{\alpha}{2R^4} + 2\pi a_S[k(R)]|\varphi_{ns0}(R)|^2 + 6\pi a_P[k(R)]\vec{\nabla}\varphi_{ns0}(R) \cdot \vec{\nabla}\varphi_{ns0}(R). \quad (3)$$

At sufficiently large distances  $R$ , the kinetic energy of the electron is small and  $P$ -wave interactions are of minor importance, see Figure 1(d) for  $R > 1600 a_0$ . In this regime the PECs are proportional to the electronic density of the Rydberg electron. It has been proposed that this peculiarity could be exploited to imprint and to measure images of electronic orbitals onto a BEC [75,76]. Based on the properties of the Rydberg wave functions the depth of the  $S$ -wave dominated outer well scales as  $n^{-6}$ , which is in good agreement with experiments [13]. For smaller separations,  $P$ -wave interaction gains in significance as the kinetic energy of the electron approaches the energy of a Rb<sup>−</sup> shape resonance at approximately 26 meV [30,53,54,67,77]. Due to the resonance the  $P$ -wave scattering volume diverges and the first-order approximation (3) clearly breaks down. However, when including couplings to adjacent Rydberg states, strong level repulsion stabilises the PECs, such that the individual adiabatic PECs behave regular, i.e. they

do not diverge, see Figure 1(b). The polarisation potential  $-\alpha/(2R^4)$  contributes to the PECs only at relatively small internuclear distances. Experimentally, its impact has been verified by exciting a single Rydberg atom in a Bose–Einstein condensate to high  $n = 190$ , where the otherwise dominant electron-atom interaction is suppressed since the Rydberg orbit exceeds the size of the typical internuclear separations [22].

An approximate expression for the trilobite PEC can be obtained within (degenerate) first-order perturbation theory [1]

$$E(R) = -\frac{1}{2n^2} - \frac{\alpha}{2R^4} + 2\pi a_S[k(R)] \sum_{l>3} \frac{2l+1}{4\pi} R_{nl}^2(R), \quad (4)$$

where  $R_{nl}(r)$  is the radial wave function associated to  $\varphi_{nlm}(\vec{r})$ . Contributions of  $P$ -wave interactions are neglected in (4). In addition to the energy curves also the trilobite wave function  $\psi(\vec{r}; \vec{R})$  can be expressed analytically within first-order degenerate perturbation theory. The characteristic nodal structure of these states visible in Figure 1 can be understood semiclassically. In a path integral picture  $\psi(\vec{r}; \vec{R})$  results from interference of electron states associated to elliptical Kepler trajectories that pass simultaneously through the points  $\vec{r}$  and  $\vec{R}$ . Minima in the PECs arise when these trajectories satisfy semiclassical Einstein–Brillouin–Keller quantisation conditions which imply that the wave function has a certain integer number of nodes  $n_\xi$  and  $n_\eta$  along two different elliptical directions [78,79]. Interestingly, trilobite wave functions can also be realised by applying a sequence of electric and magnetic field pulses even when the ground-state atom is not present [80].

Once the PECs  $E(R)$  are determined, stationary vibrational states  $\chi_\nu(R)$  with energy index  $\nu$  can be deduced numerically by means of standard shooting methods or finite difference schemes. Resonances that are bound by quantum reflection, see gray curve with red filling in Figure 1(d), are in this context treated similarly to shape resonances. However, in the case of ULRMs these resonances result from inward scattering as opposed to conventional outward scattering [12,81]. The molecular line strengths of these states, i.e. the probability to excite  $\chi_\nu(R)$  out of an ultracold atomic ensemble is proportional to the vibrational part of the Franck–Condon factor  $\Gamma_\nu$ . The states  $\chi_\nu(R)$  are typically rather localised around the bond length  $R_\nu$ , in which case  $\Gamma_\nu \approx |\int dR R^2 \chi(\vec{R})|^2 g^{(2)}(R_\nu)$ , where  $g^{(2)}(R_\nu)$  is the pair correlation function of the atomic gas [24,25,61]. This simple form of  $\Gamma_\nu$  explains two essential properties of ULRMs. First, vibrational states  $\chi_\nu(R)$  with an approximate gerade (ungerade) symmetry have in experiments strong (weak) signal [61,82]. Second, excitation

spectra of ULRMs provide access to pair correlation functions of the gas [24,25] which has for instance been used to dynamically monitor the mott-insulator to superfluid phase transition in an optical lattice [23].

#### 4. Polyatomic ULRMs

Since ULRMs are experimentally created in ultracold samples of trapped atoms, it is a natural situation, depending on the density of the gas, to have on average more than one ground-state atom within the size of the Rydberg cloud. In this case the Rydberg atom can bind several of these ground-state atoms to form polyatomic ULRMs [10]. The generalisation of the dimer Hamiltonian (1) that describes this situation is

$$H = H_0(\vec{r}) + \sum_j (V_{ca}(R_j) + V_{ea}(|\vec{r} - \vec{R}_j|)), \quad (5)$$

where  $\vec{R}_j$  are the coordinates of the ground-state atoms. Similar to diatomic ULRMs one distinguishes polyatomic high- $l$  ULRMs with trilobite-like wave functions and polyatomic low- $l$  ULRM. First theoretical explorations of polyatomic ULRMs focused on high- $l$  ULRMs consisting of two, three, and four ground-state atoms [10]. An important insight in this context was the insight that triatomic ULRMs can form Borromean states, where the trimer is stable although the corresponding dimers interact repulsively [11]. Since angular selection rules hinder the direct one- or two-photon excitation of high- $l$  Rydberg states, most of the subsequent experimental and theoretical work concentrated, however, on low- $l$  ULRMs. In addition, there is research on a second type of polyatomic ULRM consisting of a Rydberg atom that binds one or more polar molecules, e.g. KRb [83–86], which is, however, not in the focus of this review.

Spectral signatures of Rb  $s$ -state trimers, see Figure 2, were reported shortly after the experimental discovery of ULRMs [12]. Ensuing observations confirmed additional tetramers, pentamers and hexamers [13]. Importantly, it was observed that binding energies of these polymers scale linearly with the number of ground-state atoms, i.e. the binding energies are integer multiples of dimer energies. An exemplary photoassociation spectra of polyatomic Rb  $s$ -state ULRMs is presented in Figure 3, where polyatomic lines are marked by coloured diamonds. For instance the trimer (violet) has twice the dimer energy (red) because both ground-state atoms are trapped in the energetically lowest dimer mode. This building principle has been later generalised to a shell-structure model [19], where ground-state atoms are allowed to occupy not only the energetically lowest but also excited vibrational modes, see excited state in Figure 1(d). Such polymers

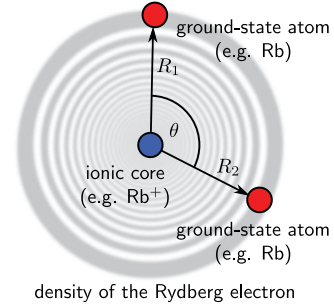


**Figure 2.** Sketch of a triatomic ultralong-range Rydberg molecule in an electronic  $s$  state.

are not addressed in Figure 3 but have been confirmed experimentally in [21].

The spectra in Figure 3 were taken at a constant atomic density of  $\rho_0 = 10^{12} \text{ cm}^{-3}$  but variable principal quantum number  $n$ . While individual polyatomic few-body states can be well resolved for  $n \leq 71$  one approaches for larger  $n$  a many-body limit where the average number of ground-state atoms within the Rydberg orbit increases as  $n^6$  while binding energies decrease as  $n^{-6}$ . In this regime the experimental spectra exhibit a single collisionally broadened Rydberg line instead of individual molecular resonances, e.g. for  $n = 111$  in Figure 3. In the mean-field limit, the broadened line will become a Gaussian peak with a certain detuning from the atomic Rydberg state – the so called pressure shift – that was observed in the pioneering experiments [38–41] and interpreted by Fermi [42]. This shift is identical to the mean centre of gravity  $\langle cg \rangle$  and given by the average interaction energy with all ground-state atoms

$$\Delta E = \int dR^3 dr^3 V_{ea}(|\vec{r} - \vec{R}|) |\varphi_{ns}(\vec{r})|^2 \rho(\vec{R}) \quad (6)$$

$$\approx 2\pi a_S[0] \rho_0, \quad (7)$$

where  $\varphi_{ns}(\vec{r})$  is the Rydberg wave function and  $\rho(\vec{R})$  the atomic density. Equation (7) follows from assuming a constant density  $\rho(\vec{R}) = \rho_0$  and replacing the electron-atom interaction  $V_{ea}$  by  $S$ -wave contact interactions (2) in the zero-energy limit, i.e. constant  $S$ -wave scattering length  $a_S[0]$ . Generalised versions of (7) include energy-dependent scattering lengths,  $P$ -wave contributions as well as inhomogenous densities and have been employed successfully to describe the spectral response of single Rydberg impurities immersed in a dense BEC [87]. An intriguing application of Rydberg impurities in ultracold atomic gases is the production of textbook-like images of atomic orbitals by imprinting the shape of the Rydberg orbital onto the BEC density, which has been proposed theoretically in [75,76]. Another application is the

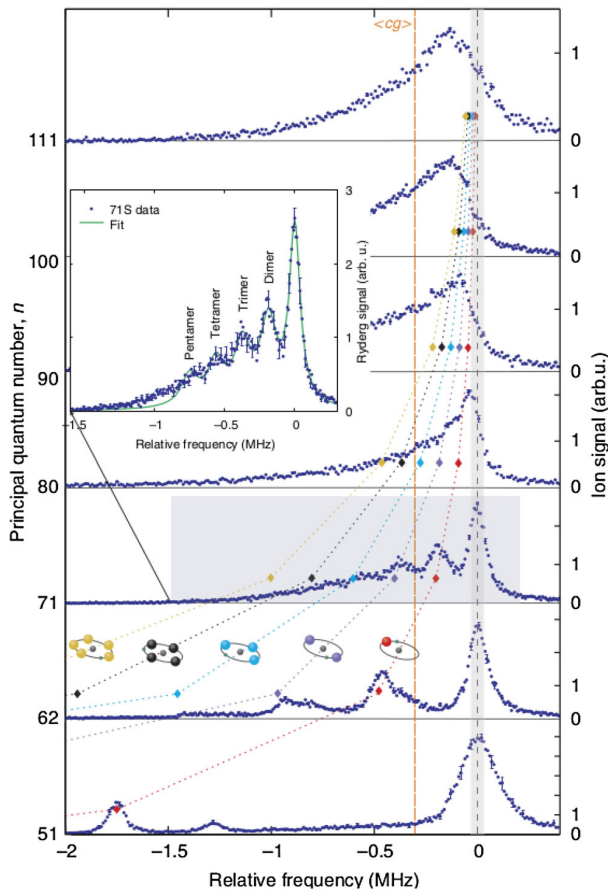


**Figure 3.** Photoassociation spectra of polyatomic Rb ULRMs in  $s$  states for different principal quantum numbers  $n$  reprinted from [13], where laser frequencies are expressed relative to the atomic  $ns$  line. Energies of trimers, tetramers, etc. are marked by coloured diamonds and appear at integer multiples of dimer energies (red diamonds). While individual polyatomic lines can be resolved at low  $n$ , see inset for  $n = 71$ , these lines merge for higher  $n$  and give rise to a mean shift of the Rydberg line. For even larger  $n \gg 111$  the spectrum is expected to become a Gaussian which localises around the mean centre of gravity  $\langle cg \rangle$  that coincides with the mean shift of the Rydberg line  $\Delta E$  in (7).

creation of ionic impurities in BECs, which can be excited in the limit of large principal quantum numbers, typically  $n \sim 160$ , when the Rydberg orbit exceeds the size of the atomic cloud [22].

Spectral lineshapes of Rydberg impurities in atomic gases as shown in Figure 3 can be modelled theoretically using two different approaches. In the first semiclassical approach the spectrum is obtained by sampling the detuning of the Rydberg line  $\Delta E$  in (6) over many realisations of  $N$  randomly distributed atoms at positions  $\vec{R}_i$ , such that the atomic density in the sample becomes  $\rho(\vec{R}) = \rho_0/N \sum_i \delta(\vec{R} - \vec{R}_i)$  [20,88]. The resulting histogram of the detuning  $\Delta E$  agrees well with the overall lineshape of the pressure shifted Rydberg line in

the mean-field limit and can be used to extract information on the  $P$ -wave scattering from experimental spectra [20]. However, the semiclassical approach does not yield molecular resonances which are relevant in the few-body regime.

An alternative fully quantum mechanical method that captures both, few-body and many-body features of polyatomic  $s$ -state ULRMs, is the functional determinant approach [19,21,89]. The resulting spectra reproduce resonance energies and the lineshape of experimental signals very accurately. Furthermore, they explain beyond mean-field effects related to the collective polaron character of the system, which are not included in the semiclassical sampling approach [19,21,89].

From a theoretical as well as from an experimental perspective Rydberg systems in  $s$ -states have certain benefits. The isotropy of the electronic states simplifies theoretical models and gives rise to comparably high experimental excitation efficiencies, due to favourable Franck–Condon factors for one- and two-photon transitions. In contrast,  $l > 0$  states have reduced Franck–Condon factors, are anisotropic and cover due to their degeneracy a larger Hilbert space, which makes ULRMs in those states more difficult to describe but leads also to richer physical properties. In particular the Born–Oppenheimer potential energy surfaces (PES) of polyatomic ULRMs with  $l > 0$  become angular dependent, i.e. they depend not only on the radial distances of the ground-state atoms but also on their relative angles [14,15,17,18,50]. As a consequence of the increased number of nuclear degrees of freedom, many theoretical investigations of the PESs focused either on randomly distributed ground-state atoms [14,16,88], or on constrained molecular geometries such as linear, planar-quadratic or cubic configurations [10,11,14]. Most important findings in this context are the prediction of triatomic trilobite molecules akin to borromean states [10], the emergence of quantum scars that appear in the form of ‘supertrilobite’ orbitals when dense and randomly distributed atoms perturb the Rydberg orbital [16] as well as the insight that computational effort in evaluating the PESs can be reduced significantly by employing basis sets of hybridised dimer orbitals [10,11,14].

The hybridised basis is typically much smaller than the full basis of Rydberg states  $\varphi_{nlm}(\vec{r})$  but yields identical PESs. Additionally, the hybridisation of dimer orbitals provides an intuitive understanding of the bond angles  $\theta$  of polyatomic URM, which are intrinsically related to the angular momentum  $l$  of the Rydberg electron. This has been demonstrated for the case of triatomic ULRMs where the number of degrees of freedom is still small enough to analyse the full electronic and vibrational structure without imposing geometrical

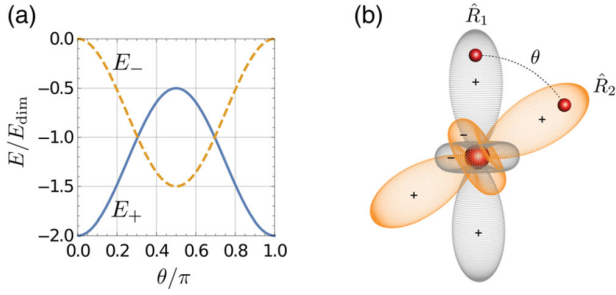


**Figure 4.** Electronic structure of  $d$ -state trimers for pure  $S$ -wave interaction reprinted from [17]. (a) The trimer possesses two PESs  $E_+$  and  $E_-$ , which are here shown as a function of the trimer angle  $\theta$  for fixed radial distances of the ground-state atoms  $R_1 = R_2 = R$ . All energies are rescaled by  $E_{\text{dim}}$ , which is the energy of the diatomic PEC evaluated at  $R$ . For instance for the outer equilibrium well of the Cs( $34d$ ) ULRM at  $R = 1868 a_0$  one has  $E_{\text{dim}} = 350 \text{ MHz} \times h$ . (b) The electronic eigenstates of the trimer are superpositions of primitive diatomic  $d$ -state orbitals (orange and gray lobes) that localise on the ground-state atoms at position  $\vec{R}_1$  and  $\vec{R}_2$ , respectively.

constraints [15,17,18]. An exemplary  $d$ -state trimer is presented in Figure 4. The primitive basis consists of the two diatomic orbitals  $\psi(\vec{r}; \vec{R}_1)$  and  $\psi(\vec{r}; \vec{R}_2)$  which are the electronic eigenstates, if there is only a single ground-state atom present at  $\vec{R}_1$  or  $\vec{R}_2$ , respectively. The angular distribution of these two  $d$  states is indicated in Figure 4(b) (gray and orange orbitals). When both ground-state atoms are present the electronic eigenstates of the trimer are superpositions of these orbitals and correspond to two PESs  $E_+(R_1, R_2, \theta)$  and  $E_-(R_1, R_2, \theta)$ . Figure 4 presents cuts of these PESs for the special situation where  $R_1 = R_2 = R$  is fixed to the radial minimum of the most outer potential well, which is  $R = 1868 a_0$  for a Cs( $34d$ ) trimer. While  $E_+$  has minima in the linear ( $\theta = \pi$ ) and anti-linear ( $\theta = 0$ ) configuration,  $E_-$  exhibits a minimum in the perpendicular configuration  $\theta = \pi/2$ . These equilibria exist since the electronic state can maximise its density on both ground-state atoms in these configurations. Due to the angular shape of the primitive  $d$  orbitals in Figure 4(b) this is the case for  $\theta = 0$ ,  $\theta = \pi$  or  $\theta = \pi/2$ . Following the same reasoning triatomic  $p$ -state ULRMs possess linear ( $\theta = \pi$ ) and anti-linear ( $\theta = \pi$ ) equilibrium geometries [15] while an even richer structure of equilibrium angles exist for trilobite trimers where the bond is established by hybridisation of two nodal trilobite orbitals [15]. The hybridisation of orbitals with different angular momenta has two important consequences. First, the binding energies of trimers with  $l > 0$  are in contrast to  $s$ -state ULRMs non-additive, since they depend on the bond angle. Second, the shape of the PESs  $E_{\pm}(R_1, R_2, \theta)$  in Figure 4 implies that the nuclei are subject to an angular-dependent force

which is, hence, an example for a three-body interaction in Rydberg systems. Both effects have been confirmed spectroscopically for  $d$ -state ULRMs in [17].

## 5. Field control

ULRMs inherit many of their characteristic features from their parent Rydberg atoms. This includes their large bond lengths as well as their extreme sensitivity to external fields. Relatively weak electric and magnetic fields on the order of tens of V/cm or tens of Gauss can already have a crucial impact on the electronic structure of ULRMs, such as the deformation of electronic orbitals as well as shifts of their energy levels. As a consequence ULRMs offer unique possibilities to control molecular properties by weak fields which is otherwise impossible for conventional ground-state molecules.

A very illustrative example for field control of ULRMs is the alignment of  $d$ -state ULRMs in magnetic fields observed in [5]. In the experiment a static magnetic field  $\vec{B} = B\vec{e}_z$  with  $B = 13.55$  Gauss was applied to lift the degeneracy of states with different magnetic quantum numbers  $m = -2, \dots, 2$ . The associated Zeeman splitting is on the order of  $22 \text{ MHz} \times h$  and exceeds the binding energy of ULRMs with quantum numbers  $n \sim 44$ . Consequently, the molecular  $S$ - and  $P$ -wave interactions perturb the energetically isolated Zeeman orbitals only weakly and the PES associated to a certain Zeeman level  $m$  are for dominant  $S$ -wave scattering well approximated by  $E(\vec{R}) = 2\pi a_S [k(R) |\varphi_{nlm}(\vec{R})|^2]$  and proportional to the spherical harmonic  $|Y_{lm}(\hat{R})|^2$ . For instance the angular distribution of  $|Y_{20}(\hat{R})|^2$  is depicted in Figure 5. Based on this shape, molecules can be either axially aligned ( $\theta = 0, \pi$ ) or perpendicular to the field axis ( $\theta = \pi/2$ ). In the latter case the ground-state atom resides in the toroidal lobe in the  $x$ - $y$  plane. The full PES  $E(\vec{R}) = E(R, \theta)$  is shown in the inset of Figure 5 and exhibits in addition to the angular structure also oscillations along the  $R$  direction which result from the radial probability density of the Rydberg state. Theoretical simulations predict that axial and toroidal equilibrium geometries possess both a series of vibrational states with certain theoretical energies (red and green diamonds). As expected from the orbital density for  $l = 2$   $m = 0$ , toroidal molecules are bound more weakly than axial molecules and possess smaller energy spacing. Comparison to experimental photoassociation spectra (blue and black dots) confirms the alignment mechanism and allows one to associate the experimental signals to different molecular geometries. Quantitative corrections due to spin-spin and spin-orbit interactions have been in the focus of [8] and will be discussed in Section 6.

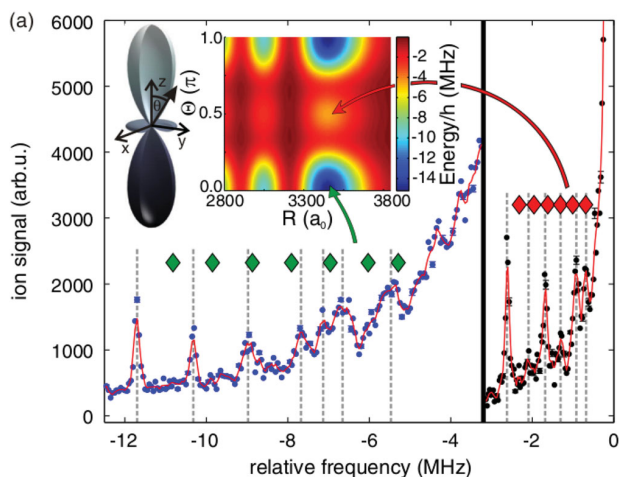


**Figure 5.** Vibrational spectrum of aligned 44d ULRMs in a magnetic field of 13.55 Gauss along the  $z$  axis reprinted from [5]. The PES  $E(R, \theta)$  (inset) depends on the bond lengths  $R$  and the orientation of the internuclear axis  $\theta$ , where the zero energy is set to the atomic  $44d, j = 5/2, m_j = 1/2$  level. The angular structure of the PES is dominated by the orbital  $|Y_{l=2, m=0}(\theta)|^2$  and supports a series of axial ( $\theta = 0, \pi$ ) and toroidal ( $\theta = \pi/2$ ) states. Theoretical energies of the axial (toroidal) states are depicted by green (red) diamonds and compared to the experimental photoassociation spectrum.

While pure magnetic fields always induce splittings of different  $m$  states, combining magnetic and electric fields offers the additional freedom to form superpositions of different atomic orbitals, e.g.  $m = 0$  and  $m = 2$  states, with mixing ratios that dependent on the field strengths. Since the geometry of ULRMs is closely related to the shape of the Rydberg orbital, this property has been exploited to tune the geometry of ULRMs continuously from axial to toroidal configurations [6].

In addition to low- $l$  ULRMs, also field control of trilobite and butterfly ULRMs has been investigated. Early theoretical work focused on the control of trilobite ULRMs via magnetic fields [3]. It has been shown that the topology of the PESs undergoes a qualitative change when the induced Zeeman splitting becomes comparable to the molecular binding energy. Due to the stronger binding of trilobite molecules the required fields are larger than for low- $l$  ULRMs. For instance for an  $n = 35$  trilobite molecule these are on the order of 500 Gauss. Fields below this threshold perturb the trilobite state only weakly and induce a confinement of the angle  $\theta$  between the molecular and the field axis to  $\theta = \pi/2$ . Contrarily, for larger fields, the PESs are characterised by energetically separated  $m$  manifolds that originate from the high- $l$  states, each supporting molecular states. Molecules belonging to the energetically lowest PES with  $m = -l$  possess a circular electronic wave function and

their vibrational states are confined in a 2D harmonic potential perpendicular to the field axis.

The impact of electric fields on trilobite molecules has been studied theoretically in [4]. In contrast to magnetic fields, electric fields tend to align the molecules to the field axis. Additionally, the field offers control over the dipole moment as well as the contribution of  $P$ -wave scattering and allows one to adjust the relative depth of the potential wells in the trilobite curve. Furthermore, sufficiently strong fields admix electronic  $s$ -state character to the polar trilobite wave function and can potentially facilitate two-photon photoassociation schemes for trilobite ULRMs. In a simple picture, the alignment results from the coupling of the electric field to the permanent dipole moment of the molecule. For butterfly molecules, which behave in this respect similar to trilobite molecules, such an alignment has been realised experimentally [7]. The measured spectrum can be described very accurately by means of a dipolar rigid rotor model or pendular state model [90]. By fitting the model parameters to the experimental spectra it is possible to extract bond lengths  $\sim 250 a_0$  and dipole moments  $\sim 500$  Debye. For trilobite molecules or ULRMs with trilobite admixture, bond lengths are larger and the pendular state spectrum is much denser at comparable field strengths. Individual pendular states of trilobite states have, therefore, not been resolved yet. Instead the electric field gives rise to an overall line broadening, which allows one to extract dipole moments [50,56]. Deviations from this line broadening have been reported in [91] and are not yet fully understood. Higher degree of control over trilobite molecules can be achieved by employing parallel electric and magnetic fields. As a function of the field strengths it is possible to tune the angle between the molecular and the fields axis from a perpendicular to a parallel configuration [92].

Even richer opportunities of control are expected to exist for polyatomic ULRMs, where fields can tune the internal angular arrangement of the nuclei in addition to the external orientation. However, only few works explored such possibilities so far [33,93]. Apart from the direct impact on the molecular geometry, it is also interesting to consider the impact of fields on the spin degrees of freedom [8,28,30]. These effects are important since the relative orientation of spins is crucial for the molecular binding and will be discussed in Section 6.

In addition to trilobite, butterfly and low- $l$  ULRMs, there is yet another species of ULRMs, called ultralong-range giant dipole molecules, that exist exclusively in the presence of crossed electric and magnetic fields [94]. Sufficiently strong fields, e.g. on the order of 1 T and 50 V/cm, modify the electronic structure of the Rydberg atom and give rise to a decentred harmonic oscillator potential for the Rydberg electron which exists due to

the non-separability of the centre-of-mass motion and the electronic motion. These states are called giant dipole states since they possess electric dipole moments on the order of many ten thousands of Debye [95–102]. Ultralong-range giant dipole molecules are predicted to form when a ground-state atom interacts with the decentered electronic cloud via the Fermi pseudopotential and becomes thereby bound to the Rydberg atom.

## 6. Spin structure

While the simple Fermi pseudopotential (2) captures many of the essential features of ULRMs, it neglects certain interactions, which are, however, indispensable for an accurate description of experimental high-resolution spectra. These interactions are related to various spin degrees of freedom present in the system, see Figure 6.

First there is the internal spin structure of the ground-state atom as well as of the Rydberg atom. The ground-state atom possesses the nuclear spin  $\vec{I}$  and a valence electron with spin  $\vec{s}_2$ , see inset in Figure 6, which couples to the hyperfine spin  $\vec{F} = \vec{I} + \vec{s}_2$ . For instance  $^{87}\text{Rb}$  has two hyperfine levels  $F = 1$  and  $F = 2$  that are separated by 6.8 GHz. The hyperfine structure of the Rydberg atom is typically negligible since it scales as  $n^{-3}$  with the principal quantum number [103]. However, there is a fine structure splitting of the Rydberg levels described by  $\vec{j} = \vec{s}_1 + \vec{l}$  where,  $\vec{l}$  and  $\vec{s}_1$  are the orbital angular momentum and the spin of the Rydberg electron, respectively. In the limit of large internuclear separation  $R$  the angular momenta  $\vec{j}$  and  $\vec{F}$  are conserved. Contrarily, at smaller separations the interaction between the electron and the ground-state atom can cause a mixing of  $\vec{j}$  and  $\vec{F}$ .

Early spectral measurements of ULRMs were described successfully by treating the electron-atom

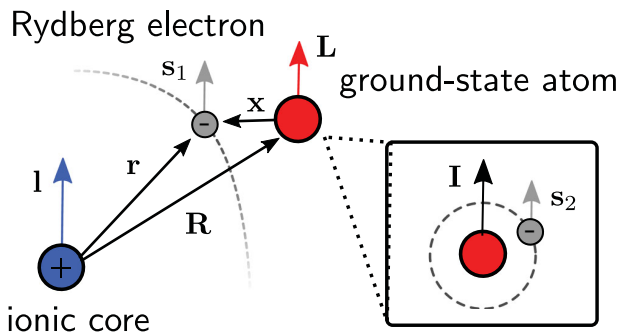


**Figure 6.** Angular momenta in ULRMs. The Rydberg electron carries a spin  $\vec{s}_1$  and an angular momentum  $\vec{l}$  or  $\vec{L}$ , depending on the frame of reference which is centred on the ionic core or the ground-state atom, respectively. The insets present the internal structure of the ground-state atom with nuclear spin  $\vec{I}$  and spin  $\vec{s}_2$  of its valence electron.

interaction only via a single scattering length  $a_S[k]$  for the  $S$ -wave channel ( $L = 0$ ) and a single scattering volume  $a_P[k]$  for the  $P$ -wave channel ( $L = 1$ ) [2,12], where  $\vec{L}$  denotes the orbital angular momentum of the Rydberg electron in the frame centred on the ground-state atom at  $\vec{R}$ , see Figure 6. These scattering lengths and volumes were associated to triplet scattering channels ( $S = 1$ ), where  $\vec{S} = \vec{s}_1 + \vec{s}_2$  is the total electron spin. The restriction to  $S = 1$  is motivated by the fact that interactions in the triplet channels are typically much stronger than in the singlet channels ( $S = 0$ ). For instance for Rb the zero-energy scattering length is  $\sim -16 a_0$  for  $S = 1$  and only  $\sim 0.5 a_0$  for  $S = 0$  [66]. Furthermore, the  $P$ -wave shape resonance occurs exclusively in the triplet channels [53,54].

However, a detailed analysis including singlet and triplet interactions as well as hyperfine and fine structure couplings reveals that singlet scattering can have a crucial impact on the molecular structure [26,81]. Due to the interplay of all interactions, the electron spin  $S$  is in general not a conserved quantity and one obtains two different classes of ULRMs. The first class is bound by pure triplet scattering and unaffected by singlet interactions, while the second class is bound by mixed singlet and triplet scattering. Typically, this mixing reduces the depth of the corresponding PECs as well as the molecular binding energies. One distinguishes therefore deep PECs belonging to the first class and shallow PECs belonging to the second class. Exemplary PECs are presented in Figure 7 close to the  $25p$  state of  $^{87}\text{Rb}$  with deep PECs (blue) and shallow PECs (orange). For experiments with ULRMs this spin mixing has two main consequences. First, mixed singlet-triplet states contain also contribution from both hyperfine states  $F$ . Excitation of these molecules can therefore be used to induce remote spin flips of ground-state atoms as well as to entangle the fine structure state of the Rydberg atom and the hyperfine state of the ground-state atom [104]. Second, measuring the binding energies of molecules in the deep and shallow PECs provides unique experimental access to low-energy singlet and triplet phase shifts. ULRMs can function therefore as high precision scattering laboratories to prepare and to probe ultra slow electron-atom collision, with electron energies below 10 meV, which is hard to achieve by alternative methods such as electron transmission [105]. Characterisation of spin-resolved scattering via ULRMs has been accomplished for  $S$ -wave phase shifts [12,27,28] as well as for  $P$ -wave phase shifts [12,20,29,30].

An important modification of the structure of the PECs in Figure 7 has been reported in [82] for Rb  $p$ -state ULRMs with relatively low principal quantum numbers  $n = 16$ . Here the deep and shallow PECs split into one, two or three subcurves which can be observed in the

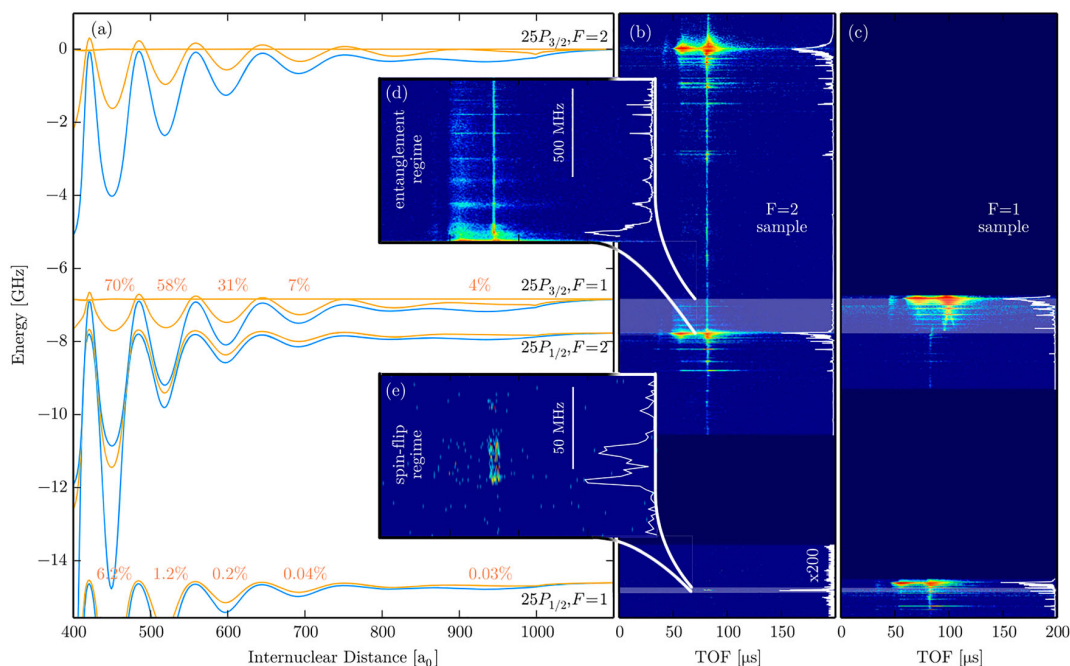


**Figure 7.** Illustration of spin-interaction effects in ULRMs reprinted from [104]. (a) PECs of diatomic  $^{87}\text{Rb}$  that correlate asymptotically to an atom in a  $25p_j$  Rydberg state and a ground-state atom in hyperfine state  $F$ . Molecules belonging to deep PECs (blue) are predominately bound by triplet scattering while those associated to shallow PECs (orange) are bound by mixed singlet/triplet scattering. The latter are also of mixed  $F$  character with admixtures of opposite spin indicated by the orange numbers. In the experiment, Rydberg states are photoexcited from an atomic BEC and detected via their ionic products  $\text{Rb}^+$  or  $\text{Rb}_2^+$  which are produced through field ionisation or spontaneous associative ionisation. (b) and (c) show the number of detected ions as a function of the laser detuning and the time of flight to the detector (TOF). The hyperfine state of the atoms in the BEC before excitation is either  $F = 2$  (b) or  $F = 1$  (c). Magnified regions of these spectra (d) and (e) demonstrate that ULRMs in the shallow potentials can be accessed from both, the  $F = 1$  and the  $F = 2$  BEC, which confirms the mixed spin characters of the associated molecules.

experiment as singlet, doublets or triplet of molecular resonances. The multiplicity of the splittings can be associated to combinations of quantum numbers  $\vec{I}$ ,  $\vec{s}_1$  and  $\vec{s}_2$  and allows thereby to correlate experimental spectral signals clearly to certain PECs, even under complicated conditions when several PECs cover the same energy range. A possible explanation for the splitting mechanism is yet another correction of the molecular interaction that arises due to spin-orbit coupling of the electron spin  $\vec{S}$  and the orbital angular momentum  $\vec{L}$  of the electron with respect to the ground-state atom, see Figure 6. As a consequence of this  $LS$  coupling the triplet phase shifts in the  $P$ -wave channel split into three subchannels  $J = 0, 1, 2$ , where  $\vec{J} = \vec{L} + \vec{S}$ . For each  $J$  channel, the  $P$ -wave shape resonance occurs at a different energy, in accordance with the fine structure splitting of the corresponding negative-ion states. It is predicted that this splitting is larger for  $\text{Cs}^-$  than for  $\text{Rb}^-$  and in both cases on the order of a few meV [53,54]. While the  $J = 1$  shape resonance in  $\text{Cs}^-$  has been confirmed using photo-detachment spectroscopy [106], a measurement of the spin-orbit split shape resonances in  $\text{Rb}$  has been achieved only recently via spectroscopy of ULRMs [30].

Extraction of these resonances as well as other scattering properties requires accurate theoretical models linking the observable molecular binding energies to the underlying scattering physics. A theoretical pseudo potential Hamiltonian which is well suited for such a purpose has been developed in [74]. It includes all the spin couplings presented in Figure 6 and generalises previous models [1,51,67,81,107]. Combining this Hamiltonian with additional magnetic fields has been accomplished in [8,9]. It was shown that couplings between the field and the spins lead to quantitative corrections of binding energies and orientation angles but also to novel opportunities for field control of ULRMs. For instance addressing molecules with different quantum numbers  $m_j$  and  $m_F$  allows one to tune the admixture of singlet and triplet scattering and thereby the depths of the PESs as well as the resulting molecular alignment [8]. Furthermore  $LS$  coupling gives rise to a novel alignment mechanism of ULRMs, which is fundamentally different from the alignment mechanism of  $d$ -state ULRMs described in Figure 5, since it does not rely on the orientation of angular orbitals  $Y_{lm}(\theta, \phi)$ . Instead, it bases on the orientation of electronic spins in the  $B$  field,

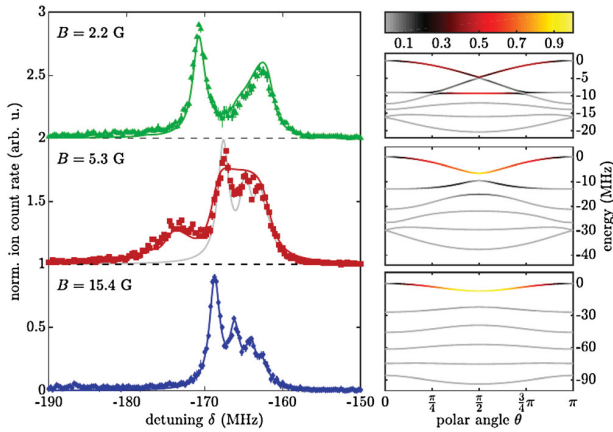


**Figure 8.** Orientation of a 31s ULRM with a bond length of ( $R \approx 890 a_0$ ) in a magnetic field reprinted from [30]. Left: Molecular spectrum as a function of the laser detuning  $\delta$  for different magnetic field strengths. The experimental signal (coloured symbols) is compared to theoretical results (solid lines). Right: Molecular PESs as a function of the angle between the field and the molecular axis for fixed bond length  $R = 890 a_0$ . Each PES corresponds to a different superposition of spin states  $|m_J, F, m_F\rangle$ . The colour code is the projection onto the state with  $m_j = 1/2$  and  $m_F = 2$  which is proportional to the strength of the laser coupling to the different PESs. The shape of the PESs together with the coupling strength determines the lineshape and the spacing of the theoretically predicted spectra (left).

which in turn couple to spatial degrees of freedom of the molecule via the  $LS$ -interaction and do thereby orient the molecule. Importantly, this alignment mechanism applies also to ULRMs in  $s$  states. This is illustrated in Figure 8 from [30], which compares experimental spectra of 31s Rb ULRMs in magnetic fields to theoretical simulations. The signals (left) can be associated to molecules with bond length of  $R \approx 890 a_0$  that are radially localised in inner potential wells which are strongly affected by  $P$ -wave interactions, c.f. Figure 1(d). The simulated signals are determined based on the angular cuts of the PESs for fixed bond length  $R = 890 a_0$  (Figure 5 right). These curves exhibit an angular dependence that can be attributed exclusively to  $LS$  coupling, i.e. without  $LS$  coupling the curves would be flat [9]. Electronic selection rules enter the simulations by taking into account that the excitation laser couples only to the electronic component with  $m_j = 1/2$  and  $m_F = 2$  which is indicated by the colour code. Consequently, for low fields (2.2 G) the laser couples to several of the energetically highest PESs, whereas for high fields (15.4 G) only the upmost PES is addressable. In the latter case the peaks in the spectrum can be clearly identified with a series of vibrational states with an anharmonic vibrational spacing on the order of 2–3 MHz that confirms the angular confinement of the molecular axis. Crucially, comparison between

the experimental and theoretical data yields information on fundamental scattering properties such as negative-ion resonances. This relation turns ULRM into a unique laboratory to realise electron-atom collisions with well-defined electronic states of ultra-low collisional energies.

## 7. Conclusions and outlook

We reviewed basic properties and recent progress in the field of ultralong-range Rydberg molecules. Ten years after the first observation of ULRMs and almost twenty years after their prediction, intense theoretical and experimental research elucidated not only the complex physical structure of the underlying interactions but revealed also many exotic and counterintuitive molecular properties as well as fascinating applications. Outstanding applications of ULRMs are field control of molecular geometry and electronic structure [6,7,92], experimental characterisation of spin-resolved slow electron-atom collisions [26–28,30] as well as the probe of interatomic correlations in ultracold atomic gases [23–25]. Furthermore, ULRMs possess an extraordinary scalability which allows one to excite not only dimers but also polymers [10,12,13,17] and, in the many-body limit, polarons [19,87,108].

In this review we focused on the three subjects, polyatomic ULRMs, field control and spin interactions by providing key experimental results and the corresponding theoretical framework. A central finding from research on polyatomic ULRMs is that binding energies of  $s$ -state ULRMs are to a good approximation additive [13], i.e. integer multiples of the number of ground-state atoms, whereas binding energies of polyatomic ULRMs with angular momenta  $l > 0$  are non-additive and involve three- and higher body forces [15,17,18,50]. Since the only experimentally confirmed polyatomic ULRMs with  $l > 0$  are  $d$ -state trimers, it is an interesting challenge for future experiments to detect novel polyatomics with more atoms, e.g.  $d$ -state tetramers, or with larger angular momenta, e.g. trilobite trimers [18].

In the context of field control, we presented possibilities to tune bond lengths, orientation as well as the shape of electronic orbitals using relatively weak electric or magnetic fields, which is impossible for conventional molecules close to their ground-state [109,110]. A so far unexplored future research direction will be to extent these opportunities to polyatomic ULRMs. In contrast to field control of dimers it is expected that field-impact on polyatomics will manipulate not only the absolute molecular orientation but also the internal configuration of the atoms. For instance, permanent dipole moments in trimers should allow one to tune the system from linear to bent geometries. First steps in this direction have been undertaken in [93] via exact diagonalisation and in [33]

employing hybridised dimer orbitals which are a useful approximation to reduce computational effort.

Lastly, we detailed how various spin degrees of freedom of the Rydberg electron and the ground-state atom impact molecular properties such as binding energies or the orientation in external fields. As a consequence, ULRMs provide a unique experimental platform to probe spin-resolved low-energy electron atom collision. Although it is remarkable, how well diagonalisation methods in combination with the Fermi pseudopotential describe such experiments, there is a strong need for a higher level theory in order to improve the accuracy of obtained observables. This is necessary since truncated diagonalisation suffers from convergence issues [72,74,111] with respect to the size of the basis set, while current Green's function methods are intrinsically convergent but neglect the hyperfine structure of the ground state atom. The most promising candidate for an improved theory would be a generalisation of the Green's function method presented in [67] that includes already spin-orbit-coupled *P*-wave interactions. Alternatively, it might be possible to develop appropriate regularisation schemes for the delta potential or to pursue a hybrid approach that deduces PESs based on existing Green's function methods while including additional spin interactions perturbatively.

Finally, it is noteworthy to mention that research on ULRMs focused so far almost exclusively on stationary properties such as binding energies, bond lengths or dipole moments. Hence, a completely novel line of research with rich opportunities is the investigation of dynamical processes in ULRMs, i.e. wave packets propagation in the oscillatory PESs. Lifetimes of ULRMs  $\sim 30 \mu\text{s}$  are large enough to observe such dynamics. A first interesting application in this direction would be the study of coherent states that perform large amplitude oscillations in the trilobite PECs, e.g. ranging from 500 to  $1800 a_0$  in Figure 1. Damping or loss rate of wave packet during the oscillations could yield information on decay processes that result from the crossing with the butterfly curves. In general this opens the doorway to study dynamics of various chemical reaction processes using ULRM, which is by no means limited to alkali atoms, but applies, due to the general binding mechanism underlying ULRM, to all kinds of single and multichannel Rydberg systems.

### Acknowledgments

The authors thank M. Eiles for fruitful discussions.

### Disclosure statement

No potential conflict of interest was reported by the authors.

### Funding

P.S. and F.H. acknowledge support from the German Research Foundation (Deutsche Forschungsgemeinschaft) within the priority programme 'Giant Interactions in Rydberg Systems' (DFG SPP 1929 GiRyd).

### References

- [1] C.H. Greene, A.S. Dickinson and H.R. Sadeghpour, *Phys. Rev. Lett.* **85**, 2458 (2000).
- [2] V. Bendkowsky, B. Butscher, J. Nipper, J.P. Shaffer, R. Löw and T. Pfau, *Nature* **458**, 1005 (2009).
- [3] I. Lesanovsky, P. Schmelcher and H.R. Sadeghpour, *J. Phys. B: At. Mol. Opt. Phys.* **39**, L69 (2006).
- [4] M. Kurz and P. Schmelcher, *Phys. Rev. A* **88**, 022501 (2013).
- [5] A. Krupp, A. Gaj, J. Balewski, P. Ilzhöfer, S. Hofferberth, R. Löw, T. Pfau, M. Kurz and P. Schmelcher, *Phys. Rev. Lett.* **112**, 143008 (2014).
- [6] A. Gaj, A. Krupp, P. Ilzhöfer, R. Löw, S. Hofferberth and T. Pfau, *Phys. Rev. Lett.* **115**, 023001 (2015).
- [7] T. Niederprüm, O. Thomas, T. Eichert, C. Lippe, J. Pérez-Ríos, C.H. Greene and H. Ott, *Nature Comm.* **7**, 12820 (2016).
- [8] F. Hummel, C. Fey and P. Schmelcher, *Phys. Rev. A* **97**, 043422 (2018).
- [9] F. Hummel, C. Fey and P. Schmelcher, *Phys. Rev. A* **99**, 023401 (2019).
- [10] I.C. Liu and J.M. Rost, *Eur. Phys. J. D* **40**, 65 (2006).
- [11] I. Liu, J. Stanojevic and J. Rost, *Phys. Rev. Lett.* **102**, 173001 (2009).
- [12] V. Bendkowsky, B. Butscher, J. Nipper, J.B. Balewski, J.P. Shaffer, R. Löw, T. Pfau, W. Li, J. Stanojevic, T. Pohl and J.M. Rost, *Phys. Rev. Lett.* **105**, 163201 (2010).
- [13] A. Gaj, A.T. Krupp, J.B. Balewski, R. Löw, S. Hofferberth and T. Pfau, *Nature Comm.* **5**, 4546 (2014).
- [14] M.T. Eiles, J. Pérez-Ríos, F. Robicheaux and C.H. Greene, *J. Phys. B: At. Mol. Opt. Phys.* **49**, 114005 (2016).
- [15] C. Fey, M. Kurz and P. Schmelcher, *Phys. Rev. A* **94**, 012516 (2016).
- [16] P.J. Luukko and J.-M. Rost, *Phys. Rev. Lett.* **119**, 203001 (2017).
- [17] C. Fey, J. Yang, S.T. Rittenhouse, F. Munkes, M. Baluktian, P. Schmelcher, H. Sadeghpour and J.P. Shaffer, *Phys. Rev. Lett.* **122**, 103001 (2019).
- [18] C. Fey, F. Hummel and P. Schmelcher, *Phys. Rev. A* **99**, 022506 (2019).
- [19] R. Schmidt, H. Sadeghpour and E. Demler, *Phys. Rev. Lett.* **116**, 105302 (2016).
- [20] M. Schlagmüller, T.C. Liebisch, H. Nguyen, G. Lochead, F. Engel, F. Böttcher, K.M. Westphal, K.S. Kleinbach, R. Löw, S. Hofferberth, T. Pfau, J. Pérez-Ríos and C.H. Greene, *Phys. Rev. Lett.* **116**, 053001 (2016).
- [21] F. Camargo, R. Schmidt, J. Whalen, R. Ding, G. Woehl, S. Yoshida, J. Burgdörfer, F. Dunning, H. Sadeghpour, and E. Demler, *Phys. Rev. Lett.* **120**, 083401 (2018).
- [22] K. Kleinbach, F. Engel, T. Dieterle, R. Löw, T. Pfau and F. Meinert, *Phys. Rev. Lett.* **120**, 193401 (2018).
- [23] T. Manthey, T. Niederprüm, O. Thomas and H. Ott, *New J. Phys.* **17**, 103024 (2015).

- [24] J.D. Whalen, R. Ding, S.K. Kanungo, T.C. Killian, S. Yoshida, J. Burgdörfer and F.B. Dunning, *Mol. Phys.* **1** (2019).
- [25] J.D. Whalen, S.K. Kanungo, R. Ding, M. Wagner, R. Schmidt, H.R. Sadeghpour, S. Yoshida, J. Burgdörfer, F.B. Dunning and T.C. Killian, *Phys. Rev. A* **100**, 011402 (2019).
- [26] D. Anderson, S. Miller and G. Raithel, *Phys. Rev. Lett.* **112**, 163201 (2014).
- [27] H. Saßmannshausen, F. Merkt and J. Deiglmayr, *Phys. Rev. Lett.* **114**, 133201 (2015).
- [28] F. Böttcher, A. Gaj, K.M. Westphal, M. Schlagmüller, K.S. Kleinbach, R. Löw, T.C. Liebisch, T. Pfau and S. Hofferberth, *Phys. Rev. A* **93**, 032512 (2016).
- [29] J.L. MacLennan, Y.-J. Chen and G. Raithel, *Phys. Rev. A* **99**, 033407 (2019).
- [30] F. Engel, T. Dieterle, F. Hummel, C. Fey, P. Schmelcher, R. Löw, T. Pfau and F. Meinert, *Phys. Rev. Lett.* **123**, 073003 (2019).
- [31] J.P. Shaffer, S.T. Rittenhouse and H.R. Sadeghpour, *Nature Comm.* **9**, 1965 (2018).
- [32] L.G. Marcassa and J.P. Shaffer, *Adv. At. Mol. Opt. Phys.* **63**, 47 (2014).
- [33] M.T. Eiles, arxiv preprint: 1902.10803 (2019).
- [34] A. Gaj, *Eur. Phys. J. Special Topics* **225**, 2919 (2016).
- [35] T.C. Liebisch, M. Schlagmüller, F. Engel, H. Nguyen, J. Balewski, G. Lochead, F. Böttcher, K.M. Westphal, K.S. Kleinbach, T. Schmid, A. Gaj, R. Löw, T. Hofferberth, Sebastian an Pfau, J. Pérez-Ríos and C.H. Greene, *J. Phys. B: At. Mol. Opt. Phys.* **49**, 182001 (2016).
- [36] H. Saßmannshausen, J. Deiglmayr and F. Merkt, *Eur. Phys. J. Spec. Top.* **225**, 2891 (2016).
- [37] C. Lippe, T. Eichert, O. Thomas, T. Niederprüm, and H. Ott, *Phys. Status Solidi B*, 1800654 (2019).
- [38] E. Amaldi and E. Segré, *Il Nuovo Cimento* **11**, 145 (1934).
- [39] E. Amaldi and E. Segré, *Nature* **133**, 141 (1934).
- [40] C. Füchtbauer and F. Gössler, *Zeitschrift für Physik* **87**, 89 (1934).
- [41] C. Füchtbauer, P. Schulz and A.F. Brandt, *Zeitschrift für Physik* **90**, 403 (1934).
- [42] E. Fermi, *Il Nuovo Cimento* (1924–1942) **11**, 157 (1934).
- [43] S.-Y. Chen and M. Takeo, *Rev. Mod. Phys.* **29**, 20 (1957).
- [44] N. Allard and J. Kielkopf, *Rev. Mod. Phys.* **54**, 1103 (1982).
- [45] I. Beigman and V. Lebedev, *Phys. Rep.* **250**, 95 (1995).
- [46] R.F. Stebbings and F.B. Dunning, *Rydberg States of Atoms and Molecules* (Cambridge University Press, Cambridge, 1983).
- [47] W.D. Phillips, *Rev. Mod. Phys.* **70**, 721 (1998).
- [48] W. Ketterle, *Rev. Mod. Phys.* **74**, 1131 (2002).
- [49] W. Li, I. Mourachko, M.W. Noel and T.F. Gallagher, *Phys. Rev. A* **67**, 052502 (2003).
- [50] W. Li, T. Pohl, J.M. Rost, S.T. Rittenhouse, H.R. Sadeghpour, J. Nipper, B. Butscher, J.B. Balewski, V. Bendkowsky, R. Low and T. Pfau, *Science* **334**, 1110 (2011).
- [51] E.L. Hamilton, C.H. Greene and H.R. Sadeghpour, *J. Phys. B: At. Mol. Opt. Phys.* **35**, L199 (2002).
- [52] M.I. Chibisov, A.A. Khuskivadze and I.I. Fabrikant, *J. Phys. B: At. Mol. Opt. Phys.* **35**, L193 (2002).
- [53] U. Thumm and D.W. Norcross, *Phys. Rev. Lett.* **67**, 3495 (1991).
- [54] C. Bahrim and U. Thumm, *Phys. Rev. A* **61**, 022722 (2000).
- [55] M.T. Eiles, *Phys. Rev. A* **98**, 042706 (2018).
- [56] D. Booth, S.T. Rittenhouse, J. Yang, H.R. Sadeghpour and J.P. Shaffer, *Science* **348**, 99 (2015).
- [57] B. Butscher, J. Nipper, J.B. Balewski, L. Kukota, V. Bendkowsky, R. Löw and T. Pfau, *Nature Phys.* **6**, 970 (2010).
- [58] B. Butscher, V. Bendkowsky, J. Nipper, J.B. Balewski, L. Kukota, R. Löw, T. Pfau, W. Li, T. Pohl and J.M. Rost, *J. Phys. B: At. Mol. Opt. Phys.* **44**, 184004 (2011).
- [59] H.R. Sadeghpour and S.T. Rittenhouse, *Mol. Phys.* **111**, 1902 (2013).
- [60] J. Tallant, S.T. Rittenhouse, D. Booth, H.R. Sadeghpour and J.P. Shaffer, *Phys. Rev. Lett.* **109**, 173202 (2012).
- [61] B.J. DeSalvo, J.A. Aman, F.B. Dunning, T.C. Killian, H.R. Sadeghpour, S. Yoshida and J. Burgdörfer, *Phys. Rev. A* **92**, 031403 (2015).
- [62] F. Camargo, J.D. Whalen, R. Ding, H.R. Sadeghpour, S. Yoshida, J. Burgdörfer, F.B. Dunning and T.C. Killian, *Phys. Rev. A* **93**, 022702 (2016).
- [63] M. Marinescu, H.R. Sadeghpour and A. Dalgarno, *Phys. Rev. A* **49**, 982 (1994).
- [64] W.F. Holmgren, M.C. Revelle, V.P.A. Lonij and A.D. Cronin, *Phys. Rev. A* **81**, 053607 (2010).
- [65] A. Omont, *J. Phys. (Paris)* **38**, 1343 (1977).
- [66] C. Bahrim, U. Thumm and I.I. Fabrikant, *J. Phys. B: At. Mol. Opt. Phys.* **34**, L195 (2001).
- [67] A. Khuskivadze, M. Chibisov and I. Fabrikant, *Phys. Rev. A* **66**, 042709 (2002).
- [68] L. Spruch, T.F. O'Malley and L. Rosenberg, *Phys. Rev. Lett.* **5**, 375 (1960).
- [69] T.F. O'Malley, L. Spruch and L. Rosenberg, *J. Math. Phys.* **2**, 491 (1961).
- [70] I.I. Fabrikant, *J. Phys. B: At. Mol. Opt. Phys.* **19**, 1527 (1986).
- [71] M.T. Eiles and C.H. Greene, *Phys. Rev. Lett.* **115**, 193201 (2015).
- [72] C. Fey, M. Kurz, P. Schmelcher, S.T. Rittenhouse and H.R. Sadeghpour, *New J. Phys.* **17**, 055010 (2015).
- [73] M. Tarana and R. Čurík, *Phys. Rev. A* **93**, 012515 (2016).
- [74] M.T. Eiles and C.H. Greene, *Phys. Rev. A* **95**, 042515 (2017).
- [75] J. Wang, M. Gacesa and R. Côté, *Phys. Rev. Lett.* **114**, 243003 (2015).
- [76] T. Karpiuk, M. Brewczyk, K. Rzążewski, A. Gaj, J.B. Balewski, A.T. Krupp, M. Schlagmüller, R. Löw, S. Hofferberth and T. Pfau, *New J. Phys.* **17**, 053046 (2015).
- [77] U. Thumm and D.W. Norcross, *Phys. Rev. A* **45**, 6349 (1992).
- [78] B. Granger, E. Hamilton and C. Greene, *Phys. Rev. A* **64**, 042508 (2001).
- [79] V. Kanellopoulos, M. Kleber and T. Kramer, *Phys. Rev. A* **80**, 012101 (2009).
- [80] M.T. Eiles, Z. Tong and C.H. Greene, *Phys. Rev. Lett.* **121**, 113203 (2018).
- [81] D.A. Anderson, S.A. Miller and G. Raithel, *Phys. Rev. A* **90**, 062518 (2014).
- [82] M. Deiß, S. Haze, J. Wolf, L. Wang, F. Meinert, C. Fey, F. Hummel, P. Schmelcher and J.H. Denschlag, arXiv preprint: 1901.08792 (2019).



# Chapter 4

## Conclusion

The last two decades have seen an unprecedented resurrection of the field of Rydberg physics boosted by the advent of cooling techniques to reach quantum degeneracy. The high degree of control of single atoms and ensembles of atoms accompanying this development allows for unmatched accuracy and resolution of experimental measurements, and brought a deep understanding of the properties of Rydberg atoms and their interaction with external fields, quantum fields, ground-state atoms, and other Rydberg atoms. In ultracold ensembles of atoms, which are dominated by short-range interactions, Rydberg atoms proved especially useful as they allow for a controlled introduction of long-range interactions. One of the many new research fields that emerged in the scope of Rydberg physics is the investigation of ultra-long-range Rydberg molecules that have been first predicted in 2000 and observed experimentally since 2008. ULRM are extraordinary molecules. They feature for instance giant bond length, oscillatory adiabatic potential energy surfaces, and huge permanent electric dipole moments even for homo-nuclear molecules. Correspondingly, they offer versatile opportunities for control of molecular properties and interatomic interactions via weak external electric or magnetic fields.

### 4.1 Discussion

In this thesis, we presented our research on ultra-long-range Rydberg molecules. Additionally, we provided an introduction to this novel and exotic type of molecule covering the history of insights and research questions as well as the corresponding experiments that led to the idea and realization of them. We discussed the experiments observing ULRM since 2008 and the development and refinement of the corresponding theory to describe ULRM ranging from the simple and intuitive perturbative picture, to a detailed modeling including all spin degrees of freedom of the two-core–two-electron molecular system, the influence of external fields, and the emergence of polyatomic molecules.

Our scientific contributions [[1-10]] had three main goals: Firstly, we aimed at a deep understanding of spin-dependent and spin-orbit dependent electron–atom scattering, which is the key binding mechanism of ULRM, and its impact onto their structure and properties [[1-4]]. Secondly, we utilized this thorough understanding to propose applications of ULRM in the context of collisions between Rydberg atoms and ground-state atoms as well as in the context of molecular charge transfer and ion formation [[5-7]]. And thirdly, we particularized the transition from diatomic ULRM to triatomic ULRM [[8-9]]. A review article summarizing the development of the research field is also provided [[10]]. Our investigations are supported by experimental evidence obtained in close collaborations with experimental groups [[3,4]].

#### **Electron–atom scattering**

The attractive scattering interaction of the Rydberg electron with the neutral ground-state atom gives rise to the molecular binding mechanism. The interactions of the electronic spins of

the Rydberg electron and the valence electron of the ground-state atom among each other and with their respective orbital angular momenta as well as with the nuclear spins determine the structure of the molecule. Therefore, ULRM provide unique experimental access to the physics of slow electron–atom collisions at low energies, which have been out of reach for conventional electron scattering methods like electron-transmission spectroscopy or photodetachment spectroscopy. Our investigations of the influence of spin interactions onto  $d$ -state Rydberg molecules exposed to a weak magnetic field [[1]] proved that the current experimental resolution indeed suffices to unveil characteristic features of these interactions, by comparing our theoretical results to ionization spectra taken two years earlier. This research led to the prediction of the alignment of  $s$ -state Rydberg molecules in weak magnetic fields [[2]], which is an effect uniquely resulting from the existence of a negative-ion fine structure of the electron–atom scattering system. In a subsequent experimental collaboration with the research group of Tilman Pfau in Stuttgart [[3]], we were able to confirm this effect and to extract accurate  $s$ - and  $p$ -wave scattering phase shifts. Furthermore, the characteristic form of the  $p$ -wave scattering phase shifts for each fine structure channel allows the prediction of the exact energies of the so far unobserved resonances of anionic rubidium. Investigations of ULRM asymptotically connected to Rydberg- $p$  states reveal that the presence of spin-spin and spin-orbit couplings in the presence of resonant  $p$ -wave interactions gives rise to characteristic doublet and triplet substructures of the vibrational levels. These depend on the hyperfine state of the ground-state atom by several tens of MHz splittings, which has been confirmed experimentally in a collaboration with the group of Johannes Hecker Denschlag in Ulm [[4]].

The theoretical models linking the scattering lengths to experimentally accessible observables require a high accuracy. The Fermi-pseudo potential has some inherent convergence problems with respect to the underlying basis size: The zero-range potential does not capture that high energy basis states with small corresponding de Broglie wavelengths will at some point start to probe the spacial extend of the ground-state atom. In [[3,4]], we therefore combined the pseudo-potential approach with an analytic approach that relies on the closed-form expressions of the Coulomb Green’s function. While being more accurate describing the electron–atom interaction, this neglects, however, other essential interactions like the Rydberg fine structure and the ground-state atom’s hyperfine structure. We circumvented this issue by experimentally addressing fully spin-polarized states not susceptible to these kind of interactions. This allowed us to appropriately tune the parameters of the pseudo potential before applying it to a more general class of states. For the Green’s function method as well as for the local frame transformation procedure, there are prospects to include the full molecular spin structure to derive an accurate analytical model. Alternatively, the pseudo-potential approach could be regularized taking finite range corrections into account.

## Polyatomic ULRM

Trilobite and butterfly ULRM are to a large extent uninfluenced by spin-interaction effects and they are well approximated by pure triplet interactions. For polyatomic molecules, the complexity of their structure arises from strong anisotropy of their electronic wave function. In [[8,9]], we derived building principles to find equilibrium configurations of stable high- $l$  trimers based on the dimer configuration. This may prove as a valuable tool to experimentally realize triatomic trilobite or butterfly molecules. Opposed to low- $l$  polyatomic ULRM, which are only weakly confined in the angular vibrational coordinate, in triatomic trilobite molecules, the energy scales of stretching and bending modes is of similar order [[8]]. Triatomic butterfly molecules can be divided into two classes depending on their parity under reflection at the internuclear plane. The structure of even parity states is to a wide extend comparable to triatomic

trilobite molecules. Odd parity states, however, are co-linear molecules tightly confined in their bending and symmetric-stretch motion, but only loosely in their asymmetric stretch motion [[9]]. Our findings hint at fascinating opportunities for the dynamics of polyatomic ULRM due to their rich underlying structure. Here, also nonadiabatic effects may become important. The anisotropy of polyatomic ULRM may also influence the many-body spectra of Rydberg polarons that consist of a single Rydberg excitation binding many ground-state atoms to it and which have so far been theoretically described only via the approximately isotropic and separable  $s$ -state ULRM potential.

Experimentally, direct excitation of high- $l$  ULRM via one- or two-photon transition is hindered by angular-momentum selection rules. Current realizations rely on the energetic proximity of low- $l$  ULRM, due to their suitable quantum defect that leads to mixing with the desired state. This enabled us for example to address trilobite states in cesium via  $s$ -states or butterfly states in rubidium via  $p$ -states. Additionally, the mixing of hyperfine states allows for a limited tunability of such options, which also led to the excitation of trilobites via rubidium  $s$ -states. This limitation may be overcome in the near future employing microwave fields to couple orbital angular momentum states within the same Rydberg manifold. Interest in this kind of experiment has been growing recently due to opportunities regarding the creation of circular Rydberg states [276–278] and their applications in quantum computing platforms based on neutral atoms [281].

### Charge transfer and ion formation

Another class of high-angular-momentum molecules was the focus of [[5]]. ULRM bound by weakly attractive singlet  $p$ -wave interaction in a stairwell potential are considered a candidate for photoassociation of heavy Rydberg systems, i.e. pairs of oppositely charged ions, from ultracold gases. The electronic  $^1P_1$  state of the electron–atom system provides ideal conditions for the transition to the  $^1S_0$  state of the anion. Photoassociation of molecules bound in the stairwell potential can be achieved via three-photon transition to the Rydberg- $f$  state. The internuclear distances provided by ULRM cannot be reached for HRS excited from tightly bound molecules. The corresponding high principal quantum number of the HRS leads to long radiative lifetimes and strong suppression of the decay mechanism of mutual neutralization. This uniquely suggests HRS as a candidate for the creation of ultracold negative ions deprived of an optical transition for laser cooling as well as for the creation of mass-balanced ultracold plasmas.

### Dynamical and collisional processes

Both the large permanent electric dipole moments as well as the properties of their parent Rydberg atom make ULRM extremely sensitive to external fields and allow molecular control with comparably low field strength. At the same time, in the experimental apparatus for trapping ultracold atoms optically or magnetically, weak external fields are almost always present. In [[7]], we developed an approach to study the time evolution of trilobite ULRM in the presence of weak external electric fields. The dynamical behavior strongly depends on the employed field strength and the initial configuration of the molecules. For example, an isotropic initial state obtained from field-free association shows pendular behavior in the presence of an electric field, while an angularly confined initial state shows rotational behavior. Periodic quenching of the field allows for the preparation of a molecule in a superposition of two distinct radial configurations, the bond lengths of which differ by hundreds of Bohr radii.

Additionally, the trilobite PES strongly influence the internuclear dynamics of a ground-state atom in the presence of a Rydberg atom in a low- $l$  angular-momentum state with a small quantum defect such that an avoided crossing of the corresponding PES occurs [[6]].

For a wide range of principal quantum numbers  $n$ , the adiabaticity at ultracold temperatures leads to an  $l$ -changing transition of the Rydberg state. However, the oscillatory character of both the PES as well as of the associated nonadiabatic coupling elements allows for tuning the characteristics of the crossing via  $n$ . The Rydberg electron's energy may therefore be considered as a synthetic dimension and in the two-dimensional parameter space of  $R$  and  $n$ , conical intersections occur, which allow for instant hopping between the PES. This is experimentally observable via a temperature independent, strong suppression of the  $l$ -changing rate. This type of conical intersection is unique to diatomic systems in which the exact crossing of PES is generally prohibited by the von Neumann-Wigner theorem rendering our findings to be of fundamental relevance.

Finally, with our review article [[10]], we provided an overview of the field of ULRM from their precursors dating back to the late 20s of the 20th century, their prediction in the year 2000 and the first observation in 2008, until today's experiments and applications involving this exotic type of molecules.

## 4.2 Perspectives

Besides the already mentioned prospects arising from the particular articles comprising this theses, here we want to mention some more general aspects for future research on or employing ULRM.

Some of the most urgent open questions concern their dynamical behavior. The rich structure of PES, their crossings, and their short-range internuclear attraction opens a plethora of opportunities to study the chemical properties of ULRM. Intra-molecular processes include fast, radiationless decays to other electronic states and collisional or associative ionization which are yet to be described and understood. Here, the break-down of the Born-Oppenheimer approximation plays a crucial role allowing for vibronic couplings and other nonadiabatic effects. With the methodological setup provided in [[7]], we pave the way for in-depth studies of these processes in the scope of the nuclear dynamics of ULRM. A first example considering  $l$ -changing collisions has already been provided [[6]]. Some immediate examples for further studies include the decay of trilobite molecules via resonant  $p$ -wave interactions, coupling them to the butterfly potential. It was already shown that these couplings are tunable via electric fields [98]. This may lead to controllable molecular lifetimes. Furthermore, the decay of low- $l$  angular-momentum molecules bound by quantum reflection and connecting them to the short-range physics of the polarization potential is currently under experimental investigation [164–167]. However, this requires also a better understanding of electronically excited states of tightly-bound molecules.

Beyond that, also inter-molecular processes such as collisions between ULRM provide exciting research opportunities. One could imagine a controlled transportation of ULRM via a conveyor belt or a Stark decelerator. ULRM with their large and controllable internuclear distances provide a unique means for doping surfaces with correlated patterning.

So far unaddressed research opportunities with immediate relevance are the structure of ULRM in inhomogeneous electric and magnetic fields as well as in time-dependent optical fields which both can generally be present in typical ultracold-atom experiments. Here, specifically the influence of optical tweezers onto the molecular structure may be relevant for applications in the scope of quantum simulators and quantum computers based on Rydberg interactions in neutral atom platforms.

# Bibliography

- [1] J. R. Rydberg, *Recherches sur la constitution des spectres d'émission des éléments chimiques*, Kungliga Vetenskapsakademiens Handlingar, Vol. Band 23 No 11 (Kungliga Vetenskapsakademien, 1890).
- [2] E. Schrödinger, "An undulatory theory of the mechanics of atoms and molecules," *Phys. Rev.* **28**, 1049 (1926).
- [3] W. Heisenberg, "Über den anschaulichen Inhalt der quantentheoretischen Kinematik und Mechanik," *Z. Physik* **43**, 172 (1927).
- [4] P. A. M. Dirac and R. H. Fowler, "The quantum theory of the electron," *Proc. R. Soc. Lond. A* **117**, 610 (1928).
- [5] F. B. Dunning, J. J. Mestayer, C. O. Reinhold, S. Yoshida, and J. Burgdörfer, "Engineering atomic Rydberg states with pulsed electric fields," *J. Phys. B: At. Mol. Opt. Phys.* **42**, 022001 (2009).
- [6] S. V. Stepkin, A. A. Konovalenko, N. G. Kantharia, and N. Udaya Shankar, "Radio recombination lines from the largest bound atoms in space," *Monthly Notices of the Royal Astronomical Society* **374**, 852 (2006).
- [7] E. Amaldi and E. Segré, "Effetto della pressione sui termini elevati degli alcalini," *Nuovo Cim.* **11**, 145 (1934).
- [8] E. Amaldi and E. Segré, "Effect of pressure on high terms of alkaline spectra," *Nature (London)* **133**, 141 (1934).
- [9] J. E. Mack and E. C. Barkofsky, "Atomic beam apparatus for studying the atomic spectra of gases, especially hydrogen," *Rev. Mod. Phys.* **14**, 82 (1942).
- [10] K. W. Meissner, "Application of atomic beams in spectroscopy," *Rev. Mod. Phys.* **14**, 68 (1942).
- [11] T. Maiman, "Stimulated optical radiation in ruby," *Nature (London)* **187**, 493 (1960).
- [12] M. Hugon, F. Gounand, P. R. Fournier, and J. Berlande, "Collisional properties of highly excited rubidium atoms," *J. Phys. B: At. Mol. Phys.* **12**, 2707 (1979).
- [13] A. N. Klucharev, A. V. Lazarenko, and V. Vujnovic, "The ionisation rate coefficients of radiatively excited rubidium atoms  $\text{Rb}(n^2\text{P}) + \text{Rb}(5^2\text{S})$ ," *J. Phys. B: At. Mol. Phys.* **13**, 1143 (1980).
- [14] M. Cheret, L. Barbier, W. Lindinger, and R. Deloche, "Penning and associative ionisation of highly excited rubidium atoms," *J. Phys. B: At. Mol. Phys.* **15**, 3463 (1982).
- [15] L. Barbier and M. Cheret, "Experimental study of Penning and Hornbeck-Molnar ionisation of rubidium atoms excited in a high  $s$  or  $d$  level ( $5d \leq nl \leq 11s$ )," *J. Phys. B: At. Mol. Phys.* **20**, 1229 (1987).

- [16] I. Beigman and V. Lebedev, “Collision theory of Rydberg atoms with neutral and charged particles,” *Physics Reports* **250**, 95 (1995).
- [17] M. Gross, P. Goy, C. Fabre, S. Haroche, and J. M. Raimond, “Maser oscillation and microwave superradiance in small systems of Rydberg atoms,” *Phys. Rev. Lett.* **43**, 343 (1979).
- [18] P. Goy, J. M. Raimond, M. Gross, and S. Haroche, “Observation of cavity-enhanced single-atom spontaneous emission,” *Phys. Rev. Lett.* **50**, 1903 (1983).
- [19] S. Haroche, “Nobel lecture: Controlling photons in a box and exploring the quantum to classical boundary,” *Rev. Mod. Phys.* **85**, 1083 (2013).
- [20] J. E. Bjorkholm, R. R. Freeman, A. Ashkin, and D. B. Pearson, “Observation of focusing of neutral atoms by the dipole forces of resonance-radiation pressure,” *Phys. Rev. Lett.* **41**, 1361 (1978).
- [21] W. D. Phillips and H. Metcalf, “Laser deceleration of an atomic beam,” *Phys. Rev. Lett.* **48**, 596 (1982).
- [22] E. L. Raab, M. Prentiss, A. Cable, S. Chu, and D. E. Pritchard, “Trapping of neutral sodium atoms with radiation pressure,” *Phys. Rev. Lett.* **59**, 2631 (1987).
- [23] M. H. Anderson, J. R. Ensher, M. R. Matthews, C. E. Wieman, and E. A. Cornell, “Observation of Bose-Einstein condensation in a dilute atomic vapor,” *Science* **269**, 198 (1995).
- [24] C. C. Bradley, C. A. Sackett, J. J. Tollett, and R. G. Hulet, “Evidence of Bose-Einstein condensation in an atomic gas with attractive interactions,” *Phys. Rev. Lett.* **75**, 1687 (1995).
- [25] K. B. Davis, M. O. Mewes, M. R. Andrews, N. J. van Druten, D. S. Durfee, D. M. Kurn, and W. Ketterle, “Bose-Einstein condensation in a gas of sodium atoms,” *Phys. Rev. Lett.* **75**, 3969 (1995).
- [26] D. Jaksch, J. I. Cirac, P. Zoller, S. L. Rolston, R. Côté, and M. D. Lukin, “Fast quantum gates for neutral atoms,” *Phys. Rev. Lett.* **85**, 2208 (2000).
- [27] L. Santos, G. V. Shlyapnikov, P. Zoller, and M. Lewenstein, “Bose-Einstein condensation in trapped dipolar gases,” *Phys. Rev. Lett.* **85**, 1791 (2000).
- [28] C. H. Greene, A. S. Dickinson, and H. R. Sadeghpour, “Creation of polar and nonpolar ultra-long-range Rydberg molecules,” *Phys. Rev. Lett.* **85**, 2458 (2000).
- [29] A. Reinhard, T. C. Liebisch, B. Knuffman, and G. Raithel, “Level shifts of rubidium Rydberg states due to binary interactions,” *Phys. Rev. A* **75**, 032712 (2007).
- [30] L. Béguin, A. Vernier, R. Chicireanu, T. Lahaye, and A. Browaeys, “Direct measurement of the van der Waals interaction between two Rydberg atoms,” *Phys. Rev. Lett.* **110**, 263201 (2013).
- [31] M. D. Lukin, M. Fleischhauer, R. Côté, L. M. Duan, D. Jaksch, J. I. Cirac, and P. Zoller, “Dipole blockade and quantum information processing in mesoscopic atomic ensembles,” *Phys. Rev. Lett.* **87**, 037901 (2001).

- [32] K. Singer, M. Reetz-Lamour, T. Amthor, L. G. Marcassa, and M. Weidemüller, “Suppression of excitation and spectral broadening induced by interactions in a cold gas of Rydberg atoms,” *Phys. Rev. Lett.* **93**, 163001 (2004).
- [33] D. Tong, S. M. Farooqi, J. Stanojevic, S. Krishnan, Y. P. Zhang, R. Côté, E. E. Eyler, and P. L. Gould, “Local blockade of Rydberg excitation in an ultracold gas,” *Phys. Rev. Lett.* **93**, 063001 (2004).
- [34] T. C. Liebisch, A. Reinhard, P. R. Berman, and G. Raithel, “Atom counting statistics in ensembles of interacting Rydberg atoms,” *Phys. Rev. Lett.* **95**, 253002 (2005).
- [35] E. Urban, T. A. Johnson, T. Henage, L. Isenhower, D. D. Yavuz, T. G. Walker, and M. Saffman, “Observation of Rydberg blockade between two atoms,” *Nature Phys.* **5**, 110 (2019).
- [36] P. Schauß, M. Cheneau, M. Endres, T. Fukuhara, S. Hild, A. Omran, T. Pohl, C. Gross, S. Kuhr, and I. Bloch, “Observation of spatially ordered structures in a two-dimensional Rydberg gas,” *Nature (London)* **491**, 87 (2012).
- [37] T. Wilk, A. Gaëtan, C. Evellin, J. Wolters, Y. Miroshnychenko, P. Grangier, and A. Browaeys, “Entanglement of two individual neutral atoms using Rydberg blockade,” *Phys. Rev. Lett.* **104**, 010502 (2010).
- [38] J. Honer, H. Weimer, T. Pfau, and H. P. Büchler, “Collective many-body interaction in Rydberg dressed atoms,” *Phys. Rev. Lett.* **105**, 160404 (2010).
- [39] J. B. Balewski, A. T. Krupp, A. Gaj, S. Hofferberth, R. Löw, and T. Pfau, “Rydberg dressing: understanding of collective many-body effects and implications for experiments,” *New J. Phys.* **16**, 063012 (2014).
- [40] Y.-Y. Jau, A. M. Hankin, T. Keating, I. H. Deutsch, and G. W. Biedermann, “Entangling atomic spins with a Rydberg-dressed spin-flip blockade,” *Nat. Phys.* **12**, 71 (2016).
- [41] J. Zeiher, R. van Bijnen, P. Schauß, S. Hild, J. yoon Choi, T. Pohl, I. Bloch, and C. Gross, “Entangling atomic spins with a Rydberg-dressed spin-flip blockade,” *Nat. Phys.* **12**, 1095 (2016).
- [42] V. Bendkowsky, B. Butscher, J. Nipper, J. P. Shaffer, R. Löw, and T. Pfau, “Observation of ultralong-range Rydberg molecules,” *Nature (London)* **458**, 1005 (2009).
- [43] V. Bendkowsky, B. Butscher, J. Nipper, J. B. Balewski, J. P. Shaffer, R. Löw, T. Pfau, W. Li, J. Stanojevic, T. Pohl, and J. M. Rost, “Rydberg trimers and excited dimers bound by internal quantum reflection,” *Phys. Rev. Lett.* **105**, 163201 (2010).
- [44] W. Li, T. Pohl, J. M. Rost, S. T. Rittenhouse, H. R. Sadeghpour, J. Nipper, B. Butscher, J. B. Balewski, V. Bendkowsky, R. Löw, and T. Pfau, “A homonuclear molecule with a permanent electric dipole moment,” *Science* **334**, 1110 (2011).
- [45] H. Fan, S. Kumar, J. Sedlacek, H. Kübler, S. Karimkashi, and J. P. Shaffer, “Atom based RF electric field sensing,” *J. Phys. B: At. Mol. Opt. Phys.* **48**, 202001 (2015).
- [46] C. L. Degen, F. Reinhard, and P. Cappellaro, “Quantum sensing,” *Rev. Mod. Phys.* **89**, 035002 (2017).

- [47] H. Weimer, M. Müller, I. Lesanovsky, P. Zoller, and H. P. Büchler, “A Rydberg quantum simulator,” *Nature Phys.* **6**, 382 (2010).
- [48] I. Bloch, J. Dalibard, and S. Nascimbène, “Quantum simulations with ultracold quantum gases,” *Nature Phys.* **8**, 267 (2010).
- [49] M. Saffman, T. G. Walker, and K. Mølmer, “Quantum information with Rydberg atoms,” *Rev. Mod. Phys.* **82**, 2313 (2010).
- [50] M. Saffman, “Quantum computing with atomic qubits and Rydberg interactions: progress and challenges,” *J. Phys. B: At. Mol. Opt. Phys.* **49**, 202001 (2016).
- [51] D. Petrosyan, F. Motzoi, M. Saffman, and K. Mølmer, “High-fidelity Rydberg quantum gate via a two-atom dark state,” *Phys. Rev. A* **96**, 042306 (2017).
- [52] M. Saffman and T. G. Walker, “Creating single-atom and single-photon sources from entangled atomic ensembles,” *Phys. Rev. A* **66**, 065403 (2002).
- [53] J. Honer, R. Löow, H. Weimer, T. Pfau, and H. P. Büchler, “Artificial atoms can do more than atoms: Deterministic single photon subtraction from arbitrary light fields,” *Phys. Rev. Lett.* **107**, 093601 (2011).
- [54] S. Baur, D. Tiarks, G. Rempe, and S. Dürr, “Single-photon switch based on Rydberg blockade,” *Phys. Rev. Lett.* **112**, 073901 (2014).
- [55] H. Gorniaczyk, C. Tresp, J. Schmidt, H. Fedder, and S. Hofferberth, “Single-photon transistor mediated by interstate Rydberg interactions,” *Phys. Rev. Lett.* **113**, 053601 (2014).
- [56] O. Firstenberg, C. S. Adams, and S. Hofferberth, “Nonlinear quantum optics mediated by Rydberg interactions,” *J. Phys. B: At. Mol. Opt. Phys.* **49**, 152003 (2016).
- [57] D. Tiarks, S. Schmidt-Eberle, T. Stolz, G. Rempe, and S. Dürr, “A photon–photon quantum gate based on Rydberg interactions,” *Nature Phys.* **15**, 124 (2019).
- [58] T. M. Graham, M. Kwon, B. Grinkemeyer, Z. Marra, X. Jiang, M. T. Lichtman, Y. Sun, M. Ebert, and M. Saffman, “Rydberg-mediated entanglement in a two-dimensional neutral atom qubit array,” *Phys. Rev. Lett.* **123**, 230501 (2019).
- [59] Y. Dudin, L. Li, F. Bariani, and A. Kuzmich, “Observation of coherent many-body Rabi oscillations,” *Nature Phys.* **8**, 790 (2012).
- [60] T. M. Weber, M. Hönig, T. Niederprüm, T. Mantney, O. Thomas, M. Fleischhauer, and H. Ott, “Mesoscopic Rydberg-blockaded ensembles in the superatom regime and beyond,” *Nature Phys.* **11**, 157 (2015).
- [61] J. Zeiher, P. Schauß, S. Hild, T. Macrì, I. Bloch, and C. Gross, “Microscopic characterization of scalable coherent Rydberg superatoms,” *Phys. Rev. X* **5**, 031015 (2015).
- [62] C. Ates, T. Pohl, T. Pattard, and J. M. Rost, “Antiblockade in Rydberg excitation of an ultracold lattice gas,” *Phys. Rev. Lett.* **98**, 023002 (2007).
- [63] T. Amthor, C. Giese, C. S. Hofmann, and M. Weidemüller, “Evidence of antiblockade in an ultracold Rydberg gas,” *Phys. Rev. Lett.* **104**, 013001 (2010).

- [64] F. Letscher, O. Thomas, T. Niederprüm, H. Ott, and M. Fleischhauer, “Anomalous excitation facilitation in inhomogeneously broadened Rydberg gases,” *Phys. Rev. A* **95**, 023410 (2017).
- [65] N. Sándor, R. González-Férez, P. S. Julienne, and G. Pupillo, “Rydberg optical Feshbach resonances in cold gases,” *Phys. Rev. A* **96**, 032719 (2017).
- [66] O. Thomas, C. Lippe, T. Eichert, and H. Ott, “Experimental realization of a Rydberg optical Feshbach resonance in a quantum many-body system,” *Nat. Commun.* **9**, 2238 (2018).
- [67] H. Bernien, S. Schwartz, A. Keesling, H. Levine, A. Omran, H. Pichler, S. Choi, A. S. Zibrov, M. Endres, M. Greiner, V. Vuletić, and M. D. Lukin, “Probing many-body dynamics on a 51-atom quantum simulator,” *Nature (London)* **551**, 579 (2017).
- [68] H. Labuhn, D. Barredo, S. Ravets, S. de Léséleuc, T. Macrì, T. Lahaye, and A. Browaeys, “Tunable two-dimensional arrays of single Rydberg atoms for realizing quantum ising models,” *Nature (London)* **534**, 667 (2016).
- [69] S. Ebadi, T. T. Wang, H. Levine, A. Keesling, G. Semeghini, A. Omran, D. Bluvstein, R. Samajdar, H. Pichler, W. W. Ho, S. Choi, S. Sachdev, M. Greiner, V. Vuletic, and M. D. Lukin, “Quantum phases of matter on a 256-atom programmable quantum simulator,” *Nature (London)* **595**, 227 (2021).
- [70] P. Scholl, M. Schuler, H. J. Williams, A. A. Eberharter, D. Barredo, K.-N. Schymik, V. Lienhard, L.-P. Henry, T. C. Lang, T. Lahaye, A. M. Läuchli, and A. Browaeys, “Programmable quantum simulation of 2D antiferromagnets with hundreds of Rydberg atoms,” *Nature (London)* **595**, 233 (2021).
- [71] D. Bluvstein, A. Omran, H. Levine, A. Keesling, G. Semeghini, S. Ebadi, T. T. Wang, A. A. Michailidis, N. Maskara, W. W. Ho, S. Choi, M. Serbyn, M. Greiner, V. Vuletić, and M. D. Lukin, “Controlling quantum many-body dynamics in driven Rydberg atom arrays,” *Science* **371**, 1355 (2021).
- [72] J. Preskill, “Quantum Computing in the NISQ era and beyond,” *Quantum* **2**, 79 (2018).
- [73] W. Li, “A boost to Rydberg quantum computing,” *Nat. Phys.* **16**, 820 (2020).
- [74] A. Browaeys and T. Lahaye, “Many-body physics with individually controlled Rydberg atoms,” *Nat. Phys.* **16**, 132 (2020).
- [75] M. F. Serret, B. Marchand, and T. Ayrál, “Solving optimization problems with rydberg analog quantum computers: Realistic requirements for quantum advantage using noisy simulation and classical benchmarks,” *Phys. Rev. A* **102**, 052617 (2020).
- [76] L. Henriët, L. Beguin, A. Signoles, T. Lahaye, A. Browaeys, G.-O. Reymond, and C. Jurczak, “Quantum computing with neutral atoms,” *Quantum* **4**, 327 (2020).
- [77] M. Morgado and S. Whitlock, “Quantum simulation and computing with Rydberg-interacting qubits,” *AVS Quantum Science* **3**, 023501 (2021).
- [78] J. B. Balewski, A. T. Krupp, A. Gaj, D. Peter, H. P. Büchler, R. Löw, S. Hofferberth, and T. Pfau, “Coupling a single electron to a Bose-Einstein condensate,” *Nature (London)* **502**, 664 (2013).

- [79] A. Gaj, A. T. Krupp, J. B. Balewski, R. Löw, S. Hofferberth, and T. Pfau, “From molecular spectra to a density shift in dense Rydberg gases,” *Nat. Commun.* **5**, 5546 (2014).
- [80] R. Schmidt, H. R. Sadeghpour, and E. Demler, “Mesoscopic Rydberg impurity in an atomic quantum gas,” *Phys. Rev. Lett.* **116**, 105302 (2016).
- [81] F. Camargo, R. Schmidt, J. D. Whalen, R. Ding, G. Woehl, S. Yoshida, J. Burgdörfer, F. B. Dunning, H. R. Sadeghpour, E. Demler, and T. C. Killian, “Creation of Rydberg polarons in a bose gas,” *Phys. Rev. Lett.* **120**, 083401 (2018).
- [82] R. Schmidt, J. D. Whalen, R. Ding, F. Camargo, G. Woehl, S. Yoshida, J. Burgdörfer, F. B. Dunning, E. Demler, H. R. Sadeghpour, and T. C. Killian, “Theory of excitation of Rydberg polarons in an atomic quantum gas,” *Phys. Rev. A* **97**, 022707 (2018).
- [83] C. Füchtbauer and F. Gössler, “Entgegengesetzte Unsymmetrie der Verbreiterung bei verschiedenen Linien einer Serie,” *Die Naturwissenschaften* **21**, 315 (1933).
- [84] C. Füchtbauer and F. Gössler, “Verschiebung und unsymmetrische Verbreiterung von Absorptionslinien durch Fremdgase,” *Z. Physik* **87**, 89 (1934).
- [85] C. Füchtbauer, P. Schulz, and A. F. Brandt, “Verschiebung von hohen Serienlinien des Natriums und Kaliums durch Fremdgase, Berechnung der Wirkungsquerschnitte von Edelgasen gegen sehr langsame Elektronen,” *Z. Physik* **90**, 403 (1934).
- [86] E. Fermi, “Sopra lo spostamento per pressione delle righe elevate delle serie spettrali,” *Nuovo Cim.* **11**, 157 (1934).
- [87] S.-y. Ch'en and M. Takeo, “Broadening and shift of spectral lines due to the presence of foreign gases,” *Rev. Mod. Phys.* **29**, 20 (1957).
- [88] J. Derouard and M. Lombardi, “Theoretical cross sections for collisional angular momentum transfer in atomic Rydberg states,” *J. Phys. B* **11**, 3875 (1978).
- [89] A. P. Hickman, “Relation between low-energy-electron scattering and  $l$ -changing collisions of Rydberg atoms,” *Phys. Rev. A* **19**, 994 (1979).
- [90] V. S. Lebedev and I. I. Fabrikant, “Inelastic and quasielastic collisions of Rydberg atoms with the heavy rare-gas atoms,” *Phys. Rev. A* **54**, 2888 (1996).
- [91] V. S. Lebedev and I. I. Fabrikant, “Semiclassical calculations of the  $l$ -mixing and  $n, l$ -changing collisions of Rydberg atoms with rare-gas atoms,” *J. Phys. B* **30**, 2649 (1997).
- [92] N. Allard and J. Kielkopf, “The effect of neutral nonresonant collisions on atomic spectral lines,” *Rev. Mod. Phys.* **54**, 1103 (1982).
- [93] R. F. Stebbings and F. B. Dunning, *Rydberg states of atoms and molecules* (Cambridge University Press, 1983).
- [94] A. Omont, “On the theory of collisions of atoms in Rydberg states with neutral particles,” *J. Phys. France* **38**, 1343 (1977).
- [95] W. D. Phillips, “Nobel lecture: Laser cooling and trapping of neutral atoms,” *Rev. Mod. Phys.* **70**, 721 (1998).

- [96] W. Ketterle, “Nobel lecture: When atoms behave as waves: Bose-Einstein condensation and the atom laser,” *Rev. Mod. Phys.* **74**, 1131 (2002).
- [97] I. Lesanovsky, P. Schmelcher, and H. R. Sadeghpour, “Ultra-long-range Rydberg molecules exposed to a magnetic field,” *J. Phys. B: At. Mol. Opt. Phys.* **39**, L69 (2006).
- [98] M. Kurz and P. Schmelcher, “Electrically dressed ultra-long-range polar Rydberg molecules,” *Phys. Rev. A* **88**, 022501 (2013).
- [99] M. Kurz and P. Schmelcher, “Ultralong-range Rydberg molecules in combined electric and magnetic fields,” *Phys. Rev. A* **47**, 165101 (2014).
- [100] A. T. Krupp, A. Gaj, J. B. Balewski, P. Ilzhöfer, S. Hofferberth, R. Löw, T. Pfau, M. Kurz, and P. Schmelcher, “Alignment of  $d$ -state Rydberg molecules,” *Phys. Rev. Lett.* **112**, 143008 (2014).
- [101] A. Gaj, A. T. Krupp, P. Ilzhöfer, R. Löw, S. Hofferberth, and T. Pfau, “Hybridization of Rydberg electron orbitals by molecule formation,” *Phys. Rev. Lett.* **115**, 023001 (2015).
- [102] T. Niederprüm, O. Thomas, T. Eichert, C. Lippe, J. Pérez-Ríos, C. H. Greene, and H. Ott, “Observation of pendular Butterfly Rydberg molecules,” *Nat. Commun.* **7**, 12820 (2016).
- [103] I. C. H. Liu and J. M. Rost, “Polyatomic molecules formed with a Rydberg atom in an ultracold environment,” *Europ. Phys. J. D* **40**, 65 (2006).
- [104] I. C. H. Liu, J. Stanojevic, and J. M. Rost, “Ultra-long-range Rydberg trimers with a repulsive two-body interaction,” *Phys. Rev. Lett.* **102**, 173001 (2009).
- [105] C. Fey, M. Kurz, and P. Schmelcher, “Stretching and bending dynamics in triatomic ultralong-range Rydberg molecules,” *Phys. Rev. A* **94**, 012516 (2016).
- [106] M. T. Eiles, J. Pérez-Ríos, F. Robicheaux, and C. H. Greene, “Ultracold molecular Rydberg physics in a high density environment,” *J. Phys. B: At. Mol. Opt. Phys.* **49**, 114005 (2016).
- [107] P. J. J. Luukko and J.-M. Rost, “Polyatomic Trilobite Rydberg molecules in a dense random gas,” *Phys. Rev. Lett.* **119**, 203001 (2017).
- [108] C. Fey, J. Yang, S. T. Rittenhouse, F. Munkes, M. Baluktsian, P. Schmelcher, H. R. Sadeghpour, and J. P. Shaffer, “Effective three-body interactions in  $\text{Cs}(6s)\text{--}\text{Cs}(nd)$  Rydberg trimers,” *Phys. Rev. Lett.* **122**, 103001 (2019).
- [109] M. Schlagmüller, T. C. Liebisch, H. Nguyen, G. Lochead, F. Engel, F. Böttcher, K. M. Westphal, K. S. Kleinbach, R. Löw, S. Hofferberth, T. Pfau, J. Pérez-Ríos, and C. H. Greene, “Probing an electron scattering resonance using Rydberg molecules within a dense and ultracold gas,” *Phys. Rev. Lett.* **116**, 053001 (2016).
- [110] J. Sous, H. R. Sadeghpour, T. C. Killian, E. Demler, and R. Schmidt, “Rydberg impurity in a fermi gas: Quantum statistics and rotational blockade,” *Phys. Rev. Res.* **2**, 023021 (2020).
- [111] K. S. Kleinbach, F. Engel, T. Dieterle, R. Löw, T. Pfau, and F. Meinert, “Ionic impurity in a Bose-Einstein condensate at submicrokelvin temperatures,” *Phys. Rev. Lett.* **120**, 193401 (2018).

- [112] T. Manthey, T. Niederprüm, O. Thomas, and H. Ott, “Dynamically probing ultracold lattice gases via Rydberg molecules,” *New J. Phys.* **17**, 103024 (2015).
- [113] J. D. Whalen, S. K. Kanungo, R. Ding, M. Wagner, R. Schmidt, H. R. Sadeghpour, S. Yoshida, J. Burgdörfer, F. B. Dunning, and T. C. Killian, “Probing nonlocal spatial correlations in quantum gases with ultra-long-range Rydberg molecules,” *Phys. Rev. A* **100**, 011402(R) (2019).
- [114] J. D. Whalen, R. Ding, S. K. Kanungo, T. C. Killian, S. Yoshida, J. Burgdörfer, and F. B. Dunning, “Formation of ultralong-range fermionic Rydberg molecules in  $^{87}\text{Sr}$ : role of quantum statistics,” *Mol. Phys.* **117**, 3088 (2019).
- [115] D. A. Anderson, S. A. Miller, and G. Raithel, “Photoassociation of long-range  $nd$  Rydberg molecules,” *Phys. Rev. Lett.* **112**, 163201 (2014).
- [116] H. Saßmannshausen, F. Merkt, and J. Deiglmayr, “Experimental characterization of singlet scattering channels in long-range Rydberg molecules,” *Phys. Rev. Lett.* **114**, 133201 (2015).
- [117] F. Böttcher, A. Gaj, K. M. Westphal, M. Schlagmüller, K. S. Kleinbach, R. Löw, T. C. Liebisch, T. Pfau, and S. Hofferberth, “Observation of mixed singlet-triplet  $\text{Rb}_2$  Rydberg molecules,” *Phys. Rev. A* **93**, 032512 (2016).
- [118] J. L. MacLennan, Y. J. Chen, and G. Raithel, “Deeply bound  $(24D_J + 5S_{1/2})$   $^{87}\text{Rb}$  and  $^{85}\text{Rb}$  molecules for eight spin couplings,” *Phys. Rev. A* **99**, 033407 (2019).
- [119] I. Mirgorodskiy, F. Christaller, C. Braun, A. Paris-Mandoki, C. Tresp, and S. Hofferberth, “Electromagnetically induced transparency of ultra-long-range Rydberg molecules,” *Phys. Rev. A* **96**, 011402(R) (2017).
- [120] M. Peper and J. Deiglmayr, “Formation of ultracold ion pairs through long-range Rydberg molecules,” *J. Phys. B: At. Mol. Opt. Phys.* **53**, 064001 (2020).
- [121] P. Giannakeas, M. T. Eiles, F. Robicheaux, and J. M. Rost, “Dressed ion-pair states of an ultralong-range Rydberg molecule,” *Phys. Rev. Lett.* **125**, 123401 (2020).
- [122] J. Wang and R. Côté, “Ultralong-range molecule engineering via Rydberg dressing,” *Phys. Rev. Res.* **2**, 023019 (2020).
- [123] N. V. Ewald, T. Feldker, H. Hirzler, H. A. Füst, and R. Gerritsma, “Observation of interactions between trapped ions and ultracold Rydberg atoms,” *Phys. Rev. Lett.* **122**, 253401 (2019).
- [124] T. Schmid, C. Veit, N. Zuber, R. Löw, T. Pfau, M. Tarana, and M. Tomza, “Rydberg molecules for ion-atom scattering in the ultracold regime,” *Phys. Rev. Lett.* **120**, 153401 (2018).
- [125] F. Engel, T. Dieterle, T. Schmid, C. Tomschitz, C. Veit, N. Zuber, R. Löw, T. Pfau, and F. Meinert, “Observation of Rydberg blockade induced by a single ion,” *Phys. Rev. Lett.* **121**, 193401 (2018).
- [126] T. Dieterle, M. Berngruber, C. Hölzl, R. Löw, K. Jachymski, T. Pfau, and F. Meinert, “Inelastic collision dynamics of a single cold ion immersed in a Bose-Einstein condensate,” *Phys. Rev. A* **102**, 041301 (2020).

- [127] T. Dieterle, M. Berngruber, C. Hölzl, R. Löw, K. Jachymski, T. Pfau, and F. Meinert, “Transport of a single cold ion immersed in a Bose-Einstein condensate,” *Phys. Rev. Lett.* **126**, 033401 (2021).
- [128] B. Butscher, J. Nipper, J. B. Balewski, L. Kukota, V. Bendkowsky, R. Löw, and T. Pfau, “Atom–molecule coherence for ultralong-range Rydberg dimers,” *Nature Phys.* **6**, 970 (2010).
- [129] B. Butscher, V. Bendkowsky, J. Nipper, J. B. Balewski, L. Kukota, R. Löw, T. Pfau, W. Li, T. Pohl, and J. M. Rost, “Lifetimes of ultralong-range Rydberg molecules in vibrational ground and excited states,” *J. Phys. B: At. Mol. Opt. Phys.* **44**, 184004 (2011).
- [130] J. Tallant, S. T. Rittenhouse, D. Booth, H. R. Sadeghpour, and J. P. Shaffer, “Observation of blueshifted ultralong-range Cs<sub>2</sub> Rydberg molecules,” *Phys. Rev. Lett.* **109**, 173202 (2012).
- [131] D. Booth, S. T. Rittenhouse, J. Yang, H. R. Sadeghpour, and J. P. Shaffer, “Production of Trilobite Rydberg molecule dimers with kilo-debye permanent electric dipole moments,” *Science* **348**, 99 (2015).
- [132] B. J. DeSalvo, J. A. Aman, F. B. Dunning, T. C. Killian, H. R. Sadeghpour, S. Yoshida, and J. Burgdörfer, “Ultra-long-range Rydberg molecules in a divalent atomic system,” *Phys. Rev. A* **92**, 031403(R) (2015).
- [133] F. Camargo, J. D. Whalen, R. Ding, H. R. Sadeghpour, S. Yoshida, J. Burgdörfer, F. B. Dunning, and T. C. Killian, “Lifetimes of ultra-long-range strontium Rydberg molecules,” *Phys. Rev. A* **93**, 022702 (2016).
- [134] J. D. Whalen, F. Camargo, R. Ding, T. C. Killian, F. B. Dunning, J. Pérez-Ríos, S. Yoshida, and J. Burgdörfer, “Lifetimes of ultralong-range strontium Rydberg molecules in a dense Bose-Einstein condensate,” *Phys. Rev. A* **96**, 042702 (2017).
- [135] R. Ding, S. K. Kanungo, J. D. Whalen, T. C. Killian, F. B. Dunning, S. Yoshida, and J. Burgdörfer, “Creation of vibrationally-excited ultralong-range Rydberg molecules in polarized and unpolarized cold gases of <sup>87</sup>Sr,” *J. Phys. B: At. Mol. Opt. Phys.* **53**, 014002 (2019).
- [136] J. D. Whalen, S. K. Kanungo, Y. Lu, S. Yoshida, J. Burgdörfer, F. B. Dunning, and T. C. Killian, “Heteronuclear Rydberg molecules,” *Phys. Rev. A* **101**, 060701(R) (2020).
- [137] M. Peper and J. Deiglmayr, “Heteronuclear long-range Rydberg molecules,” *Phys. Rev. Lett.* **126**, 013001 (2021).
- [138] M. A. Bellos, R. Carollo, J. Banerjee, E. E. Eyler, P. L. Gould, and W. C. Stwalley, “Excitation of weakly bound molecules to trilobitelike Rydberg states,” *Phys. Rev. Lett.* **111**, 053001 (2013).
- [139] R. A. Carollo, J. L. Carini, E. E. Eyler, P. L. Gould, and W. C. Stwalley, “High-resolution spectroscopy of Rydberg molecular states of <sup>85</sup>Rb<sub>2</sub> near the 5s + 7p asymptote,” *Phys. Rev. A* **95**, 042516 (2017).
- [140] L. Marcassa and J. Shaffer, “Rydberg atom molecules,” *Adv. At. Mol. Opt. Phys.* **63**, 47 (2014).

- [141] J. P. Shaffer, S. T. Rittenhouse, and H. R. Sadeghpour, “Ultracold Rydberg molecules,” *Nat. Commun.* **9**, 1965 (2018).
- [142] M. T. Eiles, “Trilobites, butterflies, and other exotic specimens of long-range Rydberg molecules,” *J. Phys. B: At. Mol. Opt. Phys.* **52**, 113001 (2019).
- [143] A. Gaj, “Rb ultralong-range Rydberg molecules in magnetic and electric fields,” *Eur. Phys. J. Spec. Top.* **225**, 2919 (2016).
- [144] T. C. Liebisch, M. Schlagmüller, F. Engel, H. Nguyen, J. Balewski, G. Lochead, F. Böttcher, K. M. Westphal, K. S. Kleinbach, T. Schmid, A. Gaj, R. Löw, S. Hofferberth, T. Pfau, J. Pérez-Ríos, and C. H. Greene, “Controlling Rydberg atom excitations in dense background gases,” *J. Phys. B: At. Mol. Opt. Phys.* **49**, 182001 (2016).
- [145] H. Saßmannshausen, J. Deiglmayr, and F. Merkt, “Long-range Rydberg molecules, Rydberg macrodimers and Rydberg aggregates in an ultracold Cs gas,” *Eur. Phys. J. Spec. Top.* **225**, 2891 (2016).
- [146] C. Lippe, T. Eichert, O. Thomas, T. Niederprüm, and H. Ott, “Excitation of Rydberg molecules in ultracold quantum gases,” *physica status solidi (b)* **256**, 1800654 (2019).
- [147] C. Boisseau, I. Simbotin, and R. Côté, “Macrodimers: Ultralong range Rydberg molecules,” *Phys. Rev. Lett.* **88**, 133004 (2002).
- [148] S. M. Farooqi, D. Tong, S. Krishnan, J. Stanojevic, Y. P. Zhang, J. R. Ensher, A. S. Estrin, C. Boisseau, R. Côté, E. E. Eyler, and P. L. Gould, “Long-range molecular resonances in a cold Rydberg gas,” *Phys. Rev. Lett.* **91**, 183002 (2003).
- [149] M. Kiffner, H. Park, W. Li, and T. F. Gallagher, “Dipole-dipole-coupled double-Rydberg molecules,” *Phys. Rev. A* **86**, 031401 (2012).
- [150] M. Kiffner, M. Huo, W. Li, and D. Jaksch, “Few-body bound states of dipole-dipole-interacting Rydberg atoms,” *Phys. Rev. A* **89**, 052717 (2014).
- [151] H. Saßmannshausen and J. Deiglmayr, “Observation of Rydberg-atom macrodimers: Micrometer-sized diatomic molecules,” *Phys. Rev. Lett.* **117**, 083401 (2016).
- [152] X. Han, S. Bai, Y. Jiao, L. Hao, Y. Xue, J. Zhao, S. Jia, and G. Raithel, “Cs  $62D_J$  Rydberg-atom macrodimers formed by long-range multipole interaction,” *Phys. Rev. A* **97**, 031403 (2018).
- [153] S. Hollerith, J. Zeiher, J. Rui, A. Rubio-Abadal, V. Walther, T. Pohl, D. M. Stamper-Kurn, I. Bloch, and C. Gross, “Quantum gas microscopy of Rydberg macrodimers,” *Science* **364**, 664 (2019).
- [154] P. Goy, J. M. Raimond, G. Vitrant, and S. Haroche, “Millimeter-wave spectroscopy in cesium Rydberg states. quantum defects, fine- and hyperfine-structure measurements,” *Phys. Rev. A* **26**, 2733 (1982).
- [155] W. Li, I. Mourachko, M. W. Noel, and T. F. Gallagher, “Millimeter-wave spectroscopy of cold Rb Rydberg atoms in a magneto-optical trap: Quantum defects of the  $ns$ ,  $np$ , and  $nd$  series,” *Phys. Rev. A* **67**, 052502 (2003).

- [156] J. Han, Y. Jamil, D. V. L. Norum, P. J. Tanner, and T. F. Gallagher, “Rb  $nf$  quantum defects from millimeter-wave spectroscopy of cold  $^{85}\text{Rb}$  Rydberg atoms,” *Phys. Rev. A* **74**, 054502 (2006).
- [157] J. E. Sansonetti, “Wavelengths, transition probabilities, and energy levels for the spectra of rubidium (RbI through RbXXXVII),” *J. Phys. Chem. Ref. Data* **35**, 301 (2006).
- [158] U. Thumm and D. W. Norcross, “Evidence for very narrow shape resonances in low-energy electron-Cs scattering,” *Phys. Rev. Lett.* **67**, 3495 (1991).
- [159] U. Thumm and D. W. Norcross, “Relativistic  $R$ -matrix calculations for electron-alkali-metal-atom scattering: Cs as a test case,” *Phys. Rev. A* **45**, 6349 (1992).
- [160] D. H. Lee, W. D. Brandon, D. Hanstorp, and D. J. Pegg, “Resonance states in  $\text{Li}^-$  and  $\text{B}^-$ ,” *Phys. Rev. A* **53**, R633 (1996).
- [161] C. Bahrim and U. Thumm, “Low-lying  $^3P^o$  and  $^3S^e$  states of  $\text{Rb}^-$ ,  $\text{Cs}^-$ , and  $\text{Fr}^-$ ,” *Phys. Rev. A* **61**, 022722 (2000).
- [162] C. Bahrim, U. Thumm, and I. I. Fabrikant, “Negative-ion resonances in cross sections for slow-electron-heavy-alkali-metal-atom scattering,” *Phys. Rev. A* **63**, 042710 (2001).
- [163] C. Bahrim and U. Thumm, “Angle-differential and momentum-transfer cross sections for  $e^- + \text{Rb}$ ,  $\text{Cs}$ , and  $\text{Fr}$  collisions at low energies:  $^3F^o$  shape resonances in  $\text{Rb}^-$ ,  $\text{Cs}^-$ , and  $\text{Fr}^-$  ions,” *Phys. Rev. A* **64**, 022716 (2001).
- [164] T. Niederprüm, O. Thomas, T. Manthey, T. M. Weber, and H. Ott, “Giant cross section for molecular ion formation in ultracold Rydberg gases,” *Phys. Rev. Lett.* **115**, 013003 (2015).
- [165] M. Schlagmüller, T. C. Liebisch, F. Engel, K. S. Kleinbach, F. Böttcher, U. Hermann, K. M. Westphal, A. Gaj, R. Löw, S. Hofferberth, T. Pfau, J. Pérez-Ríos, and C. H. Greene, “Ultracold chemical reactions of a single Rydberg atom in a dense gas,” *Phys. Rev. X* **6**, 031020 (2016).
- [166] S. K. Kanungo, J. D. Whalen, Y. Lu, T. C. Killian, F. B. Dunning, S. Yoshida, and J. Burgdörfer, “Loss rates for high- $n$ ,  $49 \lesssim n \lesssim 150$ ,  $5sns$  ( $^3s_1$ ) Rydberg atoms excited in an  $^{84}\text{Sr}$  Bose-Einstein condensate,” *Phys. Rev. A* **102**, 063317 (2020).
- [167] P. Geppert, M. Althön, D. Fichtner, and H. Ott, “Diffusive-like redistribution in state-changing collisions between Rydberg atoms and ground state atoms,” *Nat. Commun.* **12**, 3900 (2021).
- [168] C. E. Theodosiou, “Lifetimes of alkali-metal-atom Rydberg states,” *Phys. Rev. A* **30**, 2881 (1984).
- [169] H. R. Sadeghpour and S. T. Rittenhouse, “How do ultralong-range homonuclear Rydberg molecules get their permanent dipole moments?” *Mol. Phys.* **111**, 1902 (2013).
- [170] M. Born and R. Oppenheimer, “Zur Quantentheorie der Molekeln,” *Ann. Phys. (Leipzig)* **389**, 457 (1927).
- [171] E. L. Hamilton, C. H. Greene, and H. R. Sadeghpour, “Shape-resonance-induced long-range molecular Rydberg states,” *J. Phys. B: At. Mol. Opt. Phys.* **35**, L199 (2002).

- [172] I. I. Fabrikant, “Interaction of Rydberg atoms and thermal electrons with K, Rb and Cs atoms,” *J. Phys. B* **19**, 1527 (1986).
- [173] C. Bahrim, U. Thumm, , and I. I. Fabrikant, “ $^3S^e$  and  $^1S^e$  scattering length for  $e^- +$  Rb, Cs, and Fr collisions,” *J. Phys. B: At. Mol. Opt. Phys.* **34**, L195 (2001).
- [174] A. A. Khuskivadze, M. I. Chibisov, and I. I. Fabrikant, “Adiabatic energy levels and electric dipole moments of Rydberg states of  $Rb_2$  and  $Cs_2$  dimers,” *Phys. Rev. A* **66**, 042709 (2002).
- [175] K. Bartschat and H. R. Sadeghpour, “Ultralow-energy electron scattering from alkaline-earth atoms: the scattering-length limit,” *J. Phys. B: At. Mol. Opt. Phys.* **36**, L9 (2002).
- [176] M. T. Eiles, “Formation of long-range Rydberg molecules in two-component ultracold gases,” *Phys. Rev. A* **98**, 042706 (2018).
- [177] L. Spruch, T. F. O’Malley, and L. Rosenberg, “Modification of effective-range theory in the presence of a long-range potential,” *Phys. Rev. Lett.* **5**, 375 (1960).
- [178] T. F. O’Malley, L. Spruch, and L. Rosenberg, “Modification of effective-range theory in the presence of a long-range ( $r^{-4}$ ) potential,” *J. Math. Phys.* **2**, 491 (1961).
- [179] W. F. Holmgren, M. C. Reville, V. P. A. Lonij, and A. D. Cronin, “Absolute and ratio measurements of the polarizability of Na, K, and Rb with an atom interferometer,” *Phys. Rev. A* **81**, 053607 (2010).
- [180] M. T. Eiles and C. H. Greene, “Ultracold long-range Rydberg molecules with complex multichannel spectra,” *Phys. Rev. Lett.* **115**, 193201 (2015).
- [181] M. I. Chibisov, A. A. Khuskivadze, and I. I. Fabrikant, “Energies and dipole moments of long-range molecular Rydberg states,” *J. Phys. B: At. Mol. Opt. Phys.* **35**, L193 (2002).
- [182] C. H. Greene, E. L. Hamilton, H. Crowell, C. Vadla, and K. Niemax, “Experimental verification of minima in excited long-range Rydberg states of  $Rb_2$ ,” *Phys. Rev. Lett.* **97**, 233002 (2006).
- [183] M. Tarana and R. Curik, “Adiabatic potential-energy curves of long-range Rydberg molecules: Two-electron  $R$ -matrix approach,” *Phys. Rev. A* **93**, 012515 (2016).
- [184] M. Tarana, “Long-range Rydberg molecule  $Rb_2$ : Two-electron  $R$ -matrix calculations at intermediate internuclear distances,” *Phys. Rev. A* **102**, 062802 (2020).
- [185] P. Giannakeas, M. T. Eiles, F. Robicheaux, and J. M. Rost, “Generalized local frame-transformation theory for ultralong-range Rydberg molecules,” *Phys. Rev. A* **102**, 033315 (2020).
- [186] J. Wang, M. Gacesa, and R. Côté, “Rydberg electrons in a Bose-Einstein condensate,” *Phys. Rev. Lett.* **114**, 243003 (2015).
- [187] T. Karpiuk, M. Brewczyk, K. Rzażewski, A. Gaj, J. B. Balewski, A. T. Krupp, M. Schlagmüller, R. Löw, S. Hofferberth, and T. Pfau, “Imaging single Rydberg electrons in a Bose-Einstein condensate,” *New J. Phys.* **17**, 053046 (2015).

- [188] V. M. Borodin and A. K. Kazansky, “The adiabatic mechanism of the collisional broadening of Rydberg states via a loosely bound resonance state of ambient gas atoms,” *J. Phys. B: At. Mol. Opt. Phys.* **25**, 971 (1992).
- [189] B. E. Granger, E. L. Hamilton, and C. H. Greene, “Quantum and semiclassical analysis of long-range Rydberg molecules,” *Phys. Rev. A* **64**, 042508 (2001).
- [190] V. Kanellopoulos, M. Kleber, and T. Kramer, “Use of Lambert’s theorem for the  $n$ -dimensional Coulomb problem,” *Phys. Rev. A* **80**, 012101 (2009).
- [191] M. T. Eiles, Z. Tong, and C. H. Greene, “Theoretical prediction of the creation and observation of a ghost Trilobite chemical bond,” *Phys. Rev. Lett.* **121**, 113203 (2018).
- [192] D. A. Anderson, S. A. Miller, and G. Raithel, “Angular-momentum couplings in long-range  $\text{Rb}_2$  Rydberg molecules,” *Phys. Rev. A* **90**, 062518 (2014).
- [193] S. T. Rittenhouse and H. R. Sadeghpour, “Ultracold giant polyatomic Rydberg molecules: Coherent control of molecular orientation,” *Phys. Rev. Lett.* **104**, 243002 (2010).
- [194] S. T. Rittenhouse, M. Mayle, P. Schmelcher, and H. R. Sadeghpour, “Ultralong-range polyatomic Rydberg molecules formed by a polar perturber,” *J. Phys. B: At. Mol. Opt. Phys.* **44**, 184005 (2011).
- [195] M. Mayle, S. T. Rittenhouse, P. Schmelcher, and H. R. Sadeghpour, “Electric field control in ultralong-range triatomic polar Rydberg molecules,” *Phys. Rev. A* **85**, 052511 (2012).
- [196] R. González-Férez, H. R. Sadeghpour, and P. Schmelcher, “Rotational hybridization, and control of alignment and orientation in triatomic ultralong-range Rydberg molecules,” *New J. Phys.* **17**, 013021 (2015).
- [197] J. Aguilera-Fernández, H. R. Sadeghpour, P. Schmelcher, and R. González-Férez, “Ultralong-range  $\text{Rb} - \text{KRb}$  Rydberg molecules: Selected aspects of electronic structure, orientation and alignment,” *J. Phys.: Conf. Ser.* **635**, 012023 (2015).
- [198] J. Aguilera-Fernández, H. R. Sadeghpour, P. Schmelcher, and R. González-Férez, “Electronic structure of ultralong-range Rydberg penta-atomic molecules with two polar diatomic molecules,” *Phys. Rev. A* **96**, 052509 (2017).
- [199] R. González-Férez, S. T. Rittenhouse, P. Schmelcher, and H. R. Sadeghpour, “A protocol to realize triatomic ultralong range Rydberg molecules in an ultracold  $\text{KRb}$  gas,” *J. Phys. B: At. Mol. Opt. Phys.* **53**, 074002 (2020).
- [200] J. Pérez-Ríos, M. T. Eiles, and C. H. Greene, “Mapping Trilobite state signatures in atomic hydrogen,” *J. Phys. B: At. Mol. Opt. Phys.* **49**, 14LT01 (2016).
- [201] O. Thomas, C. Lippe, T. Eichert, and H. Ott, “Photoassociation of rotating ultra-long range Rydberg molecules,” *J. Phys. B: At. Mol. Opt. Phys.* **51**, 155201 (2018).
- [202] M. T. Eiles, H. Lee, J. Pérez-Ríos, and C. H. Greene, “Anisotropic blockade using pendular long-range Rydberg molecules,” *Phys. Rev. A* **95**, 052708 (2017).
- [203] T. F. Gallagher, *Rydberg Atoms*, Cambridge Monographs on Atomic, Molecular and Chemical Physics (Cambridge University Press, Cambridge, England, 1994).

- [204] J. Aguilera-Fernández, P. Schmelcher, and R. González-Férez, “Ultralong-range triatomic Rydberg molecules in an electric field,” *J. Phys. B: At. Mol. Opt. Phys.* **49**, 124002 (2016).
- [205] E. Arimondo, M. Inguscio, and P. Violino, “Experimental determinations of the hyperfine structure in the alkali atoms,” *Rev. Mod. Phys.* **49**, 31 (1977).
- [206] T. Niederprüm, O. Thomas, T. Eichert, and H. Ott, “Rydberg molecule-induced remote spin flips,” *Phys. Rev. Lett.* **117**, 123002 (2016).
- [207] K. S. Kleinbach, F. Meinert, F. Engel, W. J. Kwon, R. Löw, T. Pfau, and G. Raithel, “Photoassociation of Trilobite Rydberg molecules via resonant spin-orbit coupling,” *Phys. Rev. Lett.* **118**, 223001 (2017).
- [208] S. Bai, X. Han, J. Bai, Y. Jiao, J. Zhao, S. Jia, and G. Raithel, “Cesium  $nD_J + 6S_{1/2}$  Rydberg molecules and their permanent electric dipole moments,” *Phys. Rev. Res.* **2**, 033525 (2020).
- [209] P. Frey, F. Breyer, and H. Hotop, “High resolution photodetachment from the rubidium negative ion around the Rb( $5p1/2$ ) threshold,” *J. Phys. B: At. Mol. Phys.* **11**, L589 (1978).
- [210] M. Scheer, J. Thøgersen, R. C. Bilodeau, C. A. Brodie, H. K. Haugen, H. H. Andersen, P. Kristensen, and T. Andersen, “Experimental evidence that the  $6s6p^3P_J$  states of  $\text{Cs}^-$  are shape resonances,” *Phys. Rev. Lett.* **80**, 684 (1998).
- [211] S. Markson, S. T. Rittenhouse, R. Schmidt, J. P. Shaffer, and H. R. Sadeghpour, “Theory of ultralong-range Rydberg molecule formation incorporating spin-dependent relativistic effects: Cs(6s)–Cs(np) as case study,” *ChemPhysChem* **17**, 3683 (2016).
- [212] M. T. Eiles and C. H. Greene, “Hamiltonian for the inclusion of spin effects in long-range Rydberg molecules,” *Phys. Rev. A* **95**, 042515 (2017).
- [213] C. Veit, N. Zuber, O. A. Herrera-Sancho, V. S. V. Anasuri, T. Schmid, F. Meinert, R. Löw, and T. Pfau, “Pulsed ion microscope to probe quantum gases,” *Phys. Rev. X* **11**, 011036 (2021).
- [214] H.-D. Meyer, U. Manthe, and L. Cederbaum, “The multi-configurational time-dependent Hartree approach,” *Chem. Phys. Lett.* **165**, 73 (1990).
- [215] M. Beck, A. Jäckle, G. Worth, and H.-D. Meyer, “The multiconfiguration time-dependent Hartree (MCTDH) method: a highly efficient algorithm for propagating wavepackets,” *Phys. Rep.* **324**, 1 (2000).
- [216] H.-D. Meyer and G. Worth, “Quantum molecular dynamics: propagating wavepackets and density operators using the multiconfiguration time-dependent Hartree method,” *Theor. Chem. Acc.* **109**, 251 (2003).
- [217] H.-D. Meyer, “Studying molecular quantum dynamics with the multiconfiguration time-dependent Hartree method,” *Wiley Interdiscip. Rev.: Comp. Mol. Sci.* **2**, 351 (2012).
- [218] L. Cao, S. Krönke, O. Vendrell, and P. Schmelcher, “The multi-layer multi-configuration time-dependent Hartree method for bosons: Theory, implementation, and applications,” *J. Chem. Phys.* **139**, 134103 (2013).

- [219] S. Krönke, L. Cao, O. Vendrell, and P. Schmelcher, “Non-equilibrium quantum dynamics of ultra-cold atomic mixtures: the multi-layer multi-configuration time-dependent Hartree method for bosons,” *New J. Phys.* **15**, 063018 (2013).
- [220] L. Cao, V. Bolsinger, S. I. Mistakidis, G. M. Koutentakis, S. Krönke, J. M. Schurer, and P. Schmelcher, “A unified ab initio approach to the correlated quantum dynamics of ultracold fermionic and bosonic mixtures,” *J. Chem. Phys.* **147**, 044106 (2017).
- [221] H. Köppel, W. Domcke, and L. S. Cederbaum, “Multimode molecular dynamics beyond the Born-Oppenheimer approximation,” in *Advances in Chemical Physics*, Vol. 57 (John Wiley & Sons, Ltd., New York, 1984) pp. 59–246.
- [222] G. A. Worth and L. S. Cederbaum, “Beyond Born-Oppenheimer: Molecular dynamics through a conical intersection,” *Annu. Rev. Phys. Chem.* **55**, 127 (2004).
- [223] P. A. M. Dirac, “Note on exchange phenomena in the Thomas atom,” *Math. Proc. Cambridge Phil. Soc.* **26**, 376–385 (1930).
- [224] I. A. Frenkel, *Wave Mechanics* (Oxford University Press, Oxford at the Clarendon Press, 1934).
- [225] G. A. Worth, H.-D. Meyer, H. Köppel, L. S. Cederbaum, and I. Burghardt, “Using the MCTDH wavepacket propagation method to describe multimode non-adiabatic dynamics,” *Int. Rev. in Phys. Chem.* **27**, 569 (2008).
- [226] A. R. Johnston and P. D. Burrow, “Shape resonances in electron scattering from metal atoms,” *J. Phys. B* **15**, L745 (1982).
- [227] A. R. Johnston and P. D. Burrow, “Temporary negative-ion states of Na, K, Rb, and Cs,” *Phys. Rev. A* **51**, 406 (1995).
- [228] L. Hostler and R. H. Pratt, “Coulomb Green’s function in closed form,” *Phys. Rev. Lett.* **10**, 469 (1963).
- [229] V. A. Davidkyn, B. A. Zon, N. L. Manakov, and L. P. Rapoport, “Quadratic Stark effect on atoms,” *Eksp. Teor. Fiz* **60**, 124 (1971), [*Sov. Phys. JETP* 33, 70 (1971)].
- [230] S. P. Andreev, B. M. Karnakov, V. D. Mur, and V. A. Polunin, “Spectrum of weakly bound states of a particle in external electric fields,” *Eksp. Teor. Fiz* **86**, 866 (1984), [*Sov. Phys. JETP* 59, 506 (1984)].
- [231] S. P. Andreev, B. M. Karnakov, and V. D. Mur, “Energy spectrum of a particle in potentials with strongly differing ranges,” *Theor. Math. Phys.* **64**, 838 (1985).
- [232] N. Y. Du and C. H. Greene, “Interaction between a Rydberg atom and neutral perturbers,” *Phys. Rev. A* **36**, 971 (1987).
- [233] C. Fey, M. Kurz, P. Schmelcher, S. T. Rittenhouse, and H. R. Sadeghpour, “A comparative analysis of binding in ultralong-range Rydberg molecules,” *New J. Phys.* **17**, 055010 (2015).
- [234] R. G. Parsons and V. F. Weisskopf, “The spectrum of alkali-atoms,” *Z. Physik* **202**, 492 (1967).

- [235] S. Schmid, A. Härter, A. Frisch, S. Hoinka, and J. H. Denschlag, “An apparatus for immersing trapped ions into an ultracold gas of neutral atoms,” *Rev. Sci. Instrum.* **83**, 053108 (2012).
- [236] A. Härter, A. Krüchow, A. Brunner, and J. Hecker Denschlag, “Minimization of ion micromotion using ultracold atomic probes,” *Appl. Phys. Lett.* **102**, 221115 (2013).
- [237] J. Wolf, M. Deiß, A. Krüchow, E. Tiemann, B. P. Ruzic, Y. Wang, J. P. D’Incao, P. S. Julienne, and J. H. Denschlag, “State-to-state chemistry for three-body recombination in an ultracold rubidium gas,” *Science* **358**, 921 (2017).
- [238] A. Kirrander, S. Rittenhouse, M. Ascoli, E. E. Eyler, P. L. Gould, and H. R. Sadeghpour, “Approach to form long-range ion-pair molecules in an ultracold Rb gas,” *Phys. Rev. A* **87**, 031402(R) (2013).
- [239] E. Reinhold and W. Ubachs, “Heavy Rydberg states,” *Mol. Phys.* **103**, 1329 (2005).
- [240] W. A. Chupka, P. M. Dehmer, and W. T. Jivery, “High resolution photoionization study of ion-pair formation in  $H_2$ , HD, and  $D_2$ ,” *J. Chem. Phys.* **63**, 3929 (1975).
- [241] S. T. Cornett, H. R. Sadeghpour, and M. J. Cavagnero, “Interferometric line shape modulation in alkali-halide photoabsorption,” *Phys. Rev. Lett.* **82**, 2488 (1999).
- [242] T. Launoy, J. Loreau, A. Dochain, J. Liévin, N. Vaeck, and X. Urbain, “Mutual neutralization in  $Li^+ - D^-$  collisions: A combined experimental and theoretical study,” *Astrophys. J.* **883**, 85 (2019).
- [243] S. H. Pan and F. H. Mies, “Rydberg-like properties of rotational-vibrational levels and dissociation continuum associated with alkali-halide charge-transfer states,” *J. Chem. Phys.* **89**, 3096 (1988).
- [244] T. Andersen, “Atomic negative ions: structure, dynamics and collisions,” *Phys. Rep.* **394**, 157 (2004).
- [245] D. J. Pegg, “Structure and dynamics of negative ions,” *Rep. Prog. Phys.* **67**, 857 (2004).
- [246] S. Markson and H. R. Sadeghpour, “A model for charge transfer in ultracold Rydberg ground-state atomic collisions,” *J. Phys. B: At. Mol. Opt. Phys.* **49**, 114006 (2016).
- [247] C. Jungen and M. Raoult, “Spectroscopy in the ionisation continuum. Vibrational preionisation in  $H_2$  calculated by multichannel quantum-defect theory,” *Faraday Discuss. Chem. Soc.* **71**, 253 (1981).
- [248] T. Ban, R. Beuc, H. Skenderović, and G. Pichler, “rubidium pure long-range ion-pair molecules,” *Europhys. Lett.* **66**, 485 (2004).
- [249] M. O. Vieitez, T. I. Ivanov, E. Reinhold, C. A. de Lange, and W. Ubachs, “Observation of a Rydberg series in  $H^+H^-$ : A heavy Bohr atom,” *Phys. Rev. Lett.* **101**, 163001 (2008).
- [250] R. C. Ekey and E. F. McCormack, “Spectroscopic observation of bound ungerade ion-pair states in molecular hydrogen,” *Phys. Rev. A* **84**, 020501 (2011).
- [251] M. Beyer and F. Merkt, “Heavy-Rydberg states of HD and the electron affinity of the deuterium atom,” *J. Chem. Phys.* **149**, 031102 (2018).

- [252] N. Harada and E. Herbst, “Modeling carbon chain anions in L1527,” *Astrophys J.* **685**, 272 (2008).
- [253] L. Pan and D. R. Beck, “Candidates for laser cooling of atomic anions:  $\text{La}^-$  versus  $\text{Os}^-$ ,” *Phys. Rev. A* **82**, 014501 (2010).
- [254] C. W. Walter, N. D. Gibson, D. J. Matyas, C. Crocker, K. A. Dungan, B. R. Matola, and J. Rohlén, “Candidate for laser cooling of a negative ion: Observations of bound-bound transitions in  $\text{La}^-$ ,” *Phys. Rev. Lett.* **113**, 063001 (2014).
- [255] E. Jordan, G. Cerchiari, S. Fritzsche, and A. Kellerbauer, “High-resolution spectroscopy on the laser-cooling candidate  $\text{La}^-$ ,” *Phys. Rev. Lett.* **115**, 113001 (2015).
- [256] R. Tang, R. Si, Z. Fei, X. Fu, Y. Lu, T. Brage, H. Liu, C. Chen, and C. Ning, “Candidate for laser cooling of a negative ion: High-resolution photoelectron imaging of  $\text{Th}^-$ ,” *Phys. Rev. Lett.* **123**, 203002 (2019).
- [257] L. Hammarström and S. Styring, “Coupled electron transfers in artificial photosynthesis,” *Philos. Trans. R. Soc. B* **363**, 1283 (2008).
- [258] M. Barbatti, A. J. A. Aquino, J. J. Szymczak, D. Nachtigallová, P. Hobza, and H. Lischka, “Relaxation mechanisms of UV-photoexcited DNA and RNA nucleobases,” *Proc. Natl. Acad. Sci. U.S.A.* **107**, 21453 (2010).
- [259] C. Arnold, O. Vendrell, R. Welsch, and R. Santra, “Control of nuclear dynamics through conical intersections and electronic coherences,” *Phys. Rev. Lett.* **120**, 123001 (2018).
- [260] N. Mabrouk, W. Zrafi, and H. Berriche, “Theoretical study of the  $\text{LiNa}$  molecule beyond the Born–Oppenheimer approximation: adiabatic and diabatic potential energy curves, radial coupling, adiabatic correction, dipole moments and vibrational levels,” *Mol. Phys.* **118**, e1605098 (2020).
- [261] N. Moiseyev, M. Šindelka, and L. S. Cederbaum, “Laser-induced conical intersections in molecular optical lattices,” *J. Phys. B: At. Mol. Opt. Phys.* **41**, 221001 (2008).
- [262] M. Šindelka, N. Moiseyev, and L. S. Cederbaum, “Strong impact of light-induced conical intersections on the spectrum of diatomic molecules,” *J. Phys. B: At. Mol. Opt. Phys.* **44**, 045603 (2011).
- [263] S. Wüster, A. Eisfeld, and J. M. Rost, “Conical intersections in an ultracold gas,” *Phys. Rev. Lett.* **106**, 153002 (2011).
- [264] F. M. Gambetta, C. Zhang, M. Hennrich, I. Lesanovsky, and W. Li, “Exploring the many-body dynamics near a conical intersection with trapped Rydberg ions,” *Phys. Rev. Lett.* **126**, 233404 (2021).
- [265] J. von Neumann and E. P. Wigner, “Über merkwürdige diskrete Eigenwerte,” *Physik. Z.* **30**, 467 (1929).
- [266] E. Teller, “The crossing of potential surfaces.” *J. Phys. Chem.* **41**, 109 (1937).
- [267] L. Levi, M. Rechtsman, B. Freedman, T. Schwartz, O. Manela, and M. Segev, “Disorder-enhanced transport in photonic quasicrystals,” *Science* **332**, 1541 (2011).

- [268] S. Kolkowitz, S. L. Bromley, T. Bothwell, M. L. Wall, G. E. Marti, A. P. Koller, X. Zhang, M. Rey, and J. Ye, “Spin-orbit-coupled fermions in an optical lattice clock,” *Nature (London)* **542**, 66 (2017).
- [269] A. Celi, P. Massignan, J. Ruseckas, N. Goldman, I. B. Spielman, G. Juzeliūnas, and M. Lewenstein, “Synthetic gauge fields in synthetic dimensions,” *Phys. Rev. Lett.* **112**, 043001 (2014).
- [270] O. Boada, A. Celi, J. I. Latorre, and M. Lewenstein, “Quantum simulation of an extra dimension,” *Phys. Rev. Lett.* **108**, 133001 (2012).
- [271] T. Ozawa, H. M. Price, A. Amo, N. Goldman, M. Hafezi, L. Lu, M. C. Rechtsman, D. Schuster, J. Simon, O. Zilberberg, and I. Carusotto, “Topological photonics,” *Rev. Mod. Phys.* **91**, 015006 (2019).
- [272] S. K. Kanungo, J. D. Whalen, Y. Lu, M. Yuan, S. Dasgupta, F. B. Dunning, K. R. A. Hazzard, and T. C. Killian, “Realizing Su-Schrieffer-Heeger topological edge states in Rydberg-atom synthetic dimensions,” (2021), arXiv:2101.02871 [physics.atom-ph] .
- [273] D. A. Anderson, A. Schwarzkopf, R. E. Sapiro, and G. Raithel, “Production and trapping of cold circular Rydberg atoms,” *Phys. Rev. A* **88**, 031401(R) (2013).
- [274] A. Ramos, K. Moore, and G. Raithel, “Measuring the Rydberg constant using circular Rydberg atoms in an intensity-modulated optical lattice,” *Phys. Rev. A* **96**, 032513 (2017).
- [275] R. Cardman and G. Raithel, “Circularizing Rydberg atoms with time-dependent optical traps,” *Phys. Rev. A* **101**, 013434 (2020).
- [276] R. G. Cortiñas, M. Favier, B. Ravon, P. Méhaignerie, Y. Machu, J. M. Raimond, C. Sayrin, and M. Brune, “Laser trapping of circular Rydberg atoms,” *Phys. Rev. Lett.* **124**, 123201 (2020).
- [277] T. Cantat-Moltrecht, R. Cortiñas, B. Ravon, P. Méhaignerie, S. Haroche, J. M. Raimond, M. Favier, M. Brune, and C. Sayrin, “Long-lived circular Rydberg states of laser-cooled rubidium atoms in a cryostat,” *Phys. Rev. Res.* **2**, 022032(R) (2020).
- [278] R. C. Teixeira, A. Larrouy, A. Muni, L. Lachaud, J.-M. Raimond, S. Gleyzes, and M. Brune, “Preparation of long-lived, non-autoionizing circular Rydberg states of strontium,” *Phys. Rev. Lett.* **125**, 263001 (2020).
- [279] D. B. Tretyakov, I. I. Beterov, E. A. Yakshina, V. M. Entin, I. I. Ryabtsev, P. Cheinet, and P. Pillet, “Observation of the borromean three-body Förster resonances for three interacting Rb Rydberg atoms,” *Phys. Rev. Lett.* **119**, 173402 (2017).
- [280] I. I. Beterov, I. N. Ashkarin, E. A. Yakshina, D. B. Tretyakov, V. M. Entin, I. I. Ryabtsev, P. Cheinet, P. Pillet, and M. Saffman, “Fast three-qubit Toffoli quantum gate based on three-body Förster resonances in Rydberg atoms,” *Phys. Rev. A* **98**, 042704 (2018).
- [281] T. L. Nguyen, J. M. Raimond, C. Sayrin, R. Cortiñas, T. Cantat-Moltrecht, F. Assemat, I. Dotsenko, S. Gleyzes, S. Haroche, G. Roux, T. Jolicoeur, and M. Brune, “Towards quantum simulation with circular Rydberg atoms,” *Phys. Rev. X* **8**, 011032 (2018).

# Dank

Viele verschiedene Menschen haben einen Anteil daran, dass diese Dissertation entstehen konnte, und ich empfinde dafür tiefe Dankbarkeit.

Als Erstes danke ich Prof. Dr. Peter Schmelcher: Danke, dass Du mir ermöglicht hast in Deiner Arbeitsgruppe zu forschen und zu promovieren. Danke für die spannenden Diskussionen, Ideen und insbesondere für Deine willkommene Kritik, die ohne Zweifel meine Arbeit besser gemacht hat. Ich danke Dir auch für die vielen Freiheiten, sowohl im Hinblick auf die Forschungsfragen, als auch für Auslandsaufenthalte und Besuche von Konferenzen und Workshops.

Danke Prof. Dr. Henning Moritz für die Begutachtung der Arbeit und Prof. Dr. Daniela Pfannkuche für den Vorsitz der Prüfungskommission, sowie auch deren weiteren Mitgliedern Prof. Dr. Andreas Hemmerich und Priv. Doz. Dr. Tim Laarmann.

Weiterer Dank geht an Dr. Hossein R. Sadeghpour: Thank you, Hossein, for enabling my research stay at the Institute for Theoretical Atomic Molecular and Optical Physics in Cambridge. I still miss our soccer matches and Armando's pizza afterwards and I am grateful for your hospitality and proud of the results of our collaboration.

Ich danke allen Kollegen, mit denen ich Zusammenarbeiten konnte. Christian, danke, dass Du mir all Dein Wissen über Rydberg Moleküle geschenkt hast. Matt, thank you for the endless and exciting discussions. Kevin, danke für Deine MCTDH Expertise. Florian, Felix, und Thomas, danke für die tolle Zusammenarbeit an Eurem Experiment in Stuttgart; Johannes und Markus, danke für die tolle Zusammenarbeit an Eurem Experiment in Ulm; Carsten, Tanita, Max und Jana, danke für Eure Gastfreundschaft bei meinem Forschungsbesuch in Kaiserslautern und die vielen Erklärungen zu Eurem Experiment. Matt, Dan, Kevin und Florian, ich bin dankbar für Eure Versuche diese Arbeit von ihren größten Fehlern zu befreien.

Ich möchte mich auch bei allen Beteiligten von GiRyd, insbesondere bei Kati Kriesch, bedanken. Da ist eine beeindruckende wissenschaftliche Community zusammen gewachsen. Danke für tolle Workshops, eine geniale Summer School in Israel und das Ermöglichen von den ganzen Forschungsbesuchen, durch die ich von vielen Menschen lernen konnte.

Mein Dank geht an alle Kollegen am Zentrum für optische Quantentechnologien. Eine solche Kollegialität ist nicht selbstverständlich! Thomas, Jan, Sven, Andrea, Christian, Ihr wart die beste Truppe, die man sich wünschen kann, um zu lernen den Forschungsalltag durch zu stehen. Anja, danke für Deine endlose Hilfsbereitschaft. Kevin, Fabian, Friethjof, Dan, danke für den gemeinsamen Einsatz für das Fortbestehen der Kaffeetraditionen unserer Arbeitsgruppe.

Besonderer Dank gilt meinen Freunden Joschka, Patrick und Jonas, die ich immer an meiner Seite weiß. Meiner Familie bin ich dankbar für die grenzenlose Unterstützung all die Jahre lang und dafür, dass ich nie daran zweifeln brauchte diesen Weg zu gehen. Insbesondere danke ich meinen Eltern: Durch Euer Vertrauen und Euren Stolz ist das alles hier erst möglich geworden. Für den Dank an meiner Partnerin und besten Freundin Karin gibt es gar keine Worte. Danke, dass Du es mit mir aushälst.



# Eidesstattliche Versicherung

Hiermit versichere ich an Eides statt, die vorliegende Dissertationsschrift selbst verfasst und keine anderen als die angegebenen Hilfsmittel und Quellen benutzt zu haben.

Die eingereichte schriftliche Fassung entspricht der auf dem elektronischen Speichermedium.

Die Dissertation wurde in der vorgelegten oder einer ähnlichen Form nicht schon einmal in einem früheren Promotionsverfahren angenommen oder als ungenügend beurteilt.

Hamburg, den 10. Juli 2021